UNIVERSITY OF CALIFORNIA SAN DIEGO

# Interfacial Interactions of Organic Pollutants in the Marine Environment:

# Selective Transfer and Photo-Initiated Reactions

A Dissertation submitted in partial satisfaction of the requirements
for the degree Doctor of Philosophy

in

Chemistry

by

Adam Cooper

Committee in charge:

Professor Jonathan Slade, Chair
Professor Jennifer Burney
Professor Jeremy Klosterman
Professor Kimberly Prather
Professor Michael Tauber

2024

The Dissertation of Adam Cooper is approved, and it is acceptable in quality and form for publication on microfilm and electronically.

University of California San Diego

2024

# DEDICATION

In memory of my uncles: Jason for showing me how to laugh and Steve for teaching me how to stop and appreciate the world around me.

EPIGRAPH

*“So, what sunscreen do you recommend?”*

*“Clean TRV Now!”*

*“The atmosphere is a dynamic chemical reactor”*

*“CCC, si se puede”*

TABLE OF CONTENTS

LIST OF FIGURES

LIST OF TABLES

# LIST OF ABBREVIATIONS

4-BBA: 4-Benzoylbenzoic acid

AF: Aerosolization factor

AMS: Aerosol mass spectrometer

BF: Borderfield State Park

BP: Benzophenone

BP3: Benzophenone-3, oxybenzone

BPMeO: 4-methoxy benzophenone

BPOH: 2-hydroxy-benzophenone

BzO: Benzaldehyde

BzOH: Benzoic acid

CE: Collection efficiency

CEC: Contaminant of emerging concern

CHO: Oxidized hydrocarbons

CHON: Nitrogen containing oxidized hydrocarbons

CHOS: Sulfur containing oxidized hydrocarbons

CIMS: Chemical ionization mass spectrometry

CPC: Condensation particle counter

DBZ: Dibenzylamine

DMA: Differential mobility analyzer

DMS: Dimethyl sulfide

DOM: Dissolved organic matter

EE: Extraction efficiency

EESI: Extractive electrospray ionization

EPISUITE: EPA Estimation Programs Interface Suite

ESHT: Excited state hydrogen transfer

ESI: Electrospray ionization

FIGAERO: Filter inlet for gases and aerosols

GNPS: Global Natural Product Social Molecular Networking

HOMO: Highest occupied molecular orbital

IB: Imperial Beach

IE: Ionization efficiency

ISC: Intersystem crossing

ISV: Isolated sampling vessel

IVOC: Intermediate volatile organic compound

LCMS: Liquid Chromatography Mass Spectrometry

LPM: Liters per minute

LUMO: Lowest unoccupied molecular orbital

m-CDOM: Marine chromophoric dissolved organic matter

MCM: Master chemical mechanism

MS/MS: Tandem mass spectrometry

MSA: Methanesulfonic acid

OA: Organic aerosol

OFR: Oxidative flow reactor

OMC: Octinoxate

OSc: Carbon oxidation state

PAM: Potential Aerosol Mass

PFAS: Per- and polyfluoroalkyl substances

PM: Particulate matter

PTR: Proton transfer reaction

QSAR: Quantitative structure-activity relationship

RF: Response factor

RH: Relative humidity

ROS: Reactive oxygen species

SA: Surface area

SEMS: Scanning electrical mobility spectrometer

SI: Supporting information

SIO: Scripps Institution of Oceanography

SMA: Secondary marine aerosol

SML: Sea surface microlayer

SOA: Secondary organic aerosol

SS: Silver Strand State Park

SSA: Sea spray aerosol

SVOC: Semivolatile organic compound

TE: Transmission efficiency

TEST: Toxicity Estimation Software Tool

TJR: Tijuana River

TOF: Time of flight

TP: Transformation products

TRV: Tijuana River Valley

UVF: Ultraviolet filter

UV-Vis: Ultraviolet-visible spectroscopy

VBS: Volatility Basis Set

VOC: Volatile organic compound

ACKNOWLEDGEMENTS

I want to acknowledge the fantastic group of individuals who have made up the first six years of the Slade Lab, starting with my supportive advisor, Nate, without whom this work would not be possible. Nate has stuck by me through twists and turns and allowed me the freedom to pursue my unique path through graduate school. I am honored I was able to help establish his lab, and grateful for the countless hours of instructive meetings, in-depth editing, and getting to know each other.

Special thanks are due to Ryan Tumminello and Samantha Kruse, whom I started with in the first year of the Slade Lab. Being in the first group of students is challenging but rewarding, and I'm glad I had a close-knit group to navigate that with. I'll never forget our early group meetings and our times at Ralphs and the Watering Hole.

To the other members of the Slade Lab, I'm grateful for the chance to build our welcoming culture and establish our traditions. Special shout-out to Ben Carr, the reigning Galactic Emperor of Twilight Imperium 4$^{th}$ edition. I'm excited to see what new heights Lincoln, Diana, Maya, and Kanuri will take our lab.

My network at grad school stretched far beyond our group – I am grateful to have been able to work and commiserate with my cohort mates Alexia, Stephanie, Deb, and Kyle. I enjoyed being so close to the wonderful and helpful members of the Prather and Grassian labs, especially Karla, David, Matt, Jon, Kathryn, and David. My other friends – Sascha, Abi, Abby, Sarah, and Jubi kept me social.

I am eternally grateful to Mrs. Fiero, Dr. Indralingam, Anthony, Dr. Sibbald, Dr. Goodson, and Dr. Lieberman for teaching me the fundamentals of chemistry and

research. Whenever I push arrows, balance an equation, innovate on the spot, and put together a poster or PowerPoint, I have you all to thank.

My home on campus has always been with the members of the Green New Deal at UCSD. I was able to help build our campus into the one I pictured when I first arrived here, and we made a lasting positive change on campus. I am grateful for the long nights scheming, trips to Regents meetings, and time chanting on the megaphone with Monica, Maxwell, Adam, SuZ, Kina, Nan, Cathy, Joyce, Aliya, Megyn, Stephanie, Ann, Luke, Sofia, Elise, and so many more wonderful souls.

I'm grateful to the external teams I've served on in student government for facilitating my first forays into science policy. Victor, Quynh, Cong, Gwen, Julia, Ryan and Hayden were all amazing leaders I had the privilege of learning from and procrastinating writing white papers with. I hope we see each other back on the Hill one day!

To da union, I'm glad to learn what solidarity means. Winning the first contract for graduate workers (and a 56% raise over my six years at UCSD!) was an eye-opening example of the power people have when we come together to get what we deserve. Shout-out to Conor, Hiya, Danea, Ahmed, Anna, and everyone who filled out a form, talked to their coworkers, and held a picket sign.

My roots in San Diego developed through my involvement with community organizing with the Sunrise Movement. We won the largest climate bill in world history, made the American Climate Corps, and showed up for environmental justice in the streets of San Diego, Los Angeles, San Francisco, Sacramento, DC, and Wilmington. I count my hub members among my closest friends and role models – especially Vianni,

Ido, Izzy, Simren, Alyssa, Naomy, Connor, Riley, Trinish, Czeska, Nikayla, Himma, George, Megyn, John Henry, Josiah, Julia, Avi, Simon, Michelle, Coffey, Khrizia, Moiz, Em, Chandini, and Ben.

To the broader international climate justice community, I'm so happy to have met you in the halls of the United Nations, at conferences and protests, in Korea, and on TikTok. I'm proud of helping, among many, to build the College Campus Network to revitalize the student climate movement. Special shout-out to Ray, Robert, Steve, Achal, Shahena, Ano, Jake, Ilana, Alicia, Garima, Sydney, Nkosi, Mel, Sarah, Em, Jorge, Karla, Joshua, Lex, Shannon, Luis, Sheina, Anpo, Marinda, Afra, Sharona, and Victoria.

I want to thank my roommates, Jacob, Joseph, Kenneth, and even Victor, for keeping me sane and well-socialized at the beginning and end of my graduate career. I appreciate Jacob saying yes to every chance to explore San Diego together and Joe for getting me hooked on board games.

To my best friends Jake, Matt, and Zach, I am so grateful to have stayed connected over the long years since middle and high school. Your trips to San Diego were a highlight of my time here, and I'm amazed we all made it through in one piece. You kept me sane during the lockdown playing Borderlands and stretched my imagination on Dungeons and Dragons.

To Sage, I'm glad I caught up to you in California and for all the fantastic times we had together across the whole state. Whether it was finding a trampoline in the fields of SLO, screaming into the crashing waves at Santa Monica, or climbing up waterfalls in Yosemite, you always brought adventure into my life. You mean the world to me.

To my partner Riese, you have introduced me to so much and pushed me intellectually and on the dance floor. You were able to re-teach me what love is, what I deserve, and how I can show that.

I want to thank my family for supporting me throughout this process, always answering my calls on my daily walks, and keeping me up to date on what was going on back in Florida. We weathered several storms and tragedies, and I am grateful I always had you to lean on. Mom and Dad, you dedicated your lives to enabling your kids to succeed and set us up perfectly for success. To my sisters Aimee, Alyssa, and Autumn, I'm glad we're growing even closer now that we're apart and all grown up (even you, Autumn!) I'm grateful to my cousin Trevor for driving out to San Diego with me, and I am still salty that my travel-bug cousin Brian never visited.

Chapter 3, in part, has been submitted for publication of the material as it may appear in Science Advances, 2024, Cooper, A, Pendergraft, M, Petras, D, Cancelada, L, Belcher, K, Torres, R, Small, M, Garrafa-Luna, J, Belda-Ferre, P, Simpson, R, Morris, C, Mitts, B, Aron, A, Zhang, J, Price, T, Dinasquet, J, Dorrestein, P, Knight, R, Slade, J.H., Prather, K. The dissertation author was the primary investigator and author of this material.

Chapter 4, in full, has been submitted for publication of the material as it may appear in *ACS Environmental Science & Technology: Air*, 2024, Cooper, A, Shenkiryk, A, Morris, M, Chin, H, Mehndiratta, L, Roundtree, K, Tafuri, M, Slade, J.H. The dissertation author was the primary investigator and author of this paper.

Chapter 5, in full, is currently being prepared for submission for publication of the material as it may appear in *Atmospheric Chemistry & Physics*, Cooper, A, Shenkiryk,

A, Morris, M, Chin, H, Mehndiratta, L, Roundtree, K, Tafuri, M, Slade, J.H. The dissertation author was the primary investigator and author of this paper.

Chapter 6, in part, reproduces the publication “We Need a “Keeling Curve” Approach for Contaminants of Emerging Concern” by Cooper et al., 2023, in *Environ. Sci. Technol.* This manuscript has been published with open access under license CC-BY 4.0.

# VITA

## EDUCATION

2018 Bachelor of Science in Chemistry, Stetson University

2024 Doctor of Philosophy in Chemistry, University of California San Diego

## AWARDS AND HONORS

| | |
|---|---|
| Sunrise Project Climate Finance Campaign Fellowship | 2023 |
| Certificate of Special Congressional Recognition, Office of Sen. Jacky Rosen | 2022 |
| NSF Graduate Research Fellowship | 2020 |
| Agouron Kamen/Kaplan Fellowship | 2018 |

## PUBLICATIONS

**Cooper, A,** Lin, Z, Canada, I, Kilgour, D, Moore, A, Kruse, S, Sauer, J, Mayer, K, Betram, T, Cappa, C, Prather, K, Slade, J.H, (2024) Online characterization of secondary marine aerosol using extractive electrospray ionization, in preparation for submission to *Atmospheric Chemistry & Physics*.

Aron, A, Gere, C, **Cooper, A,** Nelson, M, Thackray, V, (2024) Never doubt that a small group of the committed can change the world: celebrating the grassroots climate movement in the University of California, in review at *Frontiers in Sustainability*

**Cooper, A,** Shenkiryk, A, Morris, M, Chin, H, Mehndiratta, L, Roundtree, K, Tafuri, M, Slade, J.H, (2024) Rapid Photodegradation of UV Filter Oxybenzone in the Aerosol Phase Compared to Bulk Solution, in review at *ACS Environmental Science & Technology: Air*

**Cooper, A,** Pendergraft, M, Petras, D, Cancelada, L, Belcher, K, Torres, R, Small, M, Garrafa-Luna, J, Belda-Ferre, P, Simpson, R, Morris, C, Mitts, B, Aron, A, Zhang, J, Price, T, Dinasquet, J, Dorrestein, P, Knight, R, Slade, J.H., Prather, K, (2024) Wastewater-Derived Pollutants in Coastal Marine Aerosols: Spatiotemporal Distributions and Links to Sea Spray, in preparation for resubmission to *Science Advances*

Obanya, H, Khan, F, Carrasco-Navarro, V ,Rodland, E, Walker-Franklin, I, Thomas, J, **Cooper, A,** Molden, N, Amaeze, N, Patif, R, Kukkola, A, Michie, L, Green-Ojo, B, Rauert, C, Couceiro, F, Hutchison, G, Tang, J, Ugoir, J, Lee, S, Hofmann, T, Ford, A, (2024) Priority Research Questions for Tire Microplastics and their Additives - A Collective Perspective, in review at *Environmental Pollution*

**Cooper, A**, Rogers, M, Wiggin, K, Slade, J.H., (2023) We Need a “Keeling Curve” Approach for Contaminants of Emerging Concern, *Environmental Science & Technology* 57, 28, 10147-10150

Tumminello, P, James, R, Kruse, S, Kawasaki, A, **Cooper, A,** Guadalupe-Diaz, I, Lopo-Zepeda, K, Crocker, D, Mayer, K, Sauer, J, Lee, C, Prather, K, Slade, J. H., (2021) Evolution of Sea Spray Aerosol Particle Phase State Across a Phytoplankton Bloom, *ACS Earth and Space Chemistry*

ORAL PRESENTATIONS

*Photo-initiated degradation kinetics of the organic UV filter oxybenzone in the bulk and aerosol phase: Impact of salt, photosensitizers, and environmental phase, and effects on toxicity*, ACS Fall 2024 Meeting

*Non-targeted tandem mass spectrometry enables detection of molecular markers of microplastics in the coastal environment,* AGU 2021 National Meeting

*Global impact of microplastic and organic UV filter pollution on ocean stability*, ACS 2019 Fall Meeting

*Global impact of the synergistic toxicity of microplastics and organic UV filters on phytoplankton*, MICRO 2020

*Chemists Without Borders’ model for saving water and capturing carbon through biochar production and use*, ACS 2019 Fall Meeting

ACADEMIC SERVICE

| | |
|---|---|
| UCOP Pathways to a Fossil-Free UC Taskforce, Student Representative | 2023-2024 |
| UCSD Academic Senate Campus Climate Change Committee, Student Representative | 2022-2023 |
| UC Graduate and Professional Council, Director of Organizing | 2022-2023 |
| UCSD Graduate and Professional Student Association, Legislative Liaison for State Affairs | 2020-2022 |

ABSTRACT OF THE DISSERTATION

Interfacial Interactions of Organic Pollutants in the Marine Environment:

Selective Transfer and Photo-Initiated Reactions

by

Adam Cooper

Doctor of Philosophy in Chemistry

University of California San Diego, 2024

Professor Jonathan Slade, Chair

Contaminants like plastics, pharmaceuticals, illicit drugs, and personal care products enter the oceans directly or indirectly from land runoff, rivers, and atmospheric deposition. While known to accumulate at the ocean surface, the efficiency of transfer into sea spray aerosols (SSA) at the ocean-air interface and their atmospheric lifetime once airborne is relatively understudied. Photosensitizing materials found in marine dissolved organic matter may lead to enhanced photochemical removal of pollutants. A

complete analysis of these pollutants' transfer and environmental fate is warranted to improve our collective understanding of the full impact of human activities on public and ecological health. Additionally, the full complexity of the natural coastal marine atmosphere remains poorly understood, compounding the difficulty in isolating and understanding the impacts of anthropogenically introduced materials. Secondary marine aerosol (SMA) formed from the oxidation and condensation of biogenically emitted gases drives marine cloud formation, which may serve as a natural buffer system for human-caused climate change. Deepening our understanding of these complex systems requires detailed characterization of the organic compounds that constitute polluted and natural marine aerosols.

Our findings identify SSA as an important vector for transporting several illicit drugs, personal care products, and plastic additive compounds from the ocean to the atmosphere. Quantifying selected contaminants in aerosol and water samples across multiple coastal sites in San Diego revealed a regional hotspot near the Tijuana River outflow, with the amount of pollutants transferred into SSA dependent on their ocean concentration and lipophilicity. This airborne pathway underscores the need for revised health assessments in polluted coastal regions due to the heightened exposure risk for coastal residents and visitors.

An investigation of the photo-induced degradation kinetics of the toxic sunscreen ingredient oxybenzone (BP3) in seawater and SSA mimics reveals rapid degradation in aerosols compared to bulk solutions. Despite this rapid degradation, the formation of toxic transformation products suggests sustained environmental and health risks. Investigations into pure, binary, and ternary mixtures of BP3, NaCl, and the

photosensitizer 4-benzoyl benzoic acid using solar-simulated light isolated the effects of salt and photosensitization on BP3 degradation.

The first-ever measurements of SMA by extractive electrospray ionization mass spectrometry highlighted the importance of hydrocarbons such as isoprene and monoterpenes in producing organic aerosol mass, demonstrating how the organic character of SMA shifts throughout a phytoplankton bloom, and identified the role of phytoplankton and bacterial production sources of sulfur- and nitrogen-containing substituents.

This dissertation emphasizes the intricate interactions between pollutants, natural marine processes, and atmospheric dynamics. It contributes to a deeper understanding of the complex interplay between coastal contaminants and marine atmospheric chemistry, highlighting the urgent need for comprehensive environmental management strategies.

# Chapter 1 Introduction

## 1.1 Atmospheric aerosols in the anthropocene

Aerosols are suspended liquid, solid, semisolid, or amorphous particles in a gas ranging in size from about one nanometer to one hundred micrometers. Depending on their size and meteorological factors, they may persist in the atmosphere for minutes to weeks. The unique chemical and physical properties of the condensed phase suspended in air can significantly impact air quality and climate.[1–4]

Aerosols are categorized into primary aerosols, which are directly emitted from sources such as dust, pollen, volcanic ash, sea spray aerosol generation from crashing waves, and smoke from incomplete combustion,[1,5] and secondary aerosols, which are generated in the atmosphere through reactions of gases that subsequently condense onto existing aerosols or nucleate new particles.[6–8] All aerosol particles undergo “aging” in the atmosphere through physical and chemical processing, such as photochemical and oxidative reactions, vapor condensation, particle-particle interactions such as coagulation and coalescence, or incorporation into cloud droplets.[9–12] Aerosols exhibit various sizes and compositions, significantly affecting their atmospheric reactivity and impacts on air quality and Earth’s climate.

### 1.1.1. Impacts on air quality

Exposure to particulate matter (PM) is one of the leading causes of global mortality, contributing to an estimated 8 million premature deaths per year, making it the second leading cause of death worldwide.[13] PM is traditionally separated into two size categories based on its interaction with the human respiratory system: PM2.5 (exhibiting a mean diameter of less than 2.5 μm) and PM 10 (exhibiting a mean diameter of less than 10 μm.) The upper respiratory system mainly captures PM10, while PM2.5 may

penetrate the lungs. Additional size categories, such as submicron (PM1, exhibiting a mean diameter less than 1 μm) and ultrafine particles (exhibiting a mean diameter less than 100 nm), may pass through biological barriers and further penetrate the pulmonary circulation system.[3,14]

Inhalation poses an accelerated risk factor for acute and chronic toxic compounds, as the lung-blood barrier is less efficient at inhibiting toxic uptake than the dermal barrier and digestive system.[3] Recent developments in aerosol toxicology have demonstrated that not only the mass or number of particles matter but also their composition.[3,14–16] The US Environmental Protection Agency regulates aerosol-bound lead as a criteria air pollutant, and hundreds of compounds are noted as “hazardous air pollutants” without any safe levels of exposure. [17,18] Pollutants are considered toxic if they pose risks due to acute exposure (such as PM irritating lungs) or chronic exposure (such as children growing up with regular exposure to PM developing asthma.)[19,20]

Traditionally, the focus has been on compounds associated with fossil fuel combustion, such as polycyclic aromatic hydrocarbons and industrial emissions.[21–25] Recently, researchers have shifted their attention to contaminants of emerging concern, such as personal care products, pharmaceuticals, and plastics.[16,26,27]

Aerosols also impact visibility through scattering light, which can create a haze if aerosols are present in high enough concentrations. For example, the secondary organic aerosol (SOA) produced by oxidizing biogenic volatile organic compounds (BVOCs) in the Smokey Mountains gives the National Park its eponymous name. Visibility impairment is a public nuisance but can also have significant implications, especially in aviation. Indeed, a particularly bad air pollution episode has been

postulated to be a determining factor in the airplane crash that killed John F. Kennedy Jr.[28]

### 1.1.2. Impacts on climate

Aerosol interactions with Earth's climate system remain the least well-parameterized anthropogenic forcing on the planet's radiative balance, which dictates global temperature.[29,30] The climate crisis is caused primarily by the combustion of fossil fuels, which leads to emissions of heat-absorbing gases such as $CO_2$ and $CH_4$. The impacts of these gases are well parameterized, with effective radiative forcings of 2.16 ± 0.25 W $m^{-2}$ for $CO_2$ and 0.54 ± 0.11 W $m^{-2}$ for $CH_4$.[31] In contrast, anthropogenic aerosols' radiative forcings are less well-constrained. Direct aerosol-radiation interactions (-0.22 ± 0.25 W $m^{-2}$) and indirect aerosol-cloud interactions (-0.84± 0.61 W $m^{-2}$) have a net cooling effect.[31] In essence, aerosols' cooling effect masks some of the warming effects of anthropogenic greenhouse gas emissions. The high relative uncertainties for aerosols (73-114%) compared to gases (12-20%) highlight our collective lack of understanding of aerosol-climate interactions. The higher associated uncertainties are due to the large variability in aerosol properties and composition, especially in aerosol impacts on cloud properties, lifetime, and precipitation.[32–34]

Natural aerosols make up 70% of global aerosol mass load[35] with the largest contribution from sea spray aerosol (50%.)[36] Sea spray exhibits the largest direct radiative forcing of all aerosol categories (-3.5 ± 2.5 W $m^{-2}$,) which is a larger forcing than total anthropogenic greenhouse gas emissions.[35] Its indirect effect through cloud formation is twice as high (-7 ± 2.5 W $m^{-2}$.) Secondary aerosol is another major contributor to aerosol cooling, with biogenic secondary aerosol (SOA and sulfate) each exhibiting a direct radiative forcing of 1.0 ± 0.5 W $m^{-2}$ and anthropogenic aerosol (soot

and anthropogenic sulfate) each exhibiting a direct radiative forcing of +0.5 ± 1.0 W $m^{-2}$ and -0.7 ± 1.0 W $m^{-2}$, respectively. This demonstrates that all aerosol, natural and anthropogenic, lead to considerable variability in climate models.

As air quality improves globally, the subsequent loss of cooling aerosol may exacerbate the rise in global temperature, leading to an unstable climate. This effect was demonstrated in 2020 when the International Maritime Organization reduced the sulfur content of shipping fuel from a standard of 3.5% to 0.5%, sharply reducing the amount of sulfate aerosol over the world's oceans.[37] This termination shock, with an individual estimated radiative forcing of 0.2 ± 0.1 W $m^{-2}$[38], combined with an El Niño event in 2023, led to the most significant observed increase in global temperature in 2023[39], above the 1.5°C target set by the United Nations Paris Agreement.[40]

Much discussion has occurred around using aerosols' cooling effects to geoengineer the atmosphere to counteract the warming impacts of greenhouse gas emissions.[41–43] A complete understanding of aerosol interactions with Earth's climate system is necessary to fully constrain the anthropogenic forcings causing the climate crisis and promote reasonable policy to balance their beneficial cooling effects with their harmful side effects.

### 1.1.3. Regime shift from combustion to petrochemical product pollution

From the 1880s to today, humanity has extracted massive amounts of carbon from fossil fuel deposits and released them into the atmosphere.[29,40] As the world's nations race to net zero, we are focused on the emissions of greenhouse gases yet continue to produce petrochemical products, many of which are volatile. As highlighted in a seminal article by McDonald *et al.* 2018[44], the urban atmosphere is entering a regime shift. Ambient air pollution, once caused by the combustion of fossil fuels, is now

increasingly linked to volatile chemical products that serve as gaseous precursors to secondary aerosols. Similarly, as anthropogenic sulfate aerosols rapidly decrease over the world's oceans, they are replaced by ever-growing amounts of airborne microplastics transferring from the ocean's surface.

We are entering "Anthropocene 2.0" as we rapidly decarbonize our energy systems while continuing the exponential growth of our chemical product industries.[44–50] The full impacts of this shift on public health and the Earth's climate system have yet to be quantified. This dissertation seeks to contribute to our collective understanding of a subset of these petrochemical products most common at the coast: sunscreens.[51–53]

**1.2 Marine pollution**

Petrochemical products, including plastics, play an integral part in modern societies. Production growth is greater than that of steel, cement, and aluminum combined, and growth rates have increased by a factor of six since 1980.[50] About 18% of global industrial $CO_2$ emissions can be attributed to the chemical and petrochemical industries.[54] An additional environmental challenge is plastic refuse and its accumulation in the environment. An estimated 33 billion tons of plastics will be added to the planet by 2050.[55,56] Most of these plastics come from construction materials and personal care products. Almost 10% of the annual production of plastics (~37 million metric tons) accumulate in the world's oceans, where they become incorporated into the food chain, sediments, or enriched at the sea surface.[55] Over 40% of all plastics are unregulated and contain toxic chemical additives.[57] These include organic pollutants of emerging concern, such as organic UV filters, which provide skin protection from the sun in sunscreens and delay the photodegradation of some plastics.[55,56,58] These UV filters are

ubiquitous in the marine environment and are known to cause mass devastation of reef environments through coral bleaching and other developmental abnormalities in marine biota.[59–65]

Our exponential production and consumption of plastics and organic chemicals of emerging concern, and their subsequent mismanagement (only 9% of plastic produced is recycled),[47] is creating a "contaminant cocktail" in the marine environment, inciting urgency for policy action to protect the marine biosphere.[66,67] Current policies regulating plastic and UV filter inputs to the ocean cannot meet the scale of the marine productivity crisis. Proper solid waste and wastewater disposal has been neglected in high-risk coastal communities. Tourist areas such as beaches attract high volumes of consumers, perpetuating plastic and organic chemical inputs to coastal marine ecosystems.[68]

The ocean, once seen as the solution to pollution via dilution, is becoming increasingly saturated with plastics and organic contaminants and serves not only as a sink but also as a source of global transport.[27,69]

### 1.2.1. Organic UV filters: properties, sources, and marine concentrations

Organic UV filters absorb and dissipate incoming solar UV radiation. They are found in personal care products, most notably sunscreens, and are also used as additives in other materials, such as plastics and packaging materials, to protect against photodegradation.[53,70,71] The primary organic UV filters used in sunscreens are oxybenzone (benzophenone-3, BP3), homosalate, octinoxate (ethylhexyl methoxycinnamate, EHMC), and octocrylene (OC).[72] The size of the global sunscreen industry is challenging to estimate, but it was valued at $750 million in 2020 and is projected to increase to $3 billion by 2031.[73]

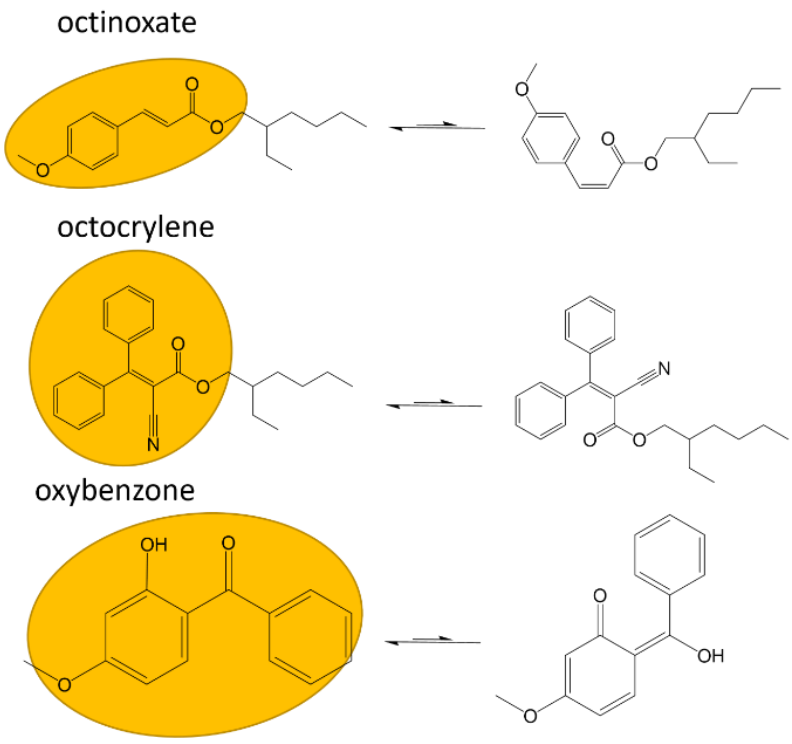


**Figure 1.1** Structures of three organic UV filters (octinoxate, octocrylene, and oxybenzone) and their photo-initiated isomers. The orange highlighted regions designate conjugated π bond networks.

UV filters' chemical structures feature conjugated systems (highlighted in orange in **Fig. 1.1)** that allow them to absorb incoming UV radiation through the absorption of photons, which excite electrons from a π to π* orbital. Another common feature is unsaturated carbon chains (such as 2-ethyl hexane moieties in octinoxate and octocrylene) that assist in their application as oily sunscreen agents. These aromatic and aliphatic groups lead to their general hydrophobicity and lipophilicity, which controls their transport in the environment and biological systems.[74–76]

In the environment, UV filters have been demonstrated to partition into the sea surface microlayer (SML) and particulate matter.[77–79] UV filters enter the marine environment through various routes. Primary pollution occurs at recreational beach

sites, where swimmers and other beachgoers wear sunscreens and other personal care products, which may contain up to 10% organic UV filters.[53,72] Concentrations at these sites range from 10 ppb upwards of 1 ppm at extremely crowded locations (Hawaii and the U.S. Virgin Islands are shown as the most prominent data points in **Fig. 1.2**),[58,59] This means that at some crowded beaches, concentrations of single compounds rival that of the entire dissolved organic matter system.[80]

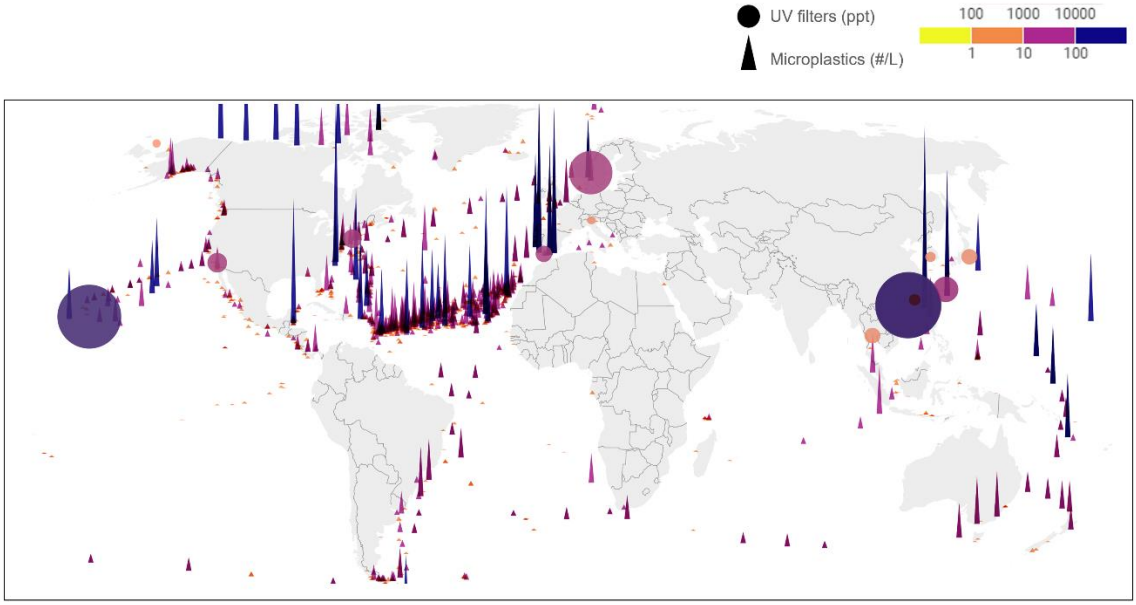


**Figure 1.2** Global distribution of organic UV filters (in mass concentration) and microplastics (in # $L^{-1}$.) Circles represent UV filters, and spikes represent microplastics.

Another major route of introduction to the oceans is through the wastewater stream, where influents can range widely from 100 ppt up to 10 ppm and release in the effluent and sludge at similar levels due to inefficient removal.[74,81] Additionally, over 80% of the world's wastewater is untreated and mostly flows into the ocean.[82] These localized hotspots can travel globally, with background concentrations

postulated to result from global transport measured in the Arctic at ~10 ppt and Central Pacific at ~10 ppb, as shown in **Figure 1.2**[58,83]

In addition to personal care products, UV filters are widely added during the manufacturing of plastics.[84] The estimated incorporation of UV filters and other plastic stabilizers is 0.05-3% by weight.[85] Roughly 8.3 million tons of plastics have been produced as of 2015[47], suggesting a UV filter and stabilizer mass of 4-250 million tons.

The UV filter BP3 is the most reported UV filter in environmental samples[58,59,74,75,78,81,86–94] and the most widely banned active ingredient in sunscreen.[51,95–99] For that reason, it often serves as a model compound for studies investigating the broad class of UV filters.[63,100–113] However, critical knowledge gaps remain regarding its environmental lifetime and reactivity in the aerosol phase. **Chapter 5** will investigate the photochemical transformations of BP3**.**

### 1.2.2. Sewage crisis in southern San Diego.

The discharge from the Tijuana River profoundly impacts coastal waters along the southern border of San Diego, California, and Tijuana, Mexico.[114–117] Originating in Mexico, the Tijuana River carries a complex mixture of raw sewage and runoff from urban and agricultural sources into the Pacific Ocean. Despite collaborative efforts between the United States and Mexico to divert and treat the river's flow, heavy precipitation events within the river's watershed can overwhelm existing infrastructure, leading to billions of gallons of untreated water entering the ocean near Imperial Beach. This environmental challenge threatens marine ecosystems and poses significant public health risks to densely populated coastal communities in both Tijuana and San Diego.

Studies have indicated a direct link between exposure to contaminated coastal waters and increased illness incidents among swimmers, notably from pathogens like norovirus.[118] Pendergraft *et al*. 2021[119] first investigated the potential ocean-to-air transfer of pollutants in this region using a pollutant mimic dye released from the Tijuana River, which was detected in aerosol samples as far as ~700 m inland. A follow-up sampling campaign demonstrated a clear link between bacterial populations in the Tijuana River and coastal air, but their analysis of chemical components was inconclusive.[120] This motivates further inquiry into the concentrations and transfer of these pollutants in this highly impacted region, which will be detailed in **Chapter 3.**

### 1.3 Marine aerosol

The marine aerosol system is vital to understanding aerosols' impact on climate and air quality, given that the ocean covers 70% of the Earth's surface and over a third of the world's population lives within 100 km of the coast.[121] Marine aerosol can be categorized as primary, directly emitted from the ocean by mechanical wave-breaking action (sea spray aerosol, SSA), and secondary, produced from chemical reactions involving marine-derived volatile compounds (secondary marine aerosol, SMA). Contaminants present along the ocean's surface can transfer into SSA or partition to the atmosphere in the gas phase, where they can contribute to SMA. The following sections detail these processes.

#### 1.3.1 Sea Spray Aerosol (SSA)

Sea spray aerosol (SSA) represents the largest particle flux by mass emitted into the atmosphere, estimated to be ~10 Pg $yr^{-1}$.[36] SSA is generated mechanically primarily from the rupture of bubbles at the sea's surface caused by crashing waves and wind-driven whitecap formation.[36,122,123] SSA contains a rich variety of components from

inorganic constituents ($Na^+$, $K^+$, $Ca^{2+}$, $Mg^{2+}$, $Cl^-$, $SO_4^{2-}$) to a wide variety of organic compounds such as fatty acids, saccharides, alkanes, anionic surfactants, dicarboxylic acids, amino acids, proteinaceous matter, and others.[5,124,125]

SSA is produced through three discrete processes: spume droplets (from shearing wind abrasion at the ocean's surface), film droplets (from the popping of bubbles at the surface), and jet droplets (from the collapse of a bubble cavity.) These three processes produce three modes of SSA size (film – ultrafine, jet – fine, spume – coarse.)[126,127]

SSA generation occurs at the ocean's surface, which is covered by the sea surface microlayer (SML.) This organic-rich film, often called the "ocean's skin," is a 1-1000 μm thick region that accumulates hydrophobic compounds such as fatty acids and many anthropogenic pollutants.[128–130] These compounds may selectively transfer—that is, undergo greater emission via SSA compared to other, more water-soluble compounds of similar oceanic concentration.[131,132] Intact biological material, such as viruses and bacteria, may be similarly concentrated in the SML and transferred into SSA.[120,133,134] The transfer of organic contaminants of emerging concern is further detailed in **Chapter 3**.

### 1.3.2. SSA as a vector for organic pollutants

Combining the widespread pollution in the ocean with research on the selective transfer of organic components in SSA, interest has developed in the role SSA can play in serving as a vector for organic pollutants.[27,69,119,120]

A major research focus has been on per- and polyfluroalkyl substances (PFAS.) PFAS are a diverse group of chemicals used in various products due to their water, oil, and heat resistance.[135] They are known as "forever chemicals" due to their persistence

in the environment.[136] PFAS have been identified to transfer into the atmosphere via SSA, where they are prone to global transport.[137–139] Incorporation into cloud droplets and subsequently deposit onto land is another major pathway that can impact freshwater and agricultural systems.[26,140]

Similarly, microplastics have been measured in SSA and shown to undergo global transport.[27,69,141] Allen *et al*. 2022[27] provided the first attempt to consolidate emerging research constraining the global fluxes of especially marine-relevant microplastics. They estimated an open ocean SSA flux of 8.5 Mt (million tons) per year with a marine atmospheric concentration of up to 25 Mt.[142–144] Most (99%) is estimated to be recycled through deposition into the ocean[144] with yearly onshore transport of 140,000 tons along the coast.[69] These estimates are inconclusive, with recent reports arguing an upper bound of 0.1 Mt $yr^{-1}$,[145] and the terrestrial atmospheric microplastic burden is mainly unknown.

The emission of personal care product pollution has not been sufficiently identified and measured in coastal aerosol. Although sunscreens are a widely used personal care product, the detection of their semivolatile UV filters is sparingly recorded in atmospheric surveys. An early note was taken of the presence of octinoxate and oxybenzone in Caribbean tradewinds in Mayol-bracero *et al.* 2001[146], suggesting large-scale transport. Schoeib *et al.* 2016 reported combined UV filter concentrations of ~10 ng $m^{-3}$ in aerosol above a wastewater treatment tank in Ontario, Canada. Pegoraro *et al.* 2020 [88] reported up to 14 pg $m^{-3}$ of octinoxate in aerosol and 960 pg $m^{-3}$ homosalate in the gas phase in urban Toronto air. Generally, concentrations were higher in the gas phase than in the aerosol phase in this environment. This held for the two UV filters

investigated in this dissertation – oxybenzone had an aerosol partitioning coefficient (i.e., percent in the aerosol phase out of total airborne concentration) of 5.3 ± 4.6% and octinoxate 1.3 ± 4.1%. One case of their detection was in SSA generated during SeaSCAPE 2019.[147,148] This dissertation aims to quantify the emissions of several emerging contaminants for the first time (**Chapter 2**) and investigate the atmospheric photochemistry of BP3 (**Chapter 3**.)

### 1.3.3. Secondary marine aerosol

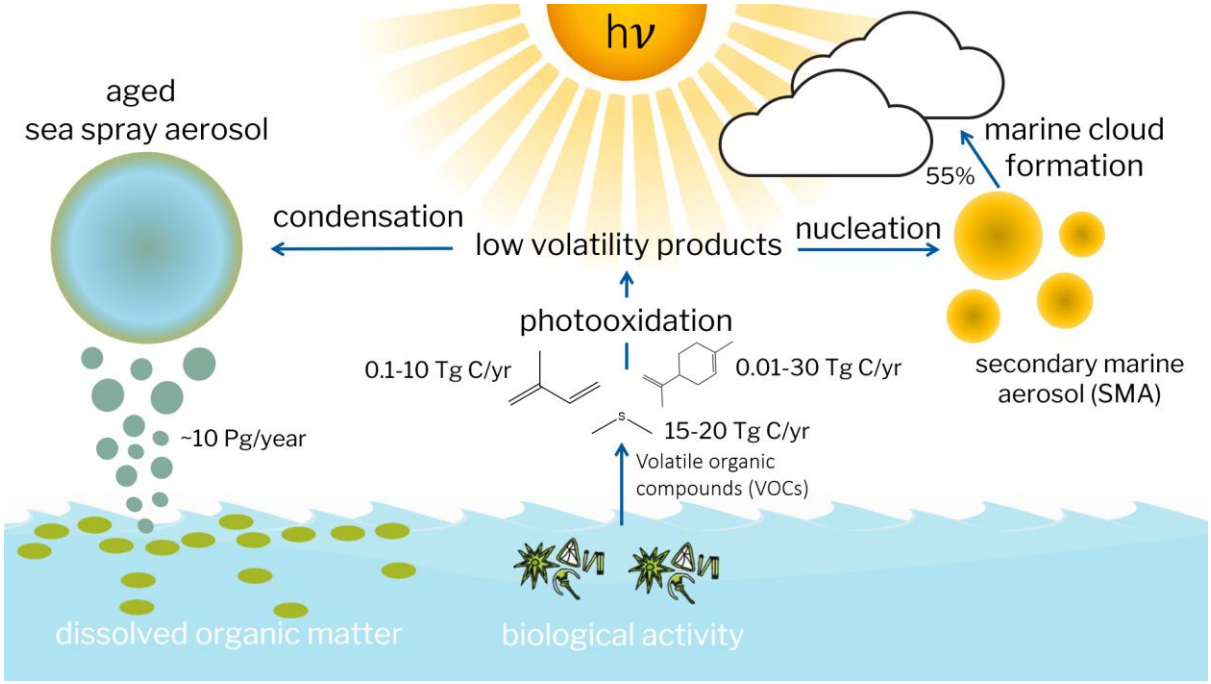


**Figure 1.3** The secondary marine aerosol system, estimated fluxes, and contributions to marine cloud formation.

As shown in **Figure 1.3,** secondary marine aerosol (SMA) is produced via the oxidation of gas phase species, primarily dimethyl sulfide (DMS,) alkyl amines, and other biogenic VOCs.[149–151] Many of these species are produced by marine phytoplankton[152–155] and algae[156–158]Species emit VOCs for various reasons, including signaling stress, serving as secondary metabolites, and protecting against predation.[158]

For this reason, the emissions of different VOCs increase and decrease at various stages of biotic life cycles, contributing to a complex and ever-changing emission profile from the ocean.[159–162]

Oxidation of VOCs adds functional groups such as aldehydes, alcohols, and carboxylic acids, lowering their volatility.[163,164] See **Figure 1.4** for a generalized scheme of these reactions. Oxidation in the presence of $NO_x$ may also produce organonitrogen species, similarly showing lowered volatility.[165,166] This allows for the condensation of organic material onto existing aerosol.[167] The nucleation of new particles is also observed, primarily through acid-base catalyzed interactions between acidic species (such as $SO_2$ and methanesulfonic acid, both oxidation products of DMS) and basic gases (such as $NH_3$ and alkyl amines.)[168–170]

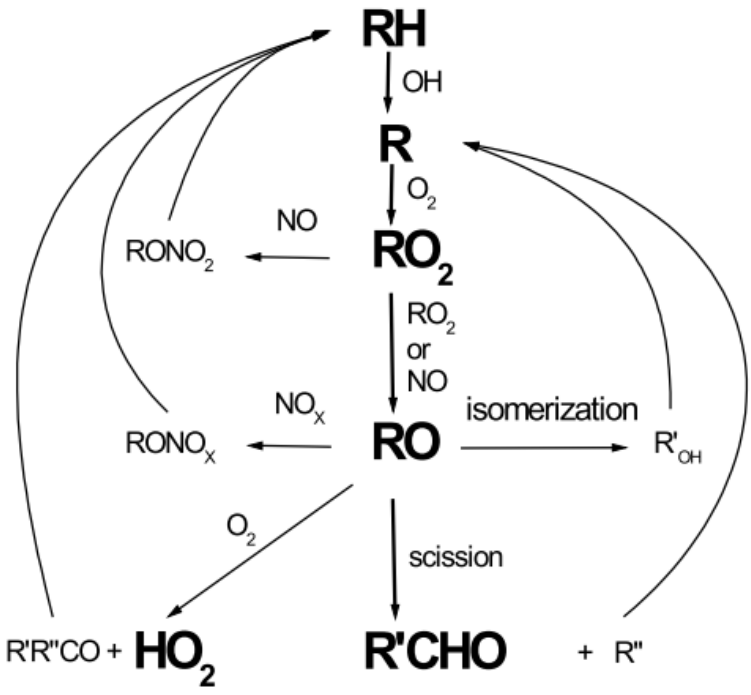


**Figure 1.4** A general ·OH oxidation scheme of an alkane species initiated via hydrogen abstraction. Adapted from Molina *et al* 2004.[171]

There is a rich variety of hydrocarbon emissions from the ocean, including isoprene and monoterpenes (the most abundant non-methane hydrocarbons and terrestrial SOA precursors.)[159,160,172] A recent survey of Eastern Atlantic marine aerosol by Kilgour *et al.*[161] found that the organic component of SMA can be well parameterized solely through the incorporation of expected isoprene and monoterpene SOA products. Unsaturated species such as isoprene and monoterpenes undergo addition reactions in the presence of ·OH (see **Fig 1.5**,) which are favored compared to hydrogen abstraction when accessible.

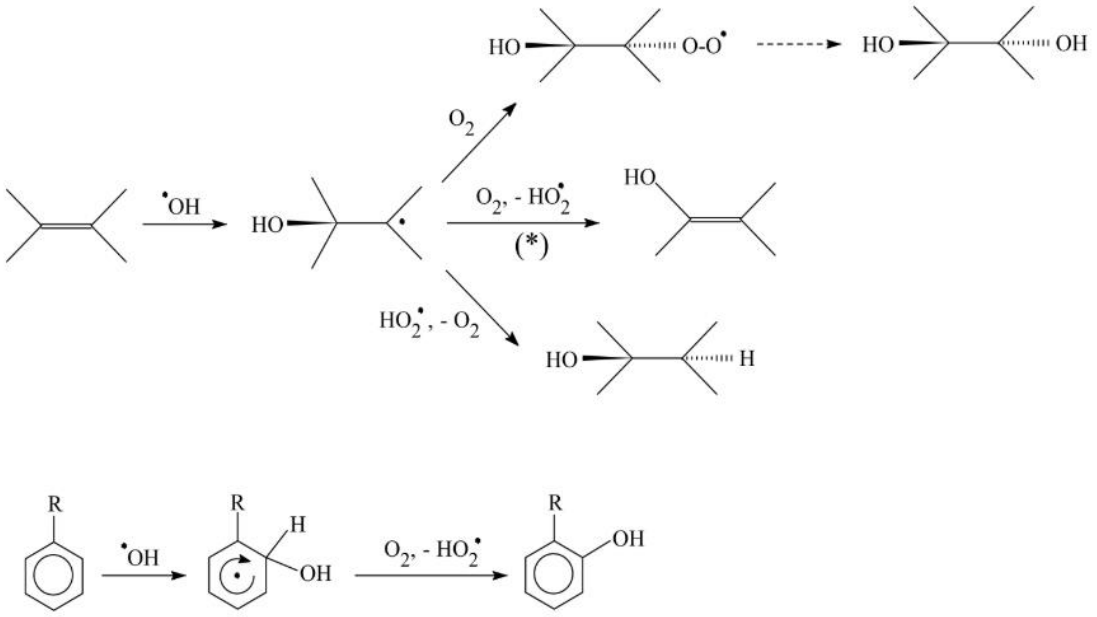


**Figure 1.5** A general ·OH oxidation scheme of unsaturated hydrocarbons initiated via addition. Adapted from Gligorovski *et al. 2015.*[173]

DMS is the precursor for most of the sulfur in SMA. Its oxidation pathway terminates with either $SO_2$, which can form $SO_4$ in the condensed phase, or other acidic sulfur-containing species, such as methanesulfonic acid (MSA). Alkyl amines are the primary source of nitrogen-containing organic mass in SMA.[174] They may directly

interact with acidic species to nucleate new particles or oxidize into less volatile organonitrate species, which may condense onto existing aerosol.[155,174–176]

The nucleation of new particles is one of the largest areas of continued inquiry in SOA and SMA research. Two main contributing factors are the formation of extremely low volatility species (for example, $I_2$[177] or very high molecular weight organic compounds[160]) as well as acid-base interactions (such as $SO_4$ or MSA with $NH_3$ or alkyl amines.)[154,172,175,176,178,179]

SMA drives cloud formation in the marine environment, especially under high biological activity.[149] SMA formation is highly dependent on ocean biological activity, as DMS and other VOCs are primarily produced by oceanic species such as phytoplankton.[152,153,180] This relationship between DMS emissions and cloud formation has been brought to prominence by the “CLAW hypothesis,” named after the initials of coauthors Charlson, Lovelock, Andreae, and Warren, who produced a seminal manuscript on a hypothesized negative feedback loop.[153] They postulate that higher sea surface temperatures in a warming climate will promote biological growth, emitting sulfurous gases into the atmosphere that condense into aerosol and seed clouds, increasing Earth’s albedo and cooling the planet. This hypothesis has been widely argued, including by Lovelock himself, who, 30 years after the CLAW paper, proposed that instead, there would exist a positive feedback loop—that increased temperatures would stratify the ocean, leading to a decrease in nutrient cycling and less biological activity.[181] In either case, the impact of SMA is a net cooling effect from the refraction of sulfate-containing aerosol and the increased albedo from cloud formation.

It is important to note that in the Anthropocene, the primary productivity of the oceans has halved in the last 50 years.[182] This suggests either the viability of the anti-CLAW hypothesis or points to additional anthropogenic stress factors such as pollution, ocean acidification, and biodiversity loss in reducing phytoplankton populations that may produce cooling aerosols.[183,184]

A complete understanding of SMA must incorporate non-DMS VOCs, which will have different temporal patterns along the lifecycle of marine phytoplankton. While the potential precursors of SMA have been identified extensively in the literature, comparatively little has been reported on its organic composition. Chemical properties of the organic components in SMA, such as molecular weight and oxidation state, can significantly impact the physical properties of aerosol, such as hygroscopicity and phase.[185–187] The ratio between organic and inorganic components of aerosol can have similar effects.[188] Thus, understanding SMA's organic carbon properties and environmental lifetime is important to better understand its interaction with Earth's climate system. **Chapter 5** highlights key pathways in the production of organosulfur, organonitrogen, and oxygenated organic compounds in SMA from measurements taken at the Scripps Institution of Oceanography in collaboration with the NSF Center for Aerosol Impacts on Chemistry of the Environment (NSF-CAICE).

## 1.4. Atmospheric photochemistry

### 1.4.1. Gas photooxidation

Solar radiation generates reactive oxygen species (ROS) such as $O_3$ and ·OH in the atmosphere. In the troposphere, $O_3$ is generated through reactions involving volatile organic compounds (VOCs), $NO_x$ ($NO+NO_2$), and $O_2$.[189] The following is the net reaction scheme in which $NO_x$ serves as a catalyst:

$$RH + 4O_2 \rightarrow R'CHO + 2O_3 + H_2O \quad R1$$

$O_3$ can also be produced through the direct oxidation of CO with ·OH. ·OH itself is produced through the photolysis of $O_3$ in the following two-step reaction scheme:

$$O_3 + \text{hv}\ (\lambda < 305\ nm) \rightarrow O(^1D) + O_2 \quad R2$$

$$O(^1D) + H_2O \rightarrow 2 \cdot OH \quad R3$$

Additional sources of ·OH are HONO photolysis and the decomposition of Criegee intermediates of reactions of $O_3$ and alkenes. ·OH is known as the "detergent of the atmosphere"[190] due to its dominance of daytime oxidation chemistry and fast reactivity compared to $O_3$. As such, the lifetime of organic species in the atmosphere is primarily dictated by their reactivity with ·OH.[173] Oxidation via ·OH occurs for alkane species via hydrogen abstraction. For functionalized molecules, ·OH generally preferentially abstracts hydrogens in order from -SH, HC-O/HC=O carbons, and -NH groups. In alkenes and aromatic compounds, ·OH preferentially adds to the double bond. Oxidation via ·OH can generate additional radicals in the aerosol phase, such as Cl· from reactions **R4** and **R5**.

$$\cdot OH + Cl^- \rightarrow HOCl\cdot^- \quad R4$$

$$HOCl\cdot^{-1} + H^+ \rightarrow H_2O + Cl\cdot \quad R5$$

### 1.4.2. Aerosol photochemistry

The Sun emits light via blackbody radiation at its surface temperature of 5250 °C, ranging from 250-2500 nm with a peak of ~500 nm (green). The ozone layer absorbs the lower end of solar irradiance, so the light reaching the troposphere has a lower end of ~290 nm. Light in this UV range can be absorbed by components in aerosol, leading to energy transfer, which results in either heat or photo-induced reactions.[42,43,191–193]

Aerosols may either scatter light through Mie scattering or absorb incoming solar light. Air molecules and the smallest ultrafine aerosols scatter light through Rayleigh scattering. This process causes the blue color of the sky, as blue light at shorter wavelengths is more efficiently scattered by ultrafine aerosol in the atmosphere. Leonardo Da Vinci first remarked on this phenomenon when he wrote: “The atmosphere assumes this azure hue by reason for the particles of moisture which catch the rays of the sun.”[194]

Aerosol color can be categorized based on how it interacts with solar light.[192] Most inorganic and organic aerosols are categorized as “white” as they scatter solar light, leading to a net cooling effect on the climate. Some organic aerosols may absorb solar light, which can further be separated into Black Carbon (BC), which absorbs over a broad spectral range from ultraviolet (UV) to infrared (IR), and Brown Carbon (BrC), which sparingly absorbs in the visible range but absorbs in atmospherically relevant ranges of UV light.[195,196] Black carbon is typically produced through the incomplete combustion of organic matter (leading to soot), while brown carbon can be made through various sources.

Exposure to solar radiation is also a major removal pathway for organic aerosols. When organic aerosol components in BC or BrC absorb light, this can lead to photo-induced reactions. BrC has been shown to “photo-bleach” with atmospheric processing due to photolytic and oxidative reactions breaking down the UV-absorbing components into smaller molecules that do not absorb as strongly at tropospherically relevant wavelengths.[197,198] Photolysis can significantly impact aerosol composition, including

degrading aerosol components into more volatile species that evaporate, reducing aerosol mass.[199–201]

#### 1.4.2.1 Direct photolysis

Here, we focus on direct interaction from photon absorption. When photons of sufficient energy (higher than the enthalpy of formation) interact with chemical bonds, the energy may be released through bond cleavage, photoisomerization, decomposition, hydrogen abstraction, or energy transfer to other compounds (photosensitization). General reaction schemes are found in **Table 1**.

**Table 1.1.** Possible photochemical reactions for an excited molecule A−B−C*, adapted from Calvert and Pitts[191]

| Reaction pathway | Name |
|---|---|
| A−B−C* → A−B• +C• | Bond cleavage (photolysis) into free radicals |
| A−B−C* → A-C-B | Photoisomerization (typically, heat is released through rotational vibration.) |
| A−B−C* → E + F | Photoisomerization followed by decomposition into stable molecules |
| A−B−C* +RH → A−B−C−H+ R• | H-abstraction from a neighboring molecule |
| A−B−C* +D → A−B−C+D* | Photosensitization (energy transfer of all kinds) |
| A−B−C* +D → A−B−$C^+$ +$D^-$ | Photosensitization (electron transfer) |

One common atmospheric photolysis reaction is the Norrish type 1 reaction, which is the homolytic cleavage of a C-C bond next to an absorbing ketone group. A representation of this reaction, using oxybenzone (a model UV filter compound investigated in (**Chapter 4**), is shown below in **Scheme 1.1.**

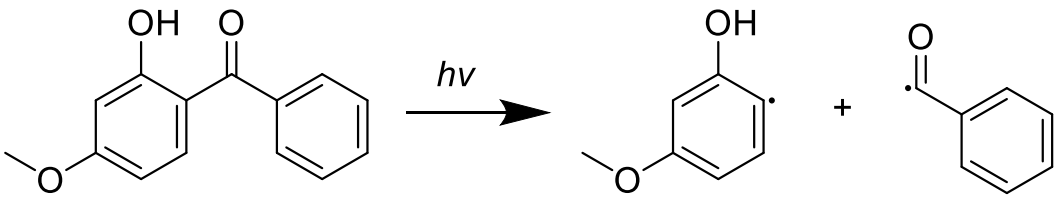


**Scheme 1.1.** Norrish Type 1 reaction of oxybenzone.

The efficiency of photochemical reactions is a function of the compound's absorption cross section (σ(λ), the effective 2-D area in which a compound's conjugated π system may accept photons of a particular energy), and the quantum yield for the reaction (φ(λ), the probability of a reaction occurring after the absorption of a photon.) It is often helpful to incorporate the spectral flux density (I(λ), the concentration of photons) to calculate the effective photochemical rate coefficient, J. This relationship is shown below:

$$J = \int \sigma(\lambda)\varphi(\lambda)\mathrm{I}(\lambda)d\lambda \qquad eq\ 1$$

### 1.4.2.2. Photosensitization

Compounds that do not directly absorb light may undergo photo-induced reactions through interactions with an intermediary "photosensitizer" species.[202,203] A representation of a photosensitized reaction is shown below in **Figure 1.6**. This Jablonski diagram represents the energy levels of electrons. Upon absorption, an electron is promoted from its ground state, $S_0$, into an excited state, $S_1$, where the excited electron maintains the same spin as in its ground state. Depending on the photon's energy, the electron may be promoted to a higher vibrational state within $S_1$. The electron typically rapidly transitions to the lowest vibrational excited state ($S_1$.)

Subsequently, it can release energy as a photon to return to its ground state (fluorescence) or undergo intersystem crossing (ISC) to access a triplet state ($T_1$) in which the spin state of the excited electron parallels that of its previous paired election. This allows the electrons to exchange between their energy levels, resulting in a more stable and longer-lived excited state. From a triplet state, energy can either be released as a photon (phosphorescence) or be transferred to a recipient molecule (energy transfer.) This energy transfer similarly promotes the electron state of the recipient molecule to an excited state. Suppose the recipient is an organic molecule or anything other than ground-state oxygen. In that case, this is defined as a **Type 1** reaction (R6.) Because of the ubiquity of oxygen in the atmosphere, its photosensitization to form $^1O_2$ from its ground state,$^3O_2$, is defined as a **Type 2** reaction (R7.) $^1O_2$ can then go on to generate additional reactive oxygen species (ROS) such as OH (R8), $HO_2\cdot$ (R9) and $O_2^-$ (R10.) a complete mechanism of ROS formation in the atmosphere can be found elsewhere.[204]

$$^3Ps^* + X \rightarrow Ps + {}^3X^* \qquad R6$$

$$^3Ps^* + {}^3O_2 \rightarrow Ps + {}^1O_2^* \qquad R7$$

$$^1O_2^* + H_2O \rightarrow 2 \cdot OH \qquad R8$$

$$\cdot OH + O_3 \rightarrow HO_2 \cdot + O_2 \qquad R9$$

$$^1O_2^* + e^- \rightarrow O_2^- \qquad R10$$

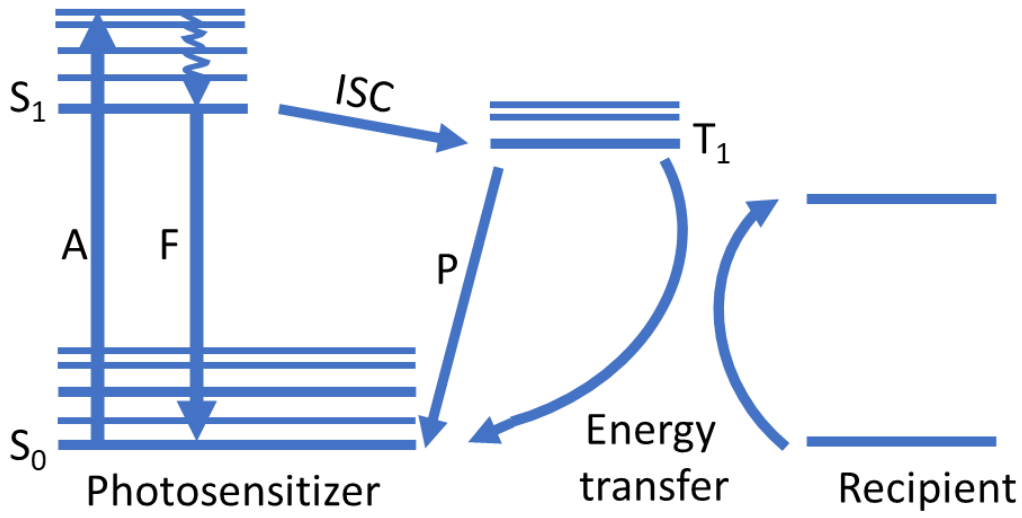


**Figure 1.6** Jablonski diagram of photon absorption and energy transfer. $S_0$: ground state (singlet). $S_1$: excited state (singlet). A: absorption. F: fluorescence. ISC: inter-system crossing. $T_1$ excited state (triplet.) P: phosphorescence.

In the marine environment, a major potential photosensitizer is a collection of compounds named in bulk as marine chromophoric dissolved organic matter (m-CDOM.) [80,198,205] This group of compounds varies significantly across locations, time, and biological activity in the ocean.[198,205] Compared to terrestrial DOM, m-CDOM contains less aromatic species and more carboxylic-rich alicyclic molecules and nitrogen-containing species.[205,206] It has been shown that m-CDOM can preferentially transfer in SSA, where it can initiate photosensitized reactions. [124,125,151,206]

### 1.4.3. Differences between solution-phase and aerosol-phase photochemistry

Aerosols exhibit accelerated reaction kinetics compared to bulk solutions. [207–209] This can largely be attributed to increased interfacial reactivity, as the surface-to-volume ratio of ultrafine particles is much larger than that of bodies of water. Compounds at the interface between solutions (or aerosols) and air have incomplete solvation shells.[209,210] This hinders organic compounds' ability to nonradiatively disperse excess energy

through vibrational relaxation and the ability of dissociated fragments of photolyzed compounds to recombine.[209,211] Additionally, the more ordered molecular orientations at particle surfaces may sterically inhibit the vibrational relaxation of excited states.[212]

While photosensitized reactions have been studied extensively in solutions[91,105,107,108,191,202,206,213,214], and more sparingly in aerosols[192,203,215] To our knowledge, no studies have directly investigated the impact of photosensitization on the same analyte in solutions and aerosols. This gap in understanding is especially relevant in the marine coastal environment, where m-CDOM in seawater and SSA may significantly enhance the photo-induced reactivity of organic species.[205,206] Chapter 4 will accomplish this investigation using the UV filter BP3 in SSA mimics as a model system**.**

### 1.5. Dissertation objectives

This dissertation focuses on constraining the presence of anthropogenic pollutants in coastal aerosol, understanding the role of organic UV filters in the coastal ocean-air system, and advancing the knowledge surrounding secondary marine aerosol composition.

The key scientific questions pursued are:

1. What is the impact of sewage release from the Tijuana River on airborne exposure to organic contaminants of emerging concern?
    a. Are organic chemical contaminants from untreated Tijuana River water transferred to the atmosphere via sea spray aerosols?
    b. How do the organic contaminant concentrations in coastal aerosols vary with proximity to the Tijuana River outflow?

    c. Do more hydrophobic organic contaminants transfer to sea spray aerosols more efficiently?

2. What factors influence the photo-induced degradation of oxybenzone in the coastal environment?
    a. How does the rate of photo-induced degradation differ in the solution vs. aerosol phase?
    b. What influence, if any, does the presence of salt and photosensitizing material have on oxybenzone's photo-induced degradation?
    c. What transformation products are produced from the photo-induced degradation of oxybenzone, and do they modulate aerosol toxicity?
3. How does the composition of secondary marine aerosol change throughout a phytoplankton bloom and as a function of oxidative aging?
    a. Which non-DMS precursor gases play the largest role in secondary marine aerosol composition?
    b. What is the abundance and role of sulfur- and nitrogen-containing organic compounds in secondary marine aerosol?

### 1.6. Dissertation synopsis

Chapter 2 details the experimental methodologies and theoretical frameworks used throughout this dissertation. This includes various techniques to characterize aerosol composition and physical properties, generate aerosols and initiate photo-induced degradation studies, and apply predictive computational tools.

Chapter 3 reproduces the manuscript by Cooper et al., 2024, currently under review in *Science Advances*. It details a field sampling campaign, IBTJ 2020, which

sampled contaminated water and air along San Diego's coast from the U.S. Mexico border to Silver Strand State Park and the Scripps Institution of Oceanography. The occurrence, spatial distribution, and possible SSA transfer of several contaminants of emerging concern, including illicit drugs, drug metabolites, pharmaceuticals, personal care products, and plastics, are reported. Chemical drivers of SSA transfer and potential public health impacts on nearby Imperial Beach are explored.

Chapter 4 reproduces the manuscript by Cooper *et al.*, 2024, currently under review in *ACS ES&T: Air*. It details the photo-induced degradation of oxybenzone, a model organic UV filter, in both the solution and aerosol phase. Through stepwise addition of secondary constituents of seawater and SSA (salt and photosensitizers,) chemical and physical drivers of oxybenzone degradation are identified, as well as potential impacts on toxicity.

Chapter 5 details measurements of secondary marine aerosol (SMA) generated from the ·OH oxidation of gaseous emissions of a phytoplankton bloom during the NSF-CAICE led SeaSCAPE 2019 field intensive study, in preparation for submission to *Atmospheric Chemistry and Physics*. This first application of online soft ionization mass spectrometry to SMA provides detailed organic compositional information of SMA throughout the progression of a phytoplankton bloom. The bulk properties of SMA are calculated and modeled based on precursor gas concentrations. Biological drivers of sulfur and nitrogen-containing components of SMA are identified.

Chapter 6 reproduces the published work by Cooper *et al*., 2023, in *ACS Environmental Science & Technology*. It details the need for a "Keeling Curve" approach to track the success of policies designed to reduce the concentration of

pollutants in the atmosphere. It also includes the policy development work undertaken during this dissertation and the policy recommendations based on the conclusions of Chapters 3-5.

Chapter 7 summarizes the work's conclusions and proposes future research directions, including an ongoing field study investigating the sea-to-air transfer of pollutants and subsequent studies of photo-induced degradation of UV filters.

# Chapter 2 Methods and Background

## 2.1 Compositional analysis of organic aerosols using mass spectrometry

Traditional techniques for studying the organic composition of aerosols have included both offline and online methods, which offer significant advantages and weaknesses.[216–218] Offline approaches are susceptible to artifacts introduced in sample handling and storage. Online techniques allow for better time resolution but often have higher detection limits and require higher labor and financial costs.

Offline techniques involve collecting aerosol, typically onto a filter or into liquid, followed by subsequent analysis using standard mass spectrometry techniques used for solid or solution analysis. These include gas chromatography coupled to mass spectrometry (GC-MS), typically using an electron impact (EI) ionization source, and liquid chromatography coupled to mass spectrometry (LC-MS), typically using an electrospray ionization (ESI) source. LCMS was used in **Chapter 3** of this dissertation and is further detailed below.

Online techniques to characterize aerosol particles offer the benefit of higher time resolution, given the ever-evolving nature of aerosol particles. Real-time single-particle mass spectrometry (RTSPMS) techniques have developed since the 1970s.[219] Current systems are primarily based on the Aerosol Time of Flight Mass Spectrometer, developed by Prather *et al.* 1994[220], which coupled aerosol sizing via light scattering and aerosol composition via a pulsed layer, and the Aerodyne Aerosol Mass Spectrometer[221], which also sizes aerosols and ionizes aerosols via flash vaporization on a heated surface followed by EI. Compared to the ATOFMS, the AMS lacks the specificity of single particle analysis but has higher throughput and is used for sampling the bulk characteristics of aerosol, such as the organic mass fraction and O:C ratio.

However, both techniques are considered “hard” ionization sources, meaning they decompose organic molecules into fragments during ionization. Continuous developments of semi- and fully online techniques and semi- and entirely soft ionization methods have been pursued to address this.

A semi-online approach to studying aerosol composition involves collecting aerosols onto a cold surface and increasing the temperature over time, collecting time-dependent spectra based on the molecules' volatility. This technique, named thermal desorption, has been used since 1999.[222] Recent novel developments have been the filter inlet for gases and aerosols (FIGAERO), which switches between the collection of aerosols for semi-online analysis and online analysis of gases[223], and the coupling of thermal desorption with fast gas chromatography and mass spectrometry.[224]

Extractive electrospray ionization (EESI) is a fully online soft ionization technique for studying aerosols. It couples real-time extraction and ionization of neutral aerosol components.[225] EESI was first developed at Aston Labs at Purdue University to analyze samples in complex matrices with limited sample preparation.[226] EESI was first used to study atmospheric aerosols seemingly independently by both Gallimore & Kalberer 2013[227] and Doezema *et al. 2012.*[228].

EESI-MS, using a time-of-flight mass analyzer (TOF), or EESI-TOF, was commercialized through the collaboration of Aerodyne, Tofwerk, and the Paul Scherrer Institute.[229] This mass spectrometer was used in **Chapters 4** and **5** of this dissertation. Below, we will explore the underlying principles behind EESI.

### 2.1.1. Extractive electrospray ionization mass spectrometry

The principle behind EESI relies upon combining a microdroplet extraction with traditional electrospray ionization.[225] **Figure 2.1** provides a representation of the EESI

inlet used in this work.[229] To ensure that EESI is only sampling aerosol-phase species, a charcoal denuder removes any gaseous background contaminants. A three-way valve that selectively passes the sample stream through a HEPA filter allows for removing aerosol-phase species. This is critical to measuring the background mass spectra of the EESI spray, which can often dominate the measured ions.[229]

A charged electrospray first intercepts a neutral sample aerosol stream. These two particle streams can interact via coalescence, bounce, disruption, or fragmentation. The branching ratios of these interactions are based on the difference in aerosol size (with similarly sized particles promoting more coalescence) and the velocity of electrospray droplets (with faster electrospray droplets promoting more bouncing.)[230] Incomplete coalescence can lead to differential ionization of compounds depending on surface activity (i.e., if a compound is present at the surface where ionization occurs or is buried in the bulk)[231] and aerosol size.[225,232] Generally, larger and more viscous aerosols exhibit higher rates of incomplete extraction and ionization. Subsequent heating promotes the evaporation of spray solvent, as in ESI, leading to a concentration of charge that results. When the droplets approach the Rayliegh limit, the maximum amount of charge a droplet can hold, Coulombic fission occurs where droplets are separated into smaller, stable droplets.[233] This cascade continues until the full desolvation of analyte species forms charged gas-phase species that can be analyzed via various mass spectrometric techniques.

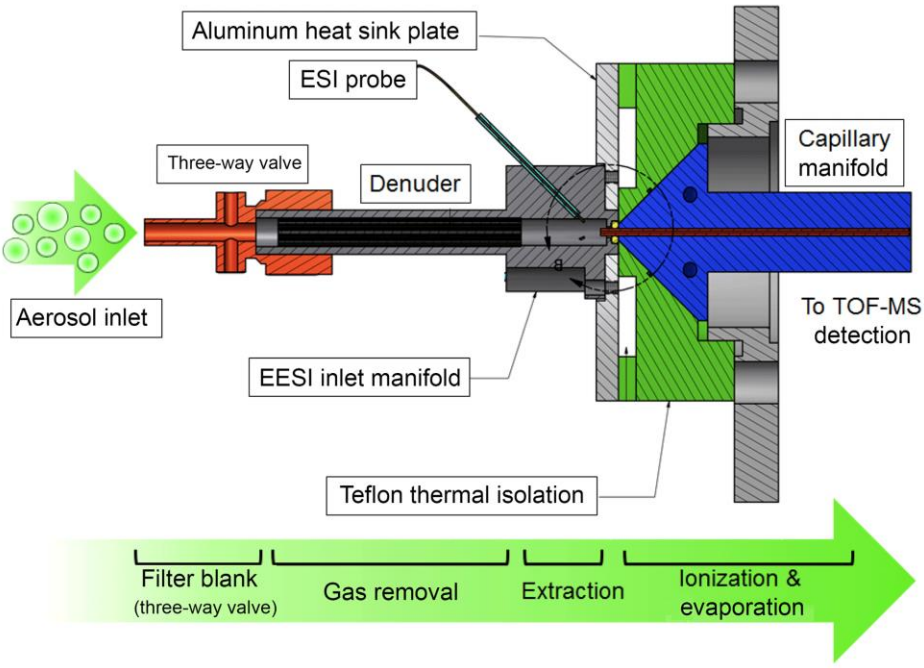


**Figure 2.1** Diagram showing the extractive electrospray ionization sampling inlet and key processes occurring in the inlet. Adapted from Lopez-Hillfiker *et al.* 2019.[229]

One of the unique benefits of EESI is that it can conduct microdroplet-phase chemical ionization by doping the charged electrospray with a specific reagent ion. Indeed, ionization of solvent alone does not promote much useful ionization as the time for charge transfer is significantly reduced compared to ESI. The most widely used reagent ions are $Na^+$ and $CH_3COO^-$. The following reaction schemes show the production of ionized species from a neutral analyte X:

$$X + Na^+ \rightarrow XNa^+ \qquad R1$$

$$XH + CH_3COO^- \rightarrow X^- + CH_3COOH \qquad R2$$

In R1, the ability for $Na^+$ to form a cluster with X is based on its binding affinity. As such, it is helpful for the detection of species with nucleophilic moieties such as carbonyls, alcohols, acids, and organic nitrates.[229] In R2, the ability of acetate to

abstract a proton depends on the analyte's acidity. As such, it is helpful for the detection of carboxylic acids and other acidic species, such as organosulfur and aromatic nitrates.[234]

The overall sensitivity (response factor – RF) of a particular compound X to EESI is parameterized by the following equation:

$$RF_X = \frac{I_{EESI}}{Mass_x} = Mass_x * EE_x * CE_x * IE_x * TE_{\frac{m}{z}} \qquad eq\ 1$$

Where EE is the extraction efficiency (how well the sample aerosol coalesces with the electrospray and dissolves in the microdroplet,) CE is the collection efficiency (how well the microdroplet is sampled into the inlet capillary to the heating region,) IE is the ionization efficiency (how well charge transfer occurs within the collected microdroplet,) and TE is the transmission efficiency (how well the charged analyte can be detected by the back end of the mass spectrometer.) For convenience, the extraction terms may be combined into an overall sensitivity term which is determined experimentally with a calibration curve. An example calibration curve is shown in **Figure 2.2**.

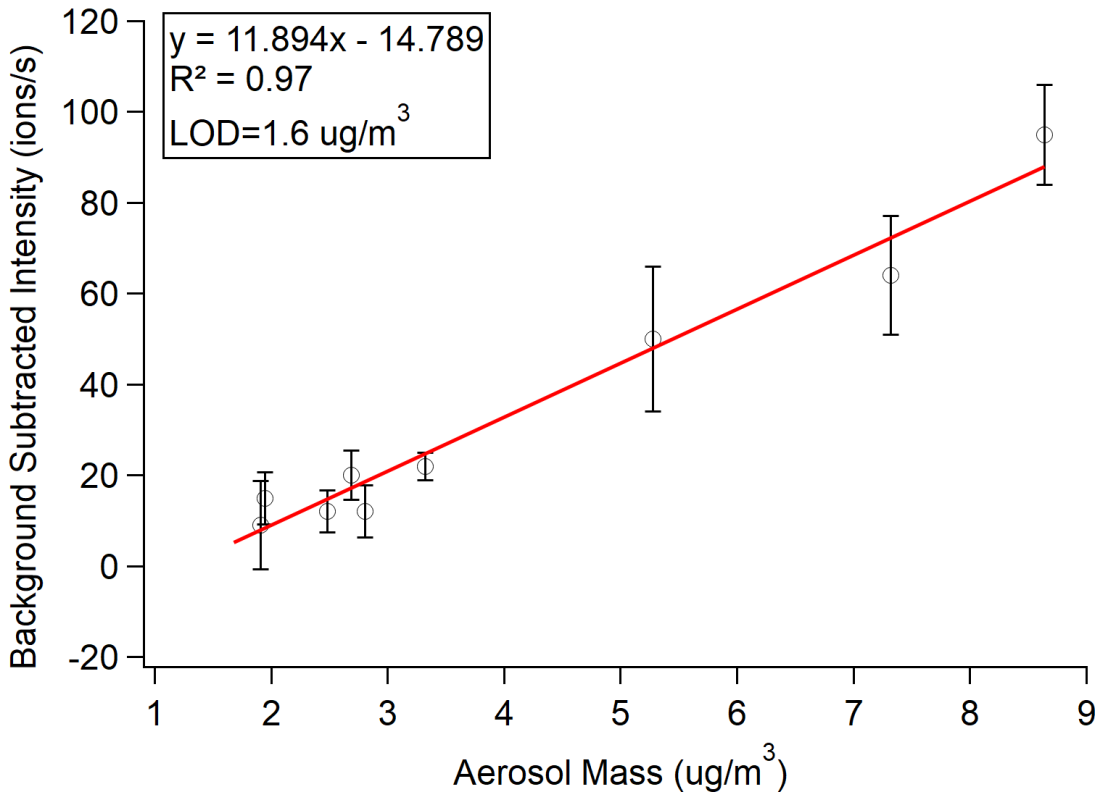


**Figure 2.2** Example calibration curve of oxybenzone detected via EESI in negative mode.

It is important to note which parameters are intrinsic to the analyte of interest or dependent on other factors. EE and CE are functions of the positioning and stability of the spray and the produced number and size distribution of charged microdroplets. These are the most variable contributors to observed sensitivity and will often be calibrated anywhere from once per day to once per hour. IE is intrinsic to the analyte of choice and determined via in-lab calibrations. TE is dependent on analyte m/z and not chemical identity. These variables can be tuned to maximize sensitivity through the selection of solvent (EE), reagent ion (IE), and voltages applied throughout the “back-end” mass analyzer (TE.)

One important factor that changes EE and CE is the sampled aerosol size. Kumbhani *et al.* 2018[231] analyzed core-shell particles with EESI and found that the technique was more sensitive to compounds present at the surface of sampled aerosol. In their conceptual model of EESI, they attribute the difference in sensitivity to incomplete extraction of larger particles.

Lee *et al.* 2021[232] further characterized this phenomenon systematically and found a negative relationship between aerosol size and sensitivity with EESI. This study used the same design EESI source as our work in this thesis. They showed that the sensitivity of some individual compounds (levoglucosan, ammonium nitrate, and sucrose) varied three orders of magnitude across a range of 20-600nm diameter particles. Complex mixtures, such as alpha-pinene SOA, varied less (1 order of magnitude over a 15-120 nm range.)

Lee tested the effects of coating thickness on the extraction of compounds found at the aerosol core and did not observe the same surface-dependent sensitivity as Kumbhani, noting complete extraction for particles up to 250 nm. Instead, they postulate that the sensitivity of EESI is based on the Brownian coagulation coefficient—i.e., the ability of two particles to coalesce based on their density and size while undergoing random (Brownian) motion. In their conceptual model of EESI, they attribute the difference in sensitivity to the reduced coalescence of larger aerosol into the charged electrospray.

Our work observed a slight size-dependent sensitivity based on aerosol size, as shown in **Figure 2.3** for pure octinoxate aerosol**.** For fine mode aerosol (<100 nm,) we observed a sensitivity three times higher than in larger aerosols (300-600 nm.) As our

studied systems (lab-generated aerosols in **Chapter 4** and nucleation mode aerosols in **Chapter 5**) had consistent sizes, we did not incorporate size-resolved sensitivities in our analysis. More discussion may be found in those chapters.

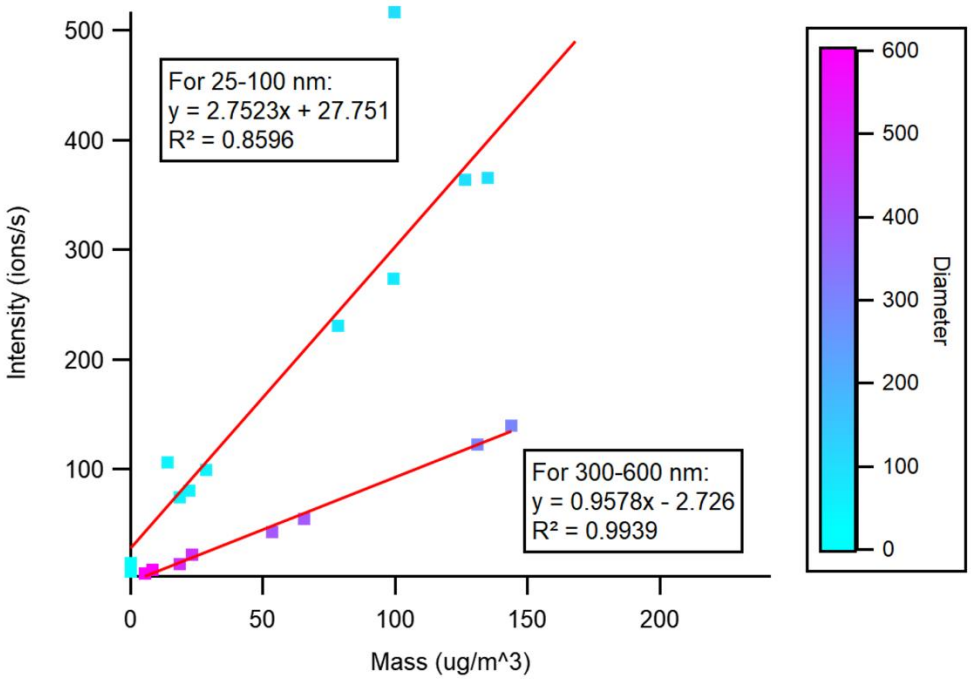


**Figure 2.3** Representative size-dependent calibration curves for octinoxate aerosol.

#### 2.1.1.1. Data processing

EESI data requires sophisticated data post-processing to isolate analyte signals from the relatively high backgrounds of the electrospray ions, determine which signals are significantly above the background, and automatically assign chemical formulas to unknown m/z values. Tofware is a graphical interface run in the Igor numerical computing environment and used for analyzing data produced by Tofwerk instruments.

EESI data is processed using a semiautomated workflow shown in **Figure 2.4.** Mass spectra data relies on mass calibration to convert instrumental response (for TOF mass analyzers, the time it takes for ions to pass along the length of the flight tube) to ion mass to charge ratios, m/z. This is accomplished by selecting ions that can be confidently predicted to be present throughout the sampling period. One benefit of EESI's high electrospray background is the presence of many known ion clusters that may be used for mass calibration. For example, in positive mode, one may use the sequence of $(NaI)_xNa^+$ ions to calibrate over a wide range that brackets most small molecules of interest.

Using a reference spectrum, often during a sampling period, you can refine the baseline (the general background intensity of the detector across the entire m/z range) and peak width and shape (the reference shape that the automatic peak fitting algorithm will use as its prototypical peak).

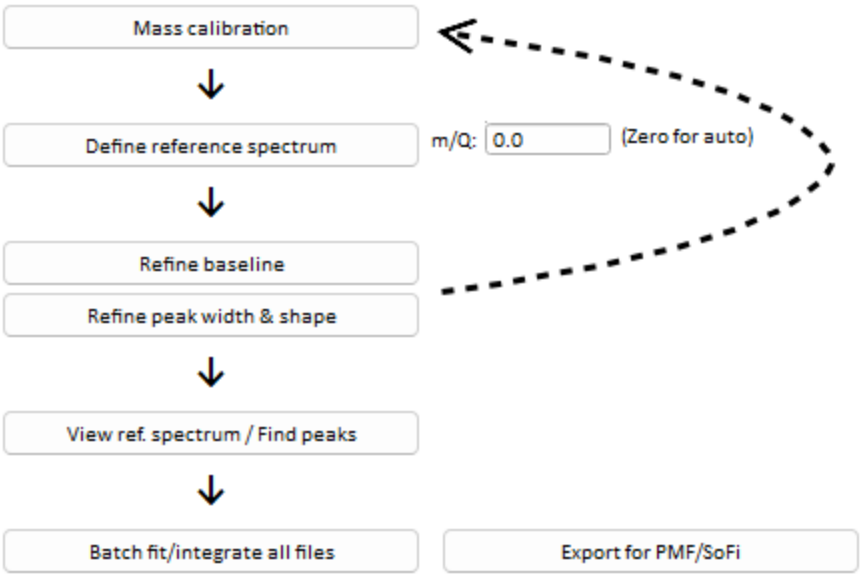


**Figure 2.4** Example Tofware workflow for post-processing of EESI data

Separately, the detection limits are determined by taking a particular region's average and standard deviation response during a blank period. Limits of detection (being able to report an ion qualitatively) are calculated by **eq 2**, and limits of quantification (being able to report the intensity of an ion) are calculated by **eq 3**.

$$LOD = I_{blank} + 3 * Std_{blank} \qquad eq\ 2$$

$$LOQ = I_{blank} + 10 * Std_{blank} \qquad eq\ 3$$

Due to the limited resolution and mass accuracy of TOF instruments, exact chemical formulas may not be easily calculated from identified unknown peaks. More rigorous assignment validation is required to estimate the chemical identity of unknown ions. To accomplish this, automatic peak fitting is performed by first generating a list of chemically likely formulas based on an algorithm that begins with several “seed”

compounds and applying chain lengthening and functionalization modifications. This reduces the likelihood of assigning an unknown peak to a chemical formula that is unlikely to exist. Then, unknown peaks are matched to the nearest formula on the list based on their exact masses. This process is explained in more detail elsewhere.[235]

Combining the previous data processing steps makes it possible to confidently report the identity and ion intensity of unknown ions. **Figure 2.5** shows representative annotated mass spectra from the photooxidation (hv + OH + $O_3$) of the UV filter octinoxate**.** Note that some compounds can be reported with a structure—such as our precursor and its known transformation products that lack structural isomers. For transformation products with many isomers, tandem mass spectrometry is required. The following section will cover the offline technique used for this analysis.

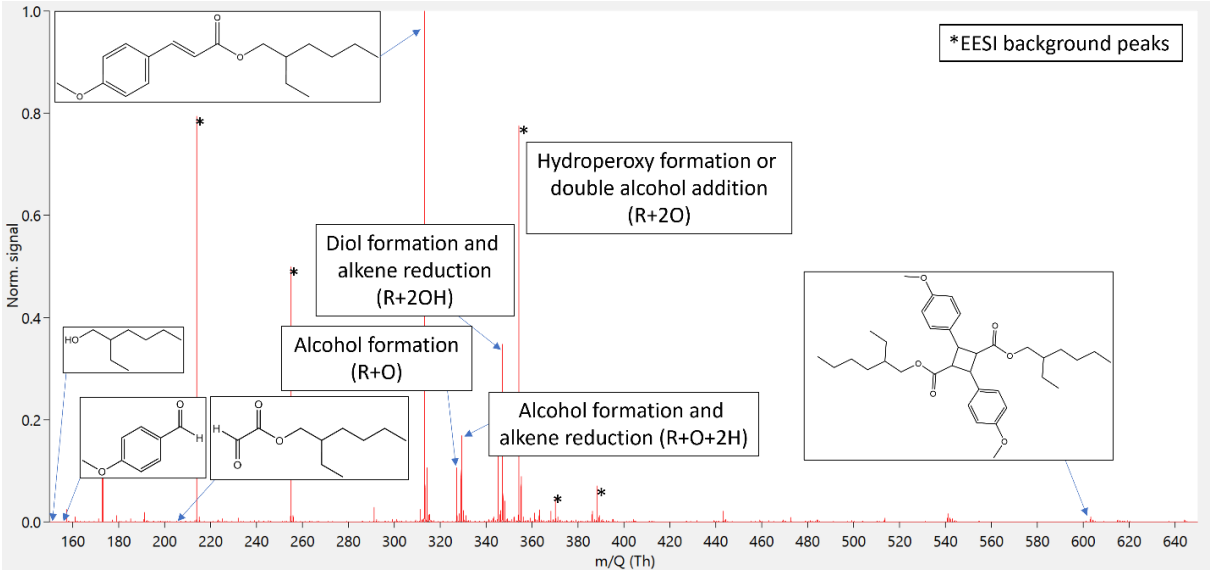


**Figure 2.5** Annotated EESI mass spectra from the photooxidation of octinoxate.

### 2.1.2 Liquid chromatography-tandem mass spectrometry

Liquid chromatography separates analytes by partitioning between the LC column surface and the mobile phase (the solvent moving through the column). This is often done as a function of polarity. Most modern columns are in the reverse phase, containing packed particles covered in a hydrophobic material, and a mixture of buffered water and a miscible organic solvent is used as the mobile phase.[236] A common column type is a “C18” column made from silica gel particles functionalized with octadecyl alkyl substituents.

The theoretical plate theory describes separation processes in which each opportunity that a compound may equilibrate between the stationary and mobile phase is assigned as a “plate,” with a column length consisting of many plates. This framework allows for the calculation of resolving power through the following relationship (**eq 4**) named the Van Deemter equation:

$$HETP = A + \frac{B}{u} + (C_s + C_m) * u \qquad eq\ 4$$

where HETP is the height equivalent to a theoretical plate (m), A is an Eddy-diffusion parameter (m,) B is a diffusion coefficient ($m^2s^{-1}$,) C is resistance to mass transfer between the stationary and mobile phase (s), and u is the speed of the mobile phase (m $s^{-1}$.) Through this relationship, the packing efficiency of particles, stationary and mobile phase selection attenuate a compound’s attractiveness, and the speed of the mobile phase can be manipulated to achieve better resolution.

Electrospray ionization functions similarly to generating the charged electrospray in EESI (ESI being the precursor technique to EESI.) A high voltage is applied to the solution containing the analyte in a solvent, which directly ionizes the solvent and some

of the analyte. Aerosolization into charged microdroplets concentrates the analyte as solvent molecules evaporate. As more solvent is evaporated, the proximity of charges in the smaller microdroplets results in a Coulombic explosion, which results in the charge transfer to analytes, which can then be analyzed via mass spectrometry.

Orbitrap mass analysis is preferred for LCMS systems, especially in nontargeted analysis, due to its high mass resolution (~100,000) and fast scan speed (~1Hz.)[237,238] Mass resolution is calculated by **eq 5** from the full width at half max of a mass spectral peak. The sharper the peak (i.e., higher the resolution,) the greater the ability to differentiate two compounds of similar mass.

$$Resolution = \frac{\frac{m}{z}}{FWHM} \qquad eq\ 5$$

The fast scan speed offered by Orbitrap allows for rapidly determining major peaks at each point in the LC chromatogram for tandem mass spectrometry (i.e., the isolation of one molecular ion to subsequently fragment via the collision of high-energy gases into smaller molecular ion fragments). Molecular identification becomes more reliable with each layer of mass spectrometry. In this thesis, secondary mass spectrometry (MS2) was performed. An example of MS2 spectra of 4-benzoyl benzoic acid is displayed in **Figure 2.6.**

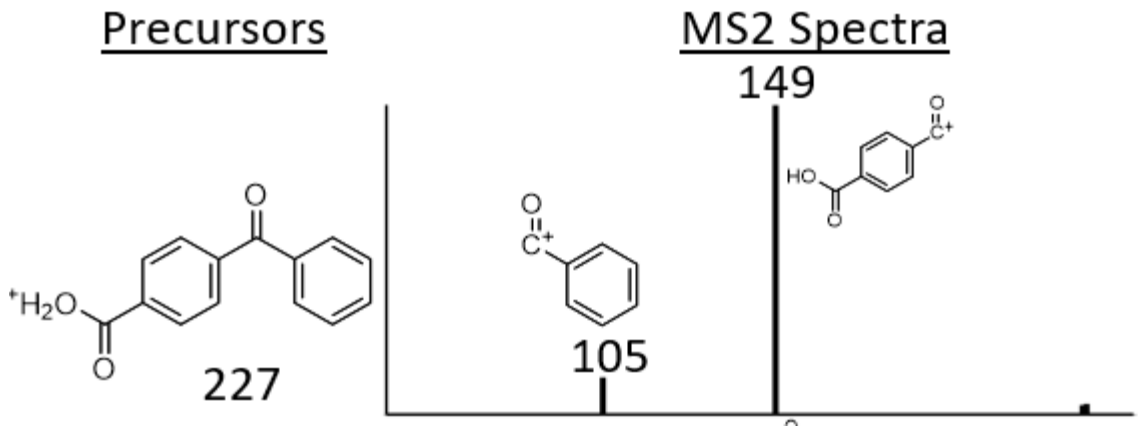


**Figure 2.6** Example MS2 spectra of 4-benzoyl benzoic acid, where ion masses are labeled.

Orbitrap combines the fast scanning of an ion trap with the highly sensitive detection of ions via an outer electrode connected to a differential amplifier (shown in **Fig. 2.7.**). It relies on the following principle, in which trapped masses (m/z) have a uniform angular frequency (ω) based on the potential applied in the analyzer (k:)

$$\omega = \sqrt{\frac{k}{m/z}} \qquad eq\ 6$$

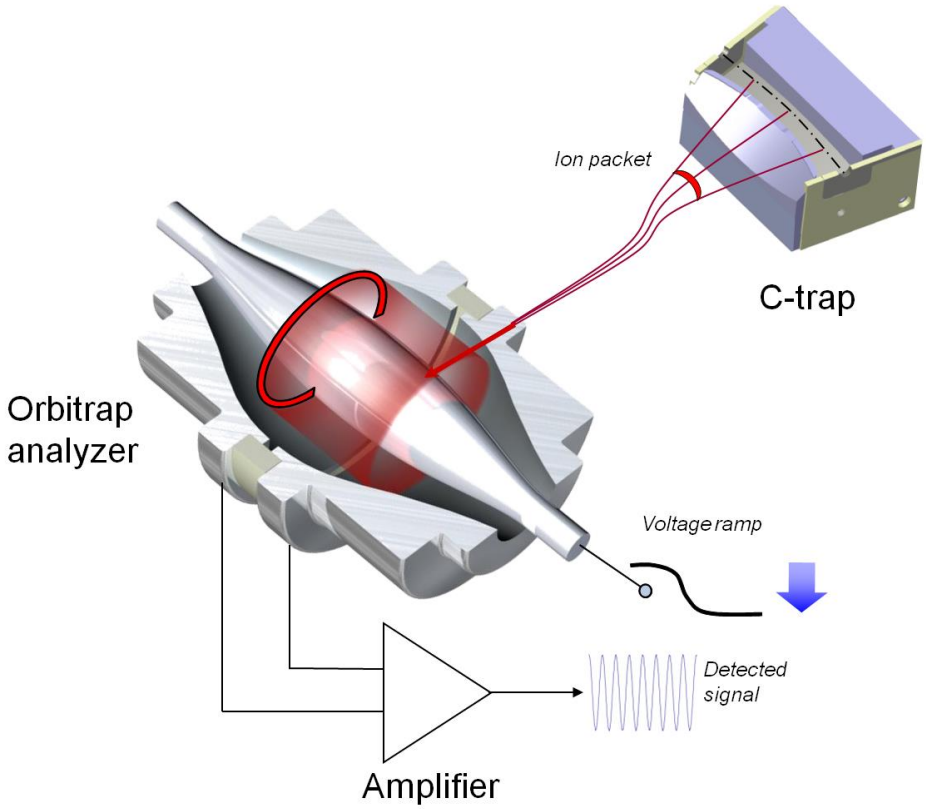


**Figure 2.7** Orbitrap mass analyzer (adapted from Wikimedia Commons.)[239]

#### 2.1.2.1 Global Natural Product Social Molecular Networking

A benefit of the wide adoption of LCMS for analysis of compounds, especially anthropogenic pollutants investigated here, is the formation of library spectra databases. These libraries are compiled through community-run resources like the Global Natural Product Social Molecular Networking (GNPS) environment[240], which provides a platform for automatic feature-based molecular networking and comparisons with other public datasets and annotated compounds from other users.

Features are conjoined MS2 spectra and retention times, which serve as identifiers for discrete chemical compounds. The GNPS platform runs a spectral matching algorithm for each feature against public, private, and community-contributed

databases to identify compounds. More discussion on data products from this may be found in **Chapter 3.** This platform also allows for exploring unknown compounds based on structural similarity (i.e., two features with similar MS2 spectra suggesting a similar structure that would fragment in similar patterns.) This feature was utilized to identify novel transformation products in **Chapter 5.**

### 2.2. UV-visible spectroscopy

UV-visible spectroscopy is a robust method for the experimental detection of light-absorbing organic compounds. This technique relies on the analyte's ability to absorb light in the UV-visible range, which was discussed comprehensively in **Chapter 1**. It applies the Beer-Lambert law, which relates the attenuation of light passing through a physical material through **eq 7** where A is the absorbance, ε is the absorptivity of the analyte, l is the optical path length, and c is the concentration of the analyte**.**

$$\log\left(\frac{I_0}{I}\right) = A = \varepsilon lc \qquad eq\ 7$$

As ε is wavelength dependent, spectrophotometers produce monochromatic light that passes through a sample container (in most cases, a quartz cuvette.) A diagram of the Perkin-Elmer Lambda 35 spectrophotometer used in this work is shown in **Figure 2.8.** This instrument is a "dual beam" instrument, in which the light beam is split to pass through a "sample" cuvette and a "blank" cuvette. The instrumental response from the blank is automatically subtracted from the response of the sample, allowing for the isolation of absorption solely from the analyte in real-time.

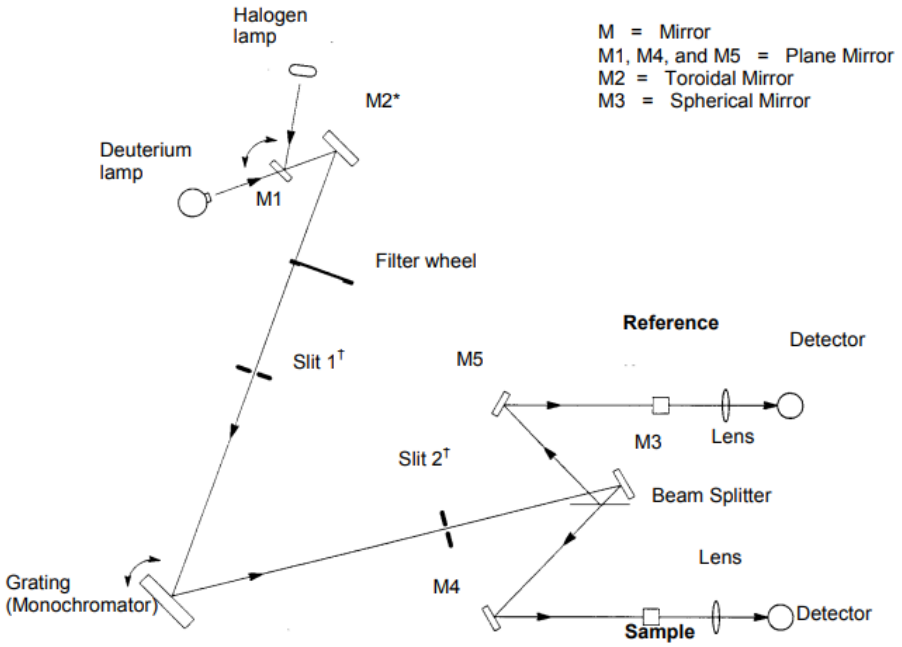


**Figure 2.8** Diagram showing the path of light in the Perkin-Elmer Lambda 35 UV-Vis Spectrophotometer. Adapted from its manual.[241]

Scanning through different wavelengths produces a UV-Vis spectrum, as shown in **Figure 2.9.** for oxybenzone. The wavelength exhibiting the maximum absorbance, $\lambda_{max}$, is used to quantify the changes in concentration using **eq 7**. The positioning of $\lambda_{max}$ and the spectra shape are dictated by the compound's electronic structure. These concepts are further explored in **Chapter 4.**

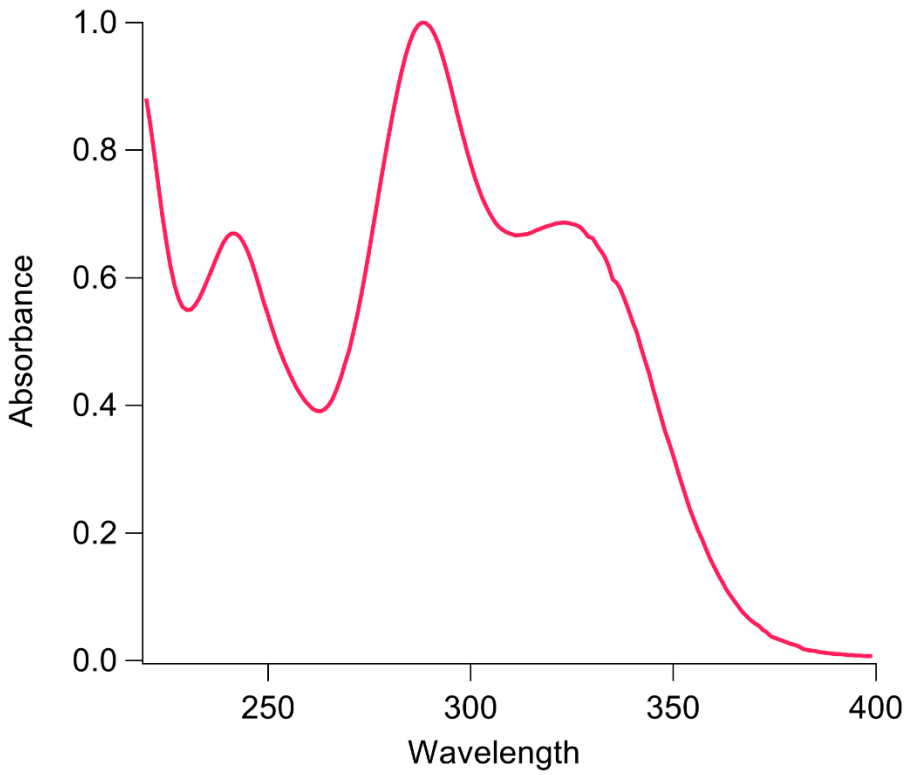


**Figure 2.9** Example UV-Vis absorption spectra of oxybenzone.

### 2.3. Aerosol and solution sample preparation

#### 2.3.1. Standard aerosol generation

For laboratory studies investigating aerosols, a standard aerosol population must be generated. Critical features include a stable number count and size distribution of aerosols, as both parameters will influence planned experiments and instrument readings. For this reason, a constant output atomizer (in our study, the TSI Model 3076) is used to generate aerosols from a prepared solution. A representation of the Model 3076 is shown in **Figure 2.10.** Compressed air from a constant pressure source forces a jet of solution drawn by the negative pressure above its sampling line into an atomizer chamber. Large droplets collide with the chamber wall and are removed, and submicron aerosol continues with the airflow.

One can modify the number concentration and size of produced aerosol through the concentration of analytes in the atomizer solution and by selecting different solvents. Higher solute concentrations will generate larger aerosols as solute molecules are closer to each other during the atomization process. Using water as a solvent results in wet particles containing water, which will increase their size, while using organic solvents will result in quick evaporation of the solvent and the production of smaller dry particles.

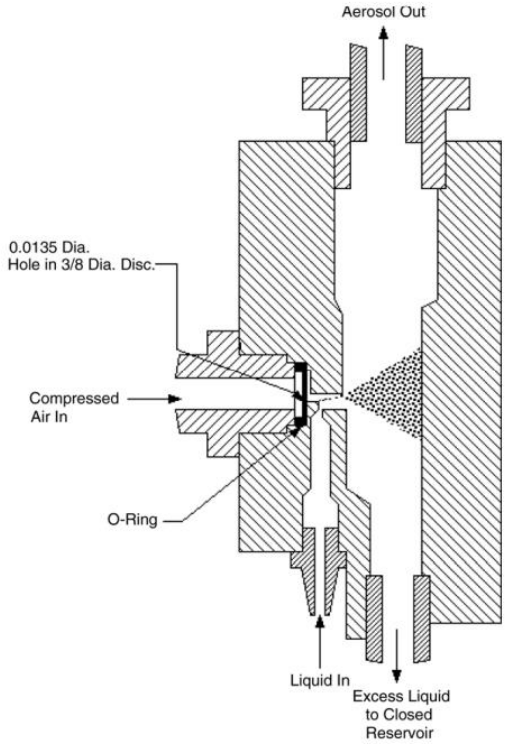


**Figure 2.10** A representation of the TSI Model 3076 constant output atomizer. Adapted from its instrument manual.[242]

### 2.3.2. Aerosol collection and extraction

Organic aerosol can also be analyzed offline by collecting it onto filters or into liquids and using solution-phase techniques. The versatility of liquid chromatography coupled with electrospray mass spectrometry has led to its widespread use in

characterizing aerosol organic composition. Gas chromatography coupled to mass spectrometry is also used depending on the volatility and molecular weight of the analytes of interest.

Various sampling and extraction techniques can target different types of pollutants. Sampling can either be active (typically using a vacuum pump) or passive (relying on air masses to travel through the filter naturally.)[243–245] Passive air sampling requires less equipment and access to electricity, but it also involves handling less air (and thus collecting less aerosol per unit time). Active air sampling has the benefit of collecting more air mass, although this may sometimes come at the cost of collection efficiency for extremely high flow rates (>100 lpm). In **Chapters 3 and 4**, offline aerosol samples are actively collected at a moderate flow rate (~5-50 lpm) onto quartz fiber filters.

We note that quartz fiber filters have been shown to adsorb semivolatile gases, increasing the apparent aerosol-bound fraction of semivolatile organic compounds.[21,246] The other filter material commonly used is polytetrafluoroethylene (PTFE), which may sometimes adsorb more water during collection and introduce additional artifacts from aqueous reactions occurring on filter media.[246,247] Quartz is also easier to combust, leading to less organic contamination. Weighing the tradeoffs between these two filter media types is essential in designing sampling methodology.

Following collection, sample extraction is performed to solubilize the organic compounds of interest and prepare them for analysis.[248] The choice of organic solvent is another critical parameter for method design. Solubility may be a rough discriminator between biogenic aerosols, which are typically more water soluble, and anthropogenic

aerosols, which are generally less water soluble.[249] Additionally, mixtures of water and organic solvents can separate the organic-soluble and water-soluble portions of collected aerosol organics.[250] As this work focuses on anthropogenic aerosols, organic solvents (acetonitrile and methanol) were used for extraction. The Methods section of **Chapter 3** provides further details on the sample preparation and method**.**

### 2.4. Measurements of aerosol physical properties

Aerosols have relevant physical properties that are important to constrain, such as size, viscosity, and hygroscopicity. For aerosol photo-induced kinetics, as determined in **Chapter 4**, and identification of the total mass of an aerosol population, as done in **Chapter 5**, aerosol sizing is an important function. This can be performed using both offline and online techniques. In sample collection for offline analysis, aerosols can be separated by size using one or several impactors to collect aerosol above a specific size. This is done in standard PM10 and PM2.5 measurements, typically gravimetrically.

Spectroscopic techniques are the most widely used method for online aerosol sizing, where particles are detected directly or first grown into larger droplets for easy detection by light scattering. The scanning electrical mobility spectrometer (SEMS)[251] is detailed in the following section.

#### 2.2.1 Scanning Electrical Mobility Spectrometer

The SEMS is a two-part instrument consisting of a differential mobility analyzer (DMA) and a condensation particle counter (CPC.) The DMA, shown in **Figure 2.11**, is a flow chamber with a charged central rod that generates an electrical field between itself and the outer chamber walls. By applying a specific voltage to the center rod, only particles of specific electrical mobility will remain in the airflow according to **eq 8**:

$$V = \frac{Q_{sheath} \ln \frac{R_{outer}}{R_{inner}}}{2\pi L_{DMA} Z_p} \qquad eq\ 8$$

where $Q_{sheath}$ is the sheath flow ($m^3\ s^{-1}$), $R_{outer}$ is the outer cylinder inner radius (m), $R_{inner}$ is the center rod outer radius (m), $L_{DMA}$ is the center rod length (m), and $Z_p$ is the particle electrical mobility ($V\ m^{-2} s^{-1}$). $Z_p$ is related to size based on **eq 9** where n is the number of charges, e is the unit of electrical charge, $C_c$ is the dimensionless Cunningham slip correction factor, μ is the air dynamic viscosity ($kg\ m^{-1}\ s^{-1}$), and $D_p$ is particle diameter (m):

$$Z_p = \frac{neC_c}{3\pi\mu D_p} \qquad eq\ 9$$

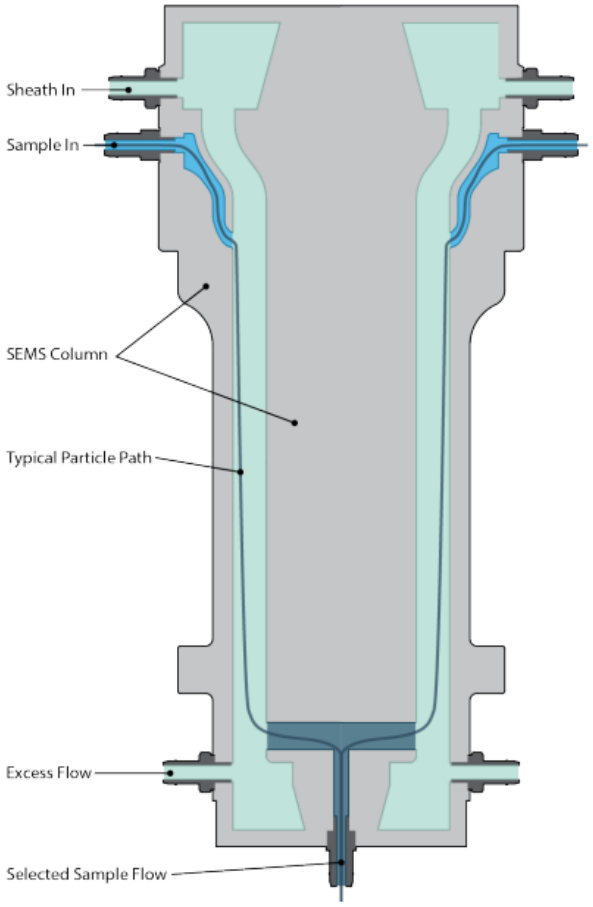


**Figure 2.11.** Cross section of a DMA. Adapted from Brechtel's SEMS manual.[252]

A neutralizer is used to apply a predictable Boltzmann distribution of charges to produce a predictable number of charges, which can be accounted for in the processing of the output data.

DMAs are either operated in "mono" mode, whereby a constant voltage is applied to the center rod to produce one size of aerosol, or in "scanning" mode, whereby voltage is changed stepwise to scan through different sizes.

A CPC typically counts particles leaving the spectrometer by first condensing a supersaturated vapor (typically either water or, in the case of the SEMS used here, butanol) onto each particle, producing larger droplets. Droplets are then sampled

through a region containing a laser. When particles interrupt the laser beam, they scatter light, which is detected via a photodiode.

An example output of a size distribution measured in scanning mode is shown in **Figure 2.12.** Size distributions are often displayed as lognormal distributions to allow for better size resolution at lower diameters and better visualization of different modes of particles which may vary in concentration several orders of magnitude. For example, in **Figure 2.12.**, a linear x-axis would squeeze the two nucleation mode peaks (at 5 and 15 nm), and a linear y-axis would obscure the Aitken-mode peak (at 150 nm.)

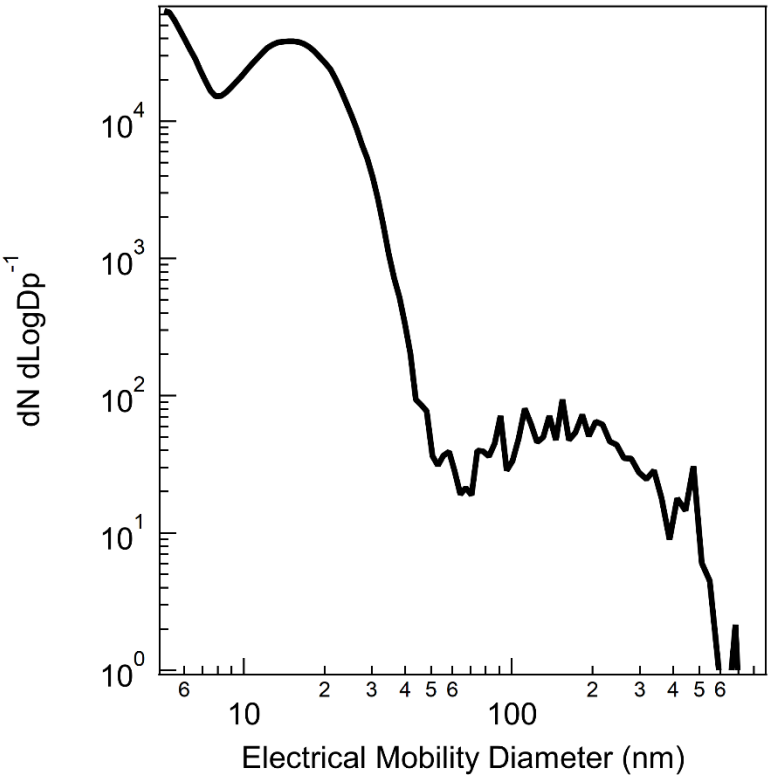


**Figure 2.12** Example size distribution of secondary marine aerosol measured via an SEMS

To account for counting aerosols within discrete sized bins, which may vary from instrument to instrument or through selecting different ranges and bin counts on the

instrument, number counts are normalized to the size of each bin. This calculation is shown in **eq 10** where dN is the number count per pin, $D_{p,u}$ is the upper limit of the bin and $D_{p,l}$ is the lower limit of the bin**.**

$$\frac{dN}{dlogD_p} = \frac{dN}{logD_{p,u} - logD_{p,l}} \qquad eq\ 10$$

**2.3 Oxidative flow tube reactors**

Flow tube reactors have long been used to study aerosols.[253,254] Compared to environmental chambers, which offer longer residence time at the expense of longer experimental time and increased particle-wall interactions, flow tube experiments can be conducted using much larger concentrations of gaseous oxidants.

This work utilized the Aerodyne Potential Aerosol Mass Oxidative Flow Reactor (PAM-OFR) in **Chapters 4** and **5**. The PAM-OFR has four quartz sleeves that interchangeable lamps can be inserted into to provide photon flux. The lamps can be tuned via a ballast to provide different voltages, which results in different photon fluxes. Nitrogen is run over the lamps to dissipate the heat produced by the lamps during experiments. Nevertheless, the heat of the lamps and the absorption of the light by the PAM-OFR walls and airborne constituents cause an increase in temperature inside the PAM-OFR compared to room temperature outside the reactor. This has been shown to lead to evaporative loss, which is generally kinetically limited to ~10% under typical experimental conditions.[255] More discussion of the evaporation of one semivolatile analyte, oxybenzone, is included in **Chapter 4**.

### 2.3.1. PAM-OFR photooxidation

For ·OH oxidation experiments, as in **Chapter 5**, 185nm and 254nm lamps in the PAM-OFR produced ·OH through the following scheme. First, the production of $O_3$ and some OH with 185 nm light:

$$O_2 + hv(185\,nm) \rightarrow 2O(^3P) \quad R3$$

$$2O(^3P) + O_2 \rightarrow O_3 \quad R4$$

$$H_2O + O_2 + hv(185\,nm) \rightarrow\rightarrow OH + HO_2 \quad R5$$

254 nm light is used to produce OH from $O_3$ in the following reaction scheme:

$$O_3 + hv(\,254\,nm) \rightarrow O(^1D) + O_2 \quad R6$$

$$O(^1D) + H_2O \rightarrow 2OH \quad R7$$

Due to $H_2O$'s involvement in both processes, it is essential to factor in the relative humidity during calibrations and experiments.

A significant weakness of the PAM-OFR when studying organic-containing aerosol is the highly energetic wavelengths used can be absorbed and initiate reactions, which may not be the focus of the study or tropospherically relevant. Therefore, $O_3$ is often generated in another chamber and introduced into the main flow tube. Because OH has an extremely short lifetime (<1s), it must be generated *in situ*. To isolate the effects of the remaining 254 nm light, control experiments should be performed, such as in Kruse *& Slade* 2023[215], where the impacts of 254 nm light with and without the presence of $O_3$ (i.e., with and without the production of OH) should be quantified.

The standard method for calibrating the OH production in a PAM-OFR is introducing a gas with a known and well-parameterized reaction rate with OH, such as CO or $SO_2$. This work uses CO as a calibrant due to the accessibility of a CO monitor and its oxidation product, $CO_2$, remaining in the gas phase. $SO_2$ oxidation may produce

nucleated $SO_4$-containing aerosols, which would take longer to remove from the system.

### 2.3.2. PAM-OFR photo-induced degradation

Nontraditional lamp types may produce other oxidants, like the Cl radical, or perform photo-degradation experiments. In **Chapter 4**, wideband UVB lamps (λ=300-350 nm) were used to simulate the most energetic region of the solar spectra present in the troposphere.

Typically, the photolysis of $NO_2$ is used to calibrate photon flux, given its quantum yield of 1 for wavelengths less than 394 nm.[256] By monitoring the decay of $NO_2$ to light under this range, as used in this work, one can calculate the photon flux. This process is described in more detail in **Chapter 4**.

### 2.3.3 Aerosol reaction kinetics

Many photooxidation reactions of interest are second-order reactions between a compound of interest A and a photooxidant B. However, most photooxidation experiments are conducted under conditions with a constant concentration of oxidants (for example, OH produced *in situ*) or under a continual photon flux. This allows for them to be treated as *pseudo*-first order reactions where the concentration of one reactant, for example, OH or a photon, is held constant and incorporated into an adjusted rate constant:

$$Rate = k'[A] \qquad eq\ 11$$

Where experimental data can be fit to the following equation:

$$[A] = [A]_o e^{-k't} \qquad eq\ 12$$

or

$$\ln\left(\frac{[A]}{[A_0]}\right) = -k' \qquad eq\ 13$$

Gas or solution phase kinetics are considered in the context of the frequency of collisions dictated by temperature. However, because aerosols have an accessible surface and a buried bulk, with many transitory layers in between, aerosol multiphase kinetics must also consider the aerosol's available surface area. This is commonly parameterized as γ, or the reactive uptake coefficient. It is the fraction of reactive collisions compared to total collisions between the reactive gas and the aerosol particles, ranging from 0 to 1. γ can be calculated using **eq 9** where $D_0$ is the mean surface-area weighted aerosol diameter, $\rho_i$ is the density of the aerosol component, $N_A$ is Avogadro's number, $c_{OH}$ is the mean molecular speed of the reactive gas-phase species, and M is the molecular weight of the aerosol component:

$$\gamma = \frac{2D_0\rho_i N_A}{3c_{Ox}M_i} \qquad eq\ 14$$

### 2.4 Computational methods to determine bulk properties of organic compounds

#### 2.4.1 Quantitative Structure-Activity Relationships

There are an estimated 100 million or more chemicals worldwide and insufficient human resources to rigorously characterize each one's chemical and physical properties. However, enough chemicals have been studied to provide a training set for machine learning models, which may help estimate their properties. Estimation tools have been developed using quantitative structure-activity relationship (QSAR) modeling.

QSAR relies on an underlying calculation of "chemical similarity," based on sharing common functional groups or sub-structures and molecular properties such as molecular mass and average carbon oxidation state. The EPA Estimation Programs Interface Suite (EPISUITE)[79] is a comprehensive platform for predicting chemical and

physical properties relevant to environmental behavior, such as volatility, partitioning coefficients between octanol, water, air, and soil, atmospheric lifetime, aerosol partitioning, bioaccumulation, and bulk aquatic toxicity.

The EPA also created the Toxicity Estimation Software Tool (TEST), a QSAR model for a variety of toxicity endpoints for rats, fathead minnows, daphnia magna, and tetrahymena pyriformis, which are model species for mammals (including humans), fish, plankton, and protists, respectively.

Such models can be useful in calculating the physical properties of chemicals that have not been determined, as in **Chapters 3 and 4**, and in estimating the toxicity of transformation products that may be less well characterized than starting analytes (as in **Chapter 4**). More details on QSAR may be found elsewhere.[257,258]

### 2.4.2 Volatility Basis Set

SOA formation relies on the oxidation and condensation of complex mixtures of organic species. As compounds become more oxidized or functionalized with heteroatoms, they tend to decrease in volatility (i.e., vapor pressure) and partition more into the condensed phase. However, experimental determination of partitioning coefficients (either via octanol to air as a proxy or *in* situ aerosol to air partitioning) is labor intensive, especially for the diverse pool of compounds that comprise SOA. To assist in describing this phenomenon, a multivariate algebraic relationship between a molecule's molecular formula and its volatility was developed by the Donahue research group at Carnegie Mellon.[259–261]

The 2-D volatility basis set (2D-VBS) plots the average carbon oxidation state ($OS_C$) against the volatility, parameterized as the saturation mass concentration ($C^0$.)

$C^{0-}$ is defined as saturation vapor pressure, in μg $m^{-3}$, above a subcooled liquid. An example of VBS is shown in **Figure 2.13**, which demonstrates the trajectory of organic compounds during the formation of SOA from VOCs and intermediate and semi-volatile compounds. Notably, SOA formed from VOCs exhibits a trajectory in which compounds may fragment into more volatile species. In contrast, SOA formed from IVOCs and SVOCs may be less prone to evaporation through oxidative fragmentation. This has implications for a shifting SOA system in the anthropocene, where more semivolatile chemical products replace biogenic and combustion-based VOC precursors in urban environments.[44,262]

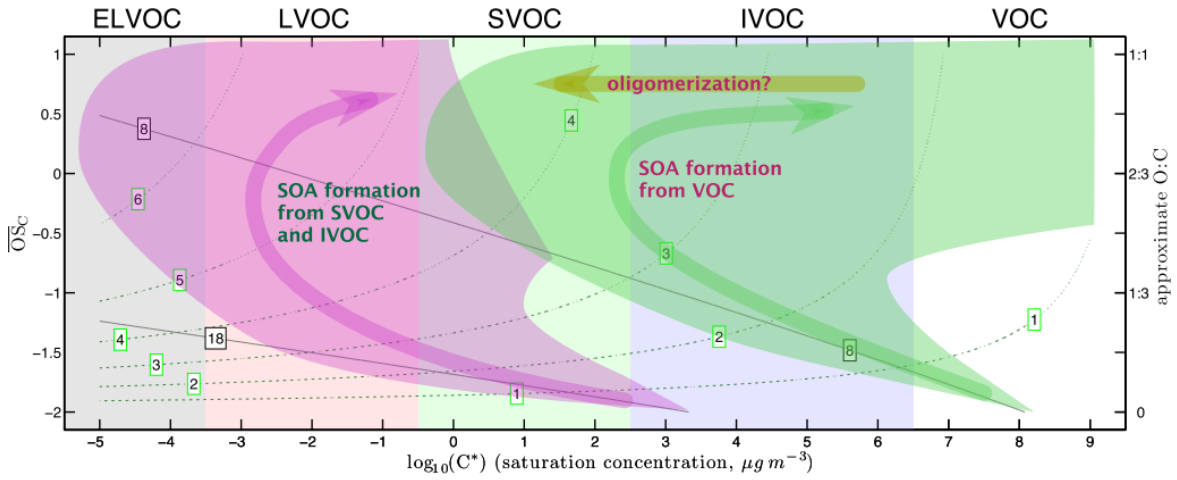


**Figure 2.13** Representation of SOA formation pathways from VOCs (green) and SVOC/IVOCs (purple) along a 2-D volatility basis set. Adapted by Donahue *et al.* 2012.[261]

One of the major benefits of the methods employed in this dissertation (namely, EESI and ESI) is the identification of molecular formulas through the formation of M+H, M+Na, and M-H ions. This allows for the simple calculation of the average $OS_C$ by using equation **eq 15**. The calculation of $C^0$ was determined using pentacosane (a $C_{25}$ alkane

with $C^0$=1 μg $m^{-3}$) as a reference compound. using available data, effects of increasing or decreasing carbon chain length as well as effects of functionalization (O=, HO(O)- and HO- groups,) they developed **eq 16**, where $n_C$ and $n_O$ are the number of C or O atoms, $n_C^0$=25, $b_C$ and $b_O$ are the contributions of each atom to $\log_{10} C_{300}^0$ and $b_{CO}$ is a nonlinearity adjustment.

$$OS_C = 2 * \frac{O}{C} - \frac{H}{C} \qquad eq\ 15$$

$$\log_{10} C_{300}^0 = (n_C^0 - n_C)b_C - n_O b_O - 2\frac{n_C n_O}{n_C + n_O} b_{CO} \qquad eq\ 16$$

However, this parameterization does not account for the presence of nitrogen and sulfur containing compounds. The presence of organonitrates and organosulfate functional groups can significantly decrease the volatility of compounds. There are a variety of approaches to account for this. Some groups attempt to subtract out these moieties and treat them as -OH groups by subtracting twice the nitrogen number from the oxygen number (essentially replacing a "-$ONO_2$" moiety with a "-O" moiety.[263]

Other attempts have been made to directly attribute volatility impacts to the number of nitrogen and sulfur atoms, as in Li *et al*. 2016.[264] In their case, they add new "$n_N b_N$" and "$n_S b_S$" terms (see **eq 17**.) They report updated b terms from the NCI database, which contains over 30,000 compounds, and rely on EPISUITE to estimate the saturation vapor pressure. This approach and **eq 17** were used in **Chapter 5**.

$$\log_{10} C_{300}^0 = (n_C^0 - n_C)b_C - n_O b_O - 2\frac{n_C n_O}{n_C + n_O} b_{CO} - n_N b_N - n_S b_S \qquad eq\ 17$$

# Chapter 3 Wastewater-Derived Pollutants in Coastal Marine Aerosols: Spatiotemporal Distributions and Links to Sea Spray

Chapter 3, in part, has been submitted for publication of the material as it may appear in Science Advances, 2024, Cooper, A, Pendergraft, M, Petras, D, Cancelada, L, Belcher, K, Torres, R, Small, M, Garrafa-Luna, J, Belda-Ferre, P, Simpson, R, Morris, C, Mitts, B, Aron, A, Zhang, J, Price, T, Dinasquet, J, Dorrestein, P, Knight, R, Slade, J.H., Prather, K. The dissertation author was the primary investigator and author of this material.

## 3.1. Abstract

At the US-Mexico border in southern San Diego, untreated and treated wastewater and water pollution contaminate the coastal ocean, increasing health risks. Previous research identified untreated sewage in the Tijuana River as a major source of airborne bacteria via sea spray. This study investigates how this water pollution impacts sea spray aerosols, revealing that wastewater-derived chemical pollutants, including illicit drugs, drug metabolites, and chemicals from tires and personal care products, enter the atmosphere. The Tijuana River notably increases ambient concentrations of these pollutants following precipitation events. The hydrophobic nature of certain pollutants makes them likely to concentrate on the ocean surface and aerosolize when waves break. This airborne contamination pathway exposes even those not entering the ocean to waterborne pollutants. This discovery highlights an overlooked atmospheric pollution source, prompting the need for updated health assessments as global waters become more polluted.

### 3.2. Introduction

Coastal waters in the San Diego-Tijuana border region are impacted by runoff from land, offshore discharge from secondary wastewater treatment plants, and the Tijuana River, which is majorly impacted by untreated sewage release.[117] Although international collaboration has enabled diversion and treatment of the Tijuana River, precipitation in the Tijuana River watershed can produce flows upwards of billions of gallons per day that enter the Pacific Ocean in the San Diego South Bay region.[265] Such events overload river diversion and treatment systems and lead to pollution entering the ocean, impacting densely populated coastal towns in Tijuana and San Diego. Even during periods of low flow conditions from the Tijuana River, untreated sewage released from the Punta Bandera wastewater treatment plant south of the US-Mexico border and insufficient removal of chemical pollutants in secondary wastewater plants can result in sewage-related water and air pollution.[118]

The water pollution flow into the ocean led to the County of San Diego declaring a regional public health crisis.[266] In 2017, an estimated 3.8% of swimmers became ill from norovirus exposure in the impacted coastal region.[118] In 2020, the US Environmental Protection Agency committed $300 million in treatment infrastructure improvements to address pollution from the Tijuana River.[267] To date, a comprehensive strategy for removing organic pollutants has not been identified.[265,268,269] Organic contaminants of emerging concern include pharmaceuticals[270], illicit drugs[268] compounds used as active ingredients or additives in manufactured biocides[271], personal care products (PCPs)[58,270], and plastics.[272] Many such compounds are not efficiently removed in wastewater treatment[269] and can be introduced into the ocean through wastewater discharge, land runoff, and direct industrial release. These compounds are often

hazardous to environmental health [58,273] and pose an emerging concern to human health through the airborne exposure pathway.[27,119,274]

Pollutants in the ocean can become enriched in sea spray aerosol (SSA), as shown in both field [69,119,138,275] and laboratory studies.[147,276,277] SSA is generated when waves break and bubbles rupture at the ocean's surface, releasing chemical components into the air in aerosol particles.[124,278] The efficiency with which components from the ocean get transferred into the atmosphere depends on their levels of surface enrichment[278,279] and coastal environmental conditions, including wind speed, wave height, and white cap coverage.[36] Most research has focused on the emissions of microplastics[27,69,276,280] and per- and poly-fluoroalkyl substances (PFAS)[137,138,275,277] in SSA. Franklin *et al.* 2022[147] identified chemicals associated with sunscreen and plastic in SSA generated in a wave flume using San Diego coastal ocean water. However, limited studies exist on this broad range of chemical pollutants in ambient SSA.

In one study conducted in San Diego, Pendergraft *et al.,* 2021[119] demonstrated that a dye used to mimic waterborne pollutants released from the mouth of the Tijuana River dispersed several kilometers along the southern San Diego coast. The dye was transferred to the atmosphere in SSA, where it was measured at distances up to 668 meters inland and 720 meters downwind of the ocean.(*28*) Later, bacteria in marine aerosols were linked to the Tijuana River flowing into coastal waters, showing that up to 76% of the airborne bacterial community near Imperial Beach, a border town south of San Diego, could be traced back to the Tijuana River. [120] However, most chemical pollutants detected in that bio-focused study showed multiple atmospheric sources;

none were quantified, and little evidence was provided to support a marine source of aerosol-phase chemical pollutants.

This current study quantified select chemical pollutants in aerosols and water sampled concurrently along coastal sites in San Diego during periods impacted by flow from the Tijuana River. We analyzed chemicals from personal care products, tires, illicit drugs, and pharmaceuticals, including metabolites and biocides. This study suggests airborne exposure could lead to health risks for people in this Imperial Beach region, where coastal water pollution has already shut down southern San Diego beaches for 900 consecutive days as of July 2024**.**[281] Organic compounds may also be emitted directly from the Tijuana River before reaching the ocean. Volatile compounds may directly evaporate, and wind-driven bubble formation can produce aerosol from rivers.[282,283] While the importance of these pathways is yet to be quantified, this study focuses on the coastline where we expect most aerosol formation to occur due to more turbulent conditions and the higher salt content of ocean water.[282]

Continuous pollution from the Tijuana River and runoff from other land-based and riverine sources impact pollutant levels in ocean water and aerosol along the San Diego coast. We show that selective transfer from the ocean to the atmosphere in SSA can significantly contribute to airborne pollutants. These findings have global implications as 3 billion people live within 100 km of coastlines[284], most of which are impacted by human sewage.[285] This work highlights an understudied route of airborne exposure to waterborne pollutants that could influence the health of millions who live within kilometers of contaminated bodies of water. As sea levels rise and flooding becomes more intense, as predicted in future climate scenarios[286], the potential for airborne

exposure to waterborne pollutants will occur even more frequently. This study serves as a first step in determining the full scale of the impact of pollutant transfer in SSA in coastal regions. Further studies are needed to understand the controlling ocean and atmospheric factors, link these new pollutant sources to specific health effects, and ultimately establish preventative policy interventions.

## 3.5. Methods

### 3.5.1. Sampling locations, collection, and study timeline

Aerosol and water samples were collected from the surf zone on the same days at various coastal locations, starting from south-to-north: Border Field State Park (BF), Tijuana River (TJR), Imperial Beach (IB), Silver Strand (SS), and the Scripps Institution of Oceanography (SIO) in La Jolla, CA, which served as a comparatively “clean” site located approximately 35 km north of the US-Mexico border (**Fig. 3.1A**). Samples were collected surrounding periods of increased flow of the TJR (**Fig. 3.1B**) due to precipitation events (**Fig. 3.1C**).

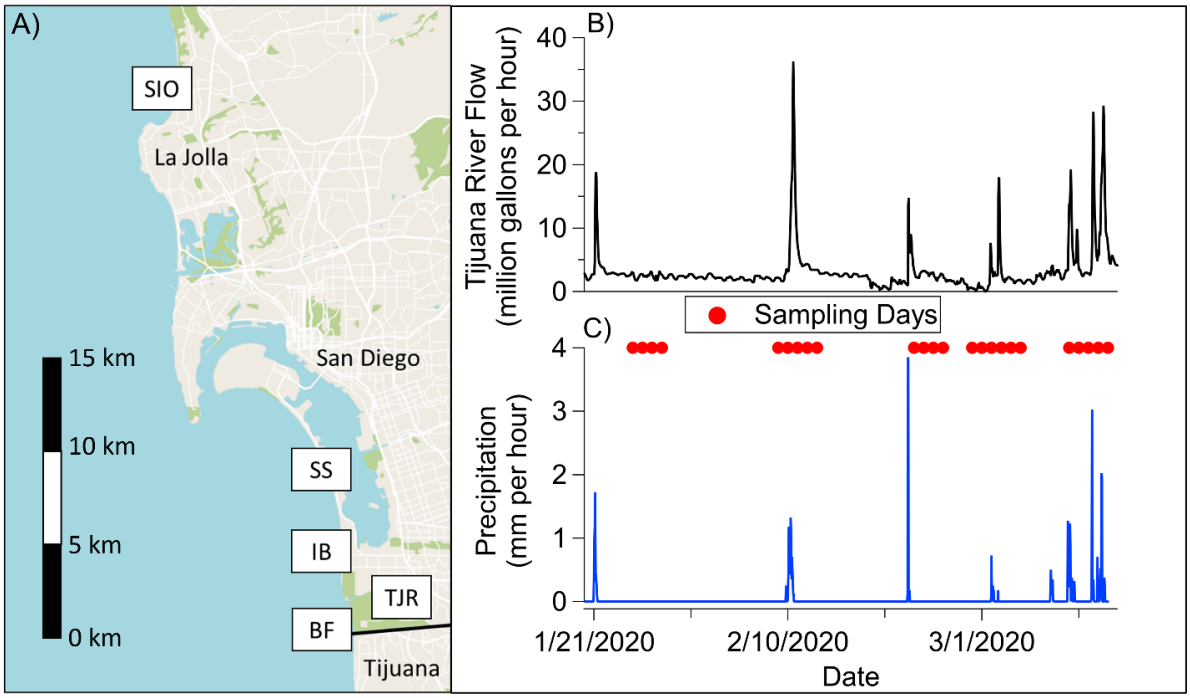


**Figure 3.1** (A) Map of the San Diego coastal region and border with Mexico. Field sites are labeled from south to north: Borderfield State Park (BF), Tijuana River (TJR), Imperial Beach (IB), Silver Strand (SS), and Scripps Institution of Oceanography (SIO). B) Hourly flow rate of the Tijuana River measured at the international boundary.[287] C) Hourly precipitation measured at the international boundary.[287] Sampling dates are designated as red markers.

Samples were collected between January 24th and March 14th, 2020, surrounding five discrete precipitation events, where sample collection typically began a few days before rainfall and continued a few days afterward. During the sampling periods, flow from the Tijuana River reached the ocean.[287] Precipitation and Tijuana River flow levels are plotted in **Figure 3.1**. Sampling locations were chosen to observe southbound and northbound ocean and atmospheric transport of pollutants from the Tijuana River. The first site was 2.4 km south of the Tijuana River outflow at Borderfield State Park (BF) (32.5351, -117.1220). Aerosol samples were collected from a trailer 250 meters from the coast from a height of 2 meters above ground level (AGL). The second site was along the U.S. portion of the Tijuana River (TJR), 4 km inland and east of its outlet as it

passes under the Hollister Street bridge (32.5514, -117.0840), whereby river samples were collected from the bridge. No aerosol samples were taken at that site. The third site was 2.6 km north of the Tijuana River outflow at the Imperial Beach (IB) Pier (32.5795, -117.1328). Aerosol samples were collected at the lifeguard tower 60 meters from the ocean at a height of 3 meters AGL. The fourth site was 8.7 km north of the Tijuana River outflow at Silver Strand State Beach (SS) (32.6357, -117.1427). Aerosol samples were collected at the lifeguard tower 150 meters from the coast at a height of 10 meters AGL. The fifth site was 36 km north of the Tijuana River outflow at the Scripps Institution of Oceanography pier (SIO) (32.8661, -117.2546). Aerosol samples were collected at the pier over the surf zone at 10 meters above sea level. Water samples were collected in the surf zone at all coastal sites by wading (BF, SS) or above from an available pier (IB, SIO).

Aerosols were collected daily on 47 mm combusted quartz-fiber filters placed in a stainless-steel sample holder for approximately 23.5-hour sampling times at a nominal flow rate of ~50 liters per minute (LPM) from a vacuum pump. Aerosol field blanks were collected by placing aerosol filters in the sample holder and immediately replacing them. Water samples were acquired while the filters in the aerosol sampler were changed. We used 5-gallon buckets (one bucket for each site), rinsing twice with collected seawater. For each day of sample collection, water and aerosol samples were acquired roughly in order: SS (10:30 AM PST), IB (12:00 PM PST), BF (3:00 PM PST), and TJR (5:00 PM PST). SIO samples were acquired roughly at 11:00 AM PST.

### 3.5.2. Environmental conditions and air mass origin

Alongshore transport was evaluated using swell data from the CDIP Imperial Beach nearshore buoy 155.(59) During this study, alongshore ocean currents were

likely weak because swell came primarily from the west, normal to the coast (**Fig. S3.1**), forcing Tijuana River outflow to the shore with some migration to the south and north. Due to westerly swell, pollution discharge from the Tijuana River is localized along the coastline.[117] During this study, wave direction was primarily from the west (60%) and southwest (40%) (see **Fig. S3.1**), predicted to drive pollution inputs to the ocean northward, although some bidirectional and outward distribution through dilution and turbulent mixing is expected.[119] While aerosols can be emitted from bubbles and foams formed in rivers,[282,283] the aerosol composition in southern California coastal areas during onshore flows or transport over maritime regions is predominantly fresh and aged sea salt aerosol, representing more than 57% of the total particles analyzed in one study,[289] attributed to wave-breaking and bubble-bursting processes in the ocean.[282]

Particle origin was assessed with local winds and a particle dispersion model. Local winds for the BF, IB, and SS southern sampling stations were acquired from the Tijuana River Estuarine Research Reserve.[290] Local winds for SIO were retrieved from the Coastal Data Information Program SIO pier station.[291] Hourly winds during each sampling period were plotted into wind roses, as shown in Figs. S2 and S3.[292] Because SSA may accumulate on land[293] and because anthropogenic pollution may accumulate over the ocean[294], wind direction alone is not entirely indicative of airborne sources.

Longer-range particle sources were evaluated using the FLEXPART Lagrangian particle dispersion model.[295] FLEXPART uses global gridded atmospheric wind data to estimate the forward or backward transport of particles or air parcels in simulated releases from a given location. Input atmospheric data came from the NCEP Climate Forecast System Version 2 (CFSv2) 6-hourly products, Research Data Archive, at the

National Center for Atmospheric Research, Computational and Information Systems Laboratory.[296] For each run, FLEXPART simulated the release of 1000 particles, releasing a fraction at intervals over five days and tracking them backward through time. Releases were simulated four times for each 23-hour sampling period, every six hours at 1600, 2200, 0400, and 1000 hrs local time, to incorporate local, daily sea breeze patterns. One set of 96 back trajectories released particles from the IB location for the southern sampling stations, and another released particles from the SIO location. Outputs from the two release locations are similar. Particles were released just above ground level, at 10 m height, and transported horizontally and vertically, according to the atmospheric winds. We limit our analysis to horizontal transport (lat/lon).

After reviewing the spatial coverage of the outputs, we used the two-day data for each back trajectory, which was sufficient for visualizing and evaluating marine vs. continental air mass origin. 48-hour FLEXPART back trajectories of each sampling period (**Figs. S3.2** and **S3.3**) indicate air masses originated from terrestrial and marine locations. Our analysis attributes each sampling day to a marine, mixed, or land influence to infer different potential terrestrial sources of varying pollutant classes. It is important to note that the local land and sea breeze diurnal cycle, not accounted for in the long-range back trajectories, can contribute to the mixing and accumulation of background aerosol populations in the coastal atmosphere.[122,297–299]

### 3.5.3. Sample preparation procedures and analysis

Preparation of water samples for analysis involved the following procedure: from 5-gallon buckets, 1 L sub-samples were collected in high-density polyethylene (HDPE) bottles rinsed in deionized water, once again rinsing twice with the water sample. These 1 L sub-samples were kept on ice throughout the sampling period from collection to

laboratory preparation at ~ 7:00 PM PST. In the lab, water samples were acidified to a pH of 2 using concentrated hydrochloric acid (HCl) following the well-established protocol for DOM extraction described by Dittmar *et al.* [300]. They were subsequently stored in a 4°C refrigerator before extraction (time between storage and extraction of the organic compounds in water samples ranged from one day to one week).

Aerosol filters were switched daily with combusted tweezers to prevent contamination, sealed in combusted aluminum foil, brought to the lab on ice, and stored in a -80°C freezer before extraction. Aerosol filter blanks (combusted quartz-fiber filters not used for aerosol collection) were handled similarly, and the time between storage and extraction of the aerosol filter samples ranged from one day to one month.

Before organic extraction, aerosol filters were thawed for 30 minutes and extracted with 2 mL of LC-MS-grade methanol. Then, the eluent was brought to 40 mL with pH 2 LC-MS-grade water and agitated. From here, organic compounds of all sample types were separated via solid-phase extraction using Priority PolLutant (PPL) resin (Bond Elut, Agilent) following the methodology described in previous works by our team.[237,301] Briefly, PPL cartridges were rinsed and activated with methanol (LC-MS grade, Fisher Scientific) and conditioned with pH 2 water (LC–MS grade, Fisher Scientific). Then, water samples and aerosol filter eluent were pulled through the cartridges at a flow rate of ~ 10 ml $min^{-1}$ under vacuum. After extraction, the cartridges were rinsed with pH 2 water and dried under nitrogen flow. The PPL cartridges were then stored in a -80°C freezer for eight months before analysis due to delays from the COVID-19 pandemic. “PPL blanks” were taken by running pH 2 LC-MS grade water through this protocol.

External standards were prepared from a mixture of 15 standard compounds for quantitative analysis and prepared at 1.37, 13.7, and 137 ng/sample, added to filters, and extracted following the same procedure as with the aerosol samples. Thus, the filter and PPL extraction efficiency was incorporated into calibrated response factors.

Strict quality assurance and quality control practices were followed. Aerosol field blanks were taken from each site and handled the same as filter samples. Method blanks were performed using deionized water and were handled the same way as water samples. All compounds detected (ion counts >300) regularly (>50%) across blank measurements were discarded from further analysis.

Organic chemical analysis was performed via a nontargeted LC-MS/MS workflow detailed elsewhere[237,301] using a Thermo Vanquish UHPLC and a Thermo Orbitrap Elite LTO Linear Ion Trap-Orbitrap MS. Briefly, PPL cartridges were eluted with 2 mL of methanol, dried under vacuum, and resuspended in 100 µL MeOH/$H_2O$/formic acid (FA) (80/19/1). 10 µL of each solution was injected into the Thermo Vanquish reverse-phase UHPLC system using a Phenomenex C18 porous core-shell column. Spectra were collected using a data-dependent nontargeted method in positive mode.

Raw spectra were converted to .mzXML files using ProteoWizard[302], and ion features were generated from extracted ion chromatograms (XIC) using MZmine2[303] and linked to their tandem mass spectra, which provides a combination of relative abundance (XIC) and qualitative (MS/MS) information. Pre-processed data is available here: https://massive.ucsd.edu/ProteoSAFe/dataset.jsp?task=b121936ced6d4deebd7654bb440bf56c. For peak picking in positive mode, an intensity threshold of 3000 ions for MS1

spectra and 10 ions for MS/MS spectra were used. For the MS1 chromatogram building, a 5 ppm mass accuracy and a minimum peak intensity of 3000 ions were used. XIC were deconvoluted using the local minimum search algorithm with the chromatographic threshold set to 1%, a minimum relative height of 10%, a minimum absolute height of 5000, a minimum ratio of 1.5 for peak top/edge, and a minimum peak duration of 0.1 min. MS1 features were then linked to MS/MS spectra within 5ppm mass accuracy and 0.3 min retention time windows. Isotope peaks were grouped using the isotope grouper module, and features from different samples were aligned with 10 ppm mass tolerance and 0.1 min retention time tolerance. MS1 features not accompanied by an MS/MS spectrum were not considered further. MS1 features that did not occur in at least two samples or contained a minimum of two peaks per isotope pattern, or both, were also filtered out. After filtering, gaps in the feature matrix were filled with the peak finder multithreaded algorithm with a retention time tolerance of 0.2 min, a mass tolerance of 5 ppm, and an intensity tolerance of 10%. Finally, peak areas were exported in a feature table as a .csv file and corresponding consensus MS/MS spectra as a .mgf file for future analysis and processing.

The Global Natural Products Social Molecular Network did spectral matching and source identification.[240] All data for this study is accessible on the Global Natural Products Social Molecular Networking site here: https://gnps.ucsd.edu/ProteoSAFe/status.jsp?task=f6ae3b3bbd1d45a9b0c02c8e503f8032. Features were automatically matched to the GNPS library spectrum, including community-provided spectra. Compound class tags were taken from GNPS and were manually checked and updated (see Table S2 for annotated compounds included in this

work). For non-targeted analysis in the SI, abundances of each compound class are calculated from the summed measured ion counts of individual compounds detected above the background in each sample. Due to unknown differences in the extraction efficiencies and sensitivities between compounds in this non-targeted analysis, a complete or quantitative comparison between the compound classes identified in this study cannot be made. However, semi-quantitative differences between sample types and as a function of sampling location still yield useful information about how these pollutants are distributed and transferred in the coastal environment.

Calibration curves and analytical figures of merit for the targeted analytes can be seen in **Fig. S3.4.** and **Table S3.1**. Each compound's intensity and standard deviation in solvent blanks determined the instrumental detection limits. The intensity and standard deviation in field blanks and PPL blanks determined the method limits of detection. Calibration limits of detection were defined as three times the error in the y-intercept of the calibration curve for each quantified pollutant.

### 3.3. Results

#### 3.3.1. Spatial distribution of targeted water pollutants between measurement sites

Fifteen compounds representing common and toxic PCPs, drugs, metabolites, plastic additives, and biocides were quantified, exhibiting concentration gradients in the water samples with sampling location; all were most concentrated in the Tijuana River and least concentrated at SIO. Details of the collection, extraction, quantification, and data analysis procedures are described in the Methods. **Table S3.2** shows the median water concentrations and detection frequencies. **Figure 3.5A** shows the concentration distributions for each quantified pollutant from the different water collection sites, arranged according to the highest median concentration in Tijuana River water.

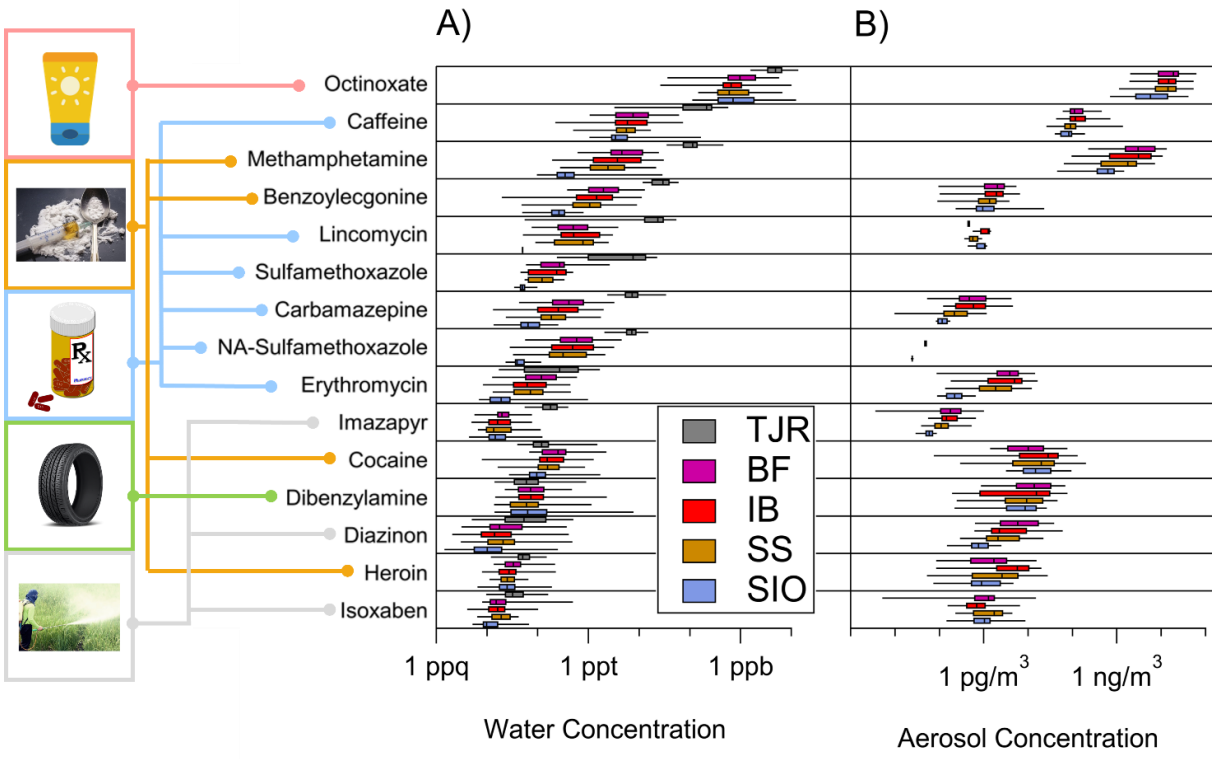


**Figure 3.2** Concentrations of quantified pollutants in A) water and B) aerosol across all sampling sites. Compounds are organized from top-to-bottom based on their highest-to-lowest median concentrations in the water samples from the TJR site. Representative pollutant categories and sources of the quantified compounds are shown: sunscreen additive/personal care product marker (pink), illicit drugs and their metabolites (orange), pharmaceutical drugs and their metabolites (blue), plastic/rubber residue (green), and biocides (gray). The sampling sites are as follows: TJR (Tijuana River), BF (Borderfield State Park), IB (Imperial Beach), SS (Silver Strand State Park), SIO (Scripps Institution of Oceanography pier.)

The most concentrated pollutant quantified in water samples was octinoxate (octyl methoxycinnamate), an organic UV filter in sunscreens. Octinoxate and other UV filters enter coastal marine waters through wastewater effluent, heavily trafficked beach areas, and diving locations.[52] It should be noted its quantification exhibited some challenges further explained in previous studies[237] and had a higher relative standard deviation in its sensitivity (20%) compared to other compounds (typically <3%). Octinoxate

concentrations in the water samples ranged from 600 ppt at Silver Strand (SS), a site north of the Tijuana River, to almost a factor of ten higher at five ppb in the Tijuana River samples (TJR). In comparison, these concentrations are similar to levels measured off the coast of Hong Kong (89 ppt – 4 ppb)[58] but two orders of magnitude lower than measurements made at Trunk Bay in the U.S. Virgin Islands (1.5 ppm).[59] As shown in **Figure S3.5A**, which compares each day's concentration at SIO to southern sites on the same day (i.e., the ratio of octinoxate at southern sites to SIO), their concentrations were greater, approximately 1:10.

The stimulant caffeine, a well-studied chemical marker for human activity[304], exhibited median concentrations ranging from 3 ppt in the ocean water at SIO to 200 ppt in river water at the TJR site. For comparison, the riverine concentrations of caffeine measured in this study are on the same order of magnitude as other measurements in rivers such as the Thames (London, UK), Hai (Tianjin, China), and the Lambro (Milan, Italy).[305] Ocean concentrations were typically on the lower end of other reported measurements, measured as high as 11 ppm in the Darwin Harbor of Northern Australia.[306] Caffeine showed a slight gradient of decreasing concentrations from the southernmost sites moving northward to SIO, similar to other quantified pharmaceuticals such as lincomycin, sulfamethoxazole, carbamazepine, and erythromycin. The metabolite n-acetyl sulfamethoxazole showed a similar trend to its parent compound, sulfamethoxazole.

Another waterborne compound measured was the illicit drug methamphetamine, which exhibited median concentrations of 100 ppt in river water at the TJR site of 100 ppt. In contrast, concentrations in ocean water ranged from 5 ppt at BF to 350 ppq at

SIO. These concentrations were the same magnitude reported in many wastewater-influent samples and two orders higher than the Llobregat River (Barcelona, Spain).[268] Similar gradients were observed with other illicit drugs, including heroin and cocaine, which showed overall lower concentrations in water (<100 ppq). Cocaine's metabolite, benzoylecgonine, was also detected in the Tijuana River, showing a gradient in median concentrations with the highest concentrations in the TJR (29 ppt) followed by BF, IB, and SS (1-2 ppt) and SIO (290 ppq.)

Concentrations of the biocides imazapyr, diazinon, and isoxaben were relatively low in the water samples (<100 ppq) but exhibited strong concentration gradients between the TJR site and others, with decreasing concentrations from BF to SIO and significantly higher concentrations in river water compared to the ocean. These compounds have not been previously reported in the TJR but are similar in magnitude to some (endosulfan - 29.7 ppq and endrin - 10 ppq) and lower than others (DDT - 2 ppt.) [307]

Dibenzylamine, a vulcanization activator used primarily in the rubber processing industry, showed less variability in its concentration (~100 ppq) between TJR water and all ocean samples. This compound is a component of rubber tires with a possible emission source from road wear,[308] which is a significant source of microplastics.[144] Notably, water concentrations in this study were much lower than previous measurements of dibenzylamine (400 ppt) in the polluted Cochin Backwater in Kerala, India.[309] The lack of a gradient between TJR and ocean samples suggests that the TJR is not an important point source of this compound to the ocean.

### 3.3.2. Spatial distribution of targeted aerosol pollutants between measurement sites

Median aerosol concentrations with detection frequencies are listed in **Table S3.2** and displayed graphically in **Figure 3.2B**. Median concentrations of octinoxate in aerosol ranged from ~1-10 ng $m^{-3}$. These ambient concentrations are comparable to levels observed in air samples collected above wastewater treatment plants[310] and three orders of magnitude higher than those measured in other urban locations.[88] Octinoxate has also been detected but not quantified in Caribbean trade winds.[146] To our knowledge, these are the first reported aerosol concentrations of this compound at a coastal urban site, underscoring the potential increased inhalation exposure risk for this toxic sunscreen chemical at beach sites compared to inland urban environments.

Airborne concentrations of methamphetamine (~500-3000 pg $m^{-3}$) and caffeine (~100 pg $m^{-3}$) were higher than those measured by Johnson et al. 2023[311] in urban air in Auckland, New Zealand, which reported average methamphetamine concentrations of ~25 pg $m^{-3}$ and caffeine concentrations of ~15 pg $m^{-3}$. As the cities' populations are similar, this suggests that untreated sewage from the Tijuana River amplifies the airborne presence of these compounds.

Methamphetamine showed a strong gradient across different locations, with both sites close to Imperial Beach (BF and IB) enhanced by a factor of five compared to the background site at SIO. Interestingly, airborne methamphetamine concentrations were generally higher than caffeine concentrations, even though caffeine showed higher concentrations in ocean water. This may be due to the more effective ocean-to-air transfer of methamphetamine, which will be discussed later.

Diazinon was the most concentrated airborne biocide with a concentration at BF

of 5.9 pg $m^{-3}$, significantly less than concentrations following immediate application (10 μg $m^{-3}$).[312] It exhibited a strong decreasing trend from BF to SIO, where the median concentration was 780 fg $m^{-3}$. The other biocide compounds had similar concentration gradients across all coastal sites.

Median pollutant aerosol concentrations (**Fig. 3.2B**) were highest near the TJR site. This gradient was most evident for pollutants associated with wastewater transported in the Tijuana River relative to more dilute ocean samples, including octinoxate, methamphetamine, benzoylecgonine, erythromycin, imazapyr, and diazinon. However, some pollutants in aerosol exhibited no discernable relationship to proximity to the Tijuana River, including caffeine, lincomycin, cocaine, dibenzylamine, and isoxaben. This may be attributed to different water and airborne sources along the coast, such as treated wastewater, runoff in other rivers, or direct aerosol sources. For example, while benzoylecgonine median concentrations in water and aerosol decreased at northern sites, its precursor, cocaine, had no distinct spatial concentration gradients in water or aerosol. This is consistent with benzoylecgonine as a primary wastewater pollutant[313,314], which may get transferred in SSA, whereas cocaine can be exhaled into the air directly[314] as well as secondarily through wastewater release[268,313] followed by aerosolization.

Furthermore, we categorized the quantified pollutants based on whether the air masses primarily passed over the marine environment, land, or a mixture of both, as determined by local winds and FLEXPART air mass back trajectory analysis This analysis shown in **Fig. S3.6** revealed that pollutant concentrations in aerosols were often lower under pure marine-origin local winds. However, no conclusions could be

drawn concerning whether more pollution is related to a specific air mass origin because pure marine-origin local winds were also during precipitation events, reducing their aerosol concentrations through wet deposition. This is further complicated by the limited spatiotemporal resolution of the back trajectory analysis, as it cannot capture the differences in pollutant concentrations due to variability in local wind direction, turbulence, and sea breeze circulation.

The gradients observed with proximity to the Tijuana River outflow in water and aerosol samples indicate a connection between pollution in the Tijuana River, ocean, and air. While there was no apparent correlation between the ocean water and aerosol concentrations of individual pollutants (see **Fig. S3.7**), **Figure 3.3** shows a compelling correlation between the concentrations of pollutants in ocean water and their corresponding concentrations in aerosol when viewed over their seven orders of magnitude concentration range, providing further evidence of a connection between ocean and aerosol pollutants. The lack of any significant correlation between individual pollutants' aerosol and ocean water concentrations is unsurprising, as sea-to-air transfer and detection at the measurement site will be impacted by highly variable meteorological and oceanic conditions. These include wind direction and factors affecting SSA emissions, including wind speed, white cap coverage, and sea surface temperature.[36,315–317] Therefore, it is essential to identify an SSA tracer, which could be used to compare its concentration to pollutant concentrations in aerosols to know whether the pollutants in aerosols originated from the ocean. In the following analysis, we evaluate which pollutants were present in SSA by examining their correlation with a unique indicator of polluted SSA from wastewater. Furthermore, we delve into the

potential for the quantified pollutants to become airborne in SSA based on their physicochemical properties and factors influencing selective transfer in SSA.

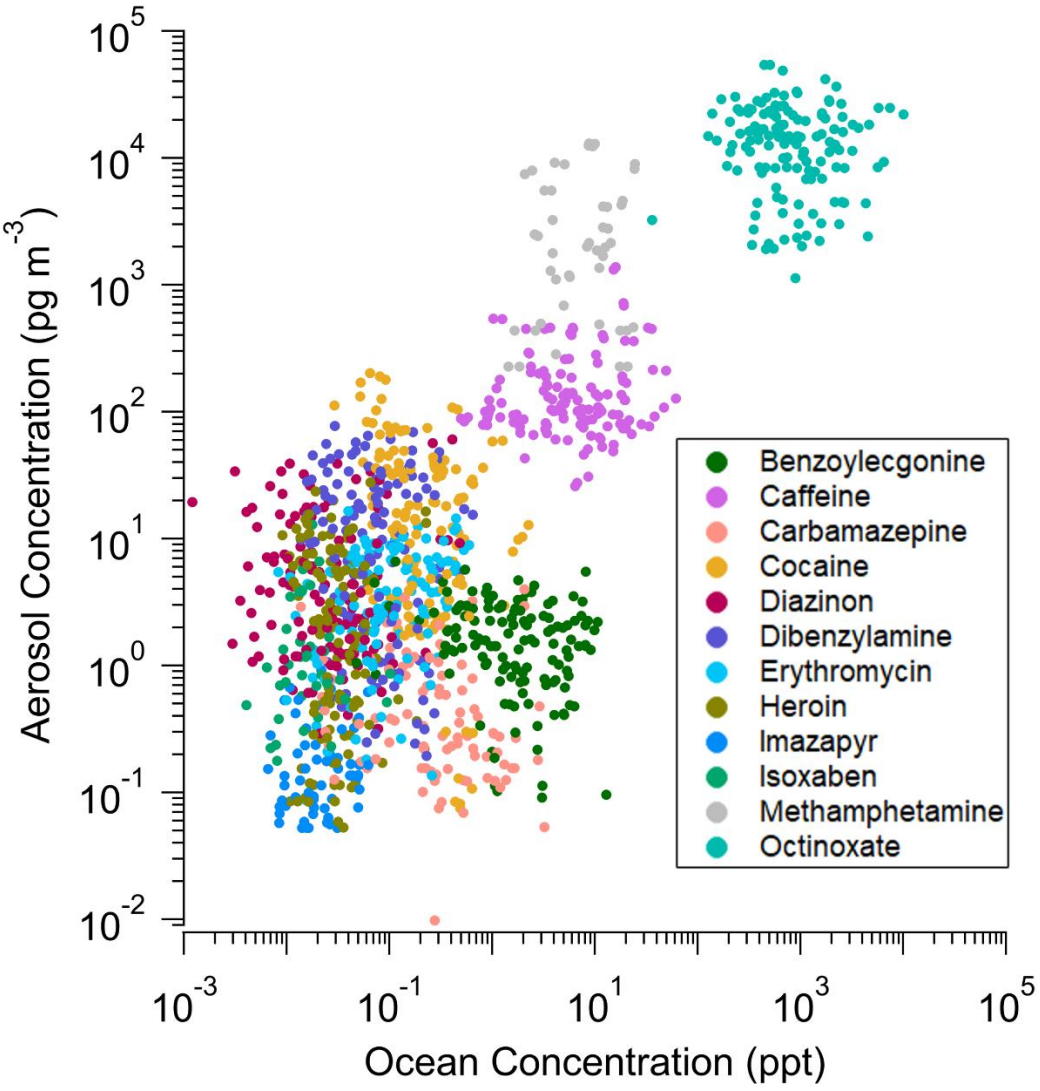


**Figure 3.3** Concentrations of all quantified pollutants in the aerosol samples are displayed against their concentrations in ocean water samples at all sampling sites

### 3.3.3. Benzoylecgonine: a novel tracer of wastewater-contaminated sea spray aerosol

While $Na^+$ is commonly used as an SSA tracer, ions in the samples were selectively removed during solid-phase extraction. This was done to concentrate the

organic components and to prevent ion suppression effects during the analysis with ESI-MS for improved detection sensitivity. Furthermore, $Na^+$ could be transported locally or regionally in both pristine and polluted SSA and, therefore, cannot be used to trace polluted SSA unambiguously. Therefore, we used a common tracer for wastewater pollution as a tracer of sewage-contaminated SSA, the cocaine metabolite benzoylecgonine. Benzoylecgonine is metabolized in the liver and primarily introduced to the environment via the wastewater stream following its excretion in human urine. This metabolite is stable in the environment and concentrates in surface waters.[313] Thus, detecting benzoylecgonine in aerosol samples can be related to the transfer of components from wastewater from the TJR that entered the surf zone into SSA in this coastal region. In other words, any pollutant that correlates with benzoylecgonine in SSA suggests that the pollutant underwent the same river-to-ocean and ocean-to-air transfer.

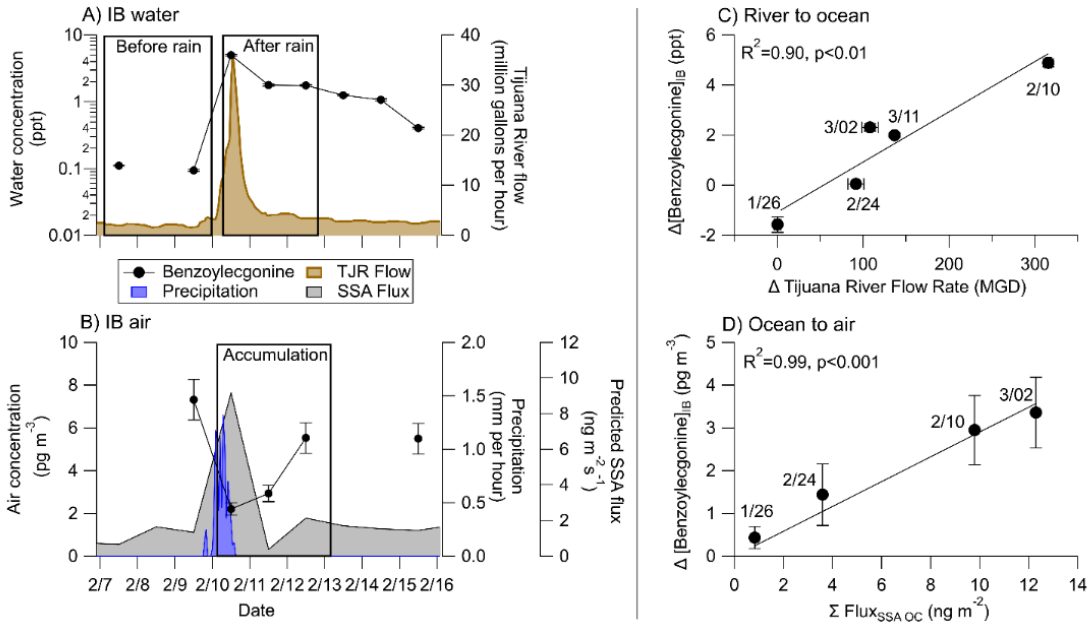


**Figure 3.4** (A) Time series of benzoylecgonine concentrations in IB water and Tijuana River flow rates surrounding the precipitation event on 2/10. Boxes indicate the before and after precipitation event used to calculate $\Delta[\text{Benzoylecgonine}]_{IB}$ in water and ΔTijuana River flow rate shown in (C). (B) Time series of benzoylecgonine concentrations in IB aerosol, precipitation rate, and predicted SSA mass flux. The box indicates the accumulation period following the precipitation event used to calculate $\Delta[\text{Benzoylecgonine}]_{IB}$ in aerosols and integrated predicted SSA mass flux, $\sum \text{Flux}_{SSA\ OC}$ in (D). (C) The correlation between the increase in Tijuana River flow and benzoylecgonine in IB water indicates river-to-ocean transfer dependent on river flow. (D) The correlation between the integrated modeled SSA organic carbon mass flux and the increase in benzoylecgonine in IB aerosols indicates ocean-to-air transfer dependent on SSA generation. Error bars represent the propagated standard deviations in the concentrations for those days.

**Figure 3.4A** demonstrates the increase in benzoylecgonine concentrations in IB water after precipitation-induced transboundary flow in the Tijuana River during one sampling period. Incorporating all five sampling periods (see **Fig. S3.8** for the complete time series) demonstrates a strong linear dependence between benzoylecgonine concentrations in ocean water and the Tijuana River transboundary flow rate (**Fig. 3.4C**, $R^2$=0.90, p<0.01), indicating a source of benzoylecgonine in IB water from the Tijuana River. While aerosol wet deposition during the precipitation event could re-supply

benzoylecgonine and other pollutants in the air to the ocean surface (shown by the decrease in benzoylecgonine concentration during the rain event in **Fig. 3.4B**), we calculated an insignificant increase of 0.02% in benzoylecgonine concentrations in IB water, assuming the deposition of ~5 pg $m^{-3}$ of aerosol-phase benzoylecgonine (difference in aerosol-phase concentration before and during 2/10 rain event in **Fig. 3.4B**) in a 200 m well-mixed marine boundary layer and 10 m surf zone width (see **SI** for calculations.) Therefore, while wet deposition can reduce airborne pollutant concentrations, it does not significantly increase waterborne concentrations in this environment.

As the pollutant concentrations in seawater increase following the Tijuana River discharge, we observe the removal of benzoylecgonine in aerosols at first due to wet deposition, followed by a sharp increase in concentration after the event (**Fig. 3.4B**.) We hypothesize that this increase after the precipitation event is related to the accumulation of SSA in the region. To test this, we compared the increase in benzoylecgonine aerosol concentrations following periods of wet deposition to the integrated estimated SSA mass flux (equivalent to total SSA mass generated) within that accumulation period (**Fig. 3.4D**.) For this analysis, we used the SSA source function model developed by De Leeuw [36] which parameterized SSA generation in the surf zone using experimental data collected in San Diego.[123] While this function over-predicts SSA flux in global models,[315] it is appropriate for predicting increased SSA generation in the surf zone compared to the open ocean. Compared to a different model[316] that parameterizes SSA generation based on wind speed and sea surface temperature, the models agree within an order of magnitude (see **Fig. S3.9** and discussion on these calculations in the

**Methods**.) This analysis revealed a strong correlation (**Fig. 3.4D**, $R^2$=0.99, p<0.01) between the increase in benzoylecgonine concentrations in aerosol and integrated SSA flux calculated over three days following each precipitation event, confirming that aerosol concentrations of benzoylecgonine are linked to its transfer via SSA. The precipitation event surrounding 3/11 was excluded from this correlation analysis because we did not have measurements after precipitation ended.

Given this strong evidence of benzoylecgonine as a SSA tracer linked to Tijuana River water pollution, positive linear correlations between the other pollutant concentrations and benzoylecgonine in the aerosol samples indicate they are produced by the same source, i.e., pollution from the Tijuana River that becomes aerosolized via SSA. Therefore, benzoylecgonine is used as a tracer to expand the analysis from IB (where we had wind speed measurements) to the other sampling sites. Two compounds were removed for this subsequent linear regression analysis due to their low detection frequency in the aerosol samples: sulfamethoxazole (DF<2%) and its metabolite N-acetyl sulfamethoxazole (DF=0%). **Figure 3.5** shows the linear regression analysis between the remaining twelve quantified pollutants in aerosols and benzoylecgonine. Spanning two orders of magnitude in aerosol concentrations, octinoxate (OCT), methamphetamine (MET), and dibenzylamine (DIB) displayed the strongest correlation coefficients (r-squared values) of 0.72, 0.76, and 0.71, respectively, with p<0.00001, indicating a shared polluted SSA source with benzoylecgonine. Notably, octinoxate did not show a clear gradient in water along the coast but still demonstrated a strong correlation with benzoylecgonine in the air. This suggests that the correlation was driven

by processes impacting sea-to-air transfer and airborne transport more than a river-to-ocean release.

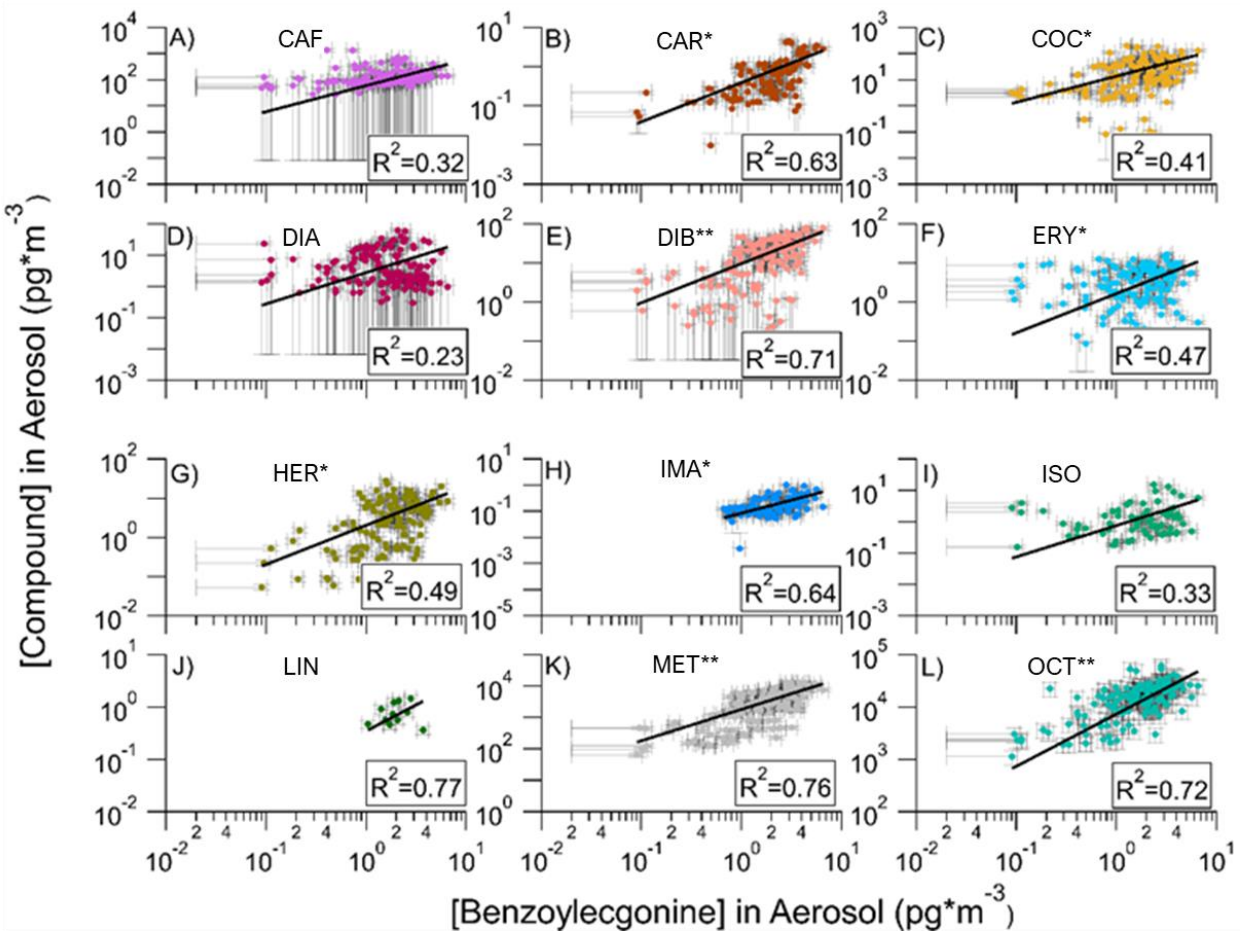


**Figure 3.5** Linear regression plots between twelve targeted pollutant compounds against benzoylecgonine concentrations in the aerosol phase from the BF, IB, and SS measurement sites. Strong correlations (**) with $R^2>0.7$ indicate a shared SSA source. Moderate correlations (*) with $0.4\leq R^2\leq 0.7$ indicate possible shared SSA and other aerosol sources. Weak correlations (no asterisk) with $R^2<0.4$ indicate different aerosol sources from SSA or insufficient data points for the analysis. List of compounds: (A) caffeine (CAF), (B) carbamazepine (CAR), (C) cocaine (COC), (D) diazinon (DIA), (E) dibenzyl amine (DIB), (F) erythromycin (ERY), (G) heroin (HER), (H) imazapyr (IMA), (I) isoxaben (ISO), (J) lincomycin (LIN), (K) methamphetamine (MET), and (L) octinoxate (OCT). Error bars reflect the relative uncertainty in the calibrated sensitivity for each compound. Horizontal error bars that extend to the left axis were below the quantification limit of benzoylecgonine and extended to its detection limit. Vertical error bars that extend to the bottom axis were below the quantification limit of the pollutant and extended to their detection limits. The intercept of the line of best fit is set to zero.

Weaker linear correlations were observed between benzoylecgonine and the other quantified pollutants, consistent with originating from sources other than sewage-contaminated SSA. For example, all biocide compounds (DIA, IMA, and ISO) exhibited weak or moderate correlations with benzoylecgonine, with r-squared values of 0.23, 0.64, and 0.33, respectively, implying additional non-SSA, likely continental primary aerosol sources. This is consistent with the common detection of biocides in agricultural dust and the ability of biocides to evaporate upon application and condense onto aerosols.[318] Similarly, both heroin and cocaine, which can be released directly into the air during use, were weakly-to-moderately correlated with benzoylecgonine in aerosols, with r-squared values of 0.49 and 0.41, respectively. Although caffeine is a common marker for human activity[304], it is found within all environmental compartments. This is consistent with caffeine's relatively weak correlation with benzoylecgonine in the aerosol phase (r-squared value of 0.32), which is exclusively present in the air due to its transfer from the river to the ocean and then the ocean into SSA. A limited number of data points prevents linking lincomycin to sewage-contaminated SSA.

Unique chemical properties can help to account for the efficiency of sea-to-air transfer. Two factors that impact the selective transfer of organic pollutants from the ocean to SSA are accumulation at the air-sea interface in the sea surface microlayer and entrainment in air bubbles.[131,278,279] Surface activity can be estimated by the octanol-water partitioning coefficient, $K_{ow}$. While $K_{ow}$ directly parameterizes hydrophobicity, it has been shown to constrain selective transfer in SSA.[278,319] Selective transfer of organic compounds in SSA is also mediated by the entrainment of compounds in air bubbles that rupture at the air-sea surface to produce SSA. This

process can be parameterized by the air adsorption coefficient ($K_a$) and the aqueous adsorption coefficient ($K_{aq}$).[131] Compounds where $K_a >> K_{aq}$ will accumulate in water and will not be efficiently transferred in SSA. Compounds where $K_a \sim K_{aq}$ will accumulate at the bubble-water interface and be incorporated into SSA. Compounds where $K_{aq} >> K_a$ will accumulate within the bubble and may transfer in the gas phase or become incorporated into SSA, depending on the compound's volatility. The ratio of $K_{aq}$:$K_a$ is represented by the bubble scavenging coefficient, $K_s$. To constrain the ocean-air partitioning of these compounds, the known $K_{ow}$ and calculated $K_s$ for each quantified pollutant (parameters provided in **Table S3.3**) were compared with an aerosolization factor (AF) (**Fig. 3.6**), calculated as the ratio of the pollutant concentration in aerosol to its concentration in water.[276] Given we had no measurements of [Na+], a marker for SSA, we could not calculate enrichment to [Na+], as done in other studies of SSA enrichment.[126,278,279] The data plotted in **Figure 3.6** takes into account sampling location and timeframe and includes only periods of marine-influenced air at the southern sampling sites (BF, IB, and SS) to rule out additional impacts from continental transport. AF is plotted directly against $K_s$ in **Figure S3.10.**

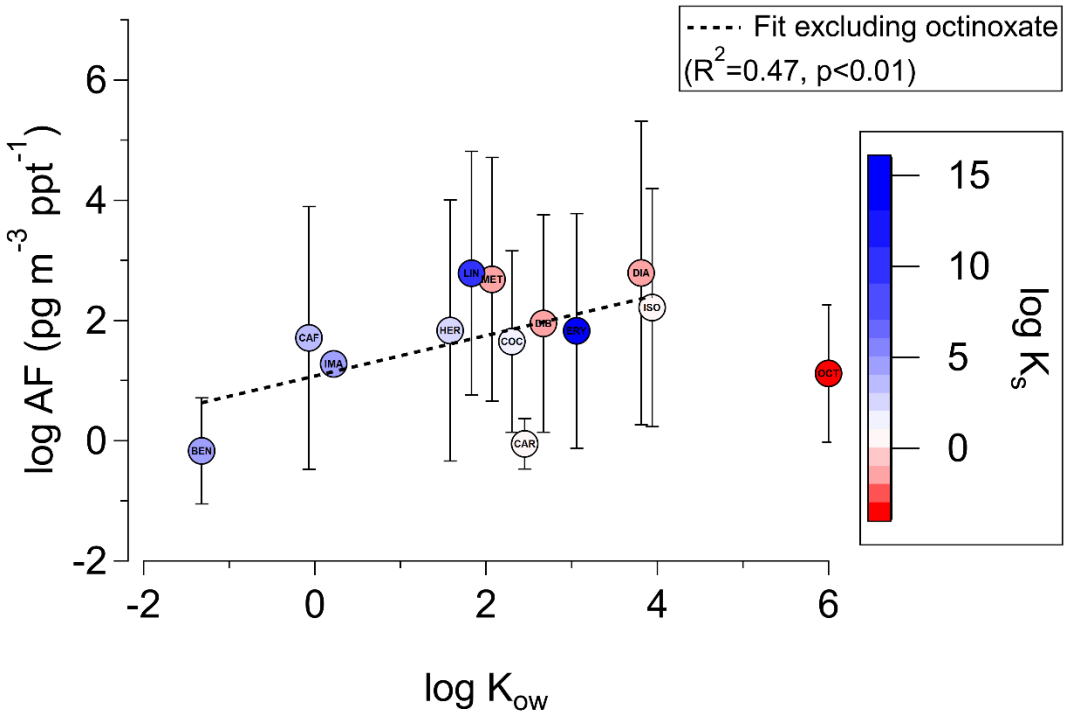


**Figure 3.6** Average aerosolization factors (AF) of 13 different pollutants as a function of their octanol-water partitioning coefficient, $K_{ow}$.[320]. Data points are colored by their scavenging coefficient, $K_s$, defined as the ratio between the aqueous adsorption coefficient ($K_{aq}$) and air adsorption coefficient ($K_a$). As octinoxate is not expected to be readily scavenged by bubble entrainment, it is not included in the linear fit. Only days exhibiting predominantly marine-influenced air masses at BF, IB, and SS are included.

This analysis shows a significant but moderate ($R^2$=0.47, p<0.01) correlation between AF and $K_{ow}$, illustrating a potential connection between pollutant enrichment in aerosols and the surface activity of these waterborne pollutants. (*15*, *46*) The uncertainties, representing one standard deviation from the mean in log AF, indicate significant variability in pollutant concentrations between measurement days and across locations.

Compounds with low $K_{ow}$ but high $K_s$, such as benzoylecgonine, caffeine, and imazapyr, may not accumulate at the surface but still be scavenged and emitted by bubble bursting. Compounds with high $K_{ow}$ but low $K_s$, such as octinoxate, may

accumulate at the surface but not be efficiently scavenged by bubbles. Thus, they do not transfer as efficiently into SSA as other compounds, as indicated by their relatively low AF. For this reason, octinoxate was not incorporated into the statistical analysis of AF vs $K_{ow}$. However, its high abundance in aerosol and ocean water samples and its large $K_{ow}$ demonstrates that even compounds not preferentially scavenged by bubbles may still exhibit transfer into SSA if enriched at the surface and in high abundance.

Processes beyond the scope of this study may influence the measured AF of octinoxate and similar compounds. One potential pathway for surface-active semivolatile compounds like octinoxate to enter SSA is through volatilization from the ocean surface, followed by partitioning into SSA, similar to the gas-to-aerosol transfer mechanisms observed with other polycyclic aromatic hydrocarbons.[321] The precise transfer mechanism of this compound from water to air warrants further investigation. Additionally, photochemical degradation of UV-absorbing compounds like octinoxate is known to occur rapidly in the aerosol phase[9]. This degradation, combined with octinoxate's estimated lower scavenging efficiency by bubbles, may contribute to its observed lower AF. Further studies are needed to understand the chemical losses of each component in the aerosol phase. For instance, considering the heterogeneous oxidative loss rate of bisphenol-A – a common plastic residue pollutant – with an e-folding lifetime of approximately four days in SSA mimics at an OH-radical concentration of $1.5\times10^{6}$ molecules $cm^{-3}$[2215], the measured aerosol pollutant concentrations after an accumulation period following a rain event (between 3 and 4 days) could be two to three times lower than those freshly emitted in SSA. These chemical losses are difficult to quantify from field measurements but suggest that the true AF, determined from

unreacted concentrations, for the most reactive species is greater than what can be measured in the field.

This analysis shows that waterborne pollutants originating from the Tijuana River and runoff that enters the ocean following precipitation events can be released into the atmosphere, where they have the potential to travel long distances,[137,322], persist in urban air,[299] and impact airborne exposure to a broad range of those living in coastal communities.

### 3.3.4. Estimated transfer between different environmental compartments

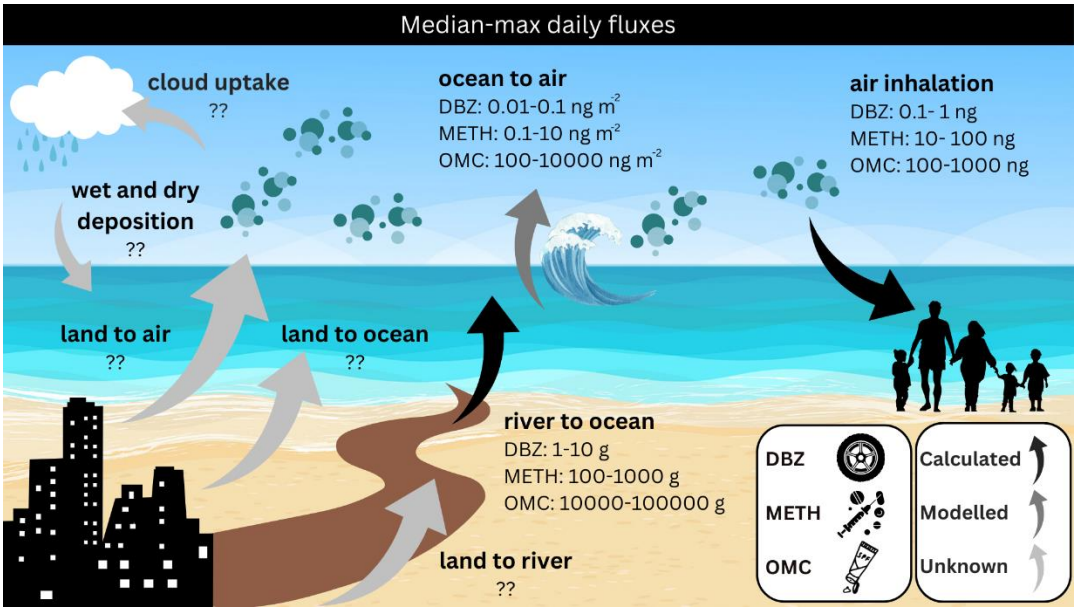


**Figure 3.7** Exploratory estimated median-to-max daily fluxes between different environmental compartments at the coast for dibenzylamine, methamphetamine, and octinoxate. Estimates based on measured concentrations are shown by the black arrows, estimates using predictive models relying on additional assumptions are in dark gray, and unknown processes are in light gray.

#### 3.3.4.1. River-to-ocean transfer

Based on the pollutant concentrations measured in the Tijuana River and the river's flow rates, we can estimate the release fluxes of individual pollutants into the Pacific

Ocean, as shown in **Figure 3.7.** For this analysis, we multiply the daily flow rate for each sampling day by each pollutant concentration measured in Tijuana River water. The more concentrated pollutants, such as octinoxate and methamphetamine, have estimated discharge rates of 10-100 kg $day^{-1}$ and 0.1-1 kg $day^{-1}$, respectively, while relatively lower concentration pollutants like dibenzylamine correspond to 1-10 g $day^{-1}$. Since dibenzylamine is a rubber additive likely representing 1% of rubber mass[308], it could indicate much higher concentrations of rubber microplastics than we can calculate here. For comparison, the mass flux of octinoxate is an order of magnitude higher than wastewater influent fluxes (pre-treatment) in Swiss cities.[93] Methamphetamine flux from the Tijuana River (0.1-1 kg $day^{-1}$) was slightly larger than that measured in Oslo, Norway sewage influent (142-295 g $day^{-1}$).[323] The large riverine fluxes of these pollutants pose serious environmental concerns for surrounding riverine and marine ecosystems and the health of hundreds of thousands of residents and beachgoers frequenting areas such as Imperial Beach and Playas de Tijuana. Moreover, some fish have exhibited addictive responses to methamphetamine at environmentally relevant levels (below median concentrations measured at BF, IB, and SS), altering their behavior and potentially influencing whole communities.[324] The UV filter octinoxate found in sunscreens has been linked to the devastation of coral reefs, which provide USD 375B annually to coastal communities worldwide through tourism and fishing. [325]

#### 3.3.4.2. Ocean-to-air transfer

The potential ocean-to-air transfer is estimated based on the previously described SSA source function (see **SI** for details.)[36] The contribution of each compound to produced organic SSA mass is predicted by applying an SSA enrichment factor (i.e., $[X]_{SSA}/[Na^+]_{SSA}/[X]_{sw}/[Na^+]_{sw}$) according to that measured for PFAS.[137] While these

calculations are exploratory due to the lack of experimentally determined enrichment factors, we predict median mass fluxes transferred into SSA (shown in **Fig. 3.7**) ranging from ~10 pg $m^{-2}$ $day^{-1}$ for dibenzylamine to ~100 pg $m^{-2}$ $day^{-1}$ for methamphetamine, and ~100 pg $m^{-2}$ $day^{-1}$ for octinoxate. These concentrations for single compounds are similar to those that Johansson *et al.* 2019[137] estimated for the sum of PFOA and PFOS compounds, which peaked at ~1 ng $m^{-2}$ $day^{-1}$ in similar polluted coastal regions.

By assuming a well-mixed marine boundary layer height of 200 m and a steady onshore breeze of 5 m $s^{-1}$ as done in Allen *et al.* 2020[69], the onshore mass transfer of airborne contaminants can be estimated based on the airborne concentrations of each compound. We estimate a transfer of ~1-10 g of dibenzylamine, ~10-100 g of methamphetamine, and ~100-1000 g of octinoxate to air over the 1 km Imperial Beach coast per day under these conditions. Allen *et al.* 2020[69], which investigated the sea-to-air transfer of microplastics, estimated a mass flux of 1 kg $day^{-1}$ of airborne microplastics over a similar 1 km coastline. These calculations demonstrate that, on the most polluted days, the mass of airborne octinoxate may be comparable to the mass of microplastics entering terrestrial air masses at Imperial Beach and similarly polluted areas. Over an annual and global scale, under the assumption that humans heavily impact half the world's coastline[326] and that wind is blowing onshore for half the time,[69] we estimate a potential median transfer of ~50 tons of DBZ, ~8000 tons of methamphetamine, and ~40,000 tons of octinoxate per year from the marine to the terrestrial atmosphere. This extrapolation will vary by location depending on meteorological and oceanic conditions and proximity to pollutant sources.

#### 3.3.4.3. Airborne exposure

Exposure to waterborne pollution in the air has significant implications for the

health of marine and terrestrial ecosystems and humans. At a low-intensity inhalation rate of 0.7 $m^3$ $hr^{-1}$, Imperial Beach inhalation levels of octinoxate and methamphetamine are approximately 1-10 ng $hr^{-1}$, as indicated in **Fig. 3.7**. For octinoxate, this ambient concentration is comparable to levels observed in air samples collected above wastewater treatment plants[310] and three orders of magnitude higher than those measured in metropolitan Toronto, Canada.[88] This finding illustrates, for the first time, the increased health exposure risk at beach sites due to inhalation compared to urban environments for this ubiquitous toxic personal care product ingredient. It represents a novel exposure pathway that needs to be considered in future sunscreen policy and investigation of these compounds in coastal aerosol. The estimated airborne exposure levels of methamphetamine are significantly less than a single “dose,” indicating minimal acute impact on public health. However, the health effects of chronic inhalation of octinoxate, methamphetamine, and other pollutants examined here have not been studied. This study serves as motivation to consider the health effects of airborne exposure to what has been previously considered solely waterborne pollutants.

### 3.4. Broader implications for public health

This study shows SSA can serve as a vector for atmospheric transport of illicit and anthropogenic chemicals. Further studies are needed to determine how far, frequently, and consistently these pollutants are transported over land. Fundamental properties of SSA, such as viscosity, which can affect the chemical lifetimes of toxic compounds, are still poorly quantified.(53) Not only does this present a potential health concern in coastal marine environments, but also regions near large freshwater bodies such as the Great Lakes, which can experience high winds leading to aerosolization in similar bubble rupture processes.(54) Further, this study has implications for other areas with

polluted riverine and estuary input into the ocean near urban centers, such as the Mississippi River, Yangtze River, and Ganges River Deltas, impacting even larger populations than San Diego.(55) While aerosols may remain in the atmosphere for days to weeks, they can be removed through wet and dry deposition, impacting ecosystems and human water and food systems.[330] This deposition can directly impact plant life and contaminate food and drinking water. To constrain the impact of pollution in this region, a comprehensive analysis of all environmental compartments should be performed.

Local, regional, and federal air monitoring organizations should monitor this novel source of organic micropollutants to better inform the public of their exposure to these pollutants and conduct long-term trend analysis to gauge whether this exposure is increasing or decreasing due to policy action.[331] There is also a critical need for source control. Wastewater treatment agencies must detect a broader range of anthropogenic pollutants before the water is released into local water. Wastewater treatment plants should continue to pursue quaternary and water recycling techniques to fully remove organic pollution from wastewater before releasing it as effluent or using it as sludge.[81,82,268,269,271,310] This study highlights that coastal populations are exposed to wastewater effluent released into the ocean and motivates an urgent need for improved wastewater treatment infrastructure, greener alternative treatments such as seagrass meadows(58) in areas with poor or no wastewater management, and consideration in any policy interventions to reduce airborne exposure to waterborne pollutants and pathogens.

As climate change accelerates the intensity of storms,[286] more coastal locations in the US and beyond will experience severe flooding, overflowing combined stormwater-

sewage systems, and increasing untreated release into oceans.(56) Beyond the airborne transport of chemical pollutants, similar transport of pathogens from wastewater streams into rivers and the ocean could increase our susceptibility to diseases due to airborne bacteria and viruses that become aerosolized and then inhaled or ingested.[120] An estimated 80% of all wastewater worldwide is untreated(57) and flows into the environment, ultimately ending in the world's oceans.[285] The traditional view is that this pollution is too dilute to have environmental implications. However, as shown in this study, this waterborne pollution can become aerosolized and expose billions living near the coast worldwide.

### 3.6. Supplemental Materials

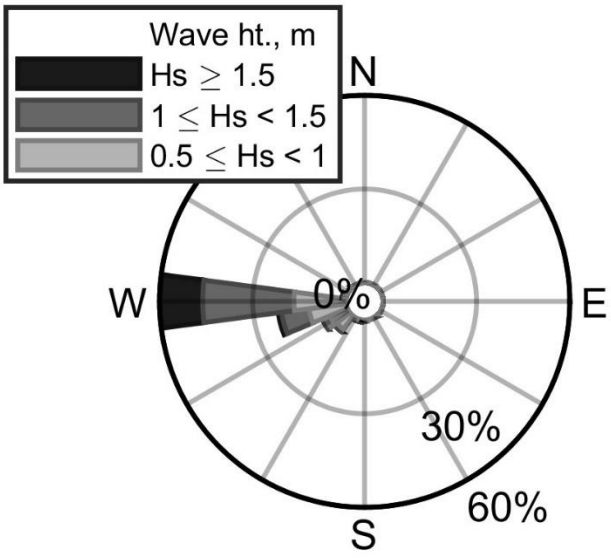


**Supplemental Figure 3.1** Local swell during the sampling periods. Swell data are shown for all sampling periods combined. Pictured is the percentage of time the swell came from a given direction with a given swell height: light gray: 0.5-1 m; dark gray: 1-1.5 m; black: 1.5+ m. The swell largely came from the west during the study period, which would not have generated strong alongshore transport. However, no transport is expected to the south, given some contribution from swell from the southwest.

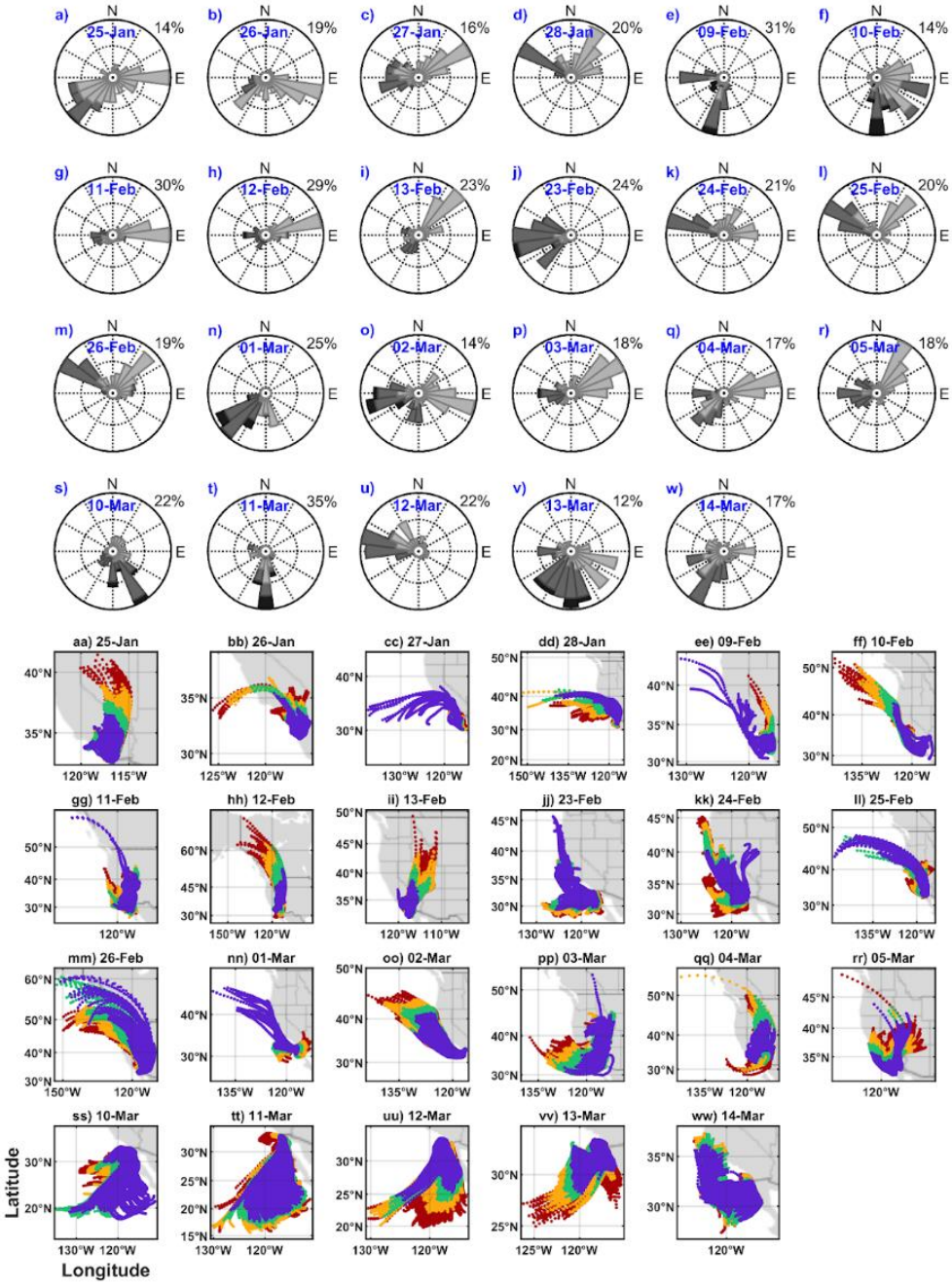


**Supplemental Figure 3.2** Local winds and back trajectories for the southern sampling locations BF, IB, and SS. Wind roses show the fraction of the sampling time wind blew from a given direction at multiple wind speed intervals: light gray: 0-2 m/s; dark gray: 2-4 m/s; black: 4+ m/s. Local winds (a-w) primarily show a mixture of onshore and offshore wind for each sampling period, common to coastal areas. Back trajectories (aa-ww) show individual simulated particles in four colors for the four FLEXPART runs for each sampling period. Like the local winds, the back trajectories show continental/terrestrial and marine air mass histories for each sampling period.

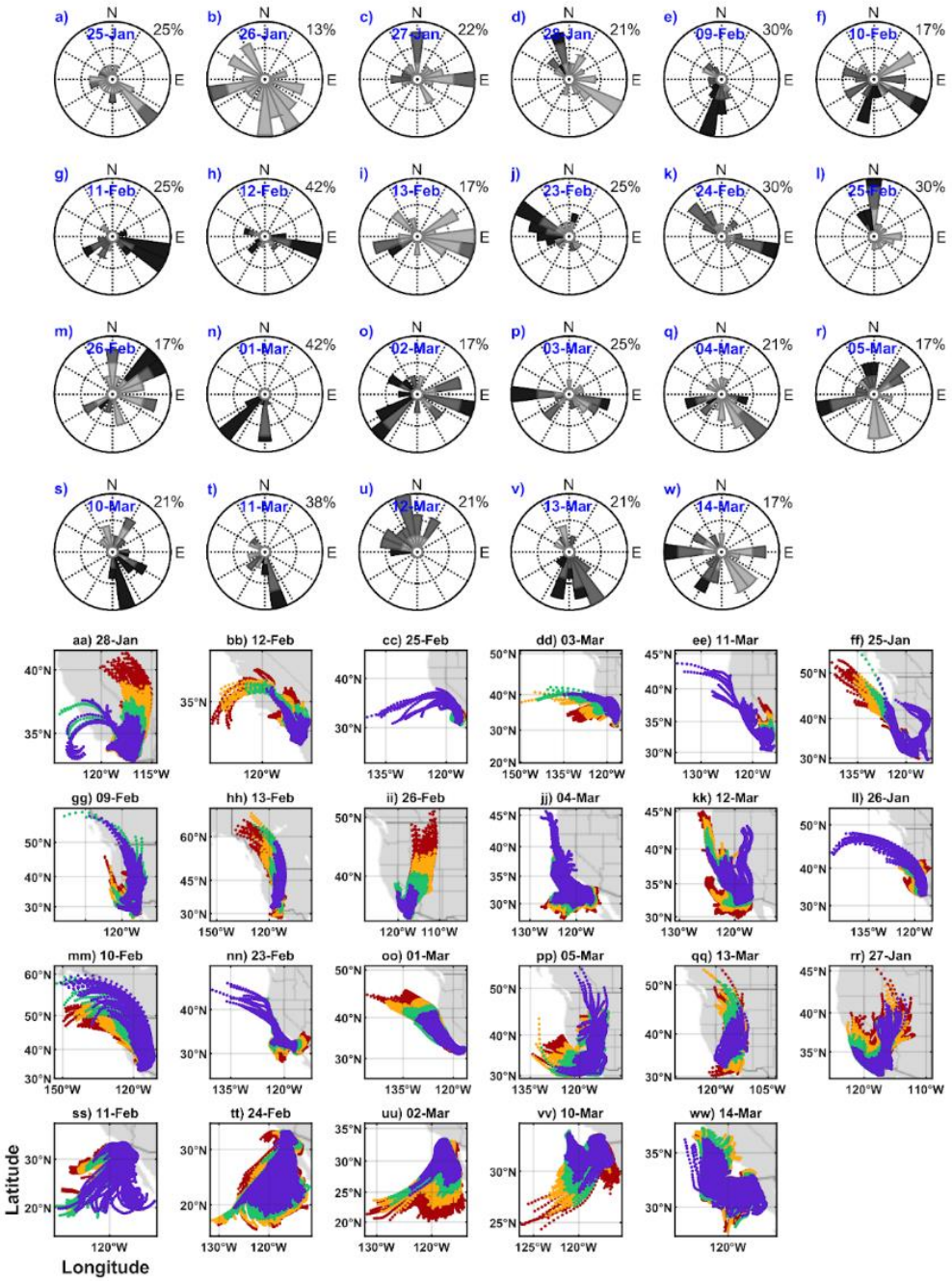


**Supplemental Figure 3.3** Local winds and back trajectories for the SIO sampling location. Wind roses show the fraction of the sampling time wind blew from a given direction at multiple wind speed intervals: light gray: 0-2 m/s; dark gray: 2-4 m/s; black: 4+ m/s. Local winds (a-w) primarily show a mixture of onshore and offshore wind for each sampling period, common to coastal areas. Back trajectories (aa-ww) show individual simulated particles in four colors for the four FLEXPART runs for each sampling period. Like the local winds, the back trajectories show continental/terrestrial and marine air mass histories for each sampling period.

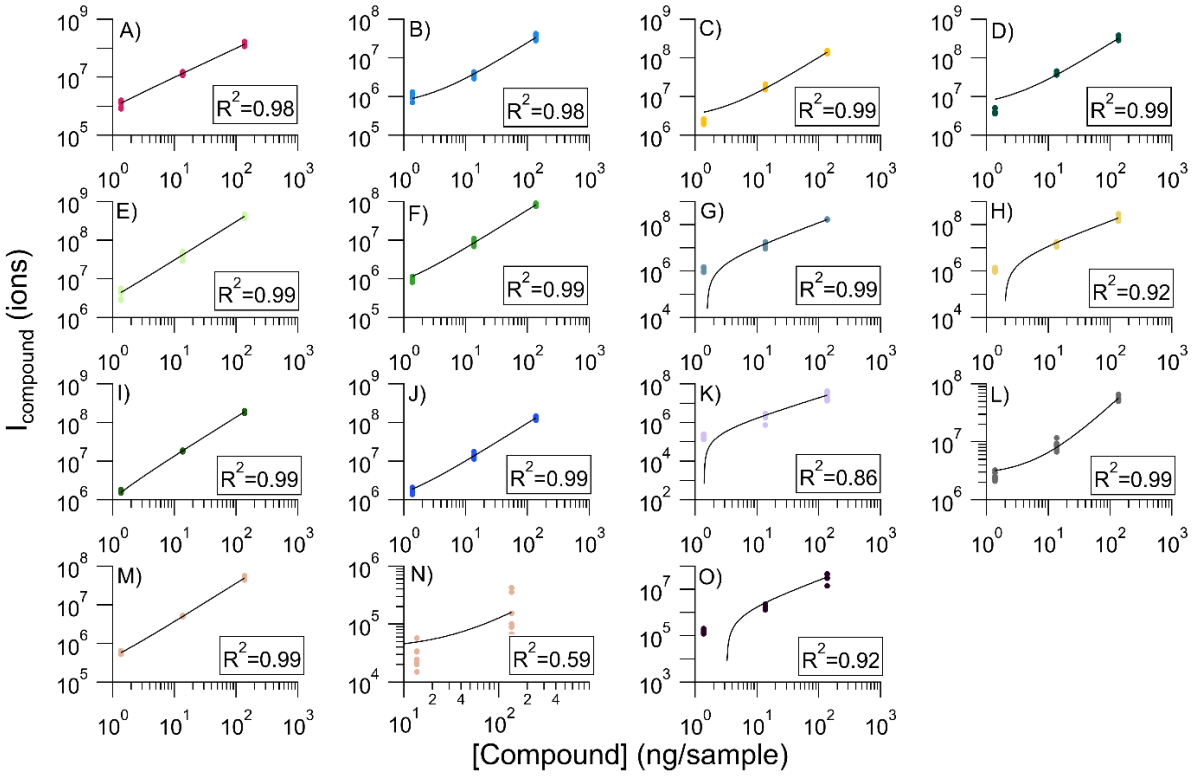


**Supplemental Figure 3.4** Calibration curve for 16 chosen pollutants. Analytical figures of merit are given in **Table S3.** List of compounds: (A) Benzoylecgonine (B) Caffeine (C) Carbamazepine (D) Cocaine (E) Diazinon (F) Dibenzylamine (G) Erythromycin (H) Heroin (I) Imazapyr (J) Isoxaben (K) Lincomycin (L) Methamphetamine (M) N-acetylsulfamethoxazole (N) Octinoxate (O) Sulfamethoxazole

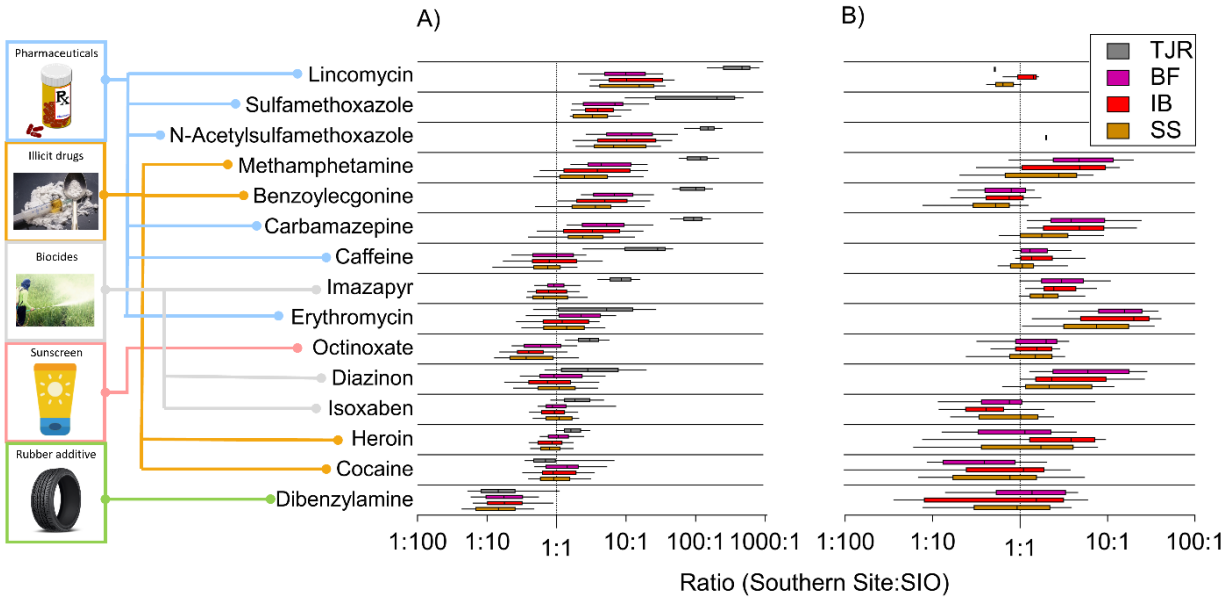


**Supplemental Figure 3.5** Ratios of quantified pollutants in A) water and B) aerosol compared to the SIO sampling site. Pollutants are organized from top-to-bottom based on their highest-to-lowest ratios in the water samples to the TJR site. Representative contaminant categories and sources of the quantified pollutants are shown: pharmaceutical drugs (blue), illicit drugs and metabolites (orange), biocides (gray), sunscreen additive/personal care product marker (pink), and plastic/rubber residue (green).

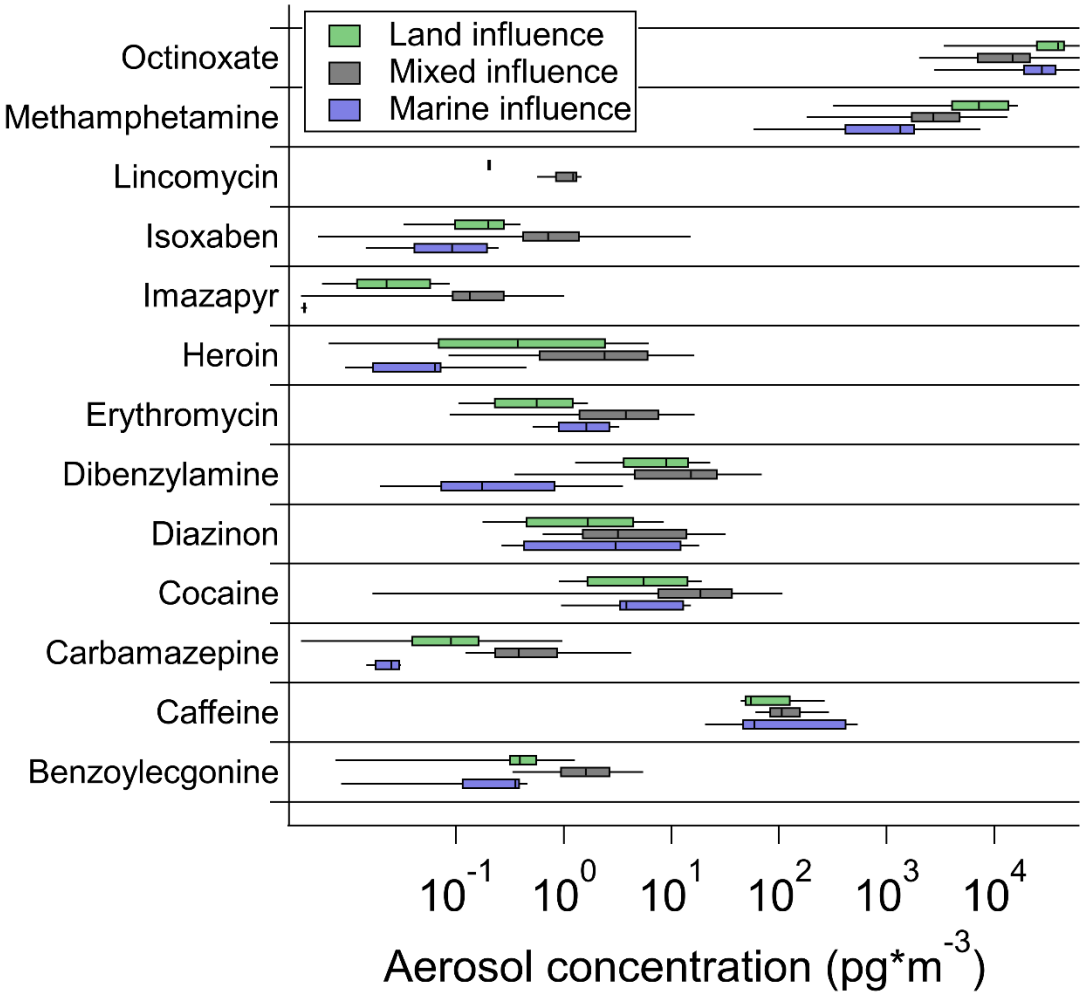


**Supplemental Figure 3.6** Concentrations of quantified micropollutants in air at southern sampling sites (BF, IB, SS) separated by air mass origin.

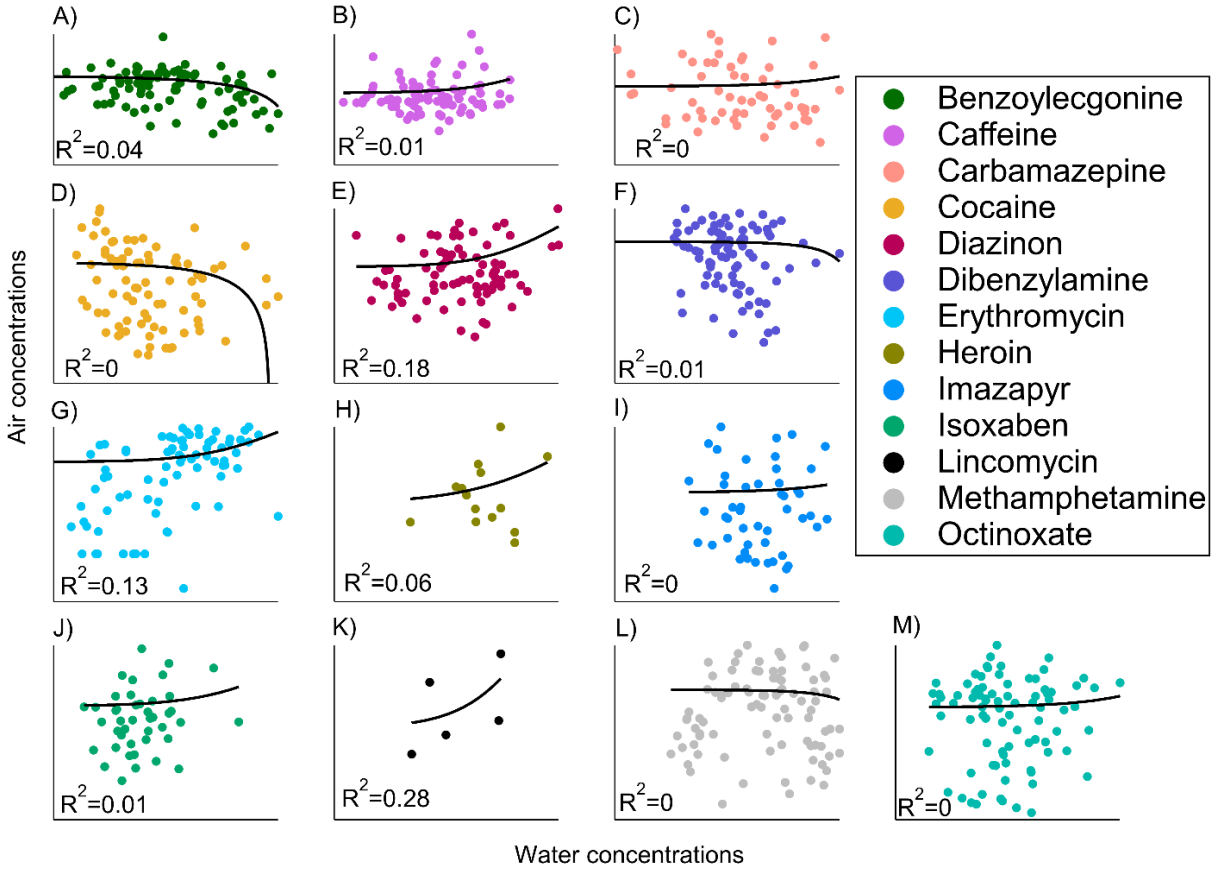


**Supplemental Figure 3.7** Correlation plots between aerosol concentrations of 13 different micropollutant compounds against water concentrations. Each data point represents one data pair collected on the same day at the same site. List of compounds: (A) Benzoylecgonine (B) Caffeine (C) Carbamazepine (D) Cocaine (E) Diazinon (F) Dibenzylamine (G) Erythromycin (H) Heroin (I) Imazapyr (J) Isoxaben (K) Lincomycin (L) Methamphetamine (M) Octinoxate.

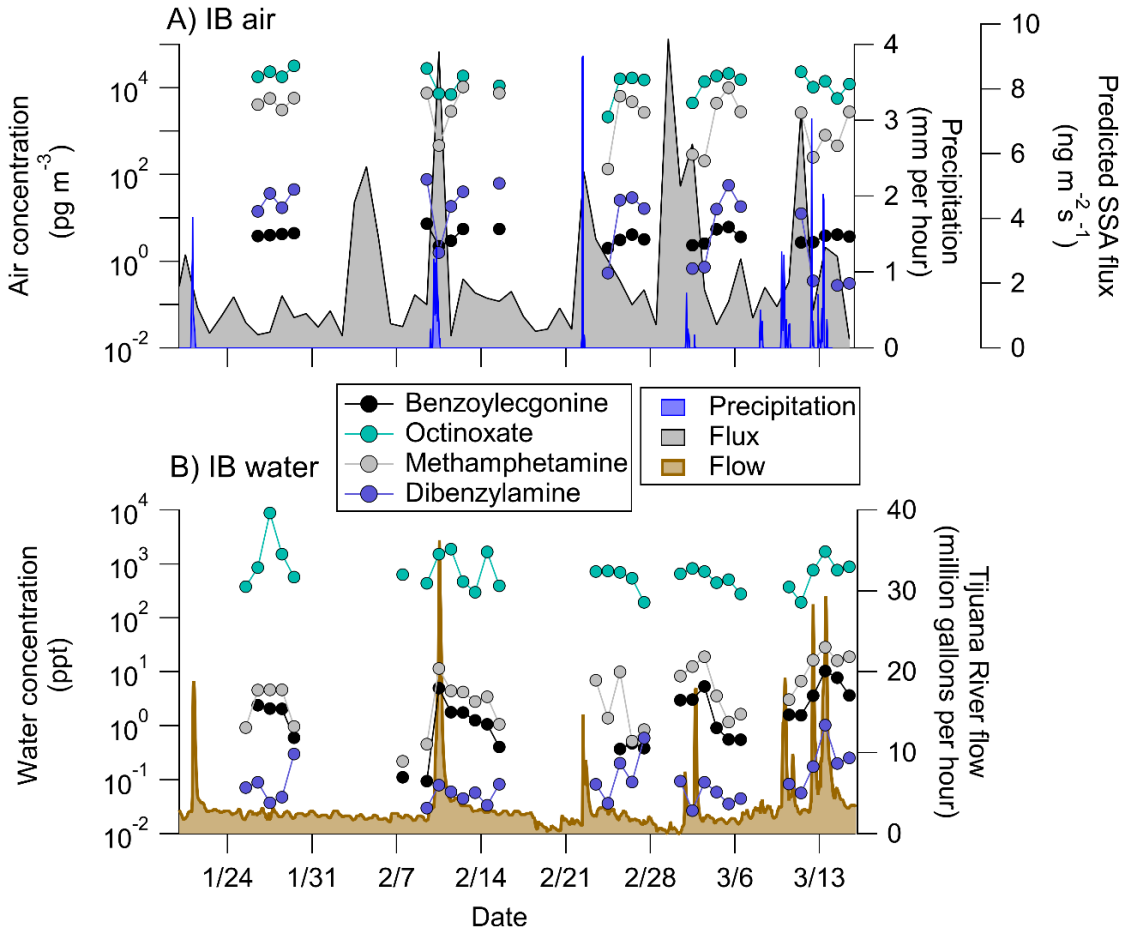


**Supplemental Figure 3.8**(A) Time series of airborne pollutant concentrations suspected to undergo sea-to-air transfer via SSA (left) as well as precipitation rates and predicted SSA flux (right.) (B) Time series of waterborne pollutant concentrations (left) and Tijuana River flow rate (right.)

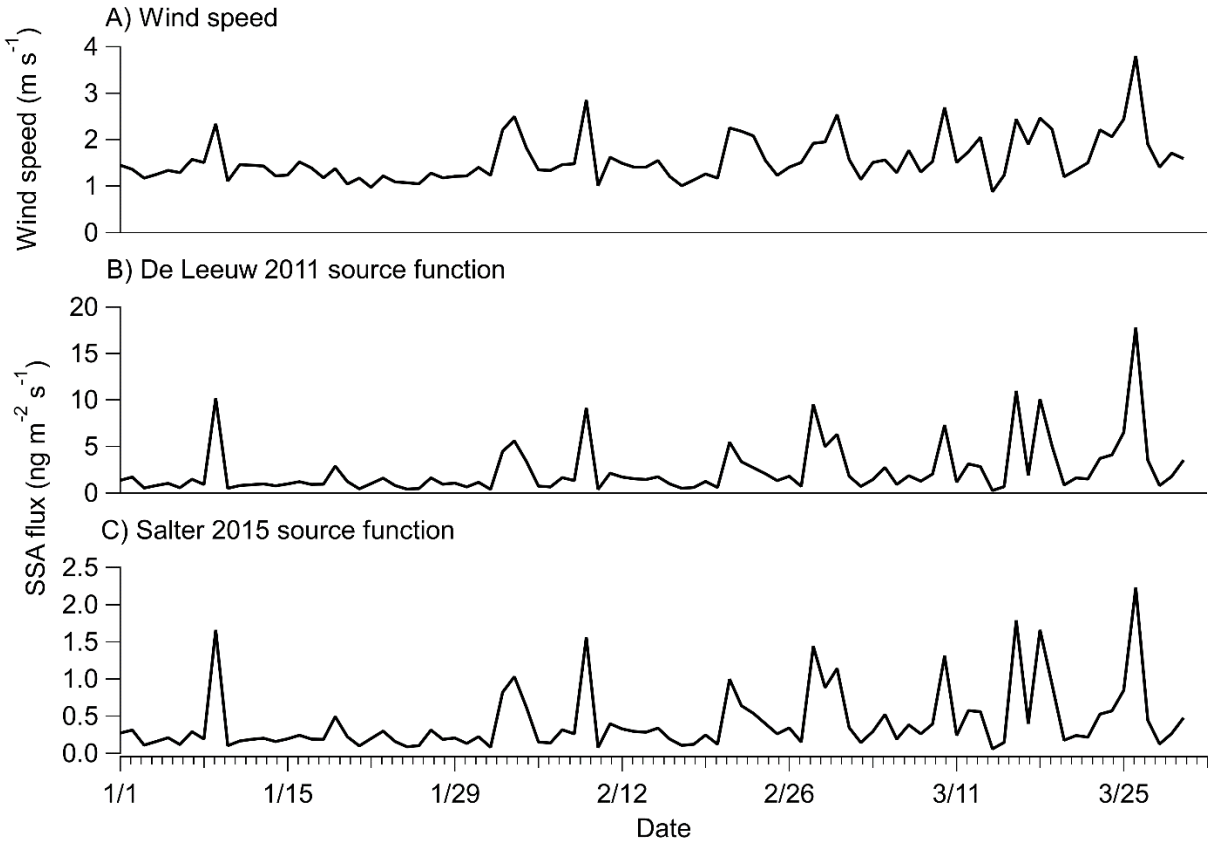


**Supplemental Figure 3.9** (A) Time series of wind speed measured by a meteorological station in IB. (B) Time series of SSA flux calculated using the De Leeuw 2011 source function. (C) Time series of SSA flux calculated using the Salter 2015 source function.

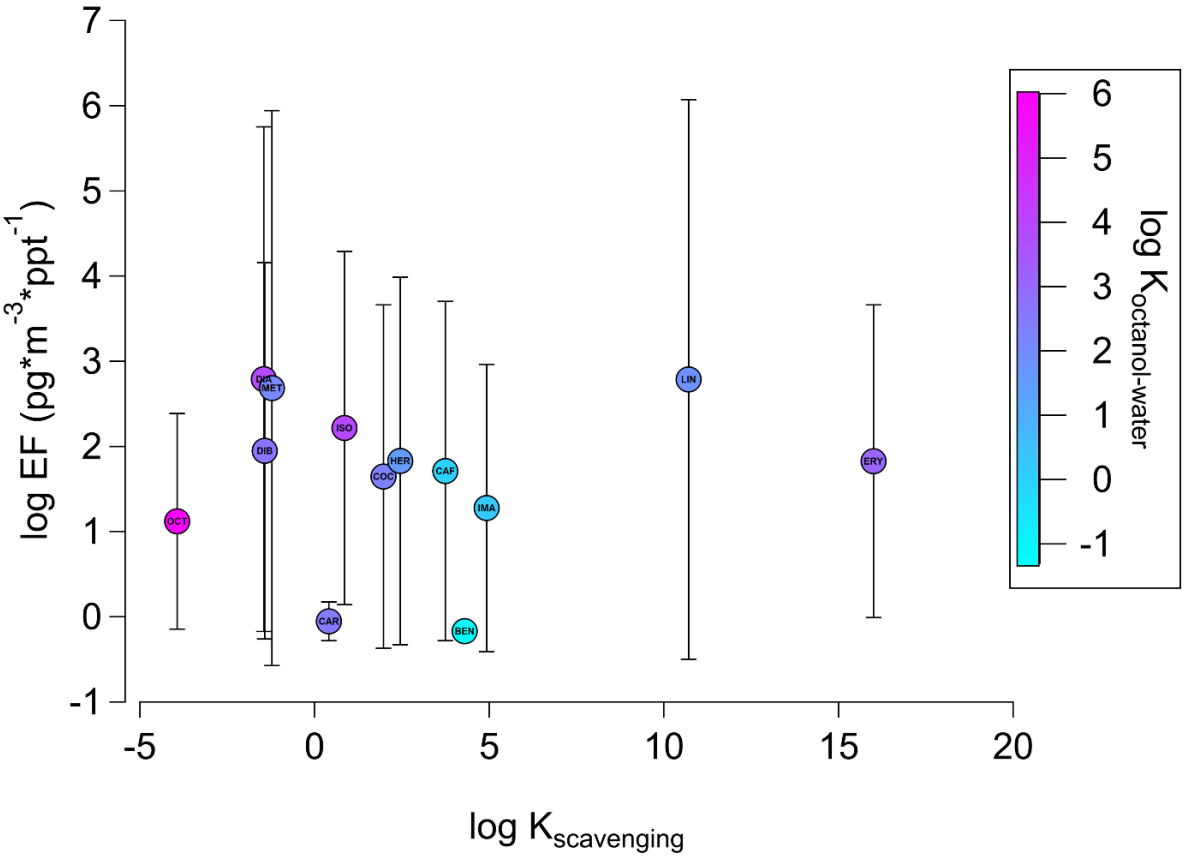


**Supplemental Figure 3.100** Average aerosol enrichment factors (EF) of 13 different micropollutant compounds as a function of their bubble scavenging coefficient, $K_s$ defined as the ratio between the aqueous adsorption coefficient ($K_{aq}$) and air adsorption coefficient ($K_a$).[320] Log $K_s$ values below -2.5 imply a compound is primarily present in water during the scavenging process. Log $K_s$ values between -2.5 and 2.5 imply a compound is present at the water-bubble interface. Log $K_s$ values above 2.5 imply a compound is primarily entrained inside the air bubble. Data points are colored by their octanol-air partitioning coefficient, $K_{ow}$. Only days exhibiting predominantly marine-influenced air masses at BF, IB, and SS are included.

**Supplemental Table 3.1** List of quantified micropollutant compounds and their classes along with figures of merit – calibration curve $R^2$, sensitivity to sample mass, instrumental limits of detection (LOD) for water and aerosol samples and calibration LOD for the same. Instrumental LOD was determined by the signal to noise ratio. Method LOD was determined by field and method blank measurements. Calibration LOD was determined by the external calibration curve. See **Figure S3.11** for plots of calibration curves.

| Compound | Class | Calibration Curve $R^2$ | Sensitivity (RSD) (ions $ng^{-1}$) (%) | Instrumental Limit of Detection | | Method Limit of Detection | | Calibration Limit of Detection | |
|---|---|---|---|---|---|---|---|---|---|
| **Benzoylecgonine** | Metabolite, Cocaine | 0.98 | 1.0E+06 (3%) | 1.2 ppq | 20 $fg*m^{-3}$ | 8.1 ppq | 140 $fg*m^{-3}$ | 120 ppq | 1.9 $pg*m^{-3}$ |
| **Caffeine** | Stimulant | 0.98 | 2.5E+05 (3%) | 4.9 ppq | 81 $fg*m^{-3}$ | 8.0 ppt | 130 $pg*m^{-3}$ | 130 ppq | 2.2 $pg*m^{-3}$ |
| **Carbamazepine** | Pharmaceutical, anticonvulsant | 1.00 | 1.0E+06 (1%) | 1.2 ppq | 20 $fg*m^{-3}$ | 7.0 ppq | 120 $fg*m^{-3}$ | 52 ppq | 870 $fg*m^{-3}$ |
| **Cocaine** | Illicit Drug | 0.99 | 2.3E+06 (3%) | 0.51 ppq | 8.5 $fg*m^{-3}$ | 11 ppq | 180 $fg*m^{-3}$ | 100 ppq | 1.7 $pg*m^{-3}$ |
| **Diazinon** | Insecticide | 0.99 | 3.0E+06 (2%) | 0.40 ppq | 6.6 $fg*m^{-3}$ | 860 ppq | 14 $pg*m^{-3}$ | 67 ppq | 1.1 $pg*m^{-3}$ |
| **Dibenzylamine** | Materials, Rubber | 0.99 | 6.0E+05 (2%) | 2.0 ppq | 33 $fg*m^{-3}$ | 320 ppq | 5.3 $pg*m^{-3}$ | 61 ppq | 1.0 $pg*m^{-3}$ |
| **Erythromycin** | Pharmaceutical, Antibiotic | 1.00 | 1.2E+06 (1%) | 1.0 ppq | 17 $fg*m^{-3}$ | 14 ppq | 230 $fg*m^{-3}$ | 64 ppq | 1.1 $pg*m^{-3}$ |
| **Heroin** | Illicit Drug | 0.92 | 1.4E+06 (6%) | 0.85 ppq | 14 $fg*m^{-3}$ | 1.9 ppq | 31 $fg*m^{-3}$ | 240 ppq | 17 $pg*m^{-3}$ |
| **Imazapyr** | Herbicide | 1.00 | 1.4E+06 (1%) | 0.87 ppq | 14 $fg*m^{-3}$ | 3.0 ppq | 50 $fg*m^{-3}$ | 49 ppq | 820 $fg*m^{-3}$ |
| **Isoxaben** | Herbicide | 0.99 | 9.6E+05 (1%) | 1.3 ppq | 21 $fg*m^{-3}$ | 1.3 ppq | 5.2 $fg*m^{-3}$ | 60 ppq | 1.0 $pg*m^{-3}$ |
| **Lincomycin** | Pharmaceutical, Antibiotic | 0.86 | 1.9E+05 (8%) | 6.3 ppq | 110 $fg*m^{-3}$ | 1.6 ppq | 26 $fg*m^{-3}$ | 330 ppq | 5.4 $pg*m^{-3}$ |

**Supplemental Table 3.2** List of quantified micropollutant compounds and their classes along with figures of merit – calibration curve $R^2$, sensitivity to sample mass, instrumental limits of detection (LOD) for water and aerosol samples and calibration LOD for the same. Instrumental LOD was determined by the signal to noise ratio. Method LOD was determined by field and method blank measurements. Calibration LOD was determined by the external calibration curve. See **Figure S3.11** for plots of calibration curves. (Continued)

| | | | | | | | | | |
|---|---|---|---|---|---|---|---|---|---|
| **Methamphetamine** | Illicit Drug | 0.99 | 4.2E+05 (2%) | 2.9 ppq | 48 $fg*m^{-3}$ | 1.2 ppt | 19 $pg*m^{-3}$ | 82 ppq | 1.4 $pg*m^{-3}$ |
| **N-Acetylsulfamethoxazole** | Metabolite, Sulfamethoxazole | 0.99 | 3.6E+05 (2%) | 3.4 ppq | 56 $fg*m^{-3}$ | 2.2 ppq | 36 $fg*m^{-3}$ | 68 ppq | 1.1 $pg*m^{-3}$ |
| **Octinoxate** | UV Filter | 0.59 | 1.2E+03 (21%) | 1.0 ppt | 17 $pg*m^{-3}$ | 56 ppt | 930 $pg*m^{-3}$ | 1.0 ppt | 17 $ng*m^{-3}$ |
| **Sulfamethoxazole** | Pharmaceutical, Antibiotic | 0.92 | 2.4E+05 (6%) | 4.9 ppq | 82 $fg*m^{-3}$ | 2.2 ppq | 37 $fg*m^{-3}$ | 240 ppq | 4.0 $pg*m^{-3}$ |

**Supplemental Table 3.3** Median concentrations in ppt and detection frequencies (DF in %) for 15 organic pollutants in water samples collected at each sampling site (Tijuana River – TJR, Border Field State Park – BF, Imperial Beach – IB, Silver Strand State Park – SS, Scripps Institution of Oceanography Pier – SIO.)

| Compound | Compound Class | Median TJR ppt (DF) | Median BF ppt (DF) | Median IB ppt (DF) | Median SS ppt (DF) | Median ppt SIO (DF) |
|---|---|---|---|---|---|---|
| **Benzoylecgonine** | Metabolite, Cocaine | 29 (100%) | 2 (100%) | 1 (100%) | 1 (100%) | 0.26 (100%) |
| **Caffeine** | Stimulant | 214 (100%) | 8 (100%) | 6 (100%) | 6 (100%) | 3 (100%) |
| **Carbamazepine** | Pharmaceutical, anticonvulsant | 7.0 (100%) | 0.41 (98%) | 0.25 (97%) | 0.183 (95%) | 0.062 (100%) |
| **Cocaine** | Illicit Drug | 0.12 (100%) | 0.252 (100%) | 0.15 (100%) | 0.16 (100%) | 0.096 (100%) |
| **Diazinon** | Insecticide | 0.054 (86%) | 0.018 (85%) | 0.014 (86%) | 0.021 (92%) | 0.010 (75%) |
| **Dibenzylamine** | Materials, Rubber | 0.060 (95%) | 0.070 (92%) | 0.073 (89%) | 0.060 (85%) | 0.061 (95%) |
| **Erythromycin** | Pharmaceutical, Antibiotic | 0.27 (95%) | 0.090 (85%) | 0.062 (79%) | 0.072 (75%) | 0.019 (56%) |
| **Heroin** | Illicit Drug | 0.051 (100%) | 0.033 (96%) | 0.027 (94%) | 0.025 (95%) | 0.025 (99%) |
| **Imazapyr** | Herbicide | 0.180 (100%) | 0.019 (80%) | 0.016 (81%) | 0.014 (80%) | 0.015 (86%) |
| **Isoxaben** | Herbicide | 0.032 (69%) | 0.015 (47%) | 0.016 (66%) | 0.019 (63%) | 0.010 (57%) |
| **Lincomycin** | Pharmaceutical, Antibiotic | 23 (100%) | 0.50 (73%) | 0.51 (64%) | 0.78 (45%) | 0.050 (2%) |
| **Methamphetamine** | Illicit Drug | 110 (100%) | 5 (100%) | 4 (100%) | 2 (100%) | 0.35 (100%) |
| **N-Acetylsulfamethoxazole** | Metabolite, Sulfamethoxazole | 7 (100%) | 0.59 (98%) | 0.49 (87%) | 0.32 (85%) | 0.039 (26%) |
| **Octinoxate** | UV Filter | 5000 (100%) | 970 (100%) | 650 (100%) | 600 (100%) | 710 (100%) |
| **Sulfamethoxazole** | Pharmaceutical, Antibiotic | 8 (100%) | 0.27 (32%) | 0.15 (42%) | 0.12 (27%) | 0.050 (15%) |

**Supplemental Table 3.4** Median concentrations in ppt and detection frequencies (DF in %) for 15 organic pollutants in air samples collected at each sampling site (Tijuana River – TJR, Border Field State Park – BF, Imperial Beach – IB, Silver Strand State Park – SS, Scripps Institution of Oceanography Pier – SIO.)

| Compound | Identity | Median BF pg*m$^{-3}$ (DF) | Median IB pg*m$^{-3}$ (DF) | Median SS pg*m$^{-3}$ (DF) | Median SIO pg*m$^{-3}$ (DF) |
|---|---|---|---|---|---|
| **Benzoylecgonine** | Metabolite, Cocaine | 2.0 (100%) | 1.9 (100%) | 1.4 (100%) | 1.0 (100%) |
| **Caffeine** | Stimulant | 110 (100%) | 120 (100%) | 90 (100%) | 84 (100%) |
| **Carbamazepine** | Pharmaceutical, anticonvulsant | 0.5 (81%) | 0.6 (75%) | 0.2 (50%) | 0.1 (12.5%) |
| **Cocaine** | Illicit Drug | 10 (100%) | 28 (96%) | 20 (100%) | 16 (100%) |
| **Diazinon** | Insecticide | 5.9 (100%) | 2.2 (100%) | 2.1 (96%) | 0.78 (98%) |
| **Dibenzylamine** | Materials, Rubber | 14 (100%) | 15 (94%) | 9.6 (100%) | 8.4 (100%) |
| **Erythromycin** | Pharmaceutical, Antibiotic | 3.9 (97%) | 5.0 (94%) | 1.9 (79%) | 0.2 (40%) |
| **Heroin** | Illicit Drug | 1.7 (100%) | 5.7 (79%) | 2.6 (92%) | 0.9 (98%) |
| **Imazapyr** | Herbicide | 0.1 (68%) | 0.1 (65%) | 0.1 (46%) | 0.1 (10%) |
| **Isoxaben** | Herbicide | 1.3 (46%) | 0.7 (56%) | 1.7 (50%) | 1.0 (60%) |
| **Lincomycin** | Pharmaceutical, Antibiotic | 0.5 (2%) | 1.3 (8%) | 0.6 (15%) | 1.0 (6%) |
| **Methamphetamine** | Illicit Drug | 3000 (100%) | 3100 (100%) | 1800 (100%) | 660 (100%) |
| **N-Acetylsulfamethoxazole** | Metabolite, Sulfamethoxazole | ND | 0.8 (2%) | ND | 0.4 (6%) |
| **Octinoxate** | UV Filter | 19000 (100%) | 15000 (100%) | 14000 (100%) | 5800 (100%) |
| **Sulfamethoxazole** | Pharmaceutical, Antibiotic | ND | ND | ND | ND |

**Supplemental Table 3.5** Physical parameters for compounds used in aerosolization factor (AF) analysis. $K_{ow}$, saturation vapor pressure, and Henry's Law constant are from the EPA EPI Suite from experimental databases or modeled estimates.[334] Ka is calculated as $RT*p^{-1}$. Kaq is calculated as $H^{-1}*p^{-1}$.[131]

| Compound | log $K_{ow}$ | Saturation vapor pressure (*p*) (Pa) | Henry's Law constant (H) ($Pa*m^3*mol$) | log $K_a$ | log $K_{aq}$ |
|---|---|---|---|---|---|
| **Benzoylecgonine** | -1.32 | 1.1E-07 | 2.0E-08 | 14.64 | 10.35 |
| **Caffeine** | -0.07 | 9.8E-07 | 7.2E-08 | 13.15 | 9.40 |
| **Carbamazepine** | 2.45 | 1.2E-05 | 1.6E-04 | 8.74 | 8.33 |
| **Cocaine** | 2.30 | 2.6E-05 | 4.3E-06 | 9.96 | 7.99 |
| **Diazinon** | 3.81 | 1.2E-02 | 1.1E-02 | 3.86 | 5.32 |
| **Dibenzylamine** | 2.67 | 7.9E-04 | 1.1E-02 | 5.07 | 6.50 |
| **Erythromycin** | 3.06 | 2.8E-23 | 4.0E-20 | 41.94 | 25.94 |
| **Heroin** | 1.58 | 1.0E-07 | 1.4E-06 | 12.84 | 10.39 |
| **Imazapyr** | 0.22 | 1.2E-08 | 4.8E-09 | 16.24 | 11.32 |
| **Isoxaben** | 3.94 | 5.5E-07 | 5.6E-05 | 10.51 | 9.65 |
| **Lincomycin** | 1.83 | 1.8E-15 | 7.9E-15 | 28.85 | 18.14 |
| **Methamphetamine** | 2.07 | 6.0E-01 | 6.7E-03 | 2.40 | 3.62 |
| **Octinoxate** | 5.80 | 1.9E-03 | 3.5E+00 | 2.19 | 6.13 |

### 3.6.1. Flux calculations

We estimate the SSA flux of compounds using the updated DL00 source function[123] from De Leeuw *et al.* 2011[36] which is appropriate for estimating fluxes of SSA in the surf zone below 9 m $s^{-1}$, as in this study. Of note, this parameterization was conducted at the Scripps pier, one of our sampling locations, making it particularly well suited for use in this study. The function shown in calculates number flux as a function of $D_p$ (particle diameter) and $U_{10}$ (wind speed at 10 m):

$$\frac{dF_N}{dD_p} = 4e^{0.23U_{10}}U_{10}^{3.41}D_p^{-1.5} \qquad eq\ 1$$

We modify this to mass flux assuming a spherical particle and a density of 2.2 g $cm^{-3}$[3317]:

$$\frac{dF_M}{dD_p} = \frac{16}{3}\pi e^{0.23U_{10}}U_{10}^{3.41}D_p^{1.5} \qquad eq\ 2$$

We separately integrate the source function for three modes of aerosol identified in Salter *et al* 2015 ($D_p$=0.095, 0.6 and 1.5 um)[316] to calculate the summed volume flux of each mode:

$$Flux_{SSA,mode\ 1} = \int_{.045}^{0.2} \frac{16}{3}\pi e^{0.23U_{10}}U_{10}^{3.41}D_p^{1.5} = 0.12e^{.23U_{10}}U_{10}^{3.41} \qquad eq\ 3$$

$$Flux_{SSA,mode\ 2} = \int_{0.35}^{1.03} \frac{16}{3}\pi e^{0.23U_{10}}U_{10}^{3.41}D_p^{1.5} = 6.73e^{.23U_{10}}U_{10}^{3.41} \qquad eq\ 4$$

$$Flux_{SSA,mode\ 3} = \int_{0.94}^{2.4} \frac{16}{3}\pi e^{0.23U_{10}}U_{10}^{3.41}D_p^{1.5} = 54e^{0.23U_{10}}U_{10}^{3.41} \qquad eq\ 5$$

We then calculate the total $Na^+$ produced in each mode by applying the mass fraction of $Na^+$ from Bertram *et al* 2018[124]:

$$Flux_{Na^+} = 0.055 * Flux_{SSA,mode\ 1} + 0.055 * Flux_{SSA,mode\ 1} + 0.26 * Flux_{SSA,mode\ 1} \qquad eq\ 6$$

As well as the total OC produced by applying the following:

$$Flux_{OC} = 0.82 * Flux_{SSA,mode\ 1} + 0.82 * Flux_{SSA,mode\ 1} + 0.08 * Flux_{SSA,mode\ 1} \qquad eq\ 7$$

For comparison, we also calculated SSA flux using the following parameterization from Salter *et al* 2015[316] where $F_{U10}$ is the volume flux in $m^3\ m^{-2}\ s^{-1}$, $N_i$ is the number flux of the i nm mode in $\#\ m^{-2}\ s^{-1}$ and T is the sea surface temperature in °C. A, B, C, and D are experimentally determined fitting parameters.

$$F_{U_{10}} = 2 * 10^{-8} * (U_{10})^{3.41} \qquad eq\ 8$$

$$N_i = F_{U_{10}} * (A_i * T^3 + B_i * T^2 + C_i * T + D_i) \qquad eq\ 9$$

The $Na^+$ and OC fluxes were calculated using eqs 6 and 7 and generally agreed within an order of magnitude with the estimates using the updated DL00 parameterization. We decided to use the updated DL00 estimates for the remainder of the analysis.

To estimate the increase in water concentrations due to wet deposition, we use the following equation where $\Delta[X]_{air}$ is the decrease in airborne concentrations, $h_{air}$ is the height of the marine boundary layer (estimated at 200 m here,) $h_{water}$ is the height of the surfzone (estimated at 10 m) and $\rho_{SW}$ is the density of seawater (~1,025,000 g $m^{-3}$):

$$\Delta[X]_{water} = -\Delta[X]_{air} * \frac{h_{air}}{h_{water}} * \rho_{SW}$$

To estimate the ocean to air transfer of each compound, we use the following equation from Johansson *et al* 2019[137] where EF is the enrichment factor of each compound, $[X]_{sw}$ is the concentration in seawater and $[X]_{particle}$ is the concentration in SSA:

$$[X]_{particle} = EF_X * \frac{[X]_{sw}}{[Na^+]_{sw}} * [Na^+]_{particle} \qquad eq\ 10$$

We calculate the mass flux release from the TJR using equation 1 where $Flux_{TJR}$ is the mass flux in kg $day^{-1}$, $[X]_{i,TJR}$ is the concentration of compound X on day i in the TJR in ppt, and $Flow_{i,TJR}$ is the flow in million gallons $day^{-1}$:

$$Flux_{TJR} = 3.8 * 10^{-3} * [X]_{i,TJR} * Flow_{i,Tijuana\ River} \quad eq\ 11$$

We calculate the $Flux_{onshore}$ in g $day^{-1}$ for compound X on day i using equation 8 from Allen *et al* 2020 [69] where $[X]_{i,IBA}$ is the concentration of compound X on day i in IB air in pg $m^{-3}$, $U_{wind}$ is the average wind speed[335] and $h_{MBL}$ is the height of the marine boundary layer (200 m.)[69]

$$Flux_{onshore} = [X]_{i,IBA} * U_{wind} * h_{MBL} \quad eq\ 12$$

We calculate the $CTE_{i,X}$, central tendency exposure, for compound X on day i, using equation 7 where $[X]_{i,IBA}$ is the concentration of compound X on day i in IB air in pg $m^{-3}$ and IR is inhalation rate (parameterized as 0.7 $m^3$ $hr^{-1}$ in the EPA Exposure Factors Handbook)[336]:

$$CTE_{i,x} = [X]_{i,IBA} * IR \quad eq\ 13$$

### 3.6.2 Addendum: Nontargeted analysis of organic pollutants in water and aerosol

Non-targeted mass spectrometry analysis allows a more significant portion of the organic pollutant pool to be considered when interpreting broad trends across sampling sites and environmental compartments of water and air. A total of 390 compounds were identified based on library and community-provided spectra and categorized based on their Global Natural Product Social Molecular Networking (GNPS)[240] source categories, which included plastics, biocides, personal care products, metabolites, and drugs (see **Methods**).

It should be noted that the extraction and ionization efficiencies (sensitivities) for many compounds within each pollutant class remain unknown. Summed ion counts for

each compound class are normalized to the total summed ion counts of all pollutants during the study for each sample type. These values should be compared between sites or compartments (aerosol and water) and not between different compound classes within the same sample type and location.

The relative abundances of pollutant ions in the water samples, integrated across all classes (the shaded bars in **Fig. S3.12A**), indicate that the TJR site had the highest abundance. In contrast, the lowest abundance was measured at the background site, SIO. Despite day-to-day variability, BF, IB, and SS exhibited similar abundances across all pollutant classes, confirming the river and ocean as significant sources of airborne pollution in southern San Diego. Waterborne pollution includes inputs from the Tijuana River and runoff in San Diego and the San Diego River.[238,337] Across all compound classes, these three southern San Diego locations are statistically like each other and the TJR except for plastics.

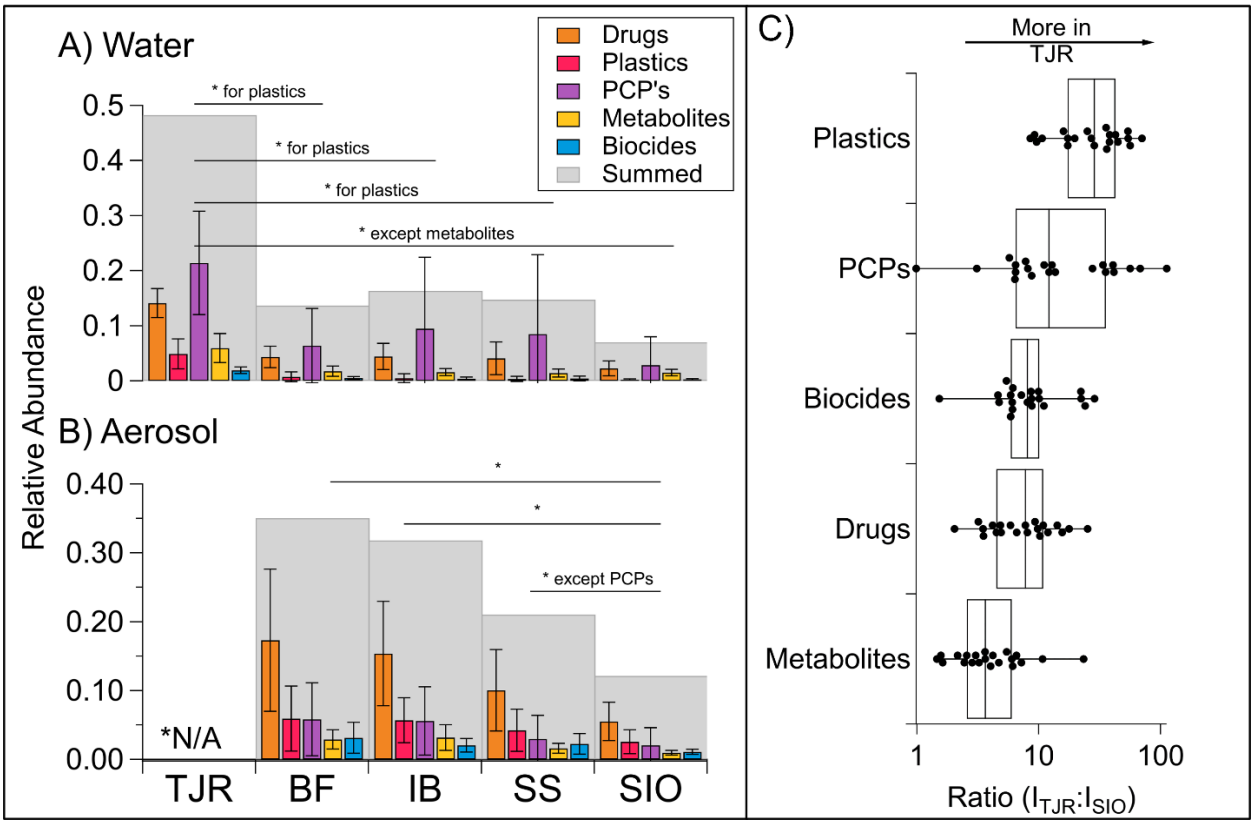


**Supplemental Figure 3.11**(A) Average relative ion abundance of pollutant classes in water samples as a fraction of shared pollutant ion signal across all measurement sites. Values should be compared between sampling sites and compartments (aerosol & water) and not between compound classes within one site. Variation between different sampling days (n=23 for aerosol and n=28 for water) is shown in error bars. *Denotes a statistically significant difference ($p<0.05$) between the same compound classes in different locations unless otherwise noted. (B) Same as (A) but for the aerosol samples. No TJR data is shown since no aerosol sampling occurred at the TJR site. (C) Ratio between pollutant levels at SIO and TJR in water samples, binned by pollutant class and matched by sampling period.

The ratio between the most polluted water (TJR) and the “cleanest” water (SIO) on each sampling day is shown in **Fig. S3.12C**. As all values are larger than one, TJR is a possible point source for various San Diego coastal region pollutants, particularly plastic-related compounds and personal care products (ratio >10). The TJR is statistically significantly enhanced in all compound types except for human metabolites, which is

unexpected as previous work investigating TJR pollution has primarily focused on untreated sewage. This may be biased from natural sources of compounds identified as human metabolites in the GNPS database. The disparity in plastic abundance is likely due to the TJR receiving urban runoff from the entire Tijuana River watershed, while SIO is less affected by localized terrestrial runoff. The difference in personal care product enhancement (generally >10) compared to biocide, drug, and drug metabolite enhancement (generally <10) suggests a more significant presence of personal care products in Tijuana River wastewater. Ratios between SIO water and BF, IB, and SS water (see **Fig. S3.13)** demonstrate higher enhancements in personal care products, followed by drugs, indicating that these pollutant classes may be persistent waterborne pollutants originating from the TJR that accumulate in southern San Diego air.

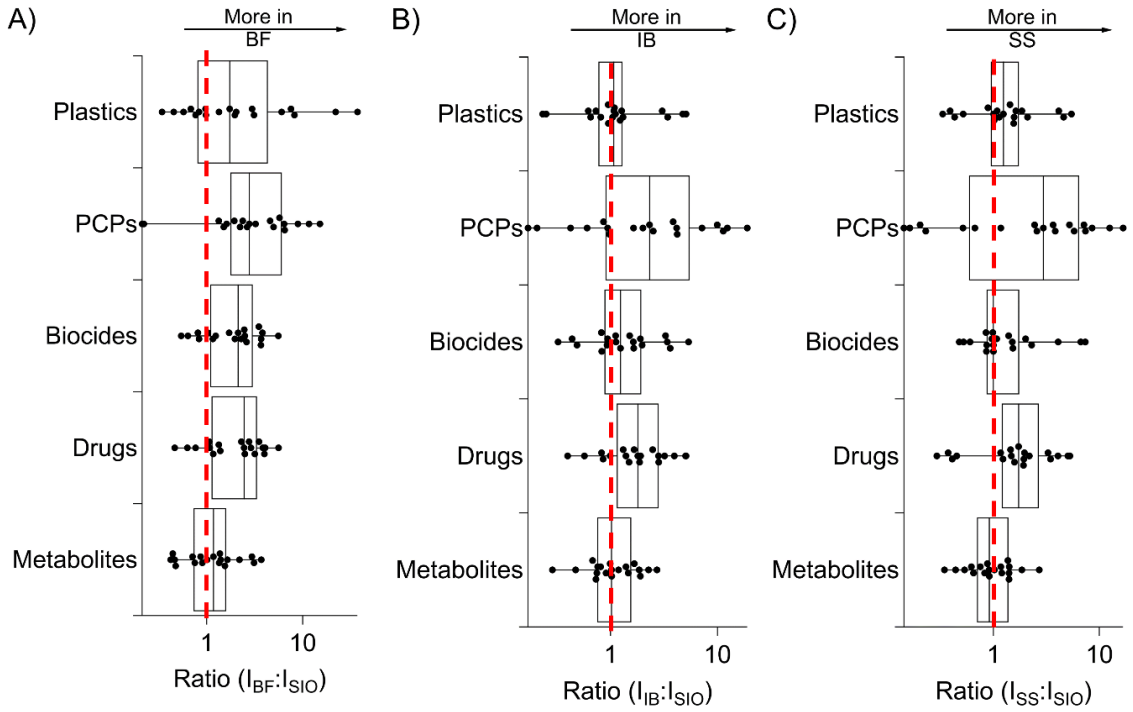


**Supplemental Figure 3.12** A) Ratio between pollutant levels at SIO and BF in water samples, binned by micropollutant class and matched by sampling period. B) Same as A) but between SIO and IB. C) Same as A) but between SIO and SS.

In aerosol samples (**Fig. S3.12B**), waterborne pollutant concentrations were highest in southern San Diego at BF and IB, the aerosol sampling locations closest to the Tijuana River outflow and Tijuana itself, followed by SS and SIO. A direct comparison between all sites and SIO is shown in **Fig. S3.14.** These gradients likely result from contributions from SSA as the polluted Tijuana River outflow becomes diluted in ocean water and migrates to other sites. Consequently, pollutant abundances in the ocean water samples decrease, resulting in lower transfer to SSA at the sites furthest away from the TJR. This hypothesis is supported by Pendergraft *et al.*, 2023, which demonstrated the presence of sewage originating from the Tijuana River in marine aerosol lofted over land at coastal sites in San Diego.[120] Similarly, waterborne pollutants in the aerosol phase will undergo

airborne dilution, photochemical degradation,[215] and deposition as air masses travel.[338] Previous research has shown that airborne pollution in southern California can travel over a hundred miles while maintaining similar aerosol concentrations at sites only 12 miles apart.[294] Thus, the observed gradients may be influenced by terrestrial airborne pollution sources, such as the urban atmosphere of the San Diego-Tijuana region itself. The following section will examine the abundances of different measured pollutant classes in aerosols according to their air mass origin.

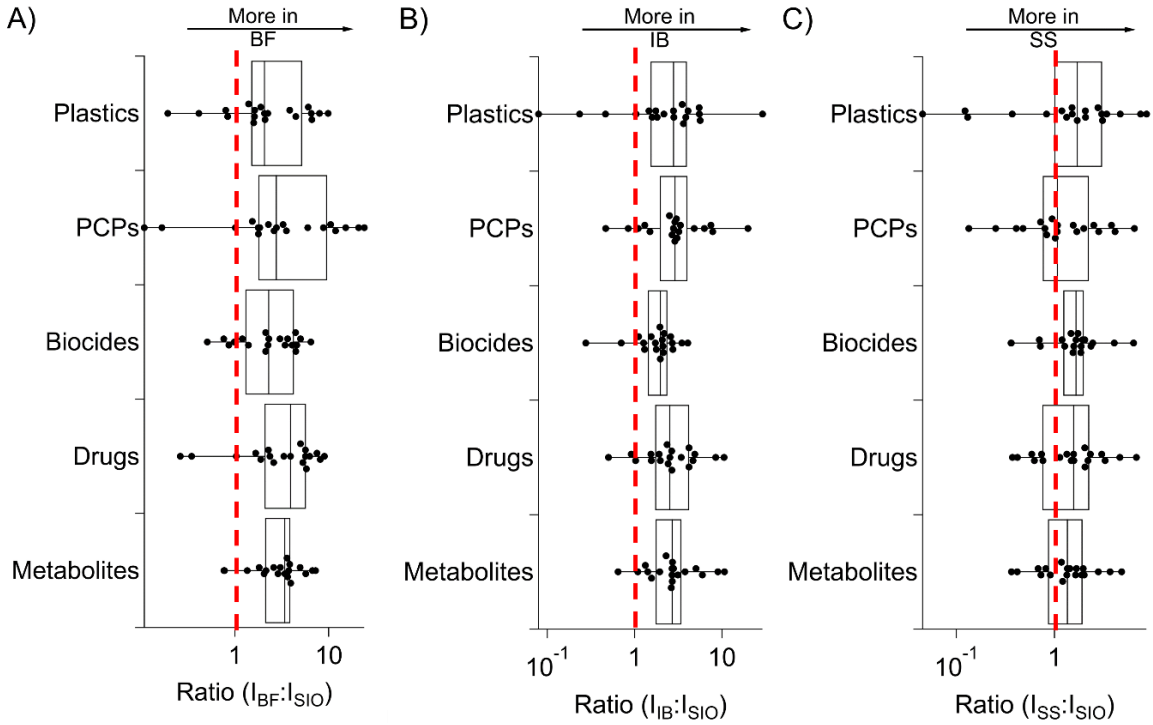


**Supplemental Figure 3.13** A) Ratio between pollutant levels at SIO and BF in aerosol samples, binned by micropollutant class and matched by sampling period. B) Same as A) but between SIO and IB. C) Same as A) but between SIO and SS.

### 3.6.1. Dependence of pollutant class abundance on air mass origin

To determine the primary marine, land, or mixed origins of different pollutant classes in aerosols, the relative abundances of these classes in aerosol samples from the most polluted sites, BF and IB, were analyzed based on their air mass origin (**Fig. S3.15**), as

determined by local winds and FLEXPART air mass back trajectories (see **Methods**). Most 23-hour sampling periods exhibited a combination of onshore and offshore winds, classified as mixed air masses (n=17). In contrast, three sampling periods had pure sea-based air mass origins, and three had purely land-based sources. Ratios of average signal intensity between marine and land-influenced air masses are presented in **Fig. 3.15B.**

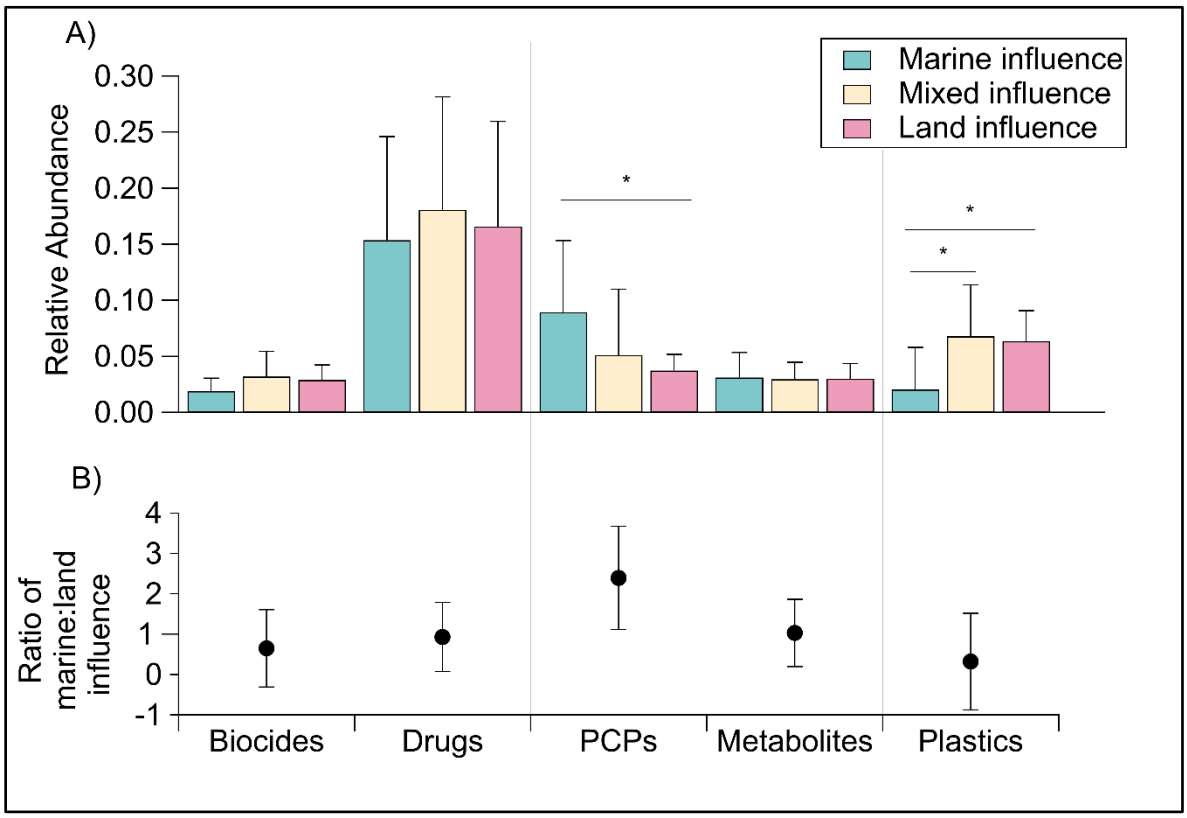


**Supplemental Figure 3.14** (A) Relative abundance (fraction of ion share) of pollutant classes in IB, BF, and SS aerosol samples separated by air mass origin (n=9 for marine and land influence, n=51 for mixed influence). Variation between different sampling days is shown in error bars. * denotes statistical difference ($p<0.05$) between compound classes in different air mass origin categories. (B) Ratios of average signals from marine-influenced to land-influenced air masses. Propagated error between signal variation is shown in error bars.

The averaged ratios of airborne biocides, drugs, and metabolites were statistically similar ($p>0.05$), with approximately equal distribution between marine- and land-influenced air masses (i.e., ratio ~1). Plastic additives, on the other hand, were statistically significantly more abundant in aerosols when air masses originated from land. This aligns with a dominant terrestrial source of plastic compounds, possibly from urban dust and direct aerosolization of tire microplastics.[27,308] In contrast, PCPs were over twice as

abundant in aerosol samples when air masses primarily originated from the ocean. This suggests the sea is a dominant source for these compounds in the coastal region sampled. The reasons behind the greater abundance of biocides, drugs, and plastics during mixed air mass influence periods are unclear but could be attributed to increased SSA production or higher levels of terrestrial pollution during those sampling periods. However, due to the significant day-to-day variability in pollutant abundance and the variability in wind direction and local sea breeze circulation within a day, we cannot conclusively attribute any pollutant class to land-influenced or marine-influenced air masses.

### 3.8. Acknowledgments

We acknowledge the support of Borderfield State Park, Imperial Beach Marine Safety, and Silver Strand State Park for serving as sampling locations and assisting us during the study. We thank Neal Arakawa and the Environmental Complex Analysis Laboratory for instrumental maintenance and assistance. I would also like to acknowledge my coauthors on this work. Chapter 3, in part, has been submitted for publication of the material as it may appear in Science Advances, 2024, Cooper, A, Pendergraft, M, Petras, D, Cancelada, L, Belcher, K, Torres, R, Small, M, Garrafa-Luna, J, Belda-Ferre, P, Simpson, R, Morris, C, Mitts, B, Aron, A, Zhang, J, Price, T, Dinasquet, J, Dorrestein, P, Knight, R, Slade, J.H. & ,Prather, K. The dissertation author was the primary investigator and author of this material.

## Chapter 4 Photo-initiated degradation kinetics of the organic UV filter oxybenzone in solutions and aerosols: impacts of salt, photosensitizers, and the medium

Chapter 4, in full, has been submitted for publication of the material as it may appear in *ACS Environmental Science & Technology: Air*, 2024, Cooper, A, Shenkiryk, A, Morris, M, Chin, H, Mehndiratta, L, Roundtree, K, Tafuri, M, Slade, J.H. The dissertation author was the primary investigator and author of this paper.

### 4.1 Abstract

Organic UV filters like oxybenzone (BP3) in sunscreens are persistent seawater pollutants suspected to transfer to the atmosphere via sea spray aerosol (SSA). This study examines the photo-initiated degradation of BP3 in artificial and real seawater compared to SSA mimics containing NaCl and 4-benzoyl benzoic acid (4-BBA). We investigated pure, binary, and ternary mixtures of BP3, NaCl, and 4-BBA using solar simulated light to isolate the effects of salt and photosensitization on BP3 degradation. Results showed significantly faster degradation in the aerosol phase ($J_{eff,env}$ ≈$10^{-3}$-$10^{-2}$ $s^{-1}$ or $t_{1/2}$<10 min) compared to bulk solutions ($J_{eff,env}$≈$10^{-6}$ $s^{-1}$ or $t_{1/2}$>1 day). The photosensitizer enhanced BP3 photodegradation in both phases, more so than when mixed with salt or all three components in solutions. BP3 photodegradation was most enhanced by salt in the aerosol phase. High-resolution molecular analysis via Orbitrap LC-MS/MS revealed rapid formation of more acutely toxic compounds (benzophenone, benzoic acid, and benzaldehyde) in aerosols. These findings highlight that seawater may serve as a reservoir for BP3 and that upon aerosolization to SSA, BP3 may rapidly transform and increase aerosol toxicity.

## 4.2 Introduction

Personal care products are an emerging environmental concern due to their increased use and ecotoxicological impacts.[339] Organic UV filters, particularly benzophenone-3 (BP3 or oxybenzone), are common in these products as well as in coatings and paints as a photo-protectant[53,111,340] and prevalent in coastal environments[48,52,58,59,74,341] due to direct application or through wastewater discharge.[58,270] BP3 is effective in absorbing incoming UV radiation and dissipating energy non-radiatively through a photo-induced keto-enol tautomerization, leading to its environmental persistence.[53,111]

BP3's extensive use and ubiquity in the marine environment raise concerns about its toxic impacts.[58,342,343] Market research by Euromonitor reports a combined use of benzophenone class UV filters at 11.4 mg capita$^{-1}$ day$^{-1}$, amounting to 1386 metric tons per annum in the U.S.[52] Marine BP3 concentrations typically range between 100 ppt and 10 ppb,[52,58] with levels as high as 1 ppm in crowded beach areas.[59] In a *National Academies* review, the HC5 (hazardous concentration for 5% of species) of BP3 is calculated at 353 ppb for acute toxicity and 48.5 ppb for chronic toxicity.[52] Additionally, BP3 is an endocrine disruptor[97,344] and may contribute to developmental disorders.[345]

Airborne BP3 has been detected in gas and aerosol phases. Studies have reported varying concentrations of BP3 in urban and indoor air,[88,346] with notable levels above wastewater treatment plants.[310] BP3 can enter aerosols directly from sunscreen sprays[347] or through evaporation and condensation processes.[88] Selective transfer from the ocean surface into sea spray aerosols (SSA) through bubble rupturing and wave-breaking processes is another pathway by which hazardous organic and biological

pollutants enter aerosols,[119,120,137–139,348] given BP3's hydrophobic nature ($K_{ow}$=3.79[349]) and tendency to accumulate at the sea surface.[48] Franklin *et al* 2022[147] demonstrated that other organic UV filters (homosalate and octisalate) may transfer into artificial SSA generated in a wave channel using real collected seawater. While BP3 has not been reported yet in SSA samples, its widespread presence in the ocean motivates this investigation into its photochemical transformations in seawater and SSA. Moreover, BP3's photochemical lifetime in aerosols is unknown, critical for understanding its environmental fate.

Previous studies have shown that BP3 in seawater is resistant to direct photolysis but susceptible to indirect photolysis, with marine chromophoric matter playing a significant role.[103] The environmental medium, e.g., solutions, thin films, or aerosols, and its physicochemical properties, such as viscosity, affect photochemical reaction pathways and rates.[192,203,206,212,215] For example, octinoxate, another UV filter, degraded rapidly in thin films or suspended colloids but minimally in solution.[212] Lignell *et al.* 2014[350] found that 2,4-dinitrophenol underwent faster photodegradation (by one order of magnitude) in a more viscous medium.[350]Barsotti *et al.* 2017 found that photolysis quantum yields for other nitrophenols were the same in both aqueous (i.e., liquid) and more viscous media, suggesting that this phenomenon may be compound-specific.[351]

Aerosols[207–209] and microdroplets[211] exhibit accelerated reaction kinetics compared to bulk solutions. Studies have shown that smaller droplets and aerosols can concentrate light and components at the particle surface, where organic compounds have incomplete solvation shells.[209,210] This can enhance molecule-to-molecule

interactions and inhibit the recombination of fragmented compounds, leading to faster degradation in aerosols.[209,211] Furthermore, more ordered molecular orientations at the particle surface may sterically inhibit the vibrational relaxation of excited states.[212]

This study aims to explore the role of environmental medium (bulk solution and aerosol) and secondary constituents (NaCl and photosensitizers) in the photo-initiated degradation of oxybenzone. By systematically increasing the complexity of mixtures and lab-generated aerosols, from pure components to real seawater and lab-generated SSA, we seek to understand the environmental fate of BP3 and its potential impact on particle toxicity.

## 4.3 Materials and Methods

### 4.3.1. Bulk solution experiments

Solutions of BP3 (TCI, 99%) and the model photosensitizer 4-benzoylbenzoic acid (4-BBA, Acros Organics, 99%) were prepared at ~10 parts per million (ppm) by weight in a 50:50 solvent mixture of methanol (MeOH, Fisher, 99.9%) and water ($H_2O$; Milli-Q, 18 MΩ cm resistivity). This solvent mixture was chosen due to the insolubility of BP3 and 4-BBA in water. NaCl (Fisher, 99.5%) was added with a final solution mixing ratio of 35 parts per thousand for mixtures mimicking ocean water's salinity.

Additionally, one set of experiments was conducted by adding 10 ppm of oxybenzone to real seawater collected from the end of Scripps Pier in La Jolla, California (32.867° N, 117.257° W) on September 7$^{th}$, 2023. The nearby Southern California Coastal Ocean Observing System (SCCOOS) Automated Shore Station[352] reported 10 μg $L^{-1}$ of chlorophyll a (the threshold for a phytoplankton bloom)[353], 8.2 mg $L^{-1}$ of dissolved oxygen, 33.14‰ salinity, and a pH of 8.11 for this date. While the 10 ppm concentration of BP3 introduced into seawater is much larger than concentrations

expected in ocean water[58], this was done to match experimental concentrations and for detection purposes via UV-Vis Spectrophotometry.

Blanks containing the full solution matrix except for oxybenzone were prepared for each experiment. For example, this would mean solutions of BP3 in 50:50 MeOH:$H_2O$ would be paired with a blank of 50:50 MeOH:$H_2O$, and solutions of BP3+4-BBA+NaCl in 50:50 MeOH:$H_2O$ would be paired with a blank solution of 4-BBA+NaCl in 50:50 MeOH:$H_2O$.

The prepared solutions were placed in 10 mm path-length quartz cuvettes (Fireflysci Type 21) sealed with a Teflon cap. The cuvettes were positioned on a magnetic stir plate and mixed with a stir bar operating at 300 revolutions per minute to ensure continuous mixing during each trial. Irradiation was achieved using an Air Mass 16S-Series Solar Simulator (Solar Light) calibrated to produce light intensity equivalent to 1 sun (1360 W $m^{-2}$). Light flux was measured by a Model PMA2144 Digital Class II Pyranometer (Solar Light) at the beginning and end of each experiment. Minimal (<1%) drift was observed in spectral irradiance.

Photodegradation was monitored with a PerkinElmer Lambda 35 UV-Vis spectrometer operating in dual beam mode, i.e., with automatic background subtraction. In this configuration, a blank cuvette was prepared consisting of the same solvent and co-solute mixture as the sample (i.e., all constituents of the sample except for BP3.) Measurements were taken at predetermined time intervals (0, 1, 5, 10, 15, 30, 60, and 120 minutes of light exposure) to monitor the evolution of the solutions over time. Separately, for offline analysis, samples of each mixture type were prepared at 100

ppm, and subsamples were exposed to solar-simulated light for 24 hours to maximize photoproduct formation.

Cuvettes were also weighed with an analytical balance (Mettler Toledo model ME204) to measure any evaporation of the solvent (typically <1% throughout the experiments.) Subsequent spectra intensities were corrected to account for changes in the analyte concentration from solvent evaporation. The collected spectra were processed and analyzed using Spectragryph.[354] Experimentally determined absorption spectra for each experimental solution type and further discussion can be seen in **Fig. S4.1** and the **SI.**

Samples were analyzed using a Vanquish UHPLC (Thermo Scientific) combined with Atmospheric Pressure Chemical Ionization (APCI) on the Orbitrap Elite Hybrid Linear Ion Trap-Orbitrap (Thermo Scientific.) 20 µL of each sample were injected onto a Waters Symmetry C18 column (100Å pore size, 5 µm particle size, 4.6 mm × 250 mm). The elution gradient consisted of pure HPLC-grade water (solvent A) and methanol (solvent B.) At a flow rate of 1 mL $min^{-1}$, the gradient was as follows: 0 to 1.0 min at 70% B, 1.0 to 2.5 min transitioning from 70% to 5% B, 3.5 to 8.5 min transitioning from 5% to 85% B, followed by a 1.5-minute equilibration phase at 70% B.

Following separation, samples were immediately analyzed using data-dependent acquisition in both positive and negative modes. APCI vaporizer temperature was set to 350°C with a sheath, auxiliary, and sweep flow rate of 10, 30, and 5 arbitrary units, respectively. Discharge current was set to 5µA with a capillary temperature of 300°C and an S-lens RF level of 60.0. MS/MS scans were collected at a resolution of

60,000, collision energy of 35kV, in an m/z range of 150.00-1500.00. Data were analyzed using Xcalibur (Thermo Scientific.)

### 4.3.2. Aerosol experiments

For experiments in the aerosol phase, solutions were atomized with a commercial constant output atomizer (TSI Inc. Model 2076) and diluted to 5 L $min^{-1}$ with zero air provided by a Zero Air Generator (ZAG; Sabio, Model 1001). The solutions were prepared at 100 ppm by weight for each substituent in 100% MeOH. This was necessary to ensure the complete dissolution of BP3 and 4-BBA, while NaCl is miscible in MeOH. The 100 ppm solution produced aerosol after atomization with mean geometric diameters between 90 and 140 nm (see **Table S4.1** for more details.) For the spiked seawater trial, the seawater sample was first diluted to a salt concentration of 100 ppm, and BP3 dissolved in MeOH was added dropwise until a final BP3 concentration of 100 ppm. Aerosol size distributions were measured with a Scanning Electrical Mobility Sizer (Brechtel Model 2100.) The differences and similarities of the atomized particles to real SSA is discussed in the **SI**.

Aerosol populations were subsequently introduced into a PAM-OFR$^{355}$ (Potential Aerosol Mass Oxidative Flow Reactor, Aerodyne.) See SI **Fig. S4.2** for a flow diagram of our experimental setup. Inside the flow reactor, aerosol was exposed to wideband UV-B light provided by two lamps (LCD Lighting.) Lamp spectral irradiance was between 300 and 350 nm, the highest energy range of incoming solar radiation at Earth's surface. Output spectra can be found in **Fig. S4.3.** Irradiance was controlled using a ballast at five different levels to the lamps.

Photon flux was measured directly by a TOCON GaP6 photodiode (sglux). It was also calculated by calibrating the lamps' output photon flux via the photodegradation of

$NO_2$ as described in Lambe *et al.* 2019[356] (see **Fig. S4.4**) and adjusted to the average $NO_2$ absorptive cross-section between 300 and 350 nm. The photon flux was fitted to a 0-D box model run in KinSim[357] (see **Fig. S4.5)** and was determined to be between $8\times10^{14}$ - $3\times10^{15}$ photons $cm^{-2}$ for the five different lamp settings. Using the standard reference solar spectrum at a 37° zenith angle, this photon flux between 300 and 350 nm is equivalent to 5%-73% solar irradiance. Both methods showed good agreement, as shown in **Fig. S4.6.** The photon flux from photodiode measurements was used for the remainder of this study.

Aerosol composition was measured with an Extractive Electrospray Ionization Time-of-Flight (EESI-TOF) Mass Spectrometer (Aerodyne.)[229] This online (1 Hz) soft ionization approach allows for determining chemical formulae due to its high resolution, ~5000 m/Δm in negative mode for *m/z*=59.013853 ($CH_3COO^-$). Thus, it is particularly well suited to kinetics experiments of simple mixtures where the targeted analyte has no isomers.[215]

The EESI-TOF was operated in negative mode using a reagent solution of 2% (by weight) acetic acid, 48% $H_2O$, and 50% acetonitrile spiked with 100 ppm NaI for mass calibration with $I^-$, $I_2^-$, and $I_3^-$. Using acetate as a reagent ion promotes the formation of [M-H] peaks via deprotonation.[215] No iodide-analyte clusters, which may form in negative mode, were observed. Data was processed using Tofware (Aerodyne.) Oxybenzone was detected as its $[M-H]^-$ peak at m/z 227.

Photodegradation experiments under constant photon flux may be treated as pseudo-first-order reactions. Kinetic data was prepared by first drift-correcting and then normalizing signal intensities to I=1 at t=0 (see **SI** for discussion on aerosol evaporation

and drift correction.) Taking the natural log of the normalized intensities for each exposure data point results in a linear decay plot where the slope represents the observed effective photolysis rate constant, $J_{eff,obs}$ (as shown in eq 1).

$$\ln \frac{[A]}{[A_o]} = -J_{eff,obs} \times t \qquad (eq\ 1)$$

This rate reflects the loss of BP3 from the sum of all photo-induced decay processes in the cuvette or the OFR. This includes both direct photolysis and photosensitized (or indirect) decay. No further analysis was performed to isolate the effects of direct and indirect photo-initiated decay.

$J_{eff,obs}$ determined under experimental conditions was converted to an effective photolysis decay constant in the environment ($J_{eff,env}$) by normalizing the output photon flux during experiments to the photon flux of standard spectral irradiance over the same wavelengths and multiplying by $J_{eff,obs}$ as shown in eq 2 from Sareen *et al* 2013.[9] This correction factor was 1 for all experiments in the bulk solution and ranged from 0.05 to 0.72 for experiments in the aerosol flow tube dependent on the different lamp voltages.

$$J_{eff,env} = J_{eff,obs} \times \frac{F_{lamp}}{F_{env}} \qquad (eq\ 2)$$

Aerosol samples for HPLC-MS/MS analysis were collected onto 90 mm quartz fiber filters inside a stainless-steel filter holder (Millipore). Samples were collected at the experimental flow rate of 3 L $min^{-1}$ without an external pump. Flow rates were monitored by a flow meter (Siargo MF5700). Separate filters were used for aerosol collection in the dark, light, and blanks. The aerosol filter blanks followed EPA Method IO-5[358], which consisted of loading the filter holder, unloading, and storing the filters the same way as the samples. Immediately after collection, the filter was submerged in ~15 mL of

acetonitrile (Fisher, 99.9%) inside a cleaned and baked Pyrex scintillation vial and sonicated for 30 minutes in an ultrasonicated bath (Branson 3800.) Since water was not used during extraction, our analysis may not include all water-soluble components in the particles. This solution was then dried via rotary evaporation (Buchi R-100) and reconstituted in 1 mL of acetonitrile for analysis using the same HP-LCMS/MS procedure described earlier.

### 4.3.3 Modeling of electronic structures and toxicity

The nuclei positions of ground state BP3 and its degradation products were constructed using the Avogadro 4.2 molecular visualization program on a Windows platform. The quantum chemistry package ORCA (version 5.0.3) performed all computations.[359,360] The initial geometry optimizations were performed using DFT with B3LYP functional with def2-TZVP basis set, and bond angle constraints were applied when appropriate. Coulomb integrals and COSX numerical integration for HF exchange were adopted for the RI-J approximation. The geometry was further optimized using ethanol as an implicit solvent. Finally, a coupled cluster technique, STEOM-DLPNO-CCSD[361], was employed to calculate the energy of the electronic transitions of the molecules.

Separately, the geometry of a BP3 molecule was optimized using ωB87x-D3 with the def2-TZVP basis set. Its anionic and cationic counterparts were subsequently computed using the same geometry to perform the analysis of the Fukui function. The representations were generated using the VESTA[362] visualization package.

Compound toxicity was estimated by calculating the rat oral $LD_{50}$ of BP3 and its detected products using EPA's Toxicity Estimation Software Tool (TEST)[363], a quantitative structure-activity relationship model that predicts toxicological endpoints

based on molecular descriptors of experimental data. When experimental data is available within TEST, as for oxybenzone and benzophenone, this value was preferentially used over simulated $LD_{50}$ values.

## 4.4. Results & Discussion

### 4.4.1. Differences in the photo-initiated decay kinetics of pure-component BP3 between bulk solutions and aerosols

We observed profound differences in photo-induced decay between the bulk solution and aerosol phase experiments. BP3 exhibited slow decay over hours in the bulk solution while undergoing rapid degradation in the aerosol phase on the order of minutes of exposure time.

Employing a pseudo-first order kinetics treatment (see **Methods**) to the average degradation observed during each experiment, we calculated effective photolysis decay constants, $J_{eff,env}$, and environmental lifetime, $\tau$, plotted in **Fig. 4.1** and listed in **Table S4.2.** The effective BP3 photodegradation rates of pure-component BP3 in bulk solution were ~$2x10^{-6}$ $s^{-1}$ compared to ~$2x10^{-3}$ $s^{-1}$ in aerosols. These are equivalent to $\tau$ = ~6 days and 8 minutes, respectively. Average decay curves are plotted in **Fig. S4.8**.

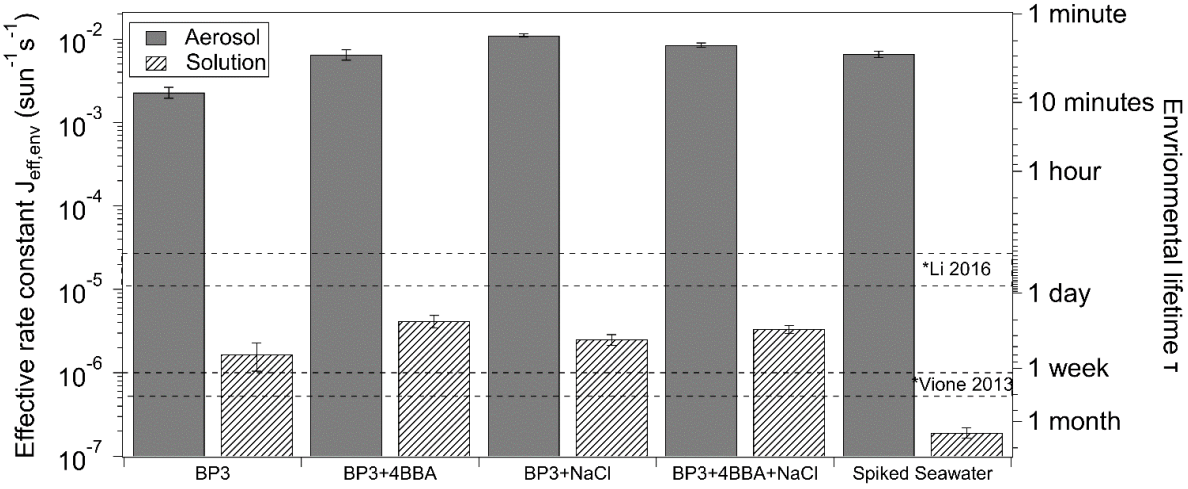


**Figure 4.1** Effective photolytic rate constants and estimated chemical lifetimes of BP3 upon exposure to solar irradiation in the aerosol and bulk solution phases for the different mixtures. Previous studies by Li *et al*. 2016 and Vione *et al*. 2013 are shown for comparison. The range for Li *et al*. 2016 is between real seawater (upper) and freshwater (lower). The range for Vione *et al*. 2013 is between low concentrations of nitrate and carbonate (upper) and high concentrations (lower).

The relatively slow photo-induced decay in solution was expected. Most studies show no significant degradation of oxybenzone in solution to solar-simulated light for experimental times up to 24 hours.[214,364,365] Vione *et al.* 2013 reported photolysis of oxybenzone in freshwater with an environmental lifetime of 9-15 days, depending on carbonate and nitrate concentrations.[107] In contrast, Li *et al*. 2016 reported an environmental lifetime of 9 hours in freshwater and 20 hours in seawater.[103]

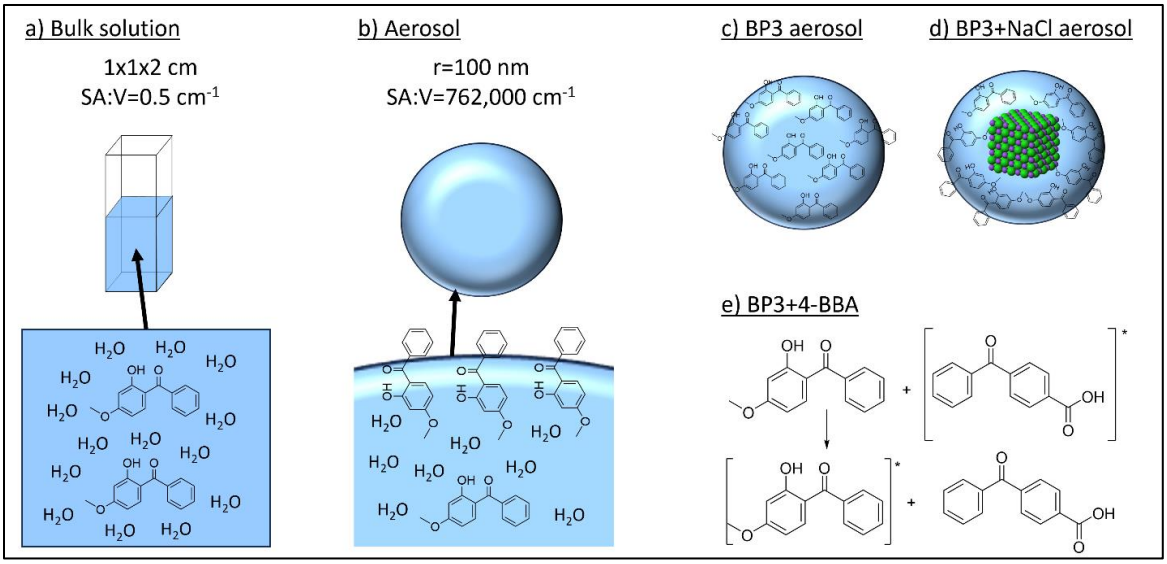


**Figure 4.2** Illustration of the different factors impacting BP3 loss in solutions and aerosols. a) BP3 solution in a cuvette with a full solvent cage. Dimensions of the cuvette, radius of the aerosol, and calculated surface area to volume ratios (SA: V) are shown. b) BP3 aerosol with incomplete solvation at the air-particle interface. c) BP3 aerosol with BP3 distributed through the bulk and interface. d) BP3+NaCl aerosol with BP3 driven to the surface. e) Type I photosensitization scheme of excited state transfer between 4-BBA and BP3.

We ascribe the enhanced degradation in aerosols primarily to the much larger surface area-to-volume ratio (see **Fig. 4.2a,b**). This leads to a higher proportion of BP3 molecules at the particle-air interface than the bulk, where incomplete solvation may greatly enhance photochemical reactivity.[207,209,211] Solvation can often slow reactions in solutions compared to the gas phase. The partial solvation at the air-particle interface often exhibits rates between that of fast gas phase reactions and slow solution phase reactions.[211]

Additionally, organic-containing aerosols may exhibit higher viscosities akin to semisolids and solids.[366] More viscous environments limit the rotational freedom of excited states' rotations,[367,368] which BP3 relies on to relax vibrationally. Thus, a higher-

viscosity molecular environment would prolong BP3's excited state, allowing it greater opportunity to decay rather than relax.

#### 4.4.1.1. BP3+NaCl binary mixtures

In bulk solutions, there was a minor but statistically insignificant ($p>0.05$) increase in BP3 degradation for the BP3+NaCl binary system compared to BP3 alone. Berembeim *et al.* 2020 found that the presence of $Na^+$ can interfere with BP3's ability to relax via keto-enol tautomerization by disrupting its intramolecular hydrogen bond.[369] This would extend the lifetime of BP3's excited state and promote its decay instead.

In contrast to the bulk solution, adding NaCl in the aerosol phase led to the greatest increase (4.5x) in rate compared to pure BP3. As shown in **Fig. S4.9**, the particles mixed with NaCl exhibited visual characteristics of phase-separated and partially engulfed particles with a possible NaCl core and BP3 coating. These are similar morphologies observed in other inorganic salt-organic carbon mixtures.[370] As illustrated in **Fig. 4.3d**, this separation of components leads to a population of BP3 molecules preferentially occupying the particle's surface, where this more viscous and less solvated molecular environment could lead to enhanced degradation,[207,209,211] suggesting the aerosol particle's morphology could significantly influence BP3's photo-induced degradation.

#### 4.4.1.2. BP3 + 4-BBA binary mixtures

In the bulk solution, there was a significant ($p<0.01$) increase (2x) in the rate constant calculated for the BP3+4-BBA binary system compared to BP3. This confirms that 4-BBA acts as a photosensitizer in increasing the photodegradation rate of BP3, either through direct triplet state energy transfer (Type 1, **Fig. 4.3e**) or through the formation of reactive oxygen species (Type 2).[202] While we did not perform oxidant

quenching experiments to determine differences between Type 1 and Type 2 initiated processes, Vione *et al.* 2013 found that both forms of photosensitization occur in freshwater systems, with Type 1 prevailing under high dissolved organic matter (DOM) concentrations (where there would be more $^{3}$Ps*-BP3 interactions) and Type 2 prevailing under low photosensitizer concentrations (where there would be less scavenging of OH by organics other than BP3.)[107]

In the aerosol phase, the addition of 4-BBA to BP3 also significantly ($p<0.01$) increased (2.5x) rates of degradation. We expect similar mechanisms of photodegradation to occur in the aerosol phase as in the bulk solution. However, the larger increase in the aerosol phase may be explained by the closer proximity and incomplete solvation of organic molecules in the condensed particle phase compared to the bulk solution leading to more BP3-4-BBA* interactions.[207,209]

#### 4.4.1.3. BP3+NaCl+4-BBA ternary mixtures

In the bulk solution, adding NaCl to the BP3+4-BBA binary system led to an insignificant ($p>0.05$) but a minor decrease in reaction rate compared to BP3+4-BBA but a significant ($p<0.05$) increase compared to BP3+NaCl. We hypothesize that this could be due to the presence of NaCl leading to vibrational collisions between NaCl and 4-BBA$^{3}$*, which may quench the triplet state that may have otherwise reacted with BP3. This effect has been seen in other mixtures of halides and photosensitizing molecules, e.g., NaCl and 4-BBA in aerosols[215] and sea salt halides and Imidazole-2-carboxaldehyde in bulk solution [371].

In the aerosol phase, a similar modulating effect was observed where the ternary mixture was faster than one binary mixture (BP3+4BBA, insignificant - $p>0.05$) and slower than the other binary mixture (BP3+NaCl, $p<0.05$.) One reason for the

decreased rate compared to the BP3+NaCl aerosol is that 4-BBA may competitively occupy the surface of the aerosol, driving more of the BP3 into the bulk of the aerosol compared to the binary mixture. Although including 4-BBA would introduce additional photosensitized decay pathways, this appears less impactful than the surface enrichment caused by NaCl.

Additionally, the quenching of 4-BBA by $Cl^-$ may lead to the formation of reactive chlorine species either directly or through ·OH-mediated oxidation pathways, which have been shown to contribute to the UV-initiated removal of BP3.[100,102,372] This may be an additional pathway leading to enhanced degradation in the bulk solution compared to the BP3+NaCl binary mixture, but it does not appear to fully compensate for the inhibitory effects of 4-BBA in the ternary aerosol compared to the BP3+NaCl binary aerosol.

#### 4.4.1.4. Photo-induced decay of BP3 in real seawater

For the bulk solution experiment conducted by spiking BP3 into real seawater, we observed no degradation and instead observed a steady enhancement (up to 8%) for the first three days of irradiation. We ascribe this to the general insolubility of BP3 in seawater and expect it first to be adsorbed to particulate matter in the seawater. Light exposure can lead to the release of organic matter from particulate matter, explaining its enhancement over time. However, after this period of enhancement, BP3 decreased steadily and we used this period to calculate its photo-induced decay. We caution that this may not account for particulate adsorption and desorption and instead reflects the decay after a steady state was reached.

The resulting decay (with an environmental lifetime of over one month) is significantly slower than the experimental mixtures (in days) and the decay observed by

Li *et al*. 2016 in real seawater (with an environmental lifetime of 20 hrs.)[103] However, other studies simply state that BP3 persists in ocean water without reporting any degradation.[214,365]

Another reason for the slower observed kinetics in the seawater solution may be the difference in the protonation state of BP3. The seawater experiment was conducted at a final pH of 7.1 compared to 6.0 in the other solutions. Because BP3 has an acid dissociation constant (pKa=7.1), a higher pH leads to more deprotonated BP3 in the solution. The impacts of the protonation state on BP3's photodegradation are inconclusive. A study by Wong *et al.* 2019, which investigated the gas-phase photodegradation of protonated, neutral, and deprotonated BP3, found reduced absorption for anionic BP3.[113] In contrast, Li *et al*. 2016, which studied BP3 in real seawater, found that only the anionic form was susceptible to direct photodegradation.[103] As oceanic pH is typically 8.0, this is a limitation of this study, and thus, the bulk solution experiments primarily serve to inform chemical mechanisms and intercomparisons between environmental phases.

Additionally, real seawater contains a more complex DOM system than the 4-BBA used in experimental mixtures. This may screen incoming light, reducing direct photolysis and quench any 3CDOM* or reactive oxygen species produced, reducing photosensitization efficiency.[107] Trueblood *et al*. 2019 found that the photosensitized degradation of nonanoic acid was slower in the presence of an extracted marine DOM sample than with 4-BBA and humic acid. They explain this as resulting from the high abundance of carboxylic-rich alicyclic molecules, which are less photoactive than aromatic photosensitizers.[206]

The experiments conducted by spiking oxybenzone into seawater followed by atomization exhibited an insignificant ($p>0.05$) decrease compared to the ternary mixture. This could mean that the components atomized in seawater have similar properties and effects on BP3 photodegradation as the ternary mixture. While this result suggests the photo-initiated decay of BP3 in SSA may be as fast as those from other mixed aerosols in this study, it is important to note that the components transferred into SSA produced from the natural process of wave breaking and bubble rupturing at the sea surface are different from those that get atomized.[126] Only dissolved materials get atomized, whereas non-dissolved components, like lipids, surfactants, and particulate organic carbon, at the sea surface can transfer into SSA.[124] These components modulate SSA's physicochemical properties, surface tension, and mixing states, potentially different from the particles generated from atomized seawater. Therefore, this analysis does not say that the same degradation rates would be observed in real SSA; instead, it shows no significant inhibition of BP3 degradation as observed in the bulk seawater solution.

### 4.4.2. Identified transformation products

Offline analysis via HPLC MS/MS was conducted in a separate set of experiments where all bulk solutions were irradiated continuously for 24 hours in the cuvettes by the solar simulator and aerosols for 8 minutes of equivalent solar exposure by the UV-B lamps inside the OFR. The resulting mass spectra of samples before irradiation (i.e., in the dark) were subtracted from mass spectra after irradiation, plotted in **Fig. 4.3.** The compounds identified in the mass spectra that were significantly above the background (i.e., 3 standard deviations above the background for at least one

sample type) are listed in **Table 4.1.** MS2 spectra of each identified BP3 product are shown in **Fig. S4.10.**

As our analysis is semiquantitative, we cannot confidently compare the branching ratios between different organic species but can compare the formation of each compound between different mixture types. Almost all transformation products (TPs) exhibited the highest production in the BP3+4-BBA binary mixture in the bulk solution. This is to be expected, as these experiments showed the greatest degradation of BP3. Indeed, the order of TP production was completely in line with the rates of photo-initiated decay.

Interestingly, this trend was not observed in the aerosol phase. Instead, the ternary aerosol showed more TP production than BP3+NaCl, which exhibited the greatest decay. This may be due to additional TPs from the transformations of 4-BBA in this aerosol sample. In subsequent sections, we will deconvolute the contributions of BP3 from those of 4-BBA.

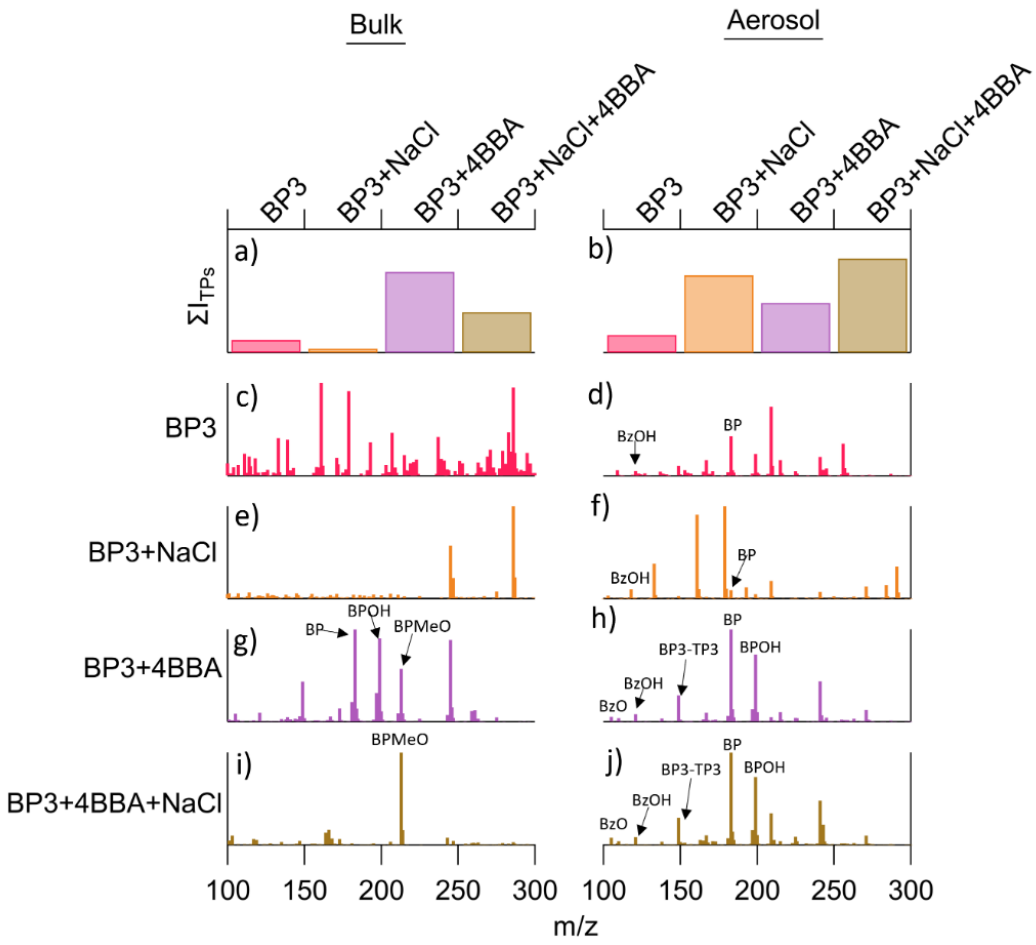


**Figure 4.3** a) Summed ion intensities of the detected transformation products in bulk solutions based on mixture type. b) Same as a) but for the aerosol phase. c-j) Photo-transformation product mass spectra for the different indicated mixtures in bulk solutions (left) and aerosols (right).

**Table 4.1** Detected compound IDs, MS1 parent ions, and major MS2 fragmentation ions.

| Compound ID | Parent ion | Major fragmentation ions |
|---|---|---|
| BP3 | 229<br>$(M+H)^+$ | 105, 151 |
| BP3-TP1<br>(Benzaldehyde, BzO) | 106 $(M-H)^+$ | N/A |
| BP3-TP2 (BzOH, Benzoic Acid) | 122 $(M-H)^+$ | N/A |
| BP3-TP3<br>(2-hydroxy-4-methoxy<br>benzaldehyde) | 153<br>$(M+H)^+$ | 109, 135 |
| BP3-TP4<br>(benzophenone, BP) | 183 $(M+H)^+$ | 105 |
| BP3-TP5<br>(2-hydroxy-benzophenone, BPOH) | 199 $(M+H)^+$ | 105, 121 |
| BP3-TP6<br>(4-methoxy benzophenone,<br>BPMeO) | 213 $(M+H)^+$ | 153, 181, 198 |
| BP3-TP7<br>(2-4-dimethoxy benzophenone) | 241 $(M-H)^+$ | 105, 163 |
| 4-BBA (4-benzoyl benzoic acid) | 227 $(M+H)^+$ | 105, 149 |
| 4-BBA-TP1 (4-benzoyl benzoic<br>methylalcohol) | 213 | 105, 135, 183 |

Previous work by Vione *et al.* 2013 identified major photoproducts of BP3 photolysis in the bulk solution to be benzoic acid and benzaldehyde resulting from the rupture of the carbon-carbon bond linking the carbonyl group to the aromatic ring containing the methoxy and hydroxyl moieties.[107] We observed the formation of benzaldehyde transformation product (BP3-TP1, BzO) in all experiments conducted in the bulk solution phase and aerosol experiments containing NaCl. In contrast, benzoic acid (BP3-TP2, BzOH) was a minor product (<1000 ions) in all bulk experiments and was detected in aerosol experiments not containing NaCl. A substituted benzaldehyde with hydroxyl and methoxy moieties (BP-TP3) was also detected in bulk experiments in the binary or ternary mixtures containing 4-BBA. This suggests that the C-C bond connecting the substituted ring and the central ketone is more prone to cleavage than the C-C bond in the unsubstituted ring.

Additional transformation products were identified by their MS2 spectra as less substituted compounds resulting from the removal of the hydroxyl and/or methoxy groups from oxybenzone. Notably, removing both constituents results in the formation of benzophenone, a known carcinogen.[373] Benzophenone (BP), 2-hyroxybenzophenone (BPOH), and 4-methoxybenzophenone (BPMeO) were all observed.

In the bulk solution, the production of BPMeO was observed in both the binary BP3+4-BBA trial and the ternary mixture. BP was only measured in the BP3+4-BBA experiment. In the aerosol phase, all experiments led to the production of BPOH and the formation of BP. To our knowledge, this is the first study reporting this sequence of degradation products from BP3.

The transformation products detected at the greatest intensity in aerosol samples were the derivatives produced by removing either the hydroxyl or methoxy group from BP3 and removing both to form benzophenone. Because these products are formed in pure BP3 aerosols, we expect them to result from direct photolysis, which results in the lysing of these C-O bonds.

As BP, BPOH, and BPMeO remain the dominant TPs, we expect these degradative pathways to be enhanced by Type 1 photosensitizing reactions with $^3$4-BBA*, which behave similarly to photon absorption. We did not observe direct evidence of Type 2 photosensitizing reactions with reactive oxygen species, which would generally result in more functionalized products.

While we could not confidently determine every transformation product observed, the relative production levels provide additional confirmation of the different rates of photodegradation of different mixtures. Notably, trials containing 4-BBA exhibited the production of products with integrated signal intensities an order of magnitude greater than other bulk experiments (**Fig. 4.4a**).

As both BP3 and 4-BBA are benzophenone derivatives, care was made to deconvolute similar transformation products. To identify transformation products of 4-BBA, experiments with only the photosensitizer were run. In the bulk solution, the primary TP (m/z of 213) was tentatively identified as 4-benzoyl benzoic methyl alcohol formed from the reduction of 4-BBA's carboxylic acid group (see **Fig. S4.11**.) It is important to note that 4-benzoyl benzoic methyl alcohol shares a chemical formula and thus *m/z* with BPMeO and were deconvoluted via LC and identified based on their MS2 spectra. In Grzyb *et al.* 2022[108], the formation of 4-benzoyl methyl aldehyde was

observed following 4-BBA's use as a photosensitizer, showing precedence for the reduction of 4-BBA while acting as a photosensitizer.

### 4.4.3. Computational investigation of photo-initiated reactive sites

We employed a computational frontier molecular orbital model to investigate the observed cleavage of C-C and C-O bonds. This approach assumes that the breakage of a bond originates from an excitation of an electron from the highest occupied molecular orbital (HOMO), and that the formation of a bond is the consequence of an acceptance of an electron from a donor to the lowest unoccupied molecular orbital (LUMO). Janak's theorem further suggests that HOMO and LUMO could serve as proxies to understand the ionization potential and electron affinity, respectively, of the molecule. In other words, through studying the HOMO and the LUMO of a molecule, we can provide an additional layer of insight if the proposed mechanism of a reaction is reasonable.

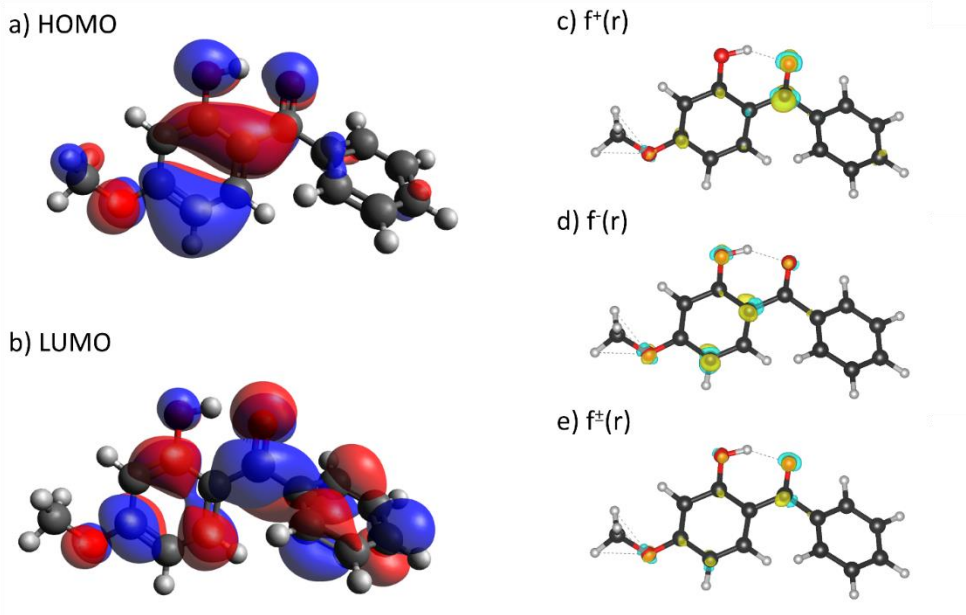


**Figure 4.4** Graphic representations of BP3's a) HOMO b) LUMO c) cationic Fukui function d) anionic Fukui function e) radical Fukui function.

A model of BP3's HOMO (see **Fig. 4.4a**.) shows a prominent orbital lobe over the C-C connecting the substituted ring (carbonyl-α carbon bond) with a mix of both n and pi-character. An available electron may be promoted to an excited state via an electromagnetic wave with an energy higher or equal to its HOMO-LUMO gap, which is 3.92 eV, or 316 nm; the electron may relax back to the ground state, or may overcome the ionization potential and dissociates, providing a pathway to photodegradation. The LUMO of BP3 (see **Fig. 4.4b**.) exhibits a dominant pi*-character across both benzene moieties. This may explain the observation of both benzaldehyde and 2-hydroxy-4-methoxy benzaldehyde production upon photolysis: carbonyl-α carbon bond breakage of either side of the two rings may be the result of an intermediate species or transition state accepting a relaxing electron to either one of the benzene moieties which will destabilize its opposing C-C bond.

The above analysis can be further investigated in conjunction with the Fukui function.[374] In short, the Fukui function takes advantage of the approach of DFT to look for changes in electron density in frontier orbitals induced by changes in the number of electrons at a specific geometry and the potential of the molecule. The Fukui functions are described below:

$$f^{+}(r) = \rho_{\{N+1\}}(r) - \rho_{\{N\}}(r) \qquad (eq.3)$$

$$f^{-}(r) = \rho_{\{N\}}(r) - \rho_{\{N-1\}}(r) \qquad (eq.4)$$

$$f^{\pm}(r) = \frac{1}{2}\left[\rho_{\{N+1\}}(r) - \rho_{\{N-1\}}(r)\right] \qquad (eq.5)$$

Where ρ is the electronic density and N is the number of electrons. For a neutrally charged molecule with the number of electrons N, N+1 will be its anionic counterpart and N-1, cationic. Hence, eq.3 is related to reactivity towards nucleophiles and eq.4 is

related to reactivity towards electrophiles. Eq.5 provides information to reactivity in the case of radical attack.

As shown in **Fig. 4.4c**, the electrophilic sites of BP3 are located almost exclusively on the carbonyl carbon, attracting nucleophiles. The tertiary structure of the carbon allows lone pair electrons or unpaired electrons to be stabilized and promotes further reactions after photo-irradiation, such as the cleavage of the α-β carbon bond discussed earlier.

The nucleophilic sites (See **Fig. 4.4d**) of BP3 are spread across the more substituted aromatic ring of the two. In particular, the oxygen on the hydroxyl and the methoxy groups are susceptible to protonation, which may promote their stability as leaving groups, leading to the observed formation of BPOH and BPMeO. We note that the increase in reactivity of the two β-carbons of the two functional groups is counteracted by their participation in the aromatic ring.

The Fukui function for radical attack is a straightforward pictorial prediction of the fate of the BP3 upon photo-irradiation (See **Fig. 4.4e**), showing prominence in electron density differences on all reactive sites leading to each observed transformation products.

### 4.4.4. Proposed mechanism of photo-induced decay and effects of medium and secondary constituents

Upon exposure to UV light, BP3 can regeneratively dissipate its energy through an excited state hydrogen transfer (ESHT) followed by a keto-enol tautomerization paired with molecular rotation.[111] If this process does not occur, it may instead undergo photo-initiated degradation.[107] **Fig. 4.5** illustrates both of these pathways. Physical and chemical changes that promote or inhibit these pathways will impact the photo-induced

degradation kinetics observed. Here, we separate the different impacts of the environmental medium and the presence of salts and photosensitizers and quantify their impacts on environmental lifetime.

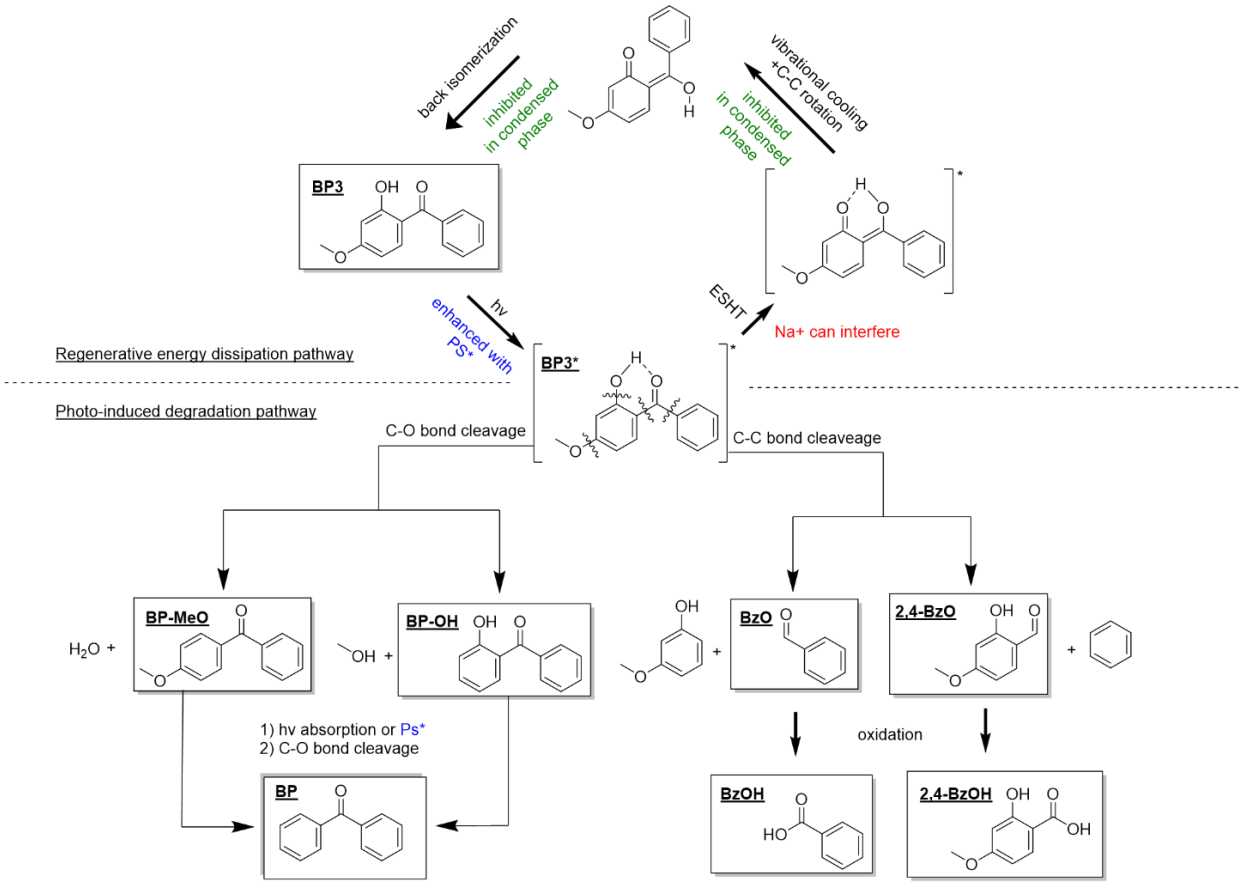


**Figure 4.5** Transformation pathways of BP3 either regenerate ground-state BP3 or undergo photo-induced degradation. Detected compounds are shown in boxes and labeled according to their abbreviations listed in **Table 4.1**. Effects of the medium are shown in green, effects of $Na^+$ are shown in red and effects of photosensitizers are shown in blue.

As explained earlier, the impact of environmental medium is predominantly concerned with the concentration of the population of BP3 at the surface and generally increased viscosity in organic aerosol layers. BP3 at the surface is less well-solvated and thus has less of a hydrogen bonding network to facilitate its ESHT.[210] Additionally,

the increased molecular order at the interface[210] and higher viscosity of organic-rich aerosol[366] may inhibit the molecular rotations needed to release its excited state energy and back isomerize into BP3.

The introduction of salt led to a small increase in photo-initiated decay in solution and the largest increase in aerosol. $Na^+$ may directly interfere with the ESHT by occupying the space between the hydroxyl and ketone groups on BP3.[369] Additionally, the presence of NaCl, especially in the moderate RH in this study, may drive the population of BP3 further to the surface due to salting-out effects[375,376], amplifying the effects of interfacial reactivity.

The introduction of 4-BBA has the combined impact of acting as a photosensitizer by directly exchanging energy with BP3 (Type 1) or producing reactive oxygen species (Type 2).[202,203,206] Our study did not observe direct evidence of any Type 2 reactions. As both BP3 and 4-BBA absorb UV radiation, they may also screen incoming light from BP3, reducing its direct photolysis. This did not seem to outcompete the effectiveness 4-BBA has as a photosensitizer except for in the ternary aerosol, where the addition of 4-BBA to BP3+NaCl aerosol led to a small but significant ($p<0.05$) decrease in reactivity.

### 4.5. Environmental implications

Notably, every transformation product identified in this study exhibits higher experimental and/or predicted toxicity than BP3 (See **Table S4.3**). This shows that the toxic loading of BP3 in the environment may not be reduced via photolysis, at least through its first few generation products. **Fig. 4.6** shows a representation of the toxic burden, calculated as the inverse of the estimated $LD_{50}$, doubling over 40 minutes in the atmosphere. Differences between pure BP3 (in pink) and BP3 in the SSA mimic (in

blue) are most pronounced within this short timescale, which may be relevant to the SSA locally generated and inhaled at the coast. In the real atmosphere, this may be representative of BP3 aerosol produced by a spray sunscreen vs. BP3 as an organic component of SSA.

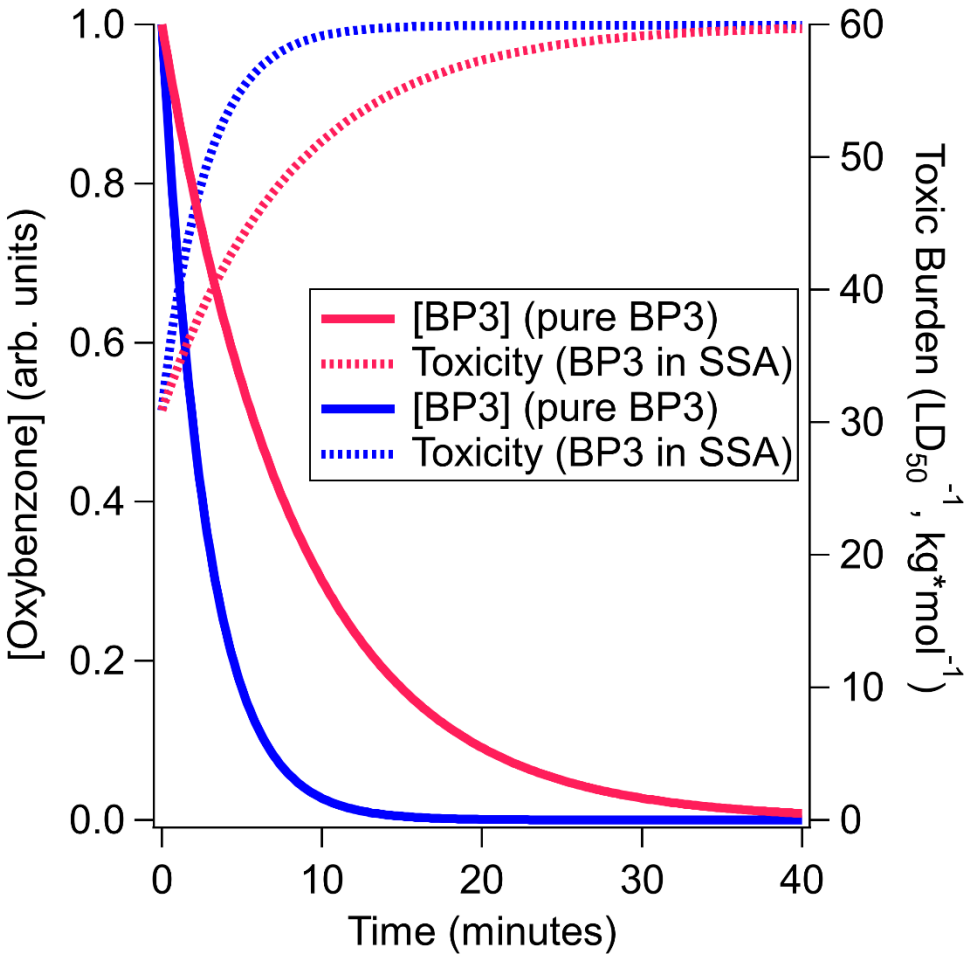


**Figure 4.6** Estimated toxic burden over time for BP3 in the aerosol phase for pure BP3 aerosol (pink) and BP3 in a SSA mimic (blue.) Experimental values were used for BP3, and the average of detected BP3 photoproducts was used to estimate product toxicity.

These results suggest that BP3 may be under-detected in environmental assays due to its rapid photo-transformations in the aerosol phase to a diversity of transformation products. This is likely the case for other UV-absorbing compounds.

This work identified the first two generations of transformation products, but subsequent reactions may occur over the lifetime of aerosols in the atmosphere (up to weeks). Generally, fragmented photoproducts shift their absorption further into the UV range, making them more resistant to photolysis at tropospherically relevant wavelengths via a process called photobleaching.[195] However, BP3 and its photoproducts may also be oxidized by reactive atmospheric trace gases, such as Cl, ·OH, and $O_3$.[11,12,215] The hydroxyl radical is often referred to as the "detergent of the atmosphere[190]" as it is the major removal pathway for many organic compounds. The EPA AOPWIN model estimates reactivity with ·OH based on structural characteristics. Estimated atmospheric lifetimes (which the model conducts in the gas phase) are listed in **Table S4.3**. This reveals that some TPs, such as benzoic acid, may be very long-lived to ·OH, with an estimated atmospheric lifetime of 9 days. Others, like 2-hydroxy-4-methoxy benzoic acid, have estimated lifetimes as short as 0.9 hrs. Thus, a more comprehensive environmental lifecycle analysis of BP3 is necessary to fully constrain the toxic burden of BP3 and its photoproducts in the atmosphere.

These results demonstrate the importance of the marine matrix when determining the environmental lifetime and fate of oxybenzone in seawater and SSA. In particular, the competing influences of photosensitizing organic molecules and NaCl modulate the environmental photo-initiated degradation of this compound. The aerosol phase promotes significantly faster photo-induced decay of BP3 compared to bulk solutions, likely due to differences in surface activity and viscosity. The role of photosensitizing material is most pronounced in the bulk solution, and NaCl is the most influential in aerosols.

Organic UV filters such as BP3 are common and increasingly found in all environmental mediums. These results suggest that BP3 may persist in the ocean but, upon aerosolization, is prone to rapid photo-induced decay which produces more toxic compounds. Further studies on the ecotoxicological impacts of its transformation products should be performed to fully constrain this compound's environmental and public health impacts.

### 4.6. Supplemental Information

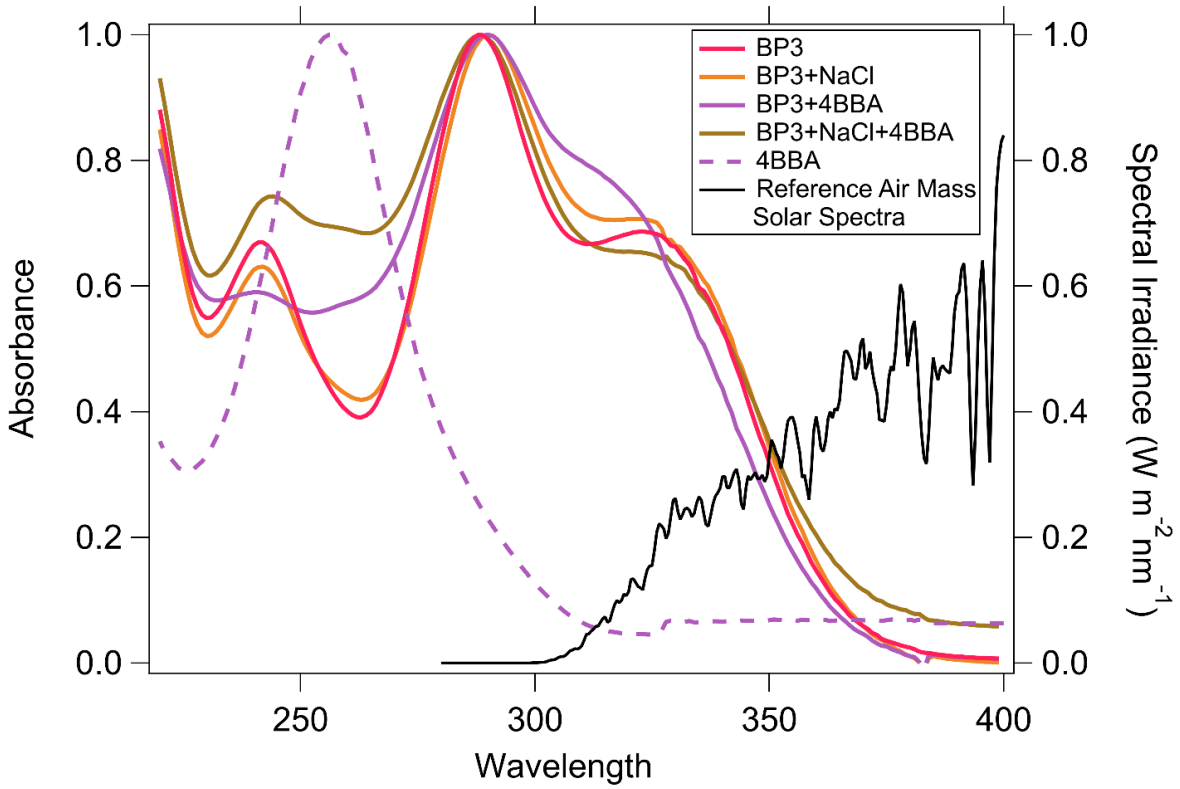


**Supplemental Figure 4.1** UV Vis absorption spectra of the pure, binary, and ternary solutions prior to irradiation normalized to $\lambda_{max}$=1. On the right axis, spectral irradiance of the standard solar spectra is shown for atmospheric reference.

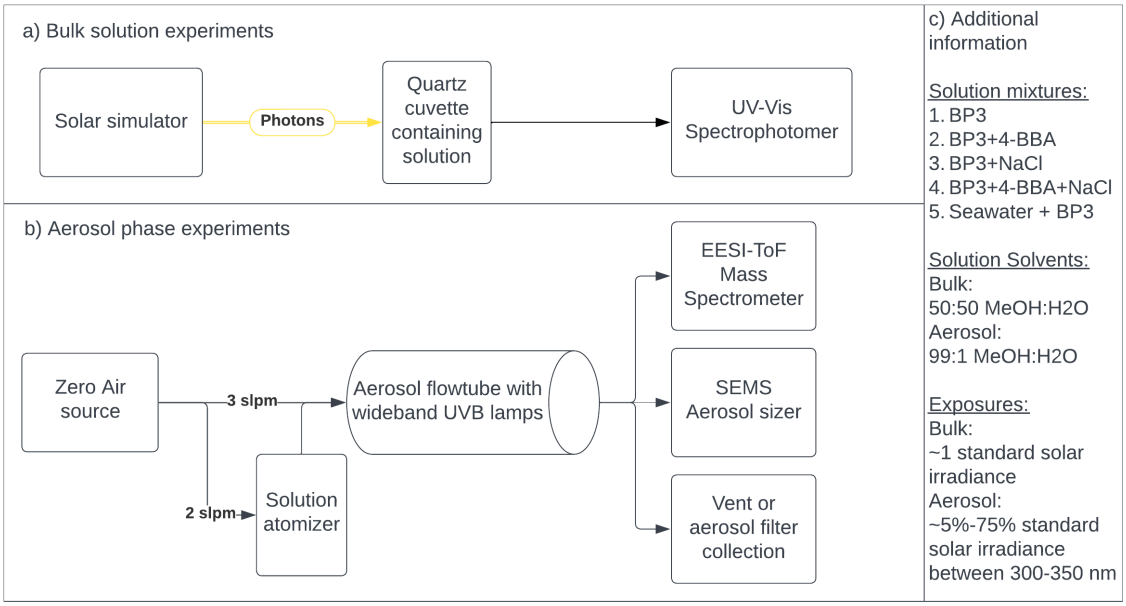


**Supplemental Figure 4.2** Experimental setup for a) bulk solution and b) aerosol phase photodegradation experiments. Brief experimental details may be found in panel c) and are detailed more in the text**.**

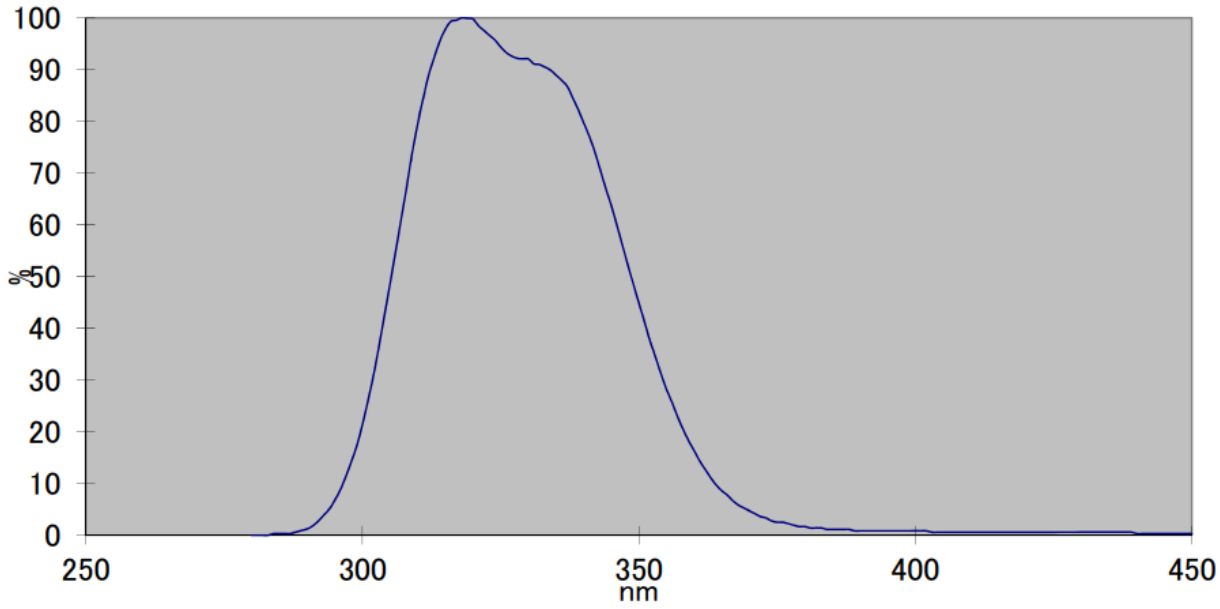


**Supplemental Figure 4.3** Lamp output spectra of the wideband UVB lamp (provided from manufacturer LCD Lighting.)

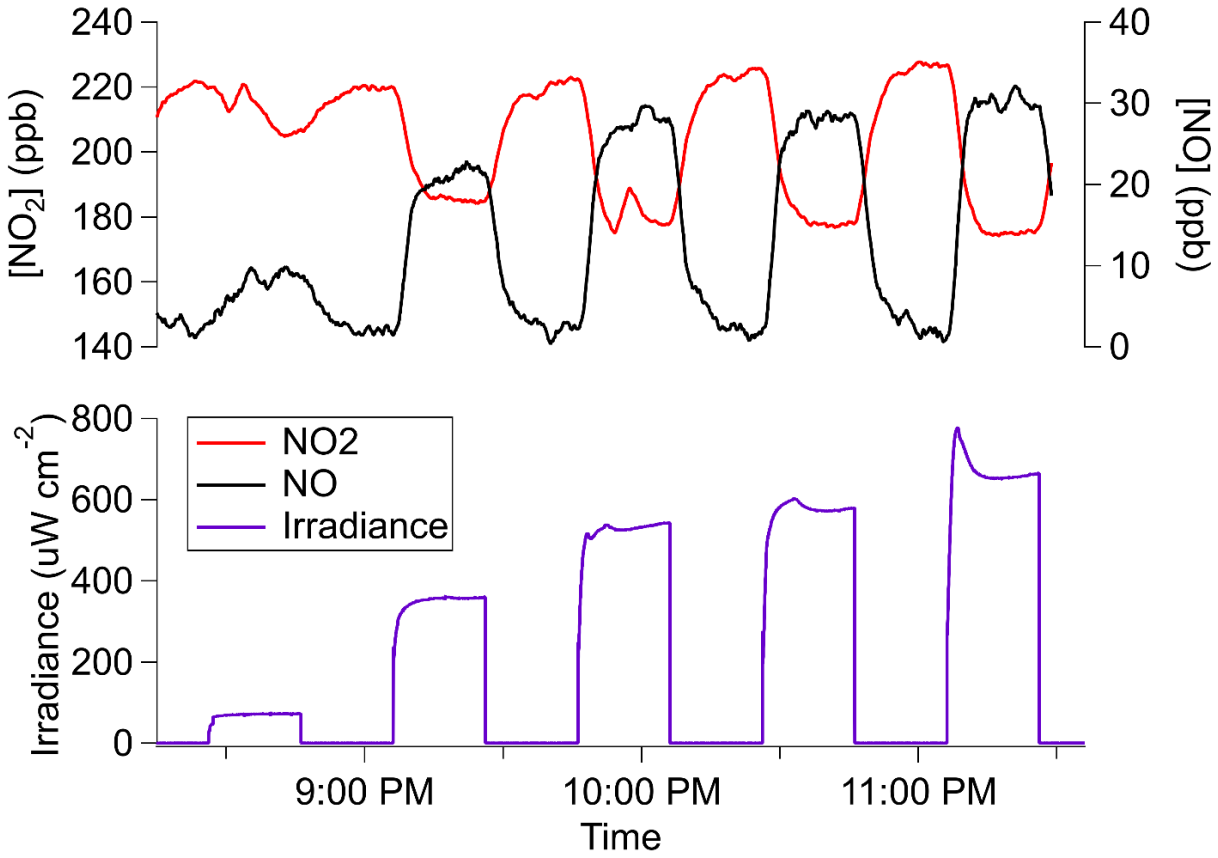


**Supplemental Figure 4.4** A time series from the calibration of the oxidative flow reactor. a) Concentrations of $NO_2$ (left) and NO (right) and b) measured irradiance via a photodiode.

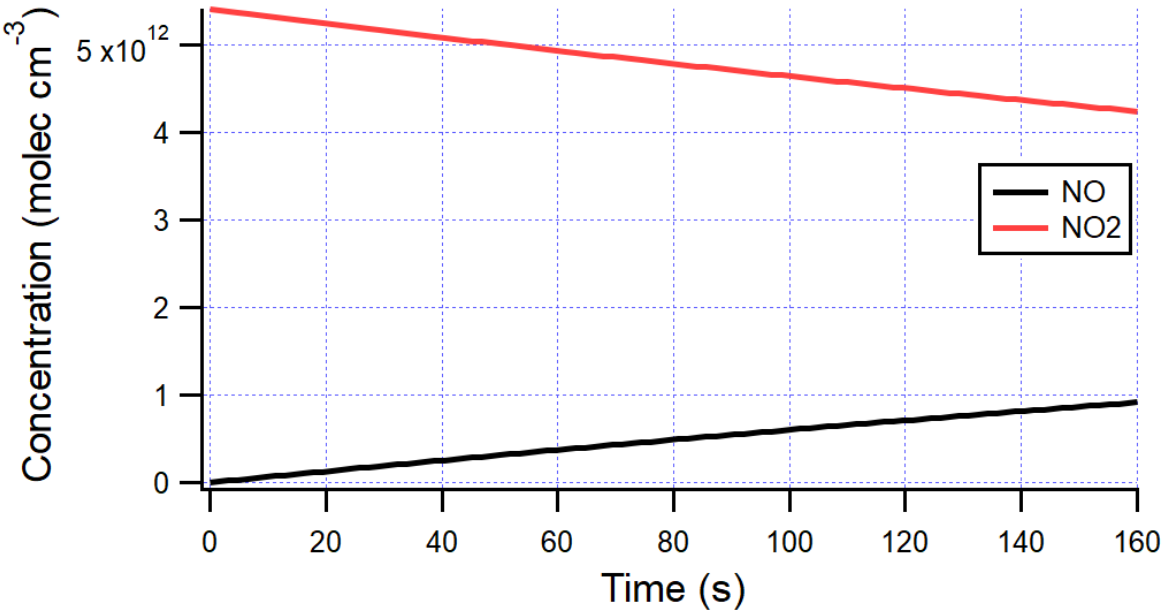


**Supplemental Figure 4.5.** Representative output from a KinSim model used to calibrate observed losses of $NO_2$ to varying levels of photon fluxes.

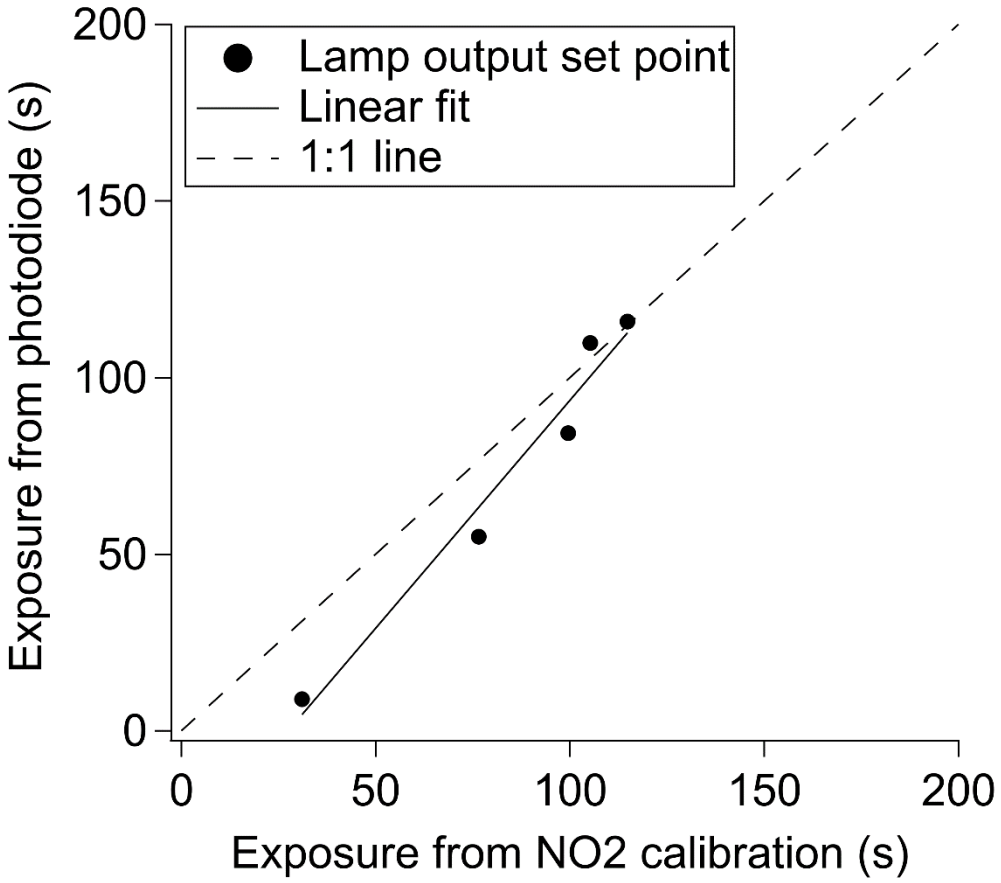


**Supplemental Figure 4.6** Equivalent solar exposure from calculated $NO_2$ photolysis rates compared to measurements from a photodiode. The dashed line is a 1:1 fit.

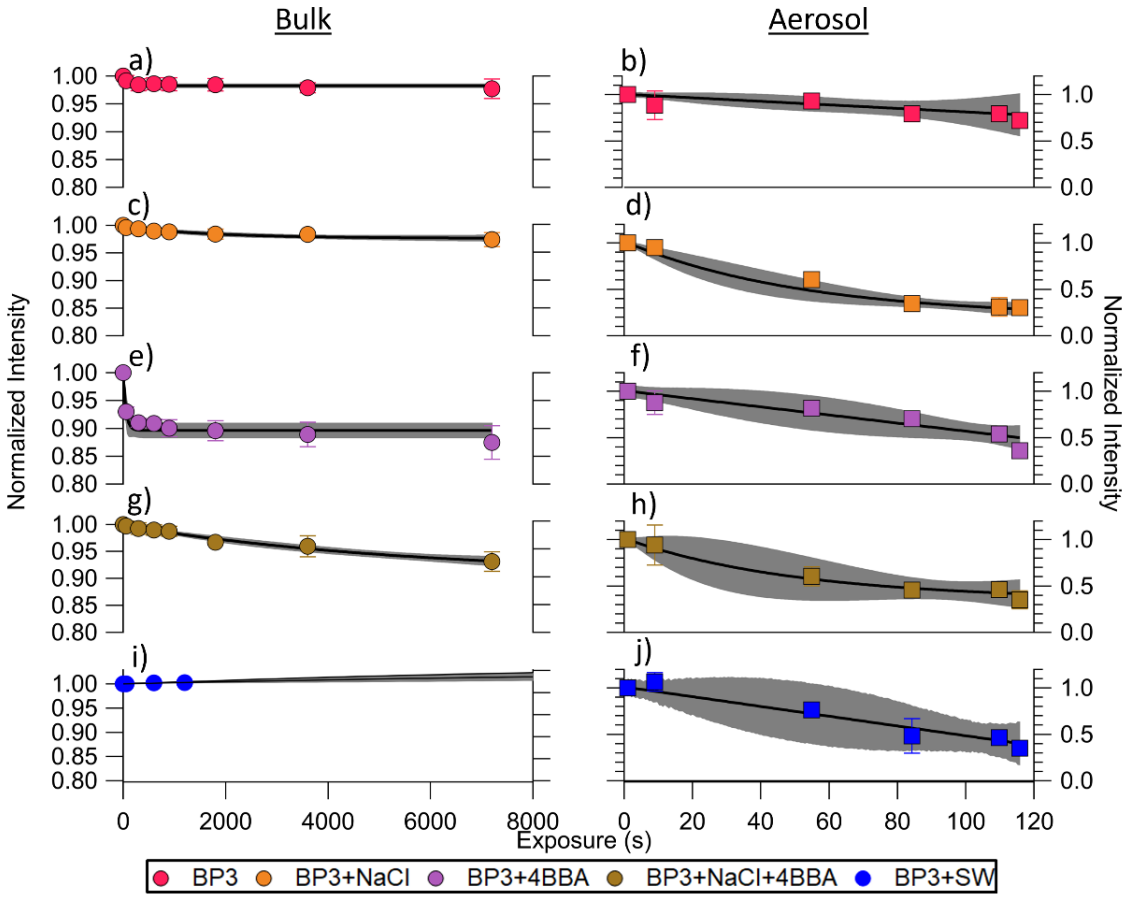


**Supplemental Figure 4.7** The normalized decay of BP3 over equivalent solar exposure times in solution (a,c,e,g,i) compared to aerosols (b,d,f,h,j). Error bars show one standard deviation from the mean normalized decay for n=3 trials at each lamp intensity, except for the solution trial in seawater, a one-week exposure. Lines of best fit for exponential decay are plotted in black with 95% confidence bands plotted as grey shading.

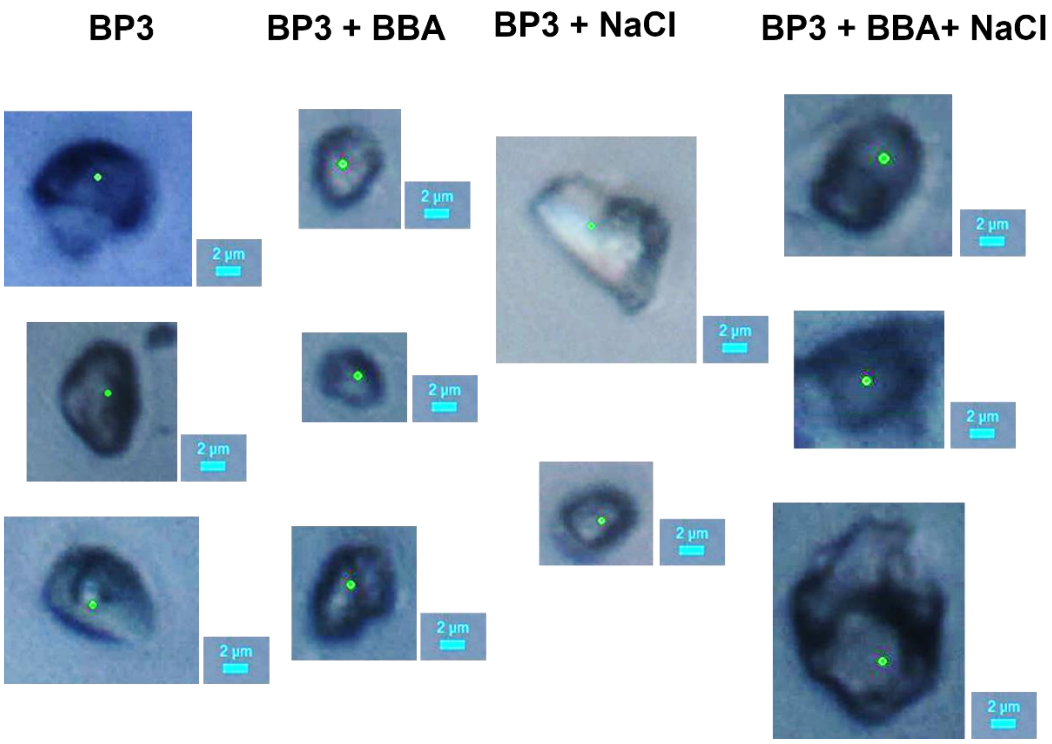


**Supplemental Figure 4.8** Confocal microscopy photos of each experimental aerosol type deposited onto quartz substrates.

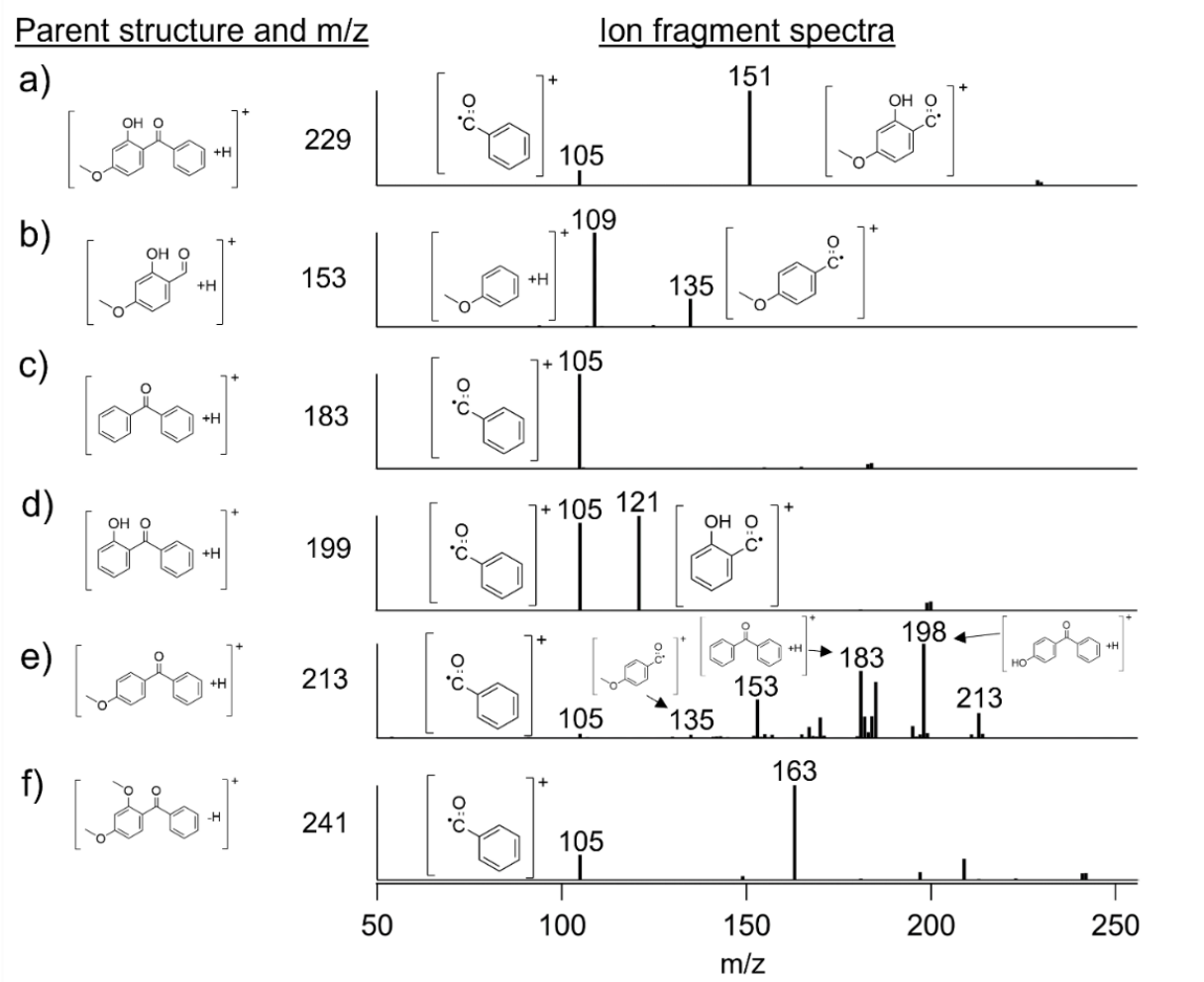


**Supplemental Figure 4.9** Secondary mass spectra of compounds identified as a) BP3, b) 2-hydroxy-4-methoxy benzaldehyde, c) benzophenone, d) 2-hydroxy benzophenone, e) 4-methoxy benzophenone, and f) 2-4 dimethoxy benzophenone. The numbers refer to the ion's mass-to-charge (m/z) ratio.

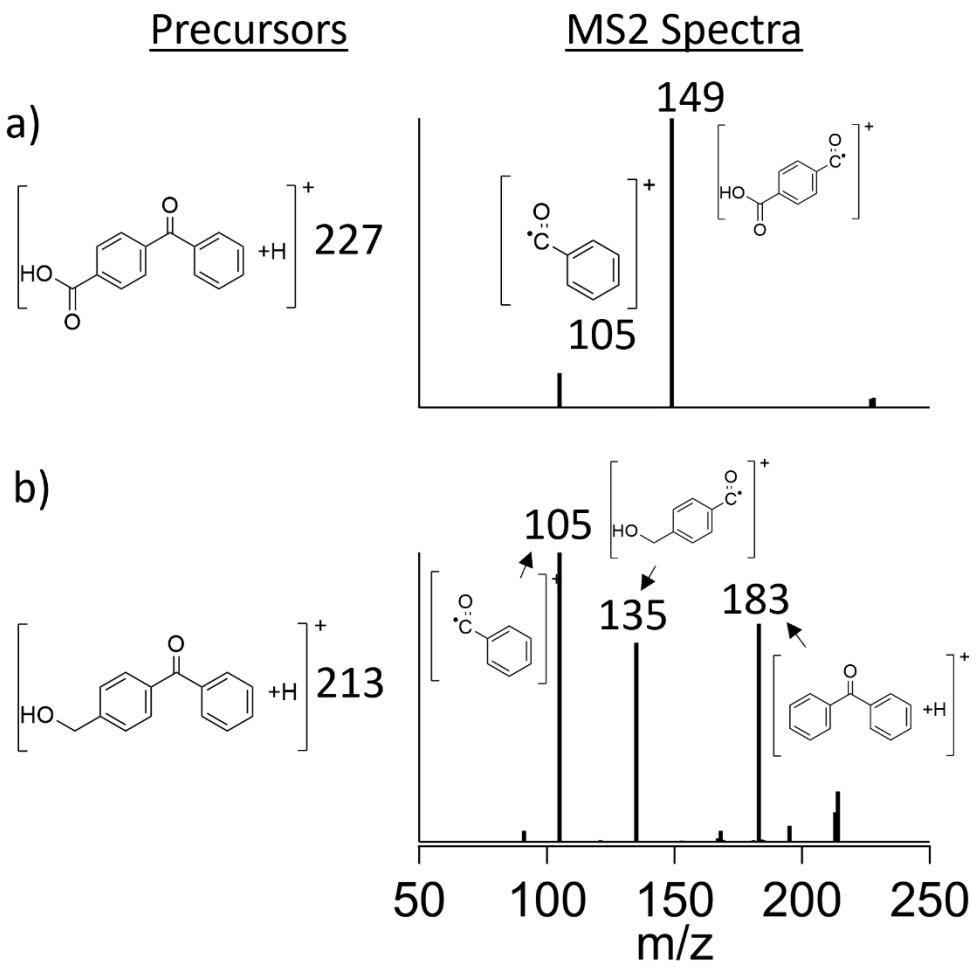


**Supplemental Figure 4.10** MS2 spectra of a) 4-BBA and b) its major photoproduct, 4benzoylbenzoic methylalcohol.

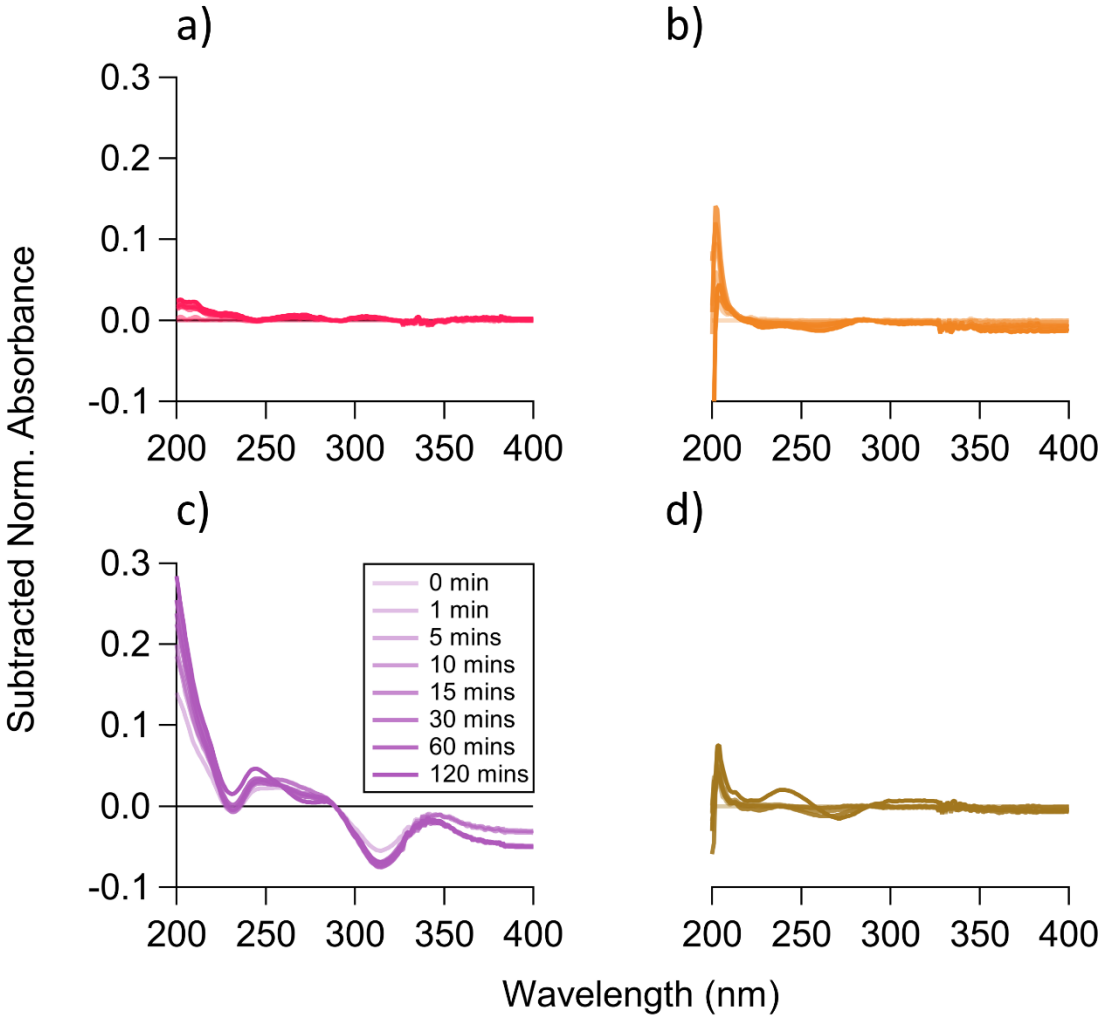


**Supplemental Figure 4.11** Subtracted UV-Vis spectra of bulk solution experiments normalized to the absorbance at 290 nm for solutions of a) pure BP3 b) BP3+NaCl c) BP3+4-BBA d) BP3+ 4-BBA+NaCl

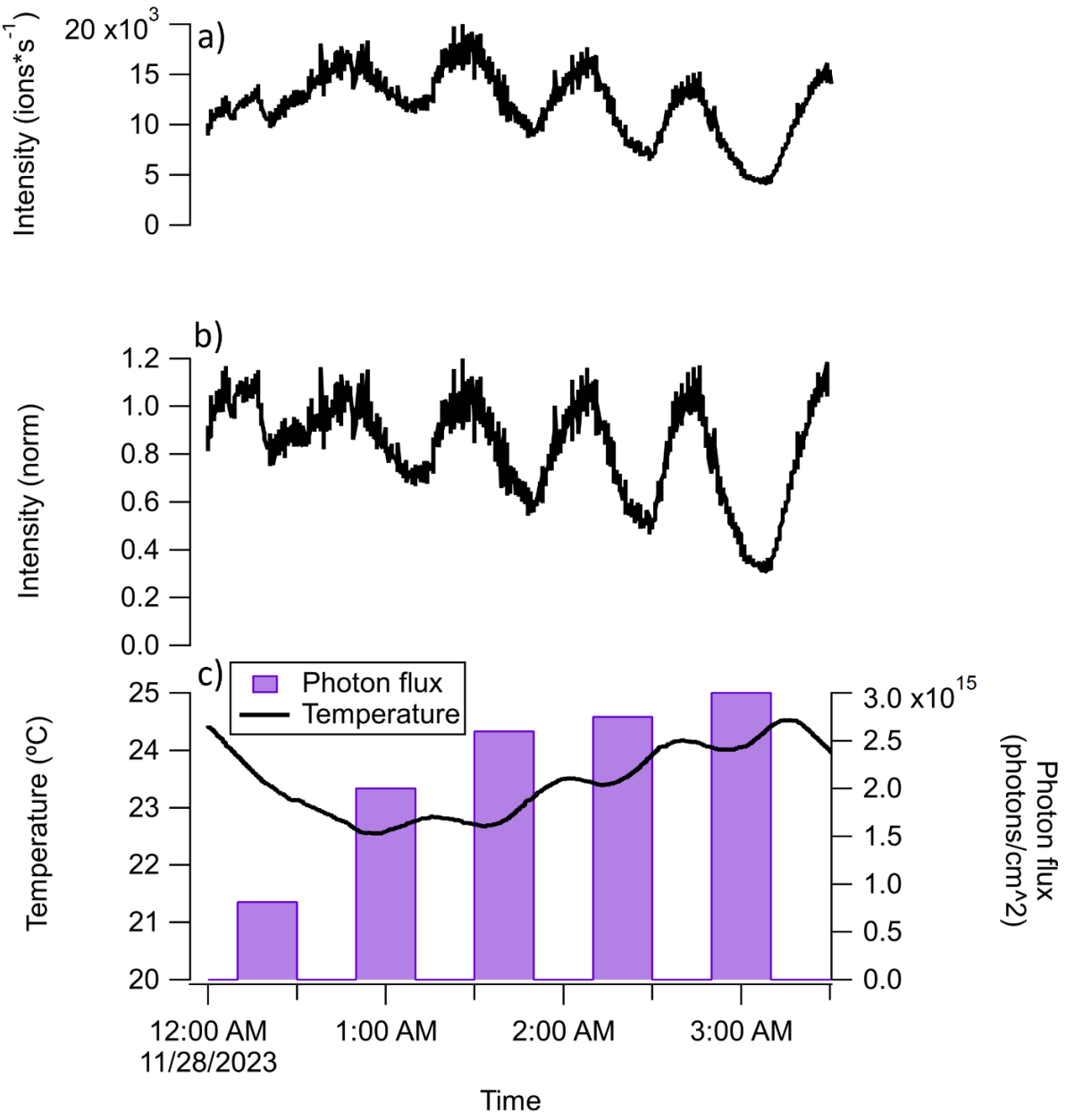


**Supplemental Figure 4.12** A representative experimental time series for one trial of BP3 decay in pure-component BP3 aerosol. a) Uncorrected measured BP3 intensity (normalized to the TIC and background subtracted). b) Corrected measured BP3 intensity. c) Change in flow tube temperature with varying photon flux.

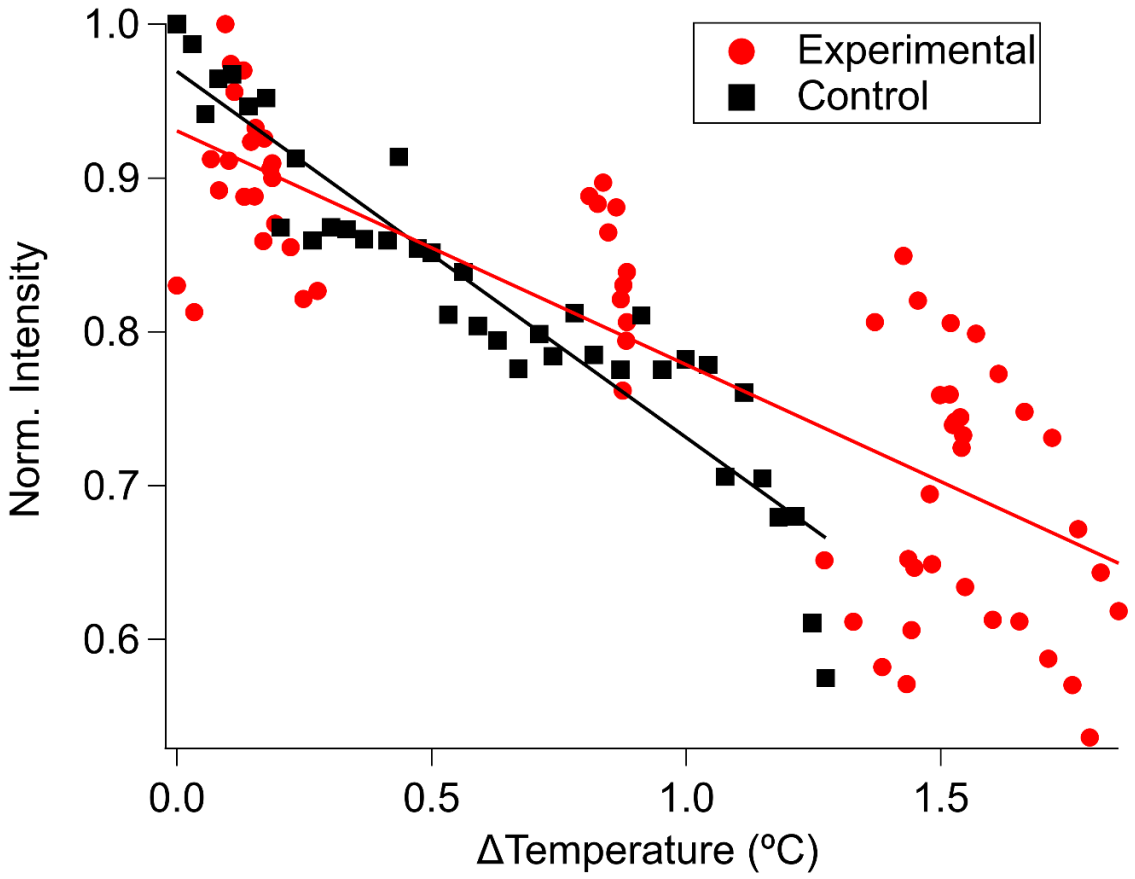


**Supplemental Figure 4.13** Comparison between temperature-driven changes in signal intensity during experimental trials and a control experiment (where no lamps were used) upon heating.

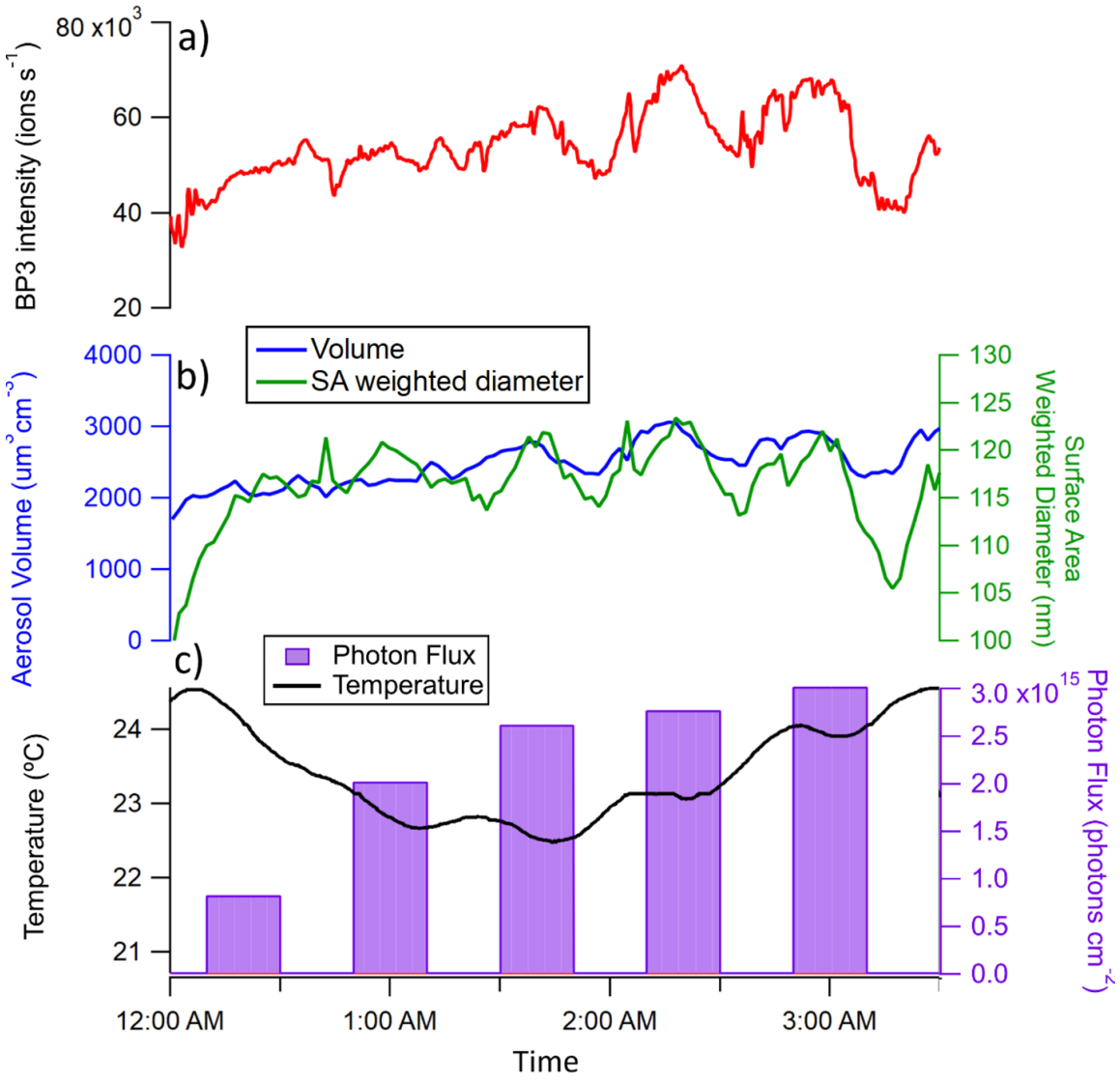


**Supplemental Figure 4.14** Example experimental trial for BP3 decay in aerosol. a) Uncorrected BP3 mass spectral signal intensity. b) Calculated aerosol volume concentration (left) and surface area weighted diameter (right.) c) Temperature (left) and photon flux (right) in the PAM-OFR.

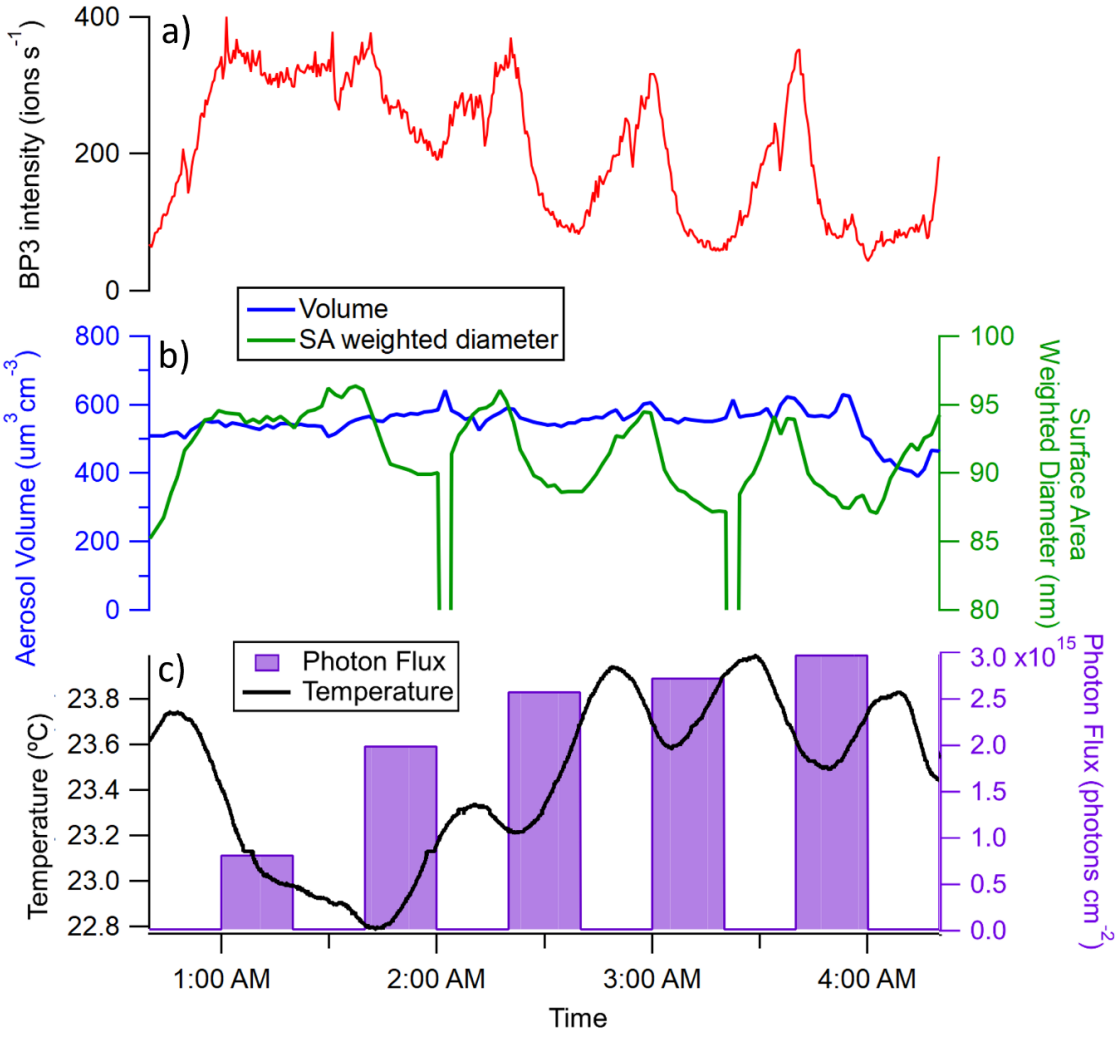


**Supplemental Figure 4.15** Example experimental trial for BP3 decay in BP3+NaCl aerosol. a) Uncorrected BP3 mass spectral signal intensity. b) Calculated aerosol volume concentration (left) and surface area weighted diameter (right.) c) Temperature (left) and photon flux (right) in the PAM-OFR.

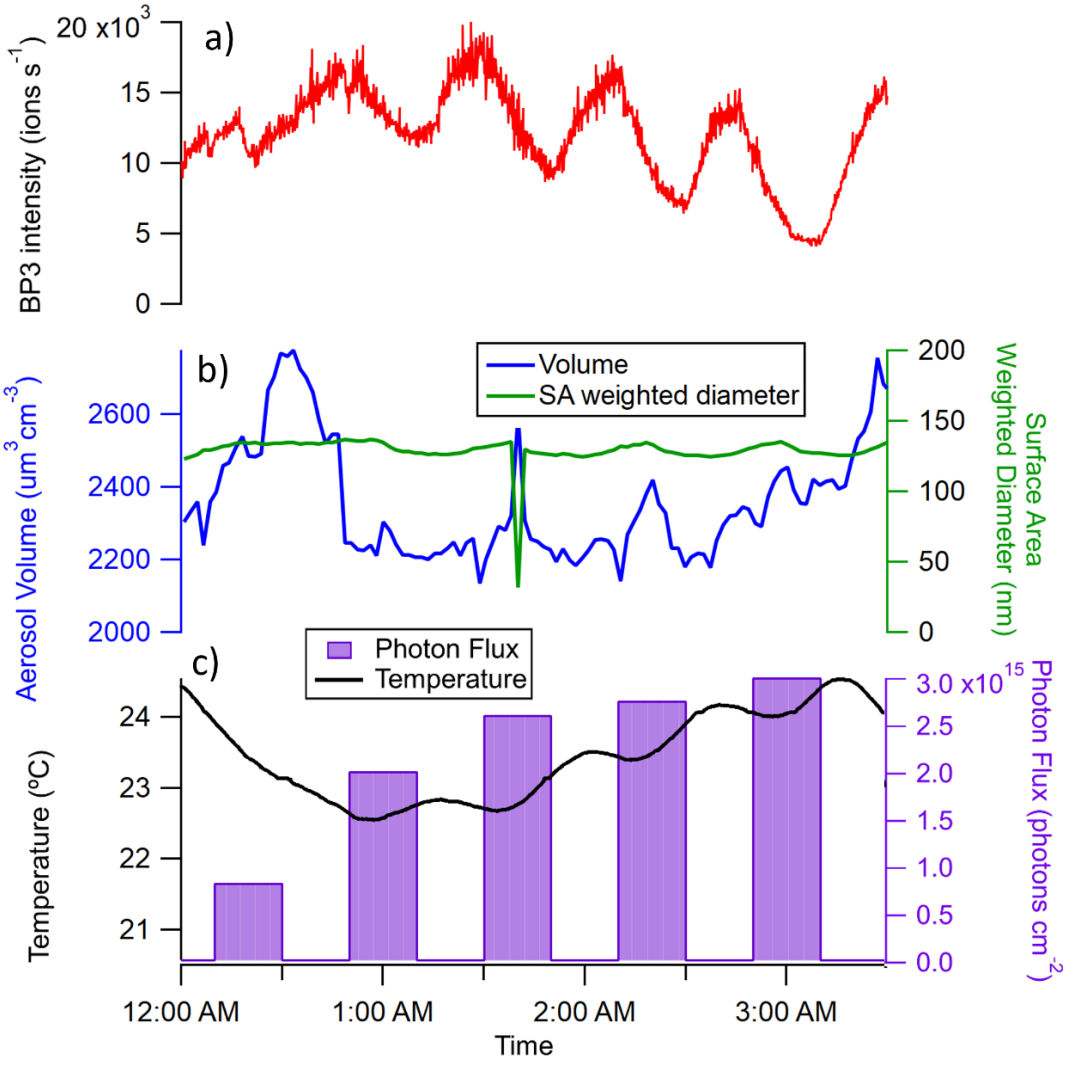


**Supplemental Figure 4.16** Example experimental trial for BP3 decay in BP3+4-BBA aerosol. a) Uncorrected BP3 mass spectral signal intensity. b) Calculated aerosol volume concentration (left) and surface area weighted diameter (right.) c) Temperature (left) and photon flux (right) in the PAM-OFR.

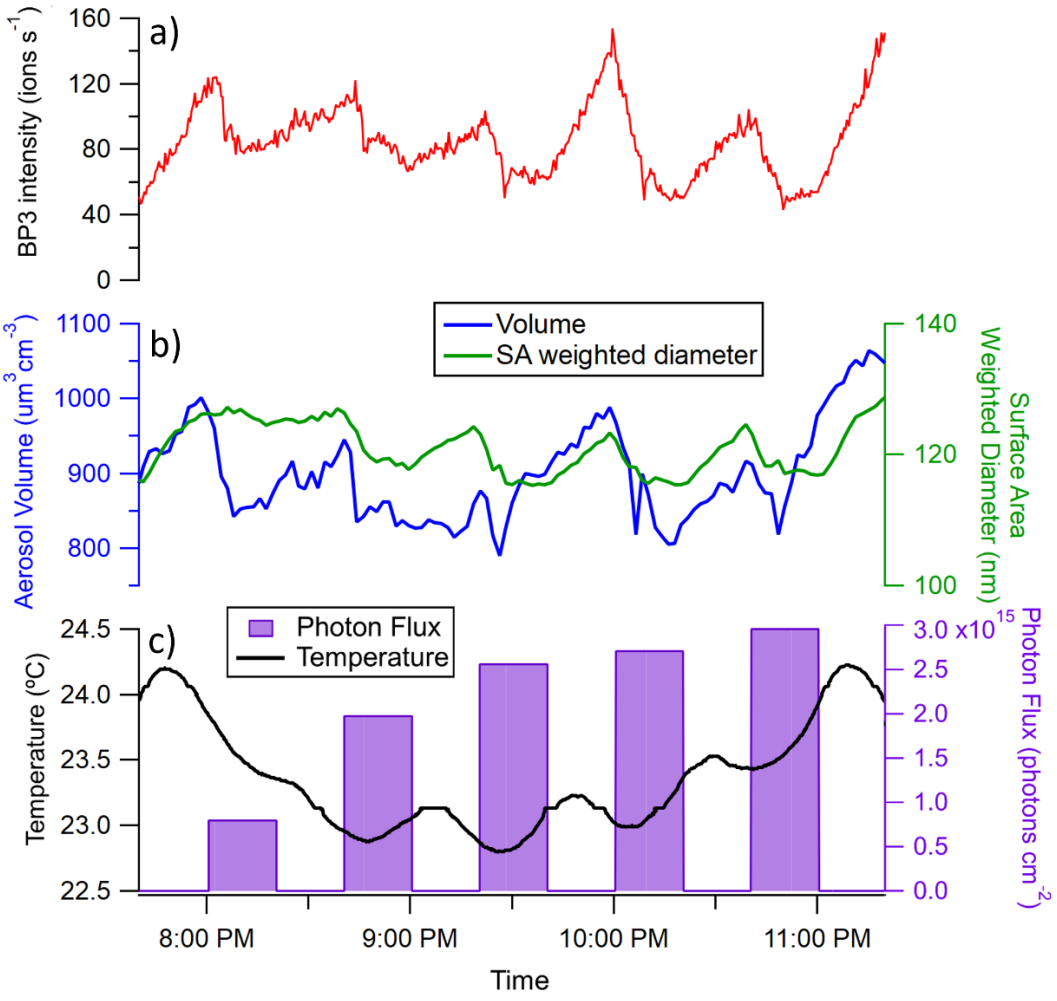


**Supplemental Figure 4.17** Example experimental trial for BP3 decay in BP3+NaCl+4-BBA aerosol. a) Uncorrected BP3 mass spectral signal intensity. b) Calculated aerosol volume concentration (left) and surface area weighted diameter (right.) c) Temperature (left) and photon flux (right) in the PAM-OFR.

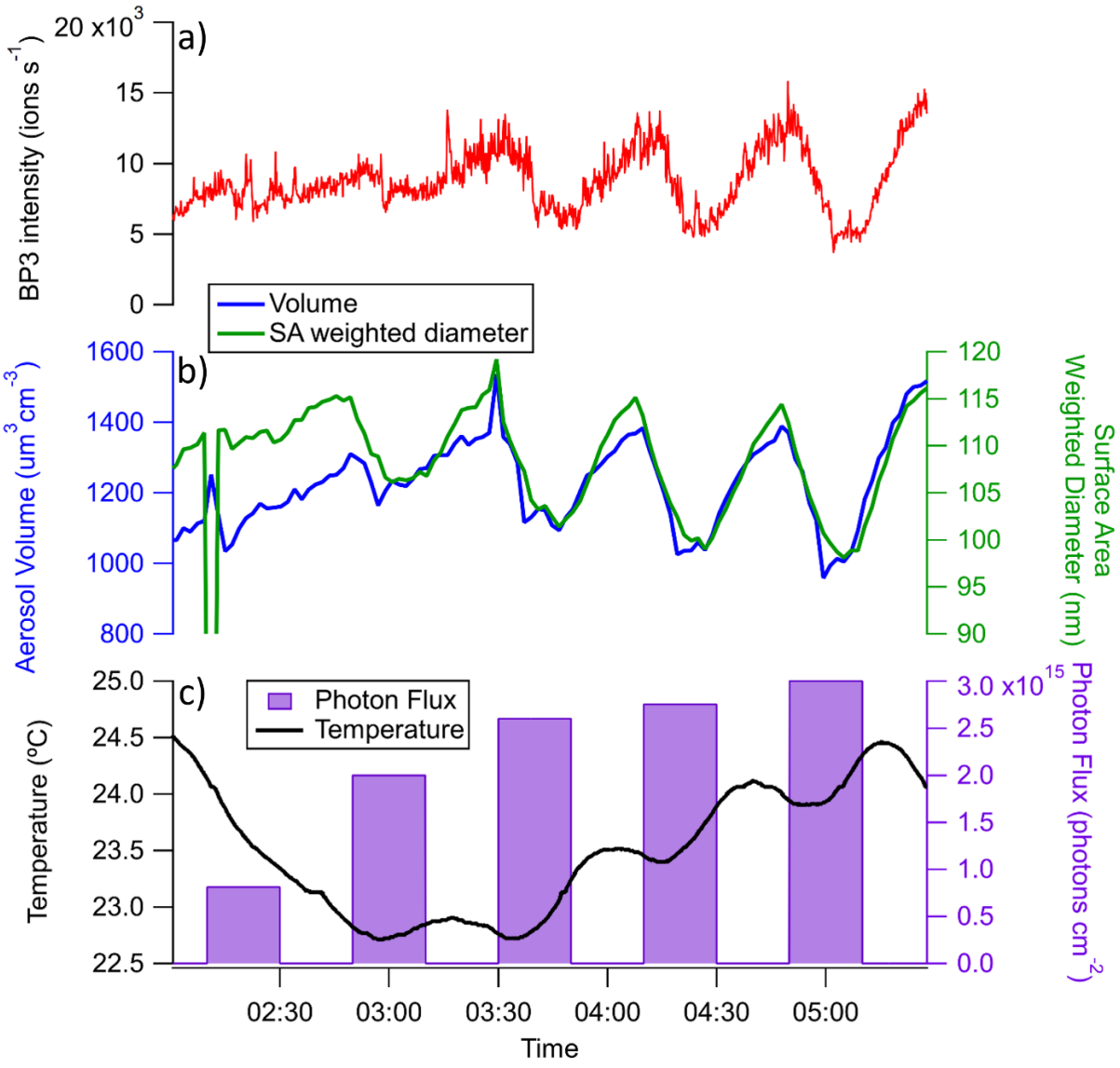


**Supplemental Figure 4.18** Example experimental trial for BP3 decay in BP3+SW aerosol. a) Uncorrected BP3 mass spectral signal intensity. b) Calculated aerosol volume concentration (left) and surface area weighted diameter (right.) c) Temperature (left) and photon flux (right) in the PAM-OFR.

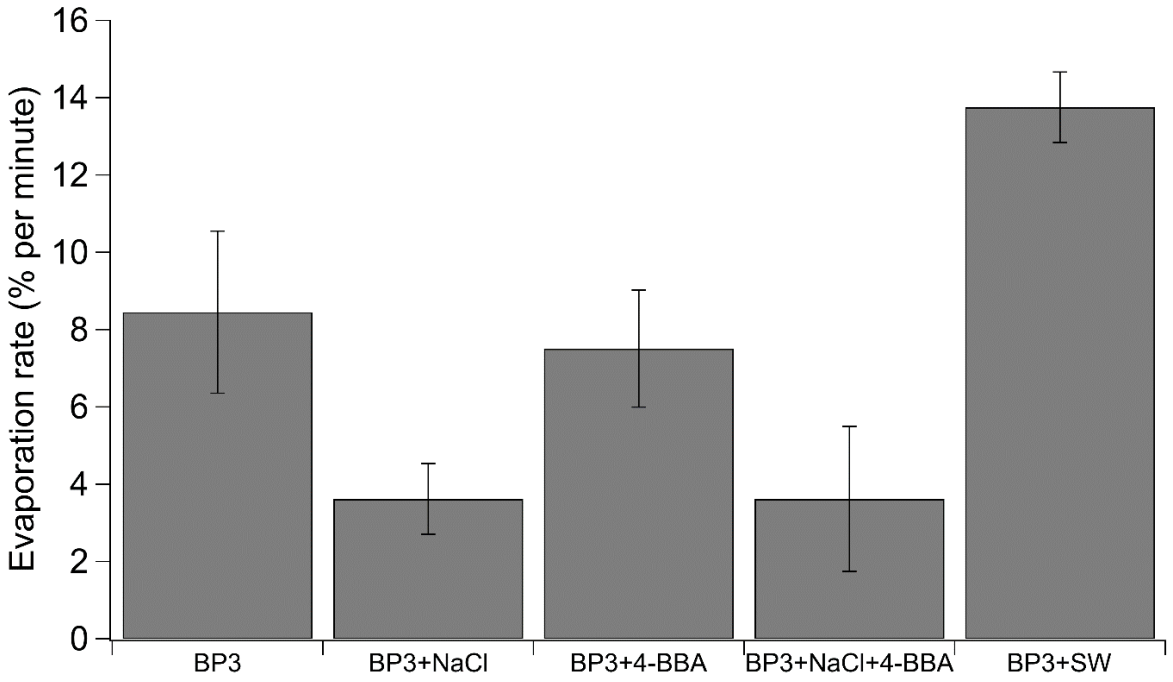


**Supplemental Figure 4.19** Aerosol evaporation rates for the different types of aerosols. Error represents the standard error in the linear regression mean between the average mass loss as a function of equivalent solar exposure.

**Supplemental Table 4.1** Experimental conditions for aerosol experiments.

| Experiment Number | Solution Type | Solution pH | Relative Humidity | Temperature | Surface Area Weighted Diameter (before exposure) |
|---|---|---|---|---|---|
| 1-3 | BP3 | ~6.1 | ~50%-55% | 22.5-24.5 C | 117 ± 2 nm |
| 4-6 | BP3+NaCl | ~6.1 | ~50%-55% | 22.5-24 C | 95 ± 2 nm |
| 7-9 | BP3+4-BBA | ~6.1 | ~35-40 % | 22.5-24 C | 140 ± 5 nm |
| 10-12 | BP3+NaCl+4-BBA | ~6.1 | ~45-50% | 23-24.5 C | 125 ± 5 nm |
| 13-14 | Spiked Seawater | ~6.9 | ~40-45% | 22.5-24.5 C | 112 ± 5 nm |

**Supplemental Table 4.2** Effective rate constant $J_{eff,env}$ for each bulk solution and aerosol mixture type.

| Mixture type | Bulk solution effective rate constant $J_{eff,env}$ ($sun^{-1}\ s^{-1}$) | Aerosol effective rate constant $J_{eff,env}$ ($sun^{-1}\ s^{-1}$) |
|---|---|---|
| BP3 | $(1.7\pm0.6)*10^{-6}$ | $(2.3\pm0.3)*10^{-3}$ |
| BP3+NaCl | $(2.5\pm0.4)*10^{-6}$ | $(11.0\pm0.5)*10^{-3}$ |
| BP3+4-BBA | $(4.2\pm0.7)*10^{-6}$ | $(6.5\pm0.9)*10^{-3}$ |
| BP3+NaCl+4-BBA | $(3.3\pm0.4)*10^{-6}$ | $(8.5\pm0.5)*10^{-3}$ |
| BP3+SW | $(0.19\pm0.03)*10^{-6}$ | $(6.6\pm0.5)*10^{-3}$ |

**Supplemental Table 4.3** Toxicity of BP3 and its photodegradation products estimated by EPA T.E.S.T. Note – these values are reported as negative log values where higher values are more toxic.

| Compound name | Experimental or predicted toxicity log (mol/kg) (EPISTAR, $LD_{50}$ rat) | Atmospheric lifetime in the gas phase to hydroxyl radicals (EPI Suite) |
|---|---|---|
| Oxybenzone | 1.49 (exp) | 1.9 hrs |
| Benzaldehyde | 1.91 (exp) | 30 hrs |
| Benzoic acid | 1.86 (exp) | 9 days |
| 2-hydroxy-4-methoxy benzaldehyde | 2.33 (pred) | 0.9 hrs |
| 2-hydroxy-4-methoxy benzoic acid | 2.27 (pred) | 0.9 hrs |
| Benzophenone | 1.58 (pred) | 36 hrs |
| 2-hydroxy-benzophenone | 1.51 (pred) | 4.0 hrs |
| 4-methoxy-benzophenone | 1.63 (exp) | 5.8 hrs |

### 4.6.1. UV-Vis Spectra of prepared solutions

For all trials, the absorbance of solutions was dominated by oxybenzone with characteristic $\lambda_{max}$ peaks at ~289 nm and a shoulder at ~323 nm.[111,113] As such, we expect oxybenzone to be neutral or protonated as the pH of all experiments was ~6-7 (determined from pH strips) and less than its pKa (7.6). Above this pKa, the anionic form of oxybenzone exhibits greatly reduced UV absorbance.[113]

The photosensitizer 4-BBA absorbs around a $\lambda_{max}$ of ~257 nm. This is blue-shifted from its previously reported absorbance at 264 nm in pure $H_2O$.[377] We expect 4-BBA to be deprotonated, as the pH of all experiments (~6-7), like pH levels in surface water, was greater than its pKa (3.4-4.85 in different solvents[377]). While care was made to subtract the influence of 4-BBA through blank subtraction, some enhancement in absorbance near its $\lambda_{max}$ can be seen in solutions containing 4-BBA (the purple and brown traces in **Fig S4.1**.) As the same concentration of 4-BBA was present in the blank, this could potentially be a product of BP3-4-BBA interaction in solution before irradiation.

Due to the shifting of $\lambda_{max}$ between the different samples and throughout some experiments, quantification was conducted by integrating within BP3's $\lambda_{max}$ region between 270 nm and 310 nm, which showed minimal influence in samples containing 4-BBA.

Upon irradiation, all experiments showed a growth in the 200-210 nm wavelength range (shown in **Fig S4.12**), suggesting the formation of less conjugated products. The BP3+4-BBA binary mixture (**Fig S4.12c**) exhibited an additional decrease in the 300-325 nm region and growth in the 240-270 nm region.

### 4.6.2. Atomized aerosol properties compared to sea spray aerosol

The MeOH in the sample evaporates immediately upon atomization, producing residual dissolved and internally mixed inorganic and organic aerosols.[378] Atomizing aerosols in the lab differs from producing SSA from bubble bursting processes.[327,370] The zero-air carrier flow had an RH of 50%, as measured by an RH probe adapted to the flow tube, which was the same for all experiments. This RH is below the deliquescence RH of pure NaCl (DRH~75%[379]) but above its efflorescence RH (ERH~45%).[379] Internally mixing organic compounds to inorganic aerosol, as done in this study, can allow for water uptake before the DRH. The combination of organic compounds and ammonium sulfate has been shown to reduce particle DRH[380,381] although this is less well explored with aerosols containing NaCl.

We visually inspected the particles' physical characteristics (i.e., morphology) at the same RH as during the experiments using confocal microscopy (Horiba LabRaman HR Evolution) after collecting the particles onto quartz substrates coated in Rain-X. The aerosol morphologies of much larger, micron-sized particles visible under the microscope were consistent with rounded particles for the pure organic aerosols and partially engulfed or phase-separated structures in the mixtures with NaCl (See SI **Fig S4.9**). In real SSA, the particle morphologies evolve with RH and differ with particle size, exhibiting both rounded and phase-separated morphologies.[370]

### 4.6.3. Aerosol phase drift correction

Aerosol signal drift was observed throughout each experimental trial and must be corrected before calculating photo-induced degradation kinetics. One representative experiment is shown in **Fig S4.13. Fig S4.13a** shows the signal of oxybenzone

(detected as its deprotonated form at 227 m/z) throughout five increasing photon fluxes, which are plotted in **Fig S4.13c.**

Note that the drift in signal maxima while under no irradiation negatively correlates with temperature. This is attributed to evaporation caused by the change in temperature inside the PAM-OFR due to each incremental step up in lamp intensity (**Fig. S4.13c**). Such temperature deviations inside the PAM-OFR have been shown before to influence aerosol mass.[255]

To account for this drift, we normalized each “dark” period to the level of the first dark period, followed by a linear interpolation between the signals in the dark upon each change in lamp intensity (see **Fig. S4.13b** for a drift-corrected time series). By performing this drift correction, changes in the normalized signal intensities after correction can be attributed to photo-initiated reactions.

We conducted a controlled study of BP3 evaporative losses in the aerosol phase by heating the OFR wrapped in heat tape in the dark in the presence of BP3 aerosol. This yielded a similar evaporative loss decay rate (24±1% loss per 1°C increase) as observed during the experiments during periods of no light exposure (18±2% loss per 1°C increase), indicating the signal drift was due to loss in aerosol mass from the lamps' heating. See **Fig. S4.14** for a direct comparison.

### 4.6.4. Aerosol evaporation

In addition to the changes in aerosol mass due to temperature fluctuations, we observed decreases in mass concurrently with decay in the BP3 signal. This suggests that BP3 transformation products, which may be less volatile than BP3, evaporate from the aerosol upon formation. This phenomenon is well studied from the fragmentation of compounds due to photooxidation.(Lambe et al., 2012; Wong et al., 2015) **Figs. S4.15-**

**S4.19** shows representative trials for each aerosol type. The simultaneous decrease in aerosol size and volume (shown in **Figs S4.15-S4.19b**) corresponds temporally with photon flux but not flow reactor temperature (shown in **Figs S4.15-S4.19c**).

Aerosol evaporation rates are plotted directly in **Fig S4.20.** Experimental mixtures containing NaCl exhibited the lowest evaporative losses (~4% $min^{-1}$), followed by pure organic aerosol (~8% $min^{-1}$), with the spiked seawater aerosol showing the largest losses (~14% $min^{-1}$). This suggests that NaCl in aerosol can lead to a stabilizing effect that inhibits the evaporation of organic matter in the particles. We hypothesize that additional, potentially more volatile components of seawater DOM led to the high observed evaporation rates in the spiked trials.

### 4.7 Acknowledgments

We thank Neal Arakawa for his support and access to the Environmental Complex Analysis Laboratory, Andrew Kummel for donating the UV Vis spectrophotometer and Michael Tauber for insightful conversations. This study was supported by the National Science Foundation (AGS-2135218 and DGE-2038238). Computation was supported in part by W. M. Keck Foundation through computing resources at the W. M. Keck Laboratory for Integrated Biology.

Chapter 4, in full, has been submitted for publication of the material as it may appear in *ACS Environmental Science & Technology: Air*, 2024, Cooper, A, Shenkiryk, A, Morris, M, Chin, H, Mehndiratta, L, Roundtree, K, Tafuri, M, Slade, J.H. The dissertation author was the primary investigator and author of this paper.

# Chapter 5 Online characterization of secondary marine aerosol using extractive electrospray ionization

Chapter 5, in full, is currently being prepared for submission for publication of the material as it may appear in *Atmospheric Chemistry & Physics*, Cooper, A, Shenkiryk, A, Morris, M, Chin, H, Mehndiratta, L, Roundtree, K, Tafuri, M, Slade, J.H. The dissertation author was the primary investigator and author of this paper.

## 5.1. Abstract

Marine aerosol plays a unique role in the stability of Earth's climate system. Secondary marine aerosol formed through the photooxidation of biogenic volatile organic compounds is important for forming marine clouds. In this work, we employ extractive electrospray ionization mass spectrometry to characterize the organic profile of secondary marine aerosol generated during a large-scale phytoplankton bloom mesocosm. Elevated biological activity increased the presence and sulfur- and nitrogen-containing compounds. We identify the major contributions of isoprene and monoterpenes to organic aerosol mass and demonstrate how their changing concentrations throughout the bloom modify the organic composition of SMA. We observed primarily fragmentation-led oxidative aging at lower exposures than in previous single and simple mixed precursor studies. These findings provide a foundational basis for the organic speciation of SMA.

## 5.2 Introduction

Secondary organic aerosol (SOA) formed from the nucleation and condensation of marine gases plays a critical role in marine cloud formation.[149,150,177,383] However, due to challenges in separating SMA from primary sea spray aerosol (SSA), they remain relatively understudied compared to SSA.[6,150] The predominant formation pathway of

SMA has been typically considered to be dominated by the oxidation of dimethylsulfide (DMS) and methanethiol (MeSH) into methanesulfonic acid (MSA) and sulfate (SO4) aerosol.[180,384] However, recent advances have demonstrated other important precursors, such as alkyl amines[154,178], benzothiazole[385] and terpenes (isoprene and monoterpene species)[159–161], to contribute to a significant fraction of the organic component of SMA.

Some studies of marine aerosol have attempted to attribute the contribution of secondary organic mass relying on detecting known terrestrial SOA tracers and performing an extrapolation, introducing large errors. Fu *et al*. 2013[386], which sampled open ocean aerosol, reported a secondary organic mass ratio (organic mass as a percentage of total mass) of 21.6% (ranging from 9.6 to 40.2%) more than that of primary marine aerosol (16.3%, ranging from 8.3 to 34.0%.)

The ratio between aerosols' organic and inorganic components may significantly impact the particle's physical properties, such as phase, hygroscopicity, and refractive index.[5,188,327,366,387] For example, $SO_4$ aerosols (which are more hygroscopic) produce clouds that reflect five times as much solar radiation as those seeded by MSA.[388] In a survey of North Atlantic SMA, Kilgour *et al.* 2024[161] report an OA:$SO_4$ ratio of 1:2.7. In a mesocosm experiment of an induced phytoplankton bloom in real seawater, Mayer *et al.* 2020[149] reported OA: $SO_4$ ratios ranging from 1:1.5 to 1:7. They also found the hygroscopicity (κ) of SMA was predicted by the ratio ranging from κ=0.52-0.64.

Additionally, the identity of the organic component of mixed aerosol can significantly affect its viscosity and hygroscopicity. While significant advancements have been made in identifying key marine VOC precursors[150,151,155,159–161,386,389,390],

comparatively little research has been done on the organic composition of SMA.[150,386,390]

Generally, organic compounds that are more functionalized (i.e., contain oxidized and heteroatom moieties) are more hygroscopic.[32,33,185,187,188] Organosulfur and organonitrate compounds significantly reduce the volatility of compounds (leading to greater incorporation in aerosols over evaporation to the gas phase)[391–396] and increase the hygroscopicity (leading to greater water uptake and eventual cloud nucleation.)[393,395] Organosulfate components of SMA may be produced via aerosol-phase reactions between sulfate and oxidized compounds[392,394,397–399] or through the oxidation of sulfur-containing compounds (such as DMS and MeSH.)[180,384] Organonitrate components of SMA may be formed in gas-phase oxidation reactions in the presence of nitrogen oxides (NO and $NO_2$)[165,166,168] or through the oxidation of nitrogen-containing compounds (such as alkyl amines.)[175,178]

This work investigates the organic composition of pure secondary marine aerosol from sampled gases produced during a phytoplankton bloom in real seawater. To our knowledge, this study represents the first high-resolution characterization of the organic components of SMA without the influence of SSA. A contributing factor to this gap in the literature is the difficulty in separating small nucleation-mode particles in the field, collecting enough small aerosols onto filters for offline analysis, or using harsh ionization schemes for standard techniques like aerosol mass spectrometry. For this reason, here we employ extractive electrospray ionization, which is highly sensitive to small aerosols and provides detailed compositional information through soft ionization.[229,263] Determining bulk molecular composition and estimating bulk molecular

properties will help identify which gas precursors may contribute most to secondary aerosol mass and their behavior in the atmosphere.

## 5.3. Methods

### 5.3.1 SMA formation at SeaSCAPE 2019

In the summer of 2019, the NSF Center for Aerosol Impacts on Chemistry of the Environment ran a controlled mesocosm experiment titled Sea Spray Chemistry and Particle Evolution (SeaSCAPE). Sauer et al. 2021 provides an overview of this study.[148] Briefly, real seawater samples were collected from the Scripps pier in La Jolla, CA, USA, and transported to the SIO Hydraulics Laboratory glass wave channel. A sequence of three phytoplankton blooms was initiated via nutrient addition and diurnal fluorescent light. This work focuses on Bloom 3, the last and longest of the blooms.

Secondary marine aerosol was generated at SeaSCAPE by sampling volatile gases from a borosilicate glass isolated sampling vessel (ISV) in which water was continuously transferred from the main wave channel to a vessel with an isolated headspace (see **Fig. 5.1**.) Zero air was introduced to the ISV with a residence time of 5 minutes. Gases that evaporated from the water's surface were sampled by this zero-air flow into a Potential Aerosol Mass Oxidative Flow Reactor (PAM-OFR, Aerodyne.)[355,400]

In the PAM-OFR, $O_3$ and ·OH radicals are generated via the following scheme:

$$O_2 + hv(185\,nm) \rightarrow 2O \qquad R1$$

$$2O + O_2 \rightarrow O_3 \qquad R2$$

$$H_2O + O_2 + hv(185\,nm) \rightarrow\rightarrow OH + HO_2 \qquad R3$$

$$O_3 + hv(\,254\,nm) \rightarrow O(^1D) + O_2 \qquad R4$$

$$O(^1D) + H_2O \rightarrow 2OH \qquad R5$$

Due to its higher reactivity and relatively high concentration, ·OH is expected to dominate OFR oxidation pathways compared to $O_3$ and $HO_2$ species.[254,400] The secondary organic aerosol produced in this manner exhibits characteristics like those generated by environmental chamber studies.[401] A ballast changed the intensity of the 185nm and 254nm lamps to generate ·OH concentrations between ~$2*10^8$-$3*10^9$ mole $cm^{-3}$. This is equivalent to ·OH exposures ranging between 0.5-8 days in the atmosphere (assuming an average of $1.5*10^6$ mole $cm^{-3}$.) Due to the effects of equilibration time after an initial “10 V blast” to warm the lamps up, the first exposure (0.5) days was discarded, and the following four exposures (1,3,5 and 8) were used for analysis.

A suite of instruments sampled the generated SMA from the PAM-OFR for aerosol composition, size distribution, hygroscopicity, and particle bounce (phase state) analysis. Before oxidation, a proton transfer reaction time-of-flight mass spectrometer (PTR-ToF-MS, Aerodyne) sampled headspace gases in a separate ISV to report gas phase species.

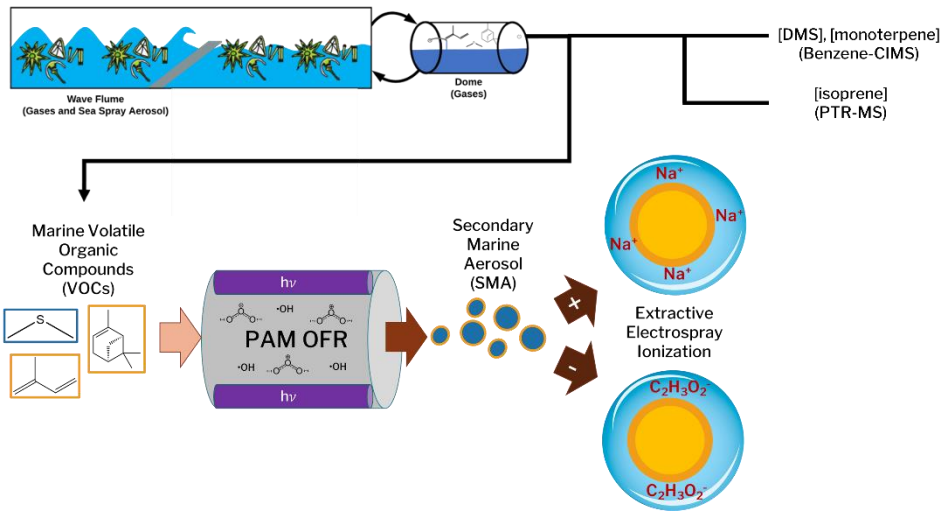


**Figure 5.1** Diagram showing the sample handling flow and measurements of marine VOCs and SMA composition. Water is exchanged from the wave flume to the dome, where volatilized gases are analyzed by Benzene-CIMS and PTR-MS and introduced to a PAM OFR to simulate oxidative aging. The produced SMA is sampled via (+) and (-) EESI-TOF MS modes.

### 5.3.2. Compositional analysis

#### 5.3.2.1. Precursor gas quantification

A Vocus proton transfer reaction time-of-flight mass spectrometer (PTR-MS, Aerodyne) was used to measure headspace gas-phase VOCs.[402] It relies upon the following scheme to ionize gases:

$$H_3O^+ + M \rightarrow H_2O + MH^+ \qquad R3$$

PTR offers the benefit of most VOCs having a higher proton affinity than water, while most ambient air molecules have a lower proton affinity. This results in the selective ionization of trace VOCs of interest.[402] Unspeciated monoterpenes were detected as $C_{10}H_{17}^{+\cdot}$ and DMS was detected as $(CH_3)_2SH^+$. Further details on the operation of the PTR at SeaSCAPE may be found elsewhere.[148,162]

Due to the PTR's inability to distinguish isoprene from the fragmentation products of larger organic molecules found in marine air/[403] A chemical ionization mass

spectrometer using benzene cation reagent ions was used to detect isoprene as a $[(C_5H_8)(C_6H_6)]^+$ cluster.[404]The instrument used was a home-built system modeled on one built by Zercher *et al.* 2009.[405] Further details on this instrument's operation may be found elsewhere.

#### 5.3.2.2. SMA compositional measurements

This study utilized an Aerodyne extractive electrospray ionization high-resolution time-of-flight chemical ionization mass spectrometer (EESI-HR-ToF-CIMS).[229] EESI is applied to aerosol systems to speciate organic aerosol with a fast time resolution (>1 Hz) and low fragmentation (detecting analytes either as (M+Na)+ or (M-H)—ions). This is accomplished via the coalescence of a sample aerosol stream with a charged electrospray, in which the electrospray extracts and then ionizes organic compounds of the sample aerosol.[225,226] To our knowledge, this study was the first time EESI was used to measure generated SMA.

We employed the following ionization schemes in positive mode (via clustering with $Na^+$ ions)[229] and negative mode (via proton abstraction)[215,327]:

$$M + Na^+ \rightarrow (M + Na)^+ \qquad R1$$

$$M + C_2H_3O_2^{-1} \rightarrow (M - H)^{-1} + C_2H_4O_2 \qquad R2$$

Positive mode detects oxidized compounds, in which electronegative moieties form strong clusters with sodium ions.[229,406,407] Negative mode is useful for detecting acidic carboxylic acids and organosulfur components.[215,234,327] During bloom 3, ionization modes were switched to capture each phase of the phytoplankton bloom in both modes.

Additionally, the bulk chemical composition of SMA was measured by high-resolution time-of-flight aerosol mass spectrometry (HR-ToF-AMS, Aerodyne).[408] The

AMS was operated in V-mode with standard MS mode (5s open, 5s closed) 410 and PTOF (10s) with typically 5-min sampling averages.

### 5.3.3. SMA sizing

SMA size distribution was measured by a scanning electrical mobility spectrometer (SEMS, Brechtel.)[251] The SEMS was operated in a scan range between 5-850 nm at a resolution of 100 bins with a total scan time of two minutes. Aerosol masses were converted from aerosol volume assuming a density of 1.2 g $cm^{-1}$, which we note is more representative of organic (ρ=1-1.2 g $cm^{-1}$) than sulfate aerosol (ρ=1.8 g $cm^{-1}$.)[409,410]

### 5.3.4. SMA formation modeling

The oxidation pathways of isoprene and monoterpene species (specifically, α-pinene, β-pinene, and limonene) are relatively well-parameterized. [163,164,411–414] Based on the speciation of monoterpenes at SeaSCAPE reported by Franklin *et al*. 2022,[147] we parameterized monoterpenes as limonene due to its overwhelming (>95%) abundance compared to other species.

To model the expected gas phase products of isoprene and limonene oxidation, the Master Chemical Mechanism (MCM)[415] using the framework for 0-D atmospheric modeling (F0AM)[416] was used. It predicted the oxidative removal of precursors and the generation of products of each in the PAM-OFR at each stage of oxidative aging.

To determine which species would partition into the aerosol phase, we estimate φ, the percentage of each compound that is bound to the aerosol phase, using the AEROWIN model as a part of the EPA EPISUITE.[79]AEROWIN estimates phi through three methods: the Junge-Pankow adsorption model (based on vapor pressure,) the Mackay adsorption model (based on a calculated gas-particle partitioning coefficient),

and the octanol-air partition coefficient model (based on the octanol-air partition coefficient.)[417] Where experimental values are unknown, AEROWIN estimates these values for each compound based on structural similarities to its training set.

## 5.4 Results

### 5.4.1. Biological activity, biogenic VOC concentrations, and SMA mass during the bloom

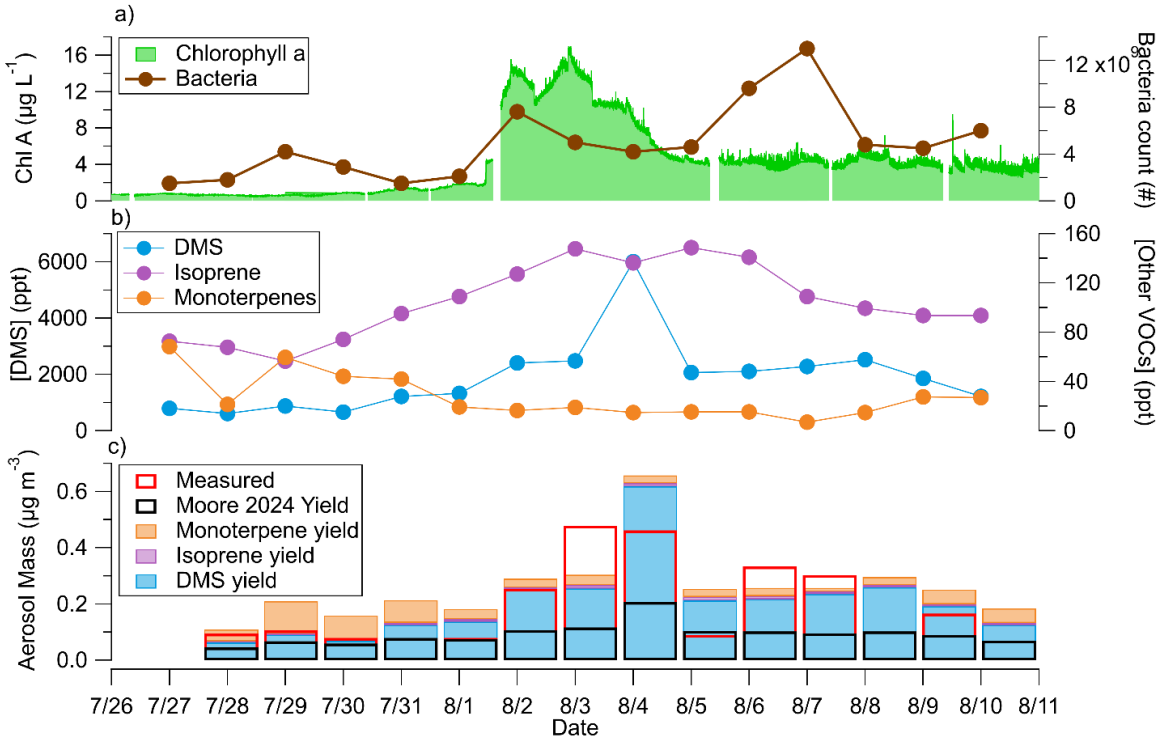


**Figure 5.2** Time series of a) chlorophyll-a and bacteria cell counts, b) DMS, isoprene, and total monoterpene concentrations, and c) modeled aerosol mass yields from individual DMS, isoprene, and monoterpene compared to measured mass (red) and modeled yield of a mixture of DMS and isoprene (red.)

The organic composition of SMA is driven by the diversity of precursor gases emitted from biological components in the water throughout a phytoplankton bloom. Chlorophyll a, as a marker for photosynthetic activity of phytoplankton, and heterotrophic bacteria counts are plotted in **Figure 5.2a** to track biological activity. This is a typical progression of the “microbial loop,” in which phytoplankton populations

bloom, as indicated by increasing chlorophyll concentrations, die off, as indicated by decreasing chlorophyll concentrations, and are replaced by bacteria that consume the discarded organic matter, as indicated by increasing bacterial cell counts.[418,419] Throughout this process, biogenic VOCs are released (see **Fig. 5.2b**.) For this analysis, we focused on DMS, isoprene, and total monoterpenes. These are major SOA precursors in the environment.[150,160,161,386,390] DMS originates from the breakdown of dimethyldisulfide (DMDS,) produced by phytoplankton and released upon mass death and cell rupture.[158] Monoterpenes exhibited a steady decline throughout the bloom. This could suggest they had a source removed during the transfer process from the ocean to the wave flume, perhaps macroscopic species removed by the 50 um used in SeaSCAPE[148], as seen with anthropogenic compounds during this study.[147] Isoprene generally increased and decreased alongside chlorophyll a, as it is emitted continuously from phytoplankton biomass (though isoprene emissions do vary with temperature and light.)[159]

The oxidation pathways of isoprene, monoterpenes, and, to a lesser extent, DMS are relatively well studied. Using SOA yield values from the literature (DMS – 36-40%, isoprene – 1-5%, and monoterpenes – 30-50%),[149,163,401] we can predict the SOA mass produced from each precursor for each equivalent OH exposure, as shown in **Figure 5.2c**. We note that this does not consider VOC mixture effects. Previous studies[172,389] have found that mixtures of DMS and isoprene led to reduced yields from DMS (due to competition for OH) and increased yields from isoprene (due to DMS forming sulfate seed particles for semi-volatile isoprene oxidation products to condense onto.) For comparison, we plot the predicted SMA generated using the yield values of

SMA+isoprene from Moore *et al.* 2024.[389] Interestingly, the predicted SOA mass from the oxidation of the VOC mixture underestimated the measured SOA mass, while during periods of relatively low chlorophyll a in the water, in general, modeled SOA mass integrated from individual SOA yields slightly overestimated the measured aerosol mass. This suggests that using individual SOA yields of individual VOC precursors in the model overestimates total SOA mass and that either additional SOA precursors were missed when using the SOA yield from a VOC mixture or there were additional interactions in the particle phase leading to lower volatility species and enhanced SOA yields.

Measurements of dry aerosol mass measured via SEMS at one day of equivalent aging by OH are shown for comparison, which generally agrees well (see **Fig 5.3.** for a direct comparison between the measured SMA mass and the modeled SMA mass from the individual contributor and mixture yield methods.) The individual contributor model overestimates produced aerosol mass for some data points, each corresponding to a sampling day. The mixture yield from Moore generally underpredicts aerosol yields, demonstrating that our mixture of real marine VOCs exhibits higher aerosol yields than the simple mixture of DMS+isoprene. This is expected, as monoterpene and alkyl amines (of which we have no measurements but expect are present) demonstrate higher yields than isoprene.[163,175,401,420]

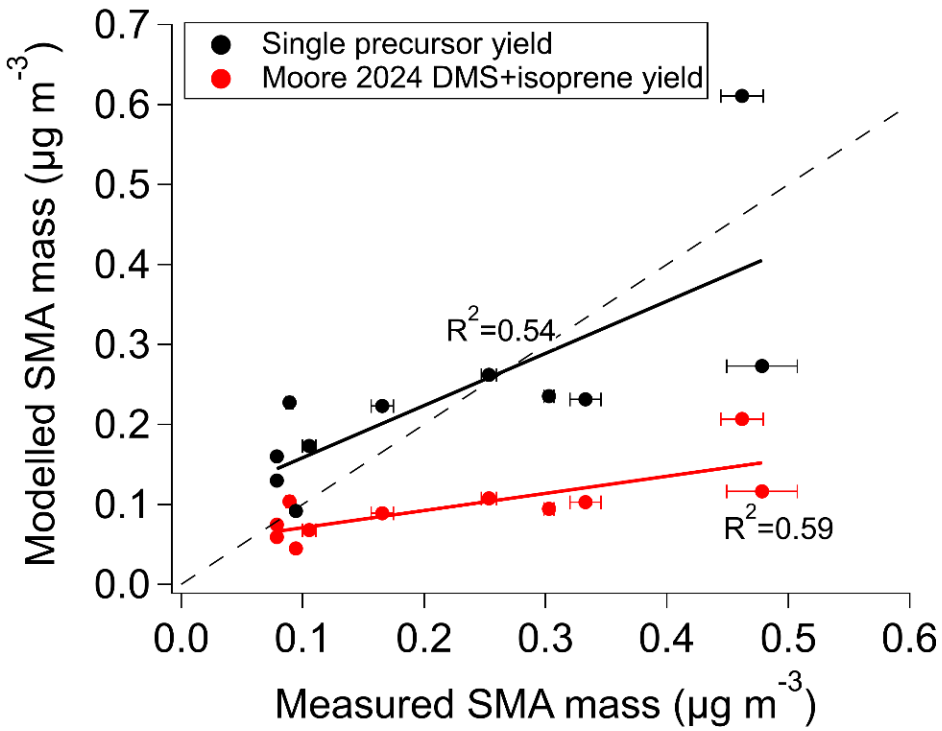


**Figure 5.3** Scatter plot of modeled SMA mass compared to measured SMA mass. Each data point represents SMA generated via one day of equivalent exposure for each study day. The dashed line is a 1:1 line. Error bars represent the standard deviation in mass measurements for each sampling period.

This demonstrates that, for this system, the contributions of DMS, isoprene, and monoterpenes are significant drivers and contributors to SMA mass and can be used to parameterize its composition and properties. This was also the case in the modeling of marine gas oxidation in Kilgour *et al.* 2024.[161] They found that oxidation of DMA, MeSH, isoprene, and monoterpenes reproduced the measured OC: $SO_4$ ratio of eastern Atlantic SMA.[161]

### 5.4.2. SMA size distributions and aerosol yield

**Figure 5.4** shows representative aerosol size distributions of SMA generated at three stages of the phytoplankton bloom: before the increase in chlorophyll a (Pre Bloom), at peak chlorophyll a (Peak Bloom), and after the decline in chlorophyll a (Post

Bloom). Strong growth in sub-10 nm diameter particles indicates newly nucleated particles that grow into Aitken mode nuclei (sub-40 nm), generally increasing with increasing OH exposure. Aerosol concentrations (>100 nm) in the accumulation mode were relatively low and near the background, exhibiting no significant difference with variable OH exposure. The largest difference in aerosol generation is between 0.5 days of equivalent aging and one day, followed by smaller increases over the range of oxidation conditions.

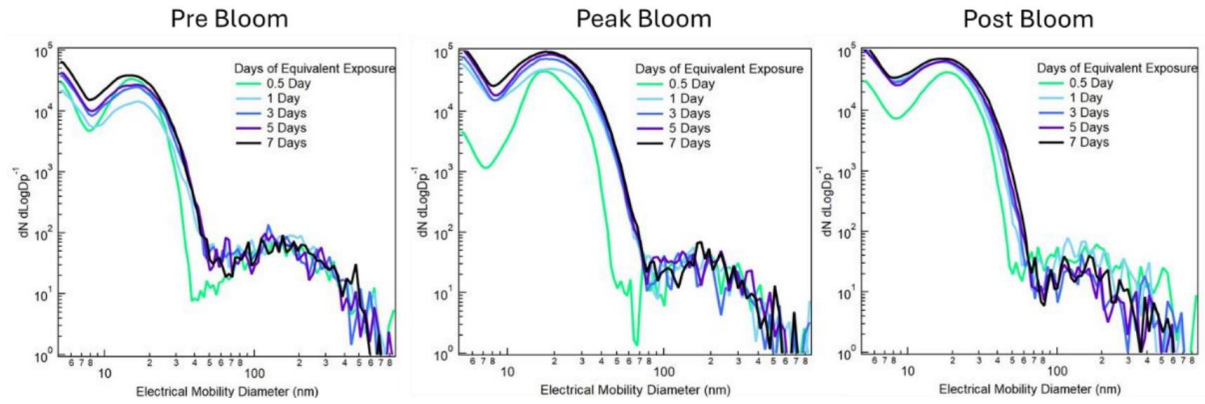


**Figure 5.4** Median size distributions of SMA produced during the SeaSCAPE experiment during three representative days during the lifetime of the phytoplankton bloom (Pre Bloom 7/30, Peak Bloom 8/4, and Post Bloom 8/10). Distributions are colored by the extent of equivalent oxidative aging ranging from 0.5 to 7 days in the atmosphere; all distributions provided are at an RH = 70%. Adapted from Tuminello 2024.

The observed steady increase over a week of equivalent aging is typical for SOA formed from DMS, in which aerosol yields increase with increasing oxidation levels as oxidation pathways terminate in inorganic sulfate.[149,172,389] In contrast, organic SOA precursors such as monoterpenes and isoprene undergo two processes during oxidation: functionalization (adding mass to organics and increasing volatility) and fragmentation (breaking carbon-carbon bonds and thus lowering volatility).[382]

For comparison, we plot the aerosol yields from this study against relevant yields from single- and two-component SOA studies in **Figure 5.5**. SOA yields ($Y_{SOA}$) were calculated as

$$Y_{SOA} = \frac{\Delta M}{\Delta [VOC]} \qquad eq\ 1$$

where Δ*M* and Δ*[VOC]* are the changes in aerosol mass and VOC concentration (units of μg $m^{-3}$) before and after VOC oxidation. We note that ΔVOC in this study was not measured but calculated from the box model from the relative change in DMS, isoprene, and monoterpene concentrations in the PAM-OFR before and after OH exposure and over the 200s timeframe of exposure in the PAM-OFR.

Lambe *et al.*[401] reported isoprene and monoterpene yields that generally increased (due to functionalization) from 0 –6 days of equivalent aging, followed by a decrease with increasing OH exposure. In contrast, Moore *et al.*[389] observed increased aerosol yields for isoprene were up to 17 days of equivalent OH exposure. The aerosol yield for DMS also increased, to a greater extent, as expected. The combined DMS+isoprene mixture exhibited lower aerosol yields, which they ascribe to competition between the different precursors for ·OH.

Our calculated aerosol yield was the highest at one day of equivalent aging. It decreased with increasing exposure, suggesting that fragmentation reactions led to a loss in organic mass greater than the increase in $SO_4$ mass expected from DMS oxidation. This indicates that highly oxidized molecules prone to fragmentation reactions are produced more in this mixed precursor system than in previous single precursor systems. This warrants additional study with direct measurements of ΔVOC for complex mixtures of SMA precursors.

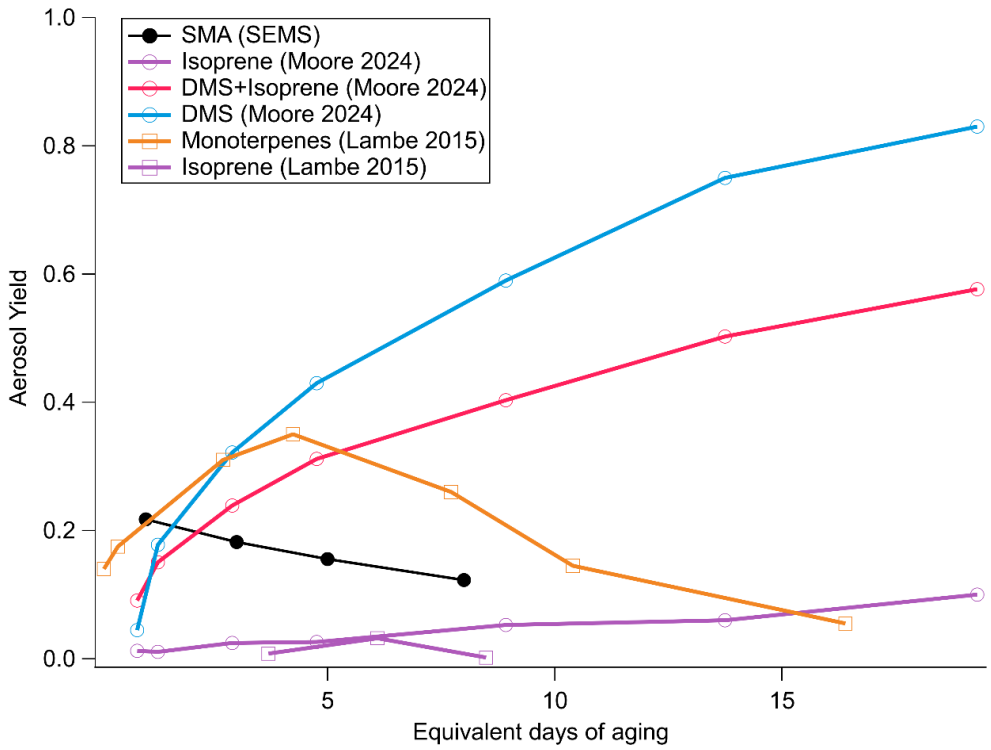


**Figure 5.5** Aerosol yields for SMA (this study) isoprene and monoterpenes (Lambe 2015), and isoprene, DMS, and isoprene+DMS (Moore 2024) plotted as a function of equivalent days of aging via OH oxidation.

### 5.4.3. Comparison between EESI-MS and AMS

To determine if the EESI-MS response represents the total organic mass, we compared the integrated EESI-MS signal to the organic mass measured via AMS in **Figure 5.6.**, as done by Qi et al. 2019.[421] We observed a higher rate of positive correlation (80% of days) in negative mode (N=5 days) and a lower rate (33%) in positive mode (N=3 days). This may indicate that the ionization scheme in the negative mode is relatively more sensitive than that of the positive mode to a broader diversity of components in SMA representative of the total organic mass. In a later section, we will further explore which subsets of SMA organics are sampled within each mode using a volatility-based approach.

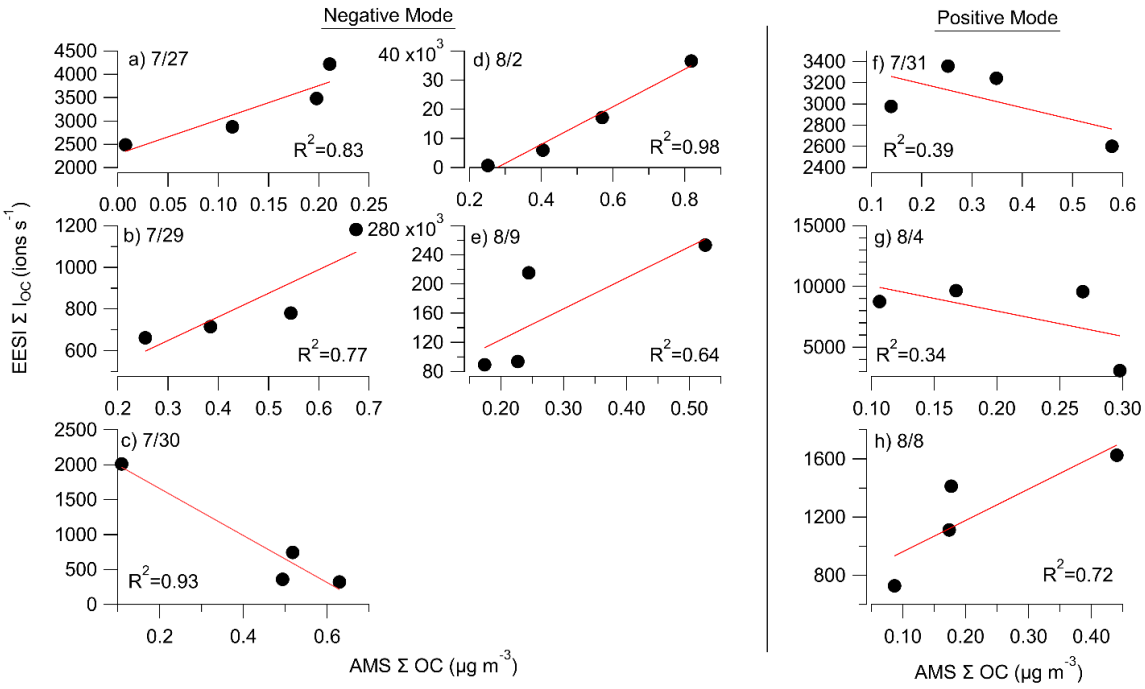


**Figure 5.6** Direct comparisons of summed EESI ion counts compared to AMS organic aerosol masses. a-e) show days with overlapping measurements in negative mode and f-h) in positive mode. The magnitude of EESI ion counts varied widely with different electrospray configurations due to switching back and forth between (+) and (-) modes.

### 5.4.4. SMA molecular composition determined by EESI-MS.

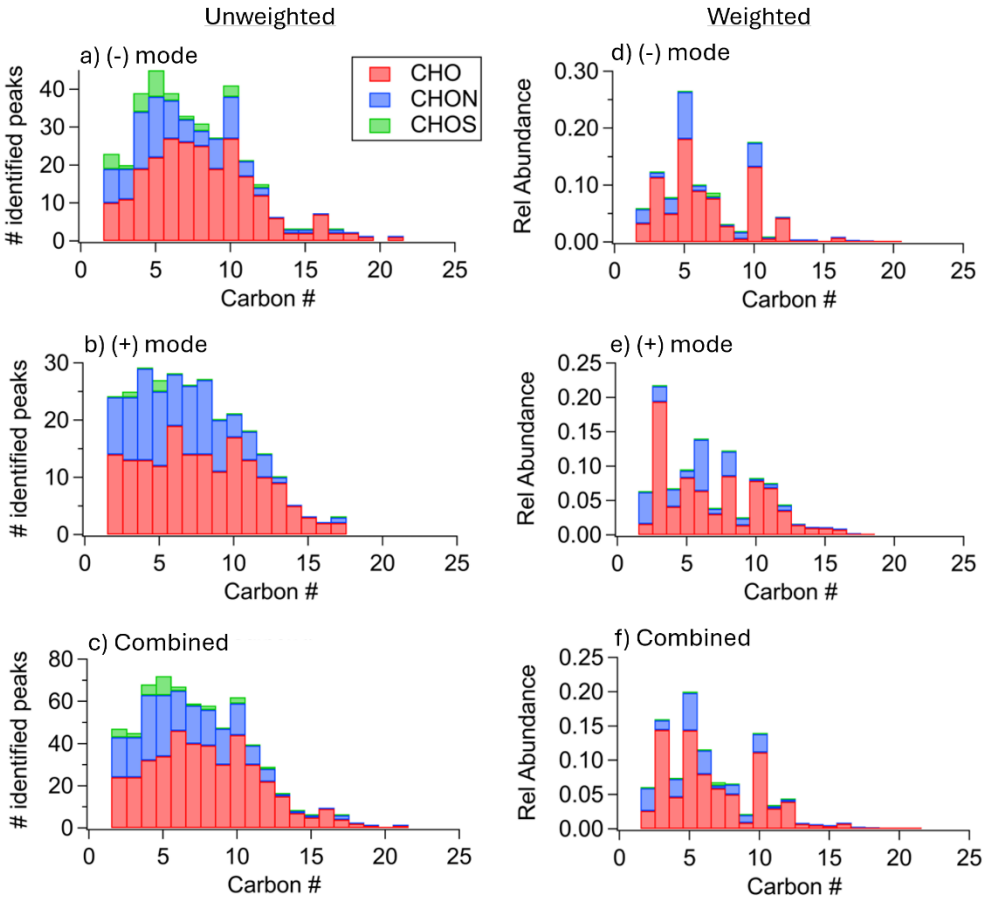


**Figure 5.7** a-c) Number of organic species identified separated by carbon number and presence of nitrogen (CHON), sulfur (CHOS), or no heteroatoms (CHO) in a) negative mode, b) positive mode, and c) both modes combined. d-f) is the same as a-c) but weighted by ion intensity and normalized to 1. This represents a full average over the course of the entire bloom in all four levels of oxidative aging.

During the 14-day phytoplankton bloom, we detected 584 unique oxidized organic components in SMA. Molecular formulas were matched with a 10 ppm tolerance to the nearest formula generated via iterative peak finding in TofWare, as described in Stark *et al.* 2015.[235]

Bulk molecular composition is displayed in **Figure 6.7,** where panels a) and d) plot qualitative (count) and semiquantitative (relative abundance) distributions in positive

mode, panels b) and e) in negative mode, and panels c) and f) show an average of the two. The most comparable investigation of SMA to ours is Siegel *et al.* 2021[422], which analyzed filter samples of collected Arctic aerosol with a large contribution from SMA. They note that the method used, FIGAERO-CIMS, is less efficient at ionizing primary SSA.[422] This method has also been shown separately to detect oxidized SOA compounds similarly to EESI.[263] Direct comparisons will be made below.

Across both methods of ionization, most detected compounds were oxidized hydrocarbons (64% CHO) with significant contributions from nitrogen (32% CHON) and sulfur (5% CHOS) containing organic compounds. As expected, the negative ionization mode was more sensitive to sulfur-containing compounds, and the positive mode was more sensitive to nitrogen-containing compounds. Assuming a uniform sensitivity, weighing the background subtracted intensity to the peak list strengthens the non-heteroatom organic signal (76%) relative to nitrogen-containing (23%) and sulfur-containing (1%) compounds. Siegal[422] observed an average of 66% CHO, 30% CHON, and 2% CHOS, demonstrating that our techniques and samples were similar at this level of compositional detail. A direct comparison can be found in **Table 5.1.**

**Table 5.1** Distribution of CHO, CHON, and CHOS compounds in this work as well as Siegal *et al*. 2021.

| | CHO | CHON | CHOS |
|---|---|---|---|
| This work, # | 64% | 32% | 5% |
| This work, I | 76% | 23% | 1% |
| Siegal[422] I | 66% | 30% | 2% |

Plotting these peaks as a function of carbon number reveals a distribution around carbon #'s 5 and 10, which is strengthened by weighing by intensity. This suggests the potential contribution of isoprene ($C_5H_8$) and monoterpene ($C_{10}H_{16}$) oxidation products[423,424], which typically maintain the carbon backbone ($C_5$ and $C_{10}$) or fragment into slightly smaller compounds ($C_{3\text{-}4}$ and $C_{7\text{-}9}$.) Notably, Siegal also saw elevated abundance at carbon numbers 5 and 10, as well as 8.

### 5.4.5. Differential detection of organic compounds in negative and positive modes

Plotting compounds on a 2-dimensional Volatility Basis Set (2-D VBS) with oxidation state on the y-axis and volatility (saturation vapor pressure, $\log_{10} C^0$) on the x-axis allows for the observation of a photooxidation trajectory, where precursor compounds become more oxidized and less volatile when undergoing photooxidation.[259–261] We use the parameterization by Li *et al.*[264], which includes volatility contributions from sulfur and nitrogen atoms, to calculate the estimated $C^0$ for each detected compound. We then plot the intensity-weighted average for each data point (four levels of oxidative exposure per sampling day) in **Figure 5.8**.

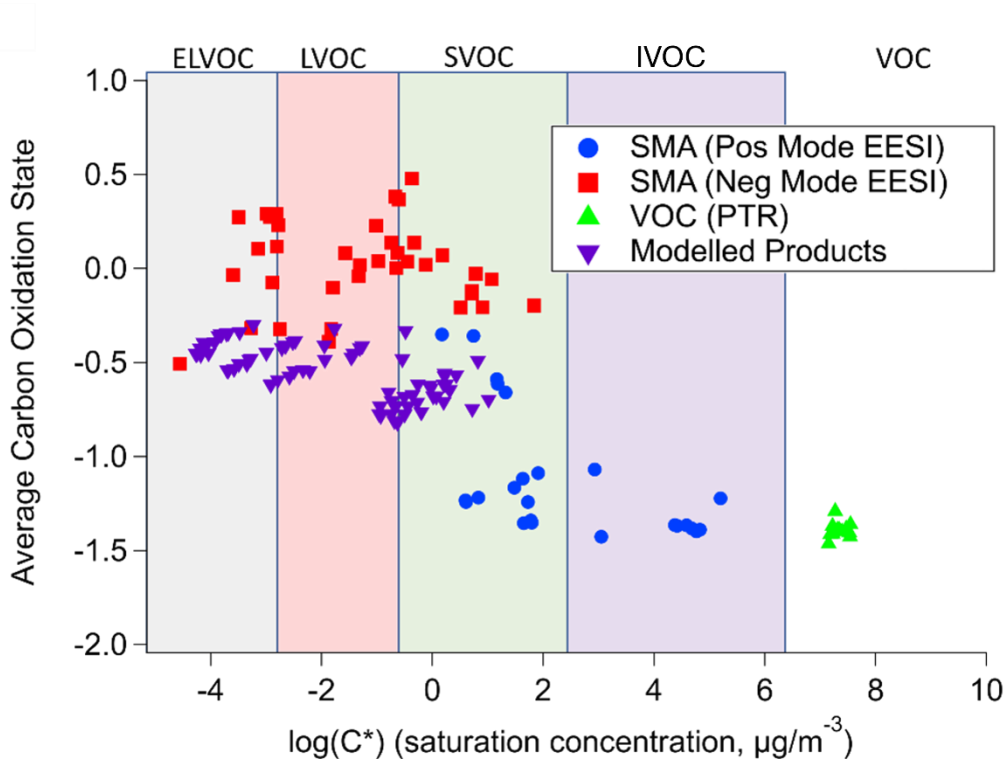


**Figure 5.8** 2-D volatility basis set showing bulk organic properties of precursor gases (green), their modeled aerosol-phase oxidation products (purple), and organic components of SMA measured by EESI in positive (blue) and negative (red) modes.

This visualization shows distinct distributions of organic compounds in volatility space depending on the ionization method. In EESI-MS(+), there was a distinct grouping of carbon-containing compounds in the intermediate (IVOC) and semi-volatile (SVOC) ranges, indicating that this ionization scheme is more selective of compounds in this volatility range. Due to their relatively low but greater carbon oxidation states than the VOCs measured by the PTR-ToF-MS, these components could be early oxidation products or fragments of lower-volatility products. This is expected, as the ionization scheme ($Na^+$ clustering) in positive mode is sensitive to organic compounds with alcohol and carbonyl (aldehydes and ketones) functionalities. In contrast, the ionization scheme in negative mode (deprotonation) detected more oxidized (-

$0.5 \leq OS_C \leq 0.5$) products spanning semi-volatile to extremely low volatile compounds. Such components may be highly oxygenated (HOMs) and acidic compounds, including carboxylic acids, organo-sulfates, and nitrates, likely more persistent to further oxidation and evaporation.[261]

We also plot the output of our F0AM model of isoprene, monoterpene & DMS oxidation for comparison (in purple.) We estimate the fraction of each compound present in the aerosol phase by adjusting the output concentration of each compound with its estimated aerosol partitioning coefficient, φ.[79] This output occupies the same volatility space as compounds measured in negative mode, although with a lower carbon oxidation state. The larger carbon oxidation state measured with the EESI-MS compared to the box model output suggests that either other non-isoprene or non-monoterpene VOCs were present or that additional oxidation reactions in the gas phase (e.g., autooxidation) and particle phase (e.g., organo-sulfate, hydrolysis, or reactions between oxidized intermediates including $RO_2\cdot$ + $RO_2\cdot$ interactions) occurred but could not be modeled.

Compared to other SOA oxidation pathways,[261] the components in SMA measured here in volatility space follow an intermediary path resembling that of a mixture of biogenic SOA from highly volatile compounds and anthropogenic SOA from semi- and intermediately volatile compounds. This is primarily driven by the presence of heteroatoms observed in SMA, which shifts the volatility of observed species to the left (lower volatility) and upwards (higher carbon oxidation state).

### 5.4.6. Organic carbon number is driven by precursor gas speciation

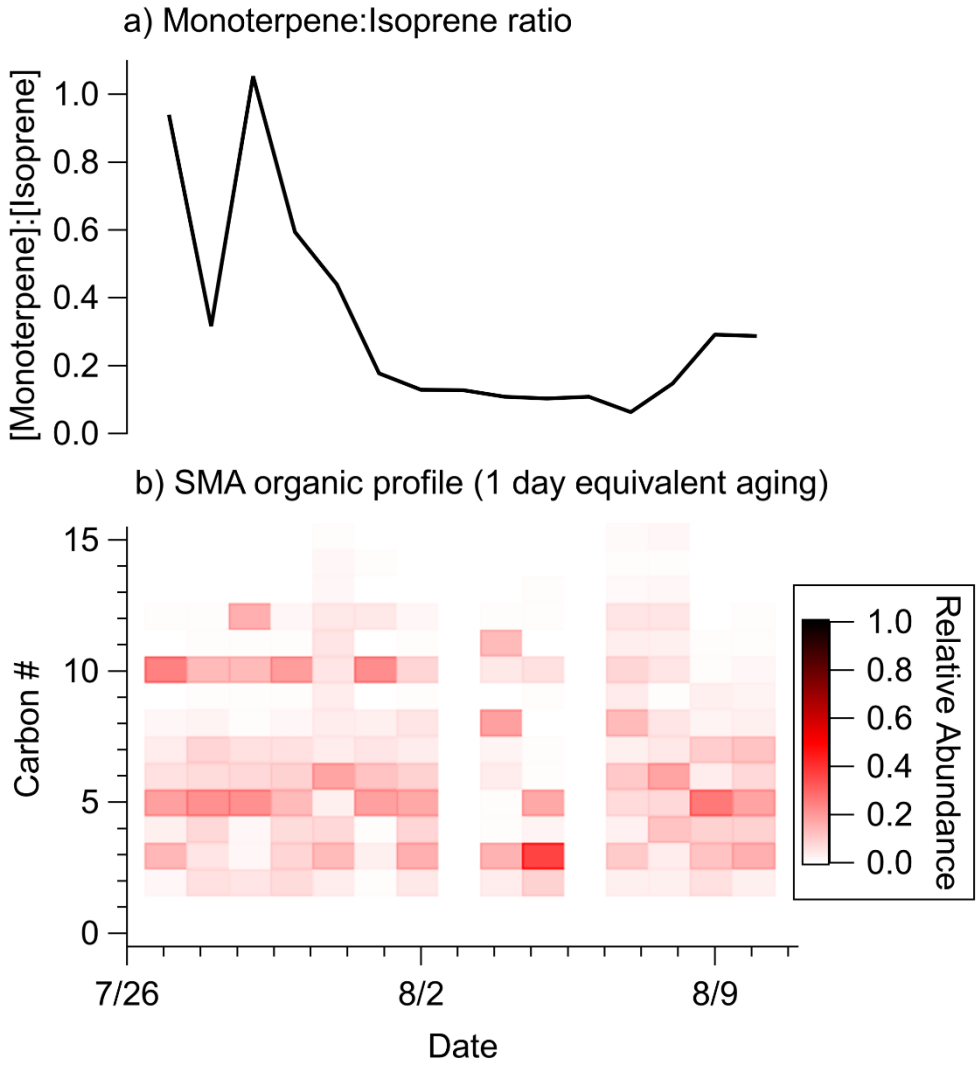


**Figure 5.9** a) time series of monoterpene: isoprene ratio. b) heat map of carbon number distribution throughout the study. All columns add to 1 relative abundance.

The ratio between monoterpene and isoprene concentrations steadily decreased throughout the bloom, as shown in **Figure 5.9a.** Concurrently, the profile of the SMA organic species measured by EESI-MS generally shifted from larger to lower carbon numbers, as shown in **Figure 5.9b**. Between 7/27 and 8/1, the relative abundances of $C_{10}$ and $C_5$ organic compounds measured by EESI-MS when $[C_{10}H_{16}]/[C_5H_8]$ was between 0.5 and 1.0 were greater than those between 8/2 and 8/7 when

$[C_{10}H_{16}]/[C_5H_8]<0.2$. After 8/2, the relative abundances of aerosol-phase organic compounds with a $C_{10}$ backbone never exceeded 0.2. In contrast, $C_3$-$C_5$ compounds were elevated during this period following the bloom's peak.

### 5.4.7. Organosulfur formation

Organosulfur abundance, measured as a percentage of the total organic signal, increased slightly with increasing oxidative exposure, as shown in **Figure 5.10a**. This is explained by increased $SO_2$ gas generated from oxidized DMS at higher exposures, leading to increased particulate sulfate (**Fig. 5.10b**) and gaseous $SO_2$, which may react with organics to form organosulfur compounds.[392,395,399]

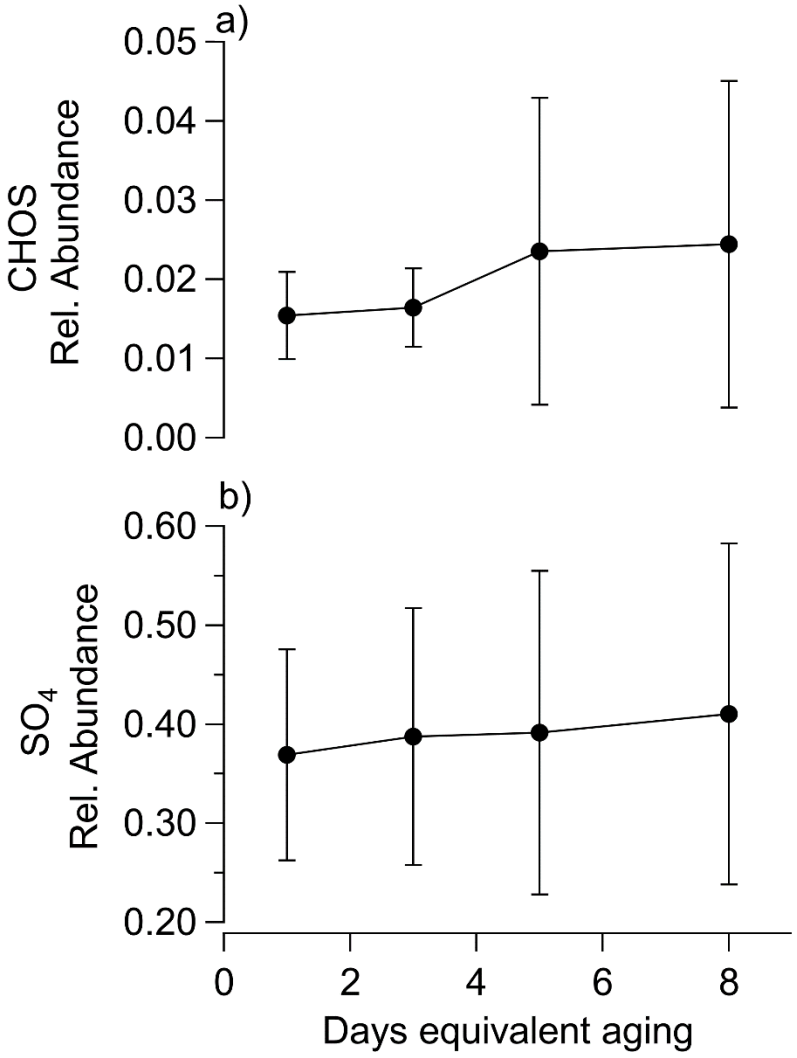


**Figure 5.10** Relative abundance of a) sulfur-containing oxidized organics (CHOS) and b) $SO_4$ as a function of oxidative aging. Error bars represent the standard deviation between different days of the bloom used for each average.

A time series of CHOS and MSA relative abundance compared to DMS concentrations is plotted in **Figure 5.11.** While there is a general increase in CHOS over time, the lack of negative mode analysis during the peak of the bloom makes any direct correlation weak and difficult to constrain. This is expected, as the abundance of CHOS components is not related solely to the oxidation of DMS but also to the availability of other organic compounds that may interact with $SO_4$ to make CHOS species. However,

a slight, statistically insignificant correlation ($R^2$=0.47, p=0.09) exists between DMS and MSA (see **Fig 5.12.**) Interestingly, the detection frequency of particulate MSA decreased with oxidative exposure from 75% at one day of equivalent aging to 38% at eight days of equivalent aging. The hydroxyl radical can further oxidize particulate MSA to produce sulfite radicals, which contribute to the production of organo-sulfates.[425]

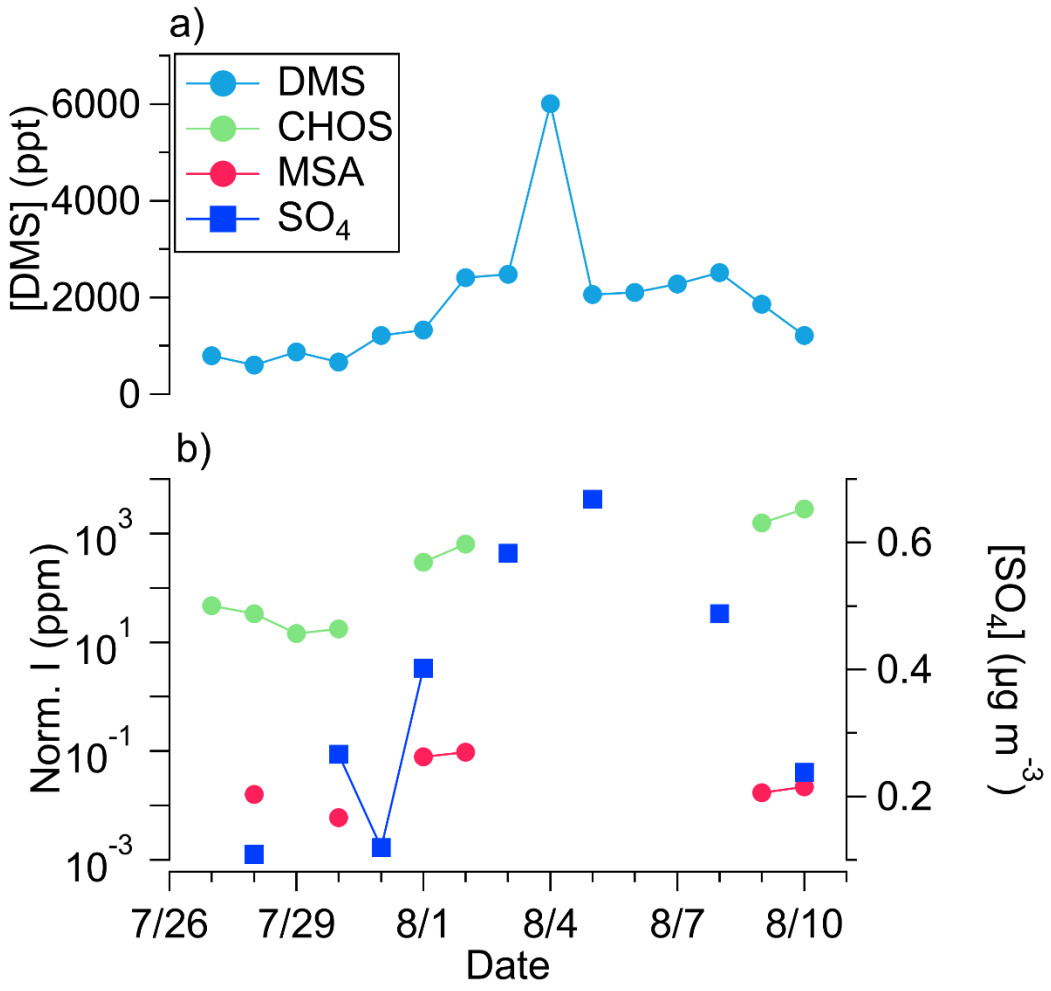


**Figure 5.11** Time series of a) gas-phase DMS concentrations and b) aerosol-phase CHOS, MSA, and $SO_4$ concentrations throughout the bloom.

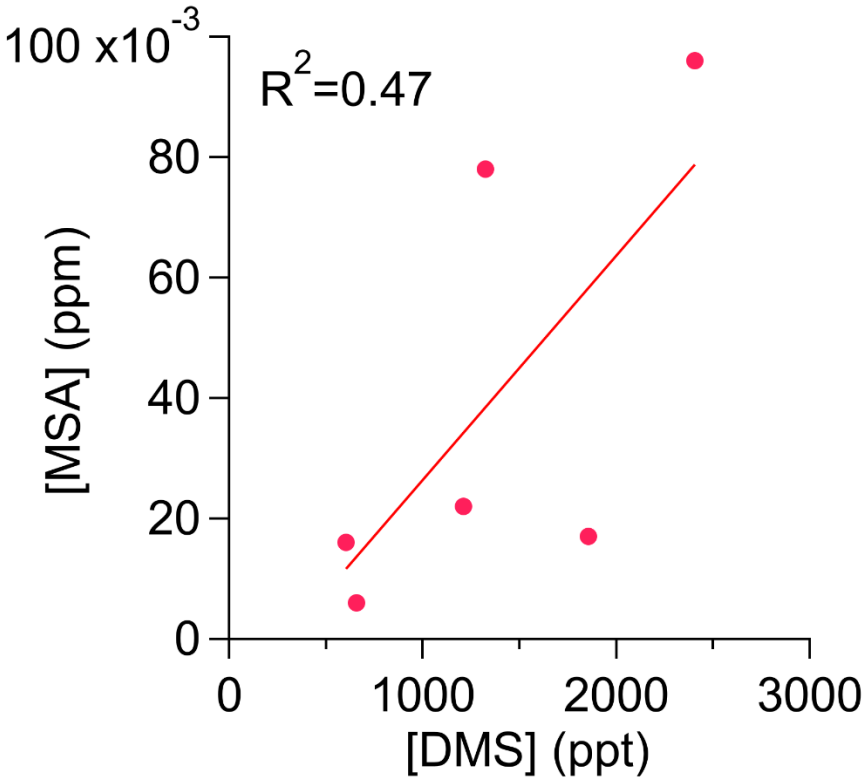


**Figure 5.12.** Correlation between aerosol-phase MSA concentrations and gas-phase DMS concentrations.

### 5.4.8. Organonitrogen formation

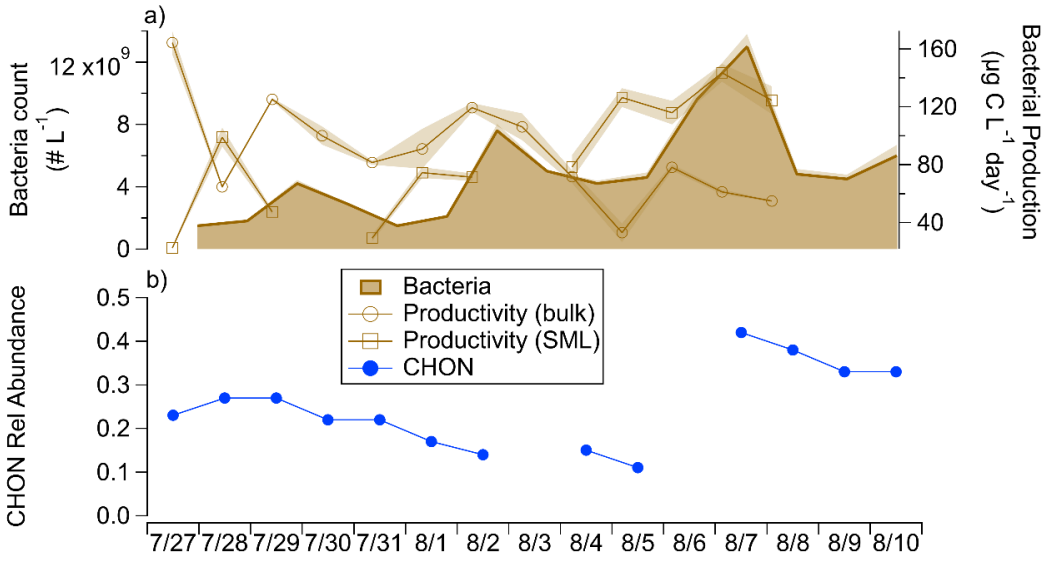


**Figure 5.13** Time series of a) bacteria counts and productivity and b) CHON species relative abundance throughout the bloom.

Higher relative amounts of nitrogen-containing organic species were detected during the early and late stages of the bloom, correlating with areas of increased bacterial production following the death of phytoplankton (see **Fig 5.13**). The first die-off followed the transport, filtration, and temperature adjustment-related stress of moving the body of water from the ocean into the laboratory, and the second from the crash of the phytoplankton bloom.[148] During periods of high bacterial production, processing of larger biomolecules into smaller reduced nitrogen species such as alkyl amines occurs, which have been shown to contribute to new particle formation.[174,175] We did not observe any direct linear correlations between CHON abundance and any markers of bacterial abundance and productivity. However, CHON abundance was greatest during and following the peak abundance in bacteria on 8/7.

### 5.5. Atmospheric implications

The results presented in this work provide a comprehensive yet preliminary analysis of the complex SMA organic profile with EESI-MS, the first time this instrument has been utilized to measure the composition of SMA. Specifically, during high biological activity and biogenic VOC release periods, increased amounts of sulfur—and nitrogen-containing compounds lead to lower volatility oxidation products, promoting SMA growth.

Phytoplankton bloom cycles control the DMS budget, which controls the general sulfur budget in the marine atmosphere, especially as coastal pollution levels fall. The source of the large amounts of nitrogen measured in SMA was not conclusively identified but may originate from alkyl amines[154,155,174,178] or other marine nitrogen-

containing gases like HONO.[426] Further study is required to isolate the impact of these potentially important species.

As studied here, the decrease in organic aerosol yields with increasing oxidative exposure observed in our study suggests a conversion from mixed organic-inorganic aerosols to predominantly inorganic aerosol surrounding areas of high biological activity. As inorganic aerosols serve as more efficient cloud nuclei[149,186], these results give evidence to the CLAW hypothesis[153] in which marine phytoplankton emissions may serve as a negative feedback loop in a warming world. However, this generation was done in the absence of SSA. Other work from SeaSCAPE, which oxidized the same mix of marine VOCs in the presence of SSA, observed a significant accumulation of new organic mass onto existing SSA particles.[427] Therefore, our simulation of SMA is likely more representative of a marine airmass with high biological activity and low SSA generation, such as an Arctic phytoplankton bloom under low wind conditions.

This study represents the first time EESI-TOF MS has been used to measure secondary marine aerosol. Our results highlight its strength in providing online measurements of bulk organic properties. Additionally, we demonstrated that specific ion chemistries are more adept at probing different portions of SMA. Specifically, positive mode ($Na^+$ clustering) ionization measured early oxidation products and SVOC-IVOCs, and negative mode (dehydrogenation) favored more oxidized organics, organosulfur compounds, and ELVOCs-SVOCs. Further development in EESI ionization schemes and coupling EESI sources to higher-resolution mass spectrometers[428] will further increase its efficacy for the online characterization of organic aerosol.

**5.6. Acknowledgements**

I would like to acknowledge the entire SeaSCAPE team, including undergraduate researchers ZY Lin and Isaac Canada, who assisted with this project. Chapter 5, in full, is currently being prepared for submission for publication of the material as it may appear in *Atmospheric Chemistry & Physics*, Cooper, A, Shenkiryk, A, Morris, M, Chin, H, Mehndiratta, L, Roundtree, K, Tafuri, M, Slade, J.H. The dissertation author was the primary investigator and author of this paper.

# Chapter 6 Policy Implications

Section 6.1. reproduces the publication “We Need a “Keeling Curve” Approach for Contaminants of Emerging Concern” by Cooper et al., 2023, in *Environ. Sci. Technol.* This manuscript has been published with open access under license CC-BY 4.0.

## 6.1. Action on monitoring contaminants of emerging concern

### 6.1.1. We need a “Keeling Curve” approach for contaminants of emerging concern

Several chemical and particulate species have been designated as contaminants of emerging concern (CECs) due to their persistence in the environment, detrimental effects on human health and ecosystems, and lack of current regulations. According to the definitions provided by the US Environmental Protection Agency (EPA) and the United Nations Environmental Programme (UNEP), CECs encompass various substances, including industrial additives such as per- and polyfluoroalkyl substances (PFAS), pharmaceuticals and personal care products (PPCPs), as well as microplastics.[16] These CECs have been detected around the globe in previously pristine environments that were once considered untouched by human influence, such as remote high-elevation mountain areas, Arctic air, snowpack, and the open ocean.[16,27] Like greenhouse gases, CECs pose a pervasive threat to all regions of the world.

Monitoring the levels of CECs in the air, land, and water is challenging due to a lack of standardized methodology for collection and analysis and uncertainty surrounding the effectiveness of regulations. Thus, a crucial question is raised: is the current approach, which relies on non-standardized measurements and reporting of CECs, effective in gaining widespread public support for reduction targets? Without clear indications that such policies are leading to reduced presence of CECs, we must

consider the need for standardization. In this viewpoint, we contend that the standardization of methodologies and consistent reporting of CEC concentrations over time, both at a single reference measurement site and across different environmental compartments, will be essential in comprehending the science behind CECs in the environment and guiding future policy decisions.

### 6.1.2. Historical precedence

The challenges of method standardization and policy action to reduce CEC concentrations can be likened to the historical challenge of measuring and reporting global atmospheric carbon dioxide (CO2) concentrations, a greenhouse gas, before the establishment of the renowned Keeling Curve in the 1950s.[429] This curve graphically displays the long-term increase and seasonal variations of $CO_2$ in the atmosphere. Prior to the Keeling Curve, measurements of $CO_2$ were conducted inconsistently using various analytical techniques and locations, resulting in less reliable data for monitoring global averages and trends over time. The creation of the curve and its effectiveness in promoting international collaboration on climate policy was based on two fundamental principles: (1) the development and widespread adoption of a single instrument, the gas manometer, and (2) the meticulous selection of a reference measurement site.

### 6.1.3. Policy recommendations

We demonstrate how the principles that underpinned the construction of the Keeling Curve and its ongoing success in fostering international collaboration can be applied to the monitoring, reporting, and implementation of policies concerning CECs. To draw a parallel, we focus on the pressing issue of airborne microplastic pollution, which serves as a representative CEC found in all environmental compartments. Microplastics are a prominent topic leading up to the anticipated UN Plastics Treaty

scheduled for 2024, which aims to establish a legally binding agreement to "End Plastic Pollution."[430]

Various techniques are currently employed to analyze microplastic particles in the air. Some rely on single-particle counting paired with spectroscopic techniques to identify plastic chemical signatures; however, these often have a limited size resolution. Conversely, promising methods can quantify the constituent polymers of the plastic in near real-time, with detection capabilities down to the picogram level. These techniques differ in physical and chemical resolution and are inconsistently applied across different monitoring sites.

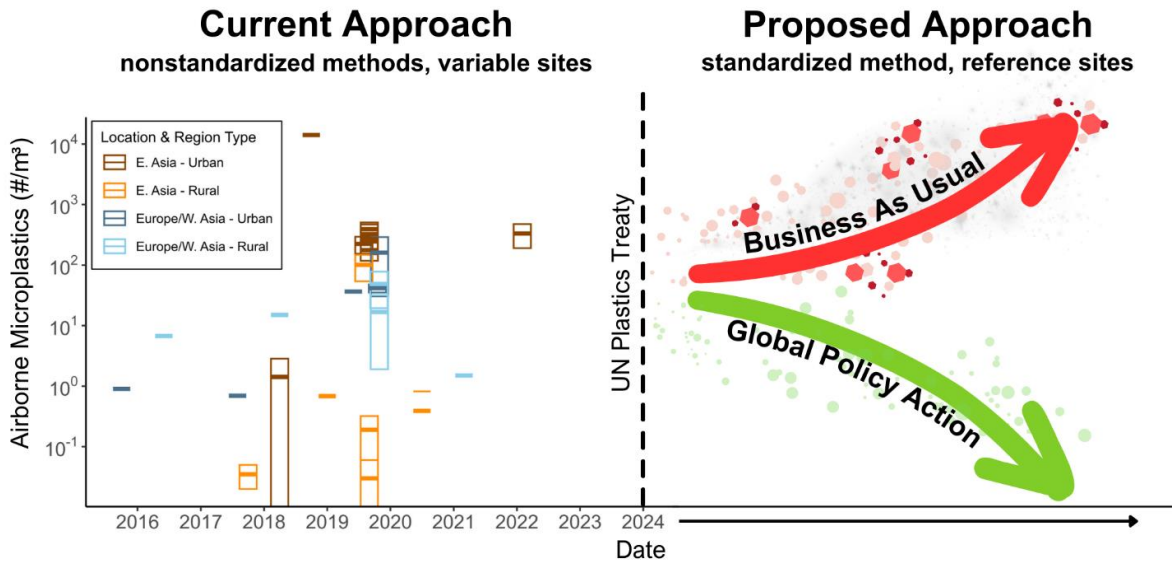


**Figure 6.1** Illustration demonstrating challenges in interpreting global trends of contaminants of emerging concern (CECs) concentrations based on current monitoring approaches, using airborne microplastics as a representative example. Number concentrations of airborne microplastics over time, as currently analyzed using various methods and measurement sites (left).[280,431–437] Anticipated outcomes using a standardized method at a reference measurement site (right). The red arrow represents an expected upward trend in airborne microplastic concentration if the 2024 UN Plastics Treaty is unsuccessful, while the green line represents an expected downward trend if the treaty succeeds.

There are limitations to using different techniques when quantifying airborne microplastics over time (**Figure 6.1**). Due to the lack of consistent measurements, there are no discernible trends over time, and there is significant variability within and between rural and urban locations. Similar graphs can be constructed for other microplastics and CECs measured in different environmental compartments. Thus, implementing a live and continuously updated graph that charts the concentrations of airborne microplastics over time, akin to the iconic Keeling Curve for $CO_2$, holds significant potential as a powerful tool in addressing the issue of microplastic pollution. This proposed solution, applicable to all CECs, consists of two critical steps that mirror the principles the Keeling Curve was founded on: (1) the adoption of a standardized technique for continuous online monitoring and (2) the identification of a representative measurement site, similar to the Mauna Loa observatory for monitoring $CO_2$, and the creation of a global sampling map that acknowledges regional variability. This is crucial as microplastics and other CECs are not as long-lived or uniformly distributed in the environment as greenhouse gases like $CO_2$. One such potential measurement site for airborne microplastics is the Pic du Midi observatory in the pristine French Pyrenees, which experiences the impact of intercontinental transport of airborne microplastics.[438] Additionally, dedicated networks like the US EPA's National Air Toxics Trends Sites (NATTS) have consistently monitored hazardous air pollutants in the US since their establishment in 2003. Similar networks and reference sites should be established to monitor CECs in terrestrial, atmospheric, and aquatic environments.

Although no single technique can unambiguously identify and quantify all CECs in various environmental compartments, the international scientific community must

reach a consensus on a standardized technique suitable for specific CECs and matrices. For airborne microplastics, techniques that directly quantify the constituent polymers in a mass-based format, eliminating biases in counting techniques, would reduce human error and particle count inflation caused by plastic breakdown in the environment. Moreover, these techniques would allow for the timely dissemination of a large volume of results. This standardized approach will ensure accurate and verified comparisons between measurements over time and enable tracking progress in reducing the presence of CECs in the environment. Such trends can be illustrated to assess the efficacy of policy action, as shown for airborne microplastics in **Figure 6.1**.

Persistent environmental contaminants of emerging concern (CECs), such as plastic, which is widely used in daily life, can endure for hundreds of years or even indefinitely.[439] Given this sobering reality, it becomes crucial to meticulously measure their background concentrations across all environmental compartments in a standardized manner to grasp the long-lasting effects of such pollution fully.

The development of a standardized and easily understandable graph, similar to the Keeling Curve, has the potential to serve as a powerful catalyst for global action against CECs. By taking these necessary steps, we can provide stakeholders with a clear and comprehensive roadmap to track progress toward policy objectives. Such a graph has the potential to inspire international collaboration as an effective response to this pressing issue.

## 6.2. Action on the Tijuana River Valley Sewage Crisis

### 6.2.1 Background and history

The Tijuana River has been a source of sewage and other pollutants for almost a century. Still, the causes of this transboundary environmental crisis have roots that

stretch back far longer.[440,441] The Kumeyaay were the original inhabitants of the San Diego-Tijuana region for more than 12,000 years. They led resistance to settler occupation throughout Spanish and Mexican rule and the early part of U.S. rule. Spanish settlers established the San Diego Mission (1769-1821), followed by Mexican rule (1821-1848). After the Mexican-American War of 1848, a new border line was drawn an arbitrary distance south of San Diego, turning the small town into an important port and border city.

Beginning in the 1880s, the San Diego region boomed as an important military base and port, eventually becoming the eighth largest city in the U.S. Tijuana grew alongside it, eventually becoming the fifth largest city in Mexico.[442] The San Diego-Tijuana border remains the most frequently crossed border in the world. American capital and tourists cross south into Tijuana, while Mexican labor crosses north. Due to Tijuana's leading industries (tourism and manufacturing) being linked to Californian population growth and foreign investment by manufacturing companies, the infrastructure of Tijuana, including its wastewater treatment systems, considerably lagged its population explosion accelerated by San Diego's growth.

In 1935, San Diego first collaborated with Tijuana in constructing a sewage outflow pipe that brought Tijuana's sewage into the Pacific Ocean just north of the border—this year also marked the formation of the International Boundary Water Commission. This outflow pipe initially resolved the issue, but from the 1930s to the 1960s, Tijuana boomed from 16,000 people to more than 340,000. San Diego offered to connect Tijuana to its wastewater system in 1958, but Tijuana decided to construct their own. The industrial boom in Tijuana, primarily from American and Asian companies,

accelerated Tijuana's growth, quickly overwhelming this new system. As Tijuana continues to grow, industrial and wastewater pollution continues to flow northwards in the Tijuana River.

Modern efforts to address the cross-boundary sewage crisis included the construction of the International Treatment Plant (ITP) in 1997. See **Figure 6.2** for a map of sewage and Tijuana River Flows. The ITP processes a portion of the raw sewage produced by Tijuana, while another portion is treated by the San Antonio de los Buenos (SAB) treatment plant. Due to disrepair, this portion is functionally untreated, leading to a steady release of raw sewage six miles south of the border. At every point along this sewage system, leaky pipes release raw sewage into the Tijuana River. Due to Tijuana's shared wastewater/stormwater system, every time a moderate amount of rain falls, wastewater plants cease to operate, and all raw sewage is released into the Tijuana River. During the summer, when the Tijuana River flows slowly or not at all, a pump processes a portion of the river (currently 25 million gallons per day.)

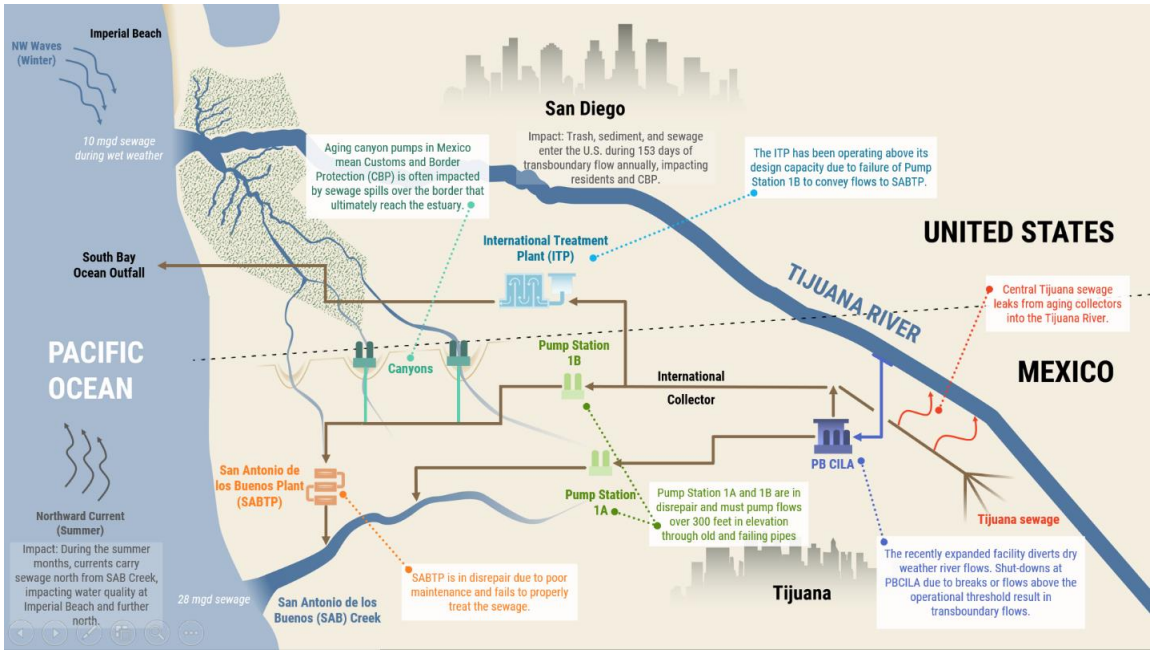


**Figure 6.2** Tijuana wastewater and river flow schematic. Adapted from EPA's "USMCA Tijuana River Watershed" webpage.[115]

Despite decades of seemingly little progress, some hope was restored in 2018 with the free trade agreement negotiations between the U.S., Mexico & Canada (USMCA.) The USMCA directed the Environmental Protection Agency (EPA) to commit $300 million to infrastructure solutions to the cross-boundary sewage crisis. This significant financial commitment prompted the EPA to review infrastructure options to address the sewage crisis comprehensively. They began stakeholder engagement with eligible public entities as well as community groups. The following section is a personal recount of this process from the community's point of view.

### 6.2.2. Personal Narrative: Clean TRV Now!

During the summer of 2021, the Tijuana River was constantly in my thoughts. A year after the field campaign investigating pollution transfer along the San Diego Coast, detailed in **Chapter 3**, we finally thawed the samples and conducted LCMS analysis in

Spring 2021. Through NSF-CAICE's summer undergraduate research program (SURP,) I mentored Katy Belcher, an undergraduate researcher from the University of Michigan, in annotating the nontargeted output of our analysis.

I was also in an intensive period of development in my role as a community organizer. One year after the summer uprisings following the murder of George Floyd, I had become a leader within the Sunrise Movement (the youth movement that helped elect President Joe Biden, pass the Inflation Reduction Act, and create the Civilian Climate Corps.) I had just finished a 70-mile, four-day march carrying the ashes of a home in Paradise, California, to Speaker Pelosi and Senator Feinstein's front doors to win their support for a Civilian Climate Corps in President Biden's Build Back Better bill.

In early July, my organizing mentor and friend, Ido Shoshani, pointed out an upcoming community-led cleanup in the Tijuana River Valley. Little did I know this would be the first step of a campaign that would challenge my skills in new ways and firmly ground me in my career path toward working at the intersection of environmental justice and science policy. The full timeline of events is listed below in **Figure 6.3**. This community-led initiative was a crucial step in our journey towards a cleaner Tijuana River Valley, highlighting the importance of grassroots efforts in addressing environmental issues.


**Figure 6.3** Timeline of events for the "Clean TRV Now" campaign.

I met Victoria Abrenica, founder of the Spring Valley Cleanup Crew and coordinator of the “Clean TRV Now” campaign that I helped to codevelop during that summer and fall. I felt my worlds collide. I was standing in the sewage-contaminated trash, explaining the early preliminary findings of my research and seeing the dedication of young volunteers put in the effort to address a crisis that decades of government neglect had caused. This work is the work of the government, and I linked the jobs that needed doing to our campaign for a Civilian Climate Corps. I led my first rally the week after going to that first clean-up to call on Senator Feinstein to support a Civilian Climate Corps. In the organizing world, a common saying is “Direct Action gets the goods.” Immediately after our protest, we met with her senior staff to pitch the benefits of the Civilian Climate Corps. We linked it to her office’s work in securing Federal money for the Tijuana River Valley Crisis.

This pattern repeats in a typical “escalation arc.” A campaign has three phrases that repeat themselves on a short (weekly) and long (yearly) cycle: Building Support, Escalating Pressure, and Negotiating a Win. SVCC’s cleanups helped to build broad awareness and support by bringing together a coalition of organizations and everyday people to the frontlines of the crisis.

Rallies and protests escalated pressure by pointing at a specific target and issuing a particular demand. We wanted the EPA to choose their most comprehensive solution to the TRV crisis, costing ~$600M, more than double the allocated $300M from USMCA. We wanted our federal representatives to “Double the Budget” –appropriate an additional $300M from the federal budget to fund the EPA fully. We wanted our local

representatives to “Close the Campground” – a newly built collection of yurts and campsites near the sewage flow.

We met with the EPA, the staff of Borderfield State Park, U.S. Senator Feinstein’s office, and Vice Chair of the San Diego County Board of Supervisors Nora Vargas. We brought stories of impacted Imperial Beach residents, insights from our scientific inquiries, and ideas on how to address the crisis holistically (see the following section.) This wasn’t easy – it took months of work, outside pressure from the campaign, and internal politics from Victoria (who was Vargas’ constituent and an elected Democratic official sitting on multiple boards and committees.) To academics privileged with access to elected officials, I recommend sharing that access with frontline communities who often are not consulted during our research or heard by our elected officials.

By building momentum through recruitment via cleanups, escalation via protests, and negotiation via meetings, we found both successes and roadblocks. The EPA chose the comprehensive solution in 2021, but in 2024, the extra funding has still not been allocated. Indeed, the vast majority of the initial $300M has not been spent or assigned to specific projects. The Civilian Climate Corps became the American Climate Corps, which President Biden formed in September 2023, with the first 9000 young workers sworn in June 2024.[443] The Tijuana River Valley Regional Park Campground was never closed, and signage was never placed on the website or in the location to alert campers of their increased exposure to pollutants.

### 6.2.3. Policy recommendations

As this dissertation is being written in June 2024, the Tijuana River Valley is a declared environmental and public health crisis in the County of San Diego. However,

despite the efforts of local leaders, an emergency declaration is still lacking at the State and Federal levels.[444] So far, in addition to the $300M promised in 2020 and transferred in 2022, $100M of emergency funding has been granted in FY 2024.[445] This funding was to make emergency repairs to the plant in preparation for the ~$600M comprehensive plan, which remains half-funded. The following policy recommendations would help meet the challenges of the Tijuana River crisis:

1. *Declare a federal state of emergency*

Following the leadership of impacted residents, local elected officials, and San Diego's congressional delegation, California and the United States should declare a state of emergency in the Tijuana River Valley and Southern San Diego to unlock additional and expedited funding mechanisms and support from Federal Agencies.

2. *Form the Tijuana River Public Health and Water Quality Restoration Program*

In current negotiations around the 2024 National Defense Authorization Act (NDAA,) the San Diego Congressional Delegation (Reps. Vargas, Peters, Jacobs, and Levin) have introduced an amendment to form the "Tijuana River Public Health and Water Quality Restoration Program."

Federal programs are congressional directives to dedicate Federal Agency funding and staff hours to collaborative projects. This would increase inter-agency collaboration and provide a mechanism for continued policy development across the Federal government.

3. *Negotiate a bilateral agreement to build a modern sewer system for Tijuana*

Ultimately, even the EPA's comprehensive solution has significant shortcomings. A treatment plant with the volume capacity to treat an entire river during periods of heavy precipitation is not feasible. Tijuana, which has grown in response to the U.S.-Mexico

border, should be treated equitably as San Diego's twin city, which provides significant economic and cultural inputs into the United States. Building a comprehensive sewer system is not simple and would likely take billions of dollars over a decade.[440,442] However, only a modern sewer system will fully respond to the Tijuana River Valley crisis and make the diversion and treatment of the Tijuana River obsolete.

*4. Invest in the public health of impacted residents*

The ultimate responsibility of governments is the health and well-being of the residents it represents. The County of San Diego declared a public health crisis, but it is still poorly understood. Long-term health monitoring studies are currently being implemented and should be well supported. Any findings of environmental damage to public health should lead to additional funding for healthcare to be allotted to impacted residents. The Social Security Act has a sparingly used provision that allows for the granting of free healthcare to residents affected by environmental crises.[446] This provision should be used more generally, especially in the impacted regions of Imperial Beach and along San Diego's Southern Coast.

As with all ambitious policy proposals, the actions outlined here have actual costs that must be weighed against other uses of funding and agency labor. However, this crisis deserves the utmost attention and more support than is currently being provided.

## 6.3. Action on sunscreen pollution

### 6.3.1 History of regulatory action

Reducing the impacts of plastic pollution is a priority for the general public.[447,448] Regulation can expedite the removal of plastic pollution and harmful chemicals like UV filters from the marketplace. Rapid environmental policy has historically successfully reversed the widespread use of chemicals, such as

coolants, in refrigerators regulated by the Montreal Protocol.[449] Following suit, society can decrease damage to marine environments and humans by drastically reducing the production and environmental input of micro(nano)plastics and UV filters.

Various regulatory approaches, shown in **Table 6.1**, have been utilized to reduce organic UV filter pollution by banning certain substances or implementing better safeguards against their release into the environment. United States jurisdictions such as the US Virgin Islands, the State of Hawaii, Key West, FL, and the Northern Mariana Islands have banned octinoxate and oxybenzone.[96,450–452] Legislation in Hawaii to expand the list of banned substances to octocrylene and avobenzone failed to pass. Other countries have more expansive lists of banned UV filters, including Palau (11 UV filters)[98] and the Marshal Islands (25 UV filters and ten preservative ingredients.)[453]

**Table 6.1** Current and proposed legislation on organic UV filters

| Year/Location/Bill Title | Summary |
|---|---|
| 2014/USA/Sunscreen Innovation Act[454] | "Amends the Federal Food, Drug, and Cosmetic Act to establish a process for the review and approval of over-the-counter (OTC) sunscreen active ingredients." |
| 2018/Hawaii, USA/SB 2571: Relating to Water Pollution. [450] | "Beginning January 1, 2021, bans the sale, offer of sale, or distribution in the State of any sunscreen that contains oxybenzone or octinoxate, or both, without a prescription issued by a licensed healthcare provider to preserve marine ecosystems. " |
| 2018/Aruba/AB2019 no.67[455] | "The Ministry of Spatial Development, Infrastructure, and Environment presented a law concept that prohibits the use of some products that are harmful to the environment in Aruba," including oxybenzone-containing sunblock. |

**Table 6.2** Current and proposed legislation on organic UV filters (Continued)

| | |
|---|---|
| 2018/Palau/Responsible Tourism Education Act[31] | "No reef-toxic sunscreen shall be manufactured or imported for sale... sold in the Republic ... no person shall bring a reef-toxic sunscreen on or after January 1, 2020." |
| 2019/US Virgin Islands/Act No. 8185[27] | "A ban on the retail sale or offer for sale, and the distribution or importation for retail purposes of topical sunscreen products containing [octocrylene,] oxybenzone and octinoxate." |
| 2019/Marshall Islands/ Safe Sunscreen Act[30] | "Prohibition on the sale, importation, and distribution of sunscreen products containing certain chemical ingredients." This law covers 25 chemical UV filters, including octinoxate, oxybenzone, octocrylene, and ten chemical preservatives. |

**Table 6.3** Current and proposed legislation on organic UV filters (Continued)

| | |
|---|---|
| 2020/Northern Mariana Islands, USA/HB No. 21-28[29] | "Beginning July 1, 2021, it shall be unlawful to sell, offer for sale, or distribute for sale any sunscreen that contains oxybenzone or octinoxate, or both, without a prescription issued by a licensed healthcare provider." |

These regulatory approaches are not always popular. The Florida state government later overruled the city of Key West's sunscreen ban. [456] Primarily, alternative sunscreens use titanium oxide and zinc oxide, which do not absorb but reflect incoming solar radiation. [53] However, these alternatives have been criticized as not providing complete UV protection, may serve as catalysts for oxidation in aquatic systems, and early inorganic UV filter sunscreen formulations led to undesired chalkiness.[457,458] This gap in safe products was brought to national attention in the US with the passage of the Sunscreen Innovation Act in 2014, which directed the FDA to streamline the approval process for new, potentially more benign, sunscreen agents.[454] However, this act was never thoroughly pursued. It was terminated by language in the 2020 Coronavirus Aid, Relief and Economic Security (CARES) Act alongside nullifying the reclassification of 15 organic UV filters as not proven safe.[95]

### 6.3.2 Policy recommendations

Given the past successes and failures of regulatory and marketplace approaches, we offer the following policy recommendations:

1. *Reintroduce and fiscally support efforts such as the Sunscreen Innovation Act to develop and test new organic UV filters*

The ban on unsafe UV filters is a pressing issue that necessitates the immediate development and rigorous testing of suitable replacements. Studies have shown promise in the efficacy of safer alternative inorganic UV filters and stabilizers, such as organic-inorganic hybrid structures.[457] These structures, composed of TiO2 nanoparticles grafted onto cellulose nanocrystals and hydroxyapatite and cerium dioxide, absorb a broad UV range and have been proven safe against degradation and skin erythema formation.[459] The development of modern high-throughput ecotoxicology assays for UV filters and other commodity chemicals should be a top priority for regulatory agencies.

2. *Phase out personal care products containing the most widely agreed-upon unsafe UV filters, namely octinoxate, oxybenzone, and octocrylene.*

This process would involve a gradual reduction in the production and sale of these products, accompanied by public education campaigns to inform consumers about the risks of these UV filters and the availability of safer alternatives. Given their toxicity and the alarming percentage of marine life, including phytoplankton and corals, affected, and the growing consensus of their toxicity to human development, personal care products containing octinoxate, oxybenzone, and octocrylene must

be phased out of production. This is a crucial step in protecting marine life and human health from the harmful effects of these UV filters.

3. *Include labels citing the dangers of organic UV filters in personal care products*

It is crucial that information on the dangers of everyday-use compounds, such as UV filters known to cause endocrine disruption and develop cancer, be quickly and succinctly labeled for public trust to be built in regulatory agencies. These labels should be part of existing lists such as California's "Safe Drinking Water and Toxic Enforcement Act of 1986," known widely as Prop 65, and should be prominently displayed on all personal care products containing these UV filters.[460] Similar lists should be available nationwide and in other countries. This will help promote public awareness and informed decision-making about personal care products, empowering individuals to make responsible choices for their health and the environment.

4. *Promote the use of less toxic mineral sunscreens*

Current legislation being debated in Hawaii would place free mineral sunscreen dispensers on state beaches to provide photoprotection for beachgoers and educate the public on the benefits of choosing mineral sunscreens to keep marine life safe.[461] Such signage should also include the health risks associated with toxic organic UV filters.

Implementing policy change concerning UV filters has historically been unpopular and complex, so additional research into the toxicity of established and newly developed UV filters will grant further insight into which are safe for use and

can be used as easily implemented alternatives. The difficulty surrounding UV filter bans is the lack of viable alternatives. Thus, future policy action must support the development of new UV filter chemicals with minimal toxicity and phase out the current harmful options. Until suitable alternatives emerge, public education around alternative means of sun protection (covering up, limiting exposure) must be prioritized. Ultimately, a cost-benefit analysis must be carefully considered before widespread bans occur.

### 6.4. Action on preserving phytoplankton populations

As demonstrated in **Chapter 5**, phytoplankton emissions play a critical role in producing SMA, which is expected to regulate Earth's radiative balance through a general cooling effect and direct and indirect albedo effects.[149,153] However, marine primary productivity has decreased by 50% since 1950, motivating concern that this crash can impact the food web and Earth's climate.[181] As discussed in the previous section, organic UV filters can exhibit ecotoxicological effects. Their interaction with another emerging contaminant- microplastics- may amplify their impact through synergistic toxicity.

#### 6.4.1 Ecotoxicology of individual & combined exposure to micro(nano)plastics & UV filters

Due to their position at the base of the marine food web, many studies looking at the impacts of micro(nano)plastics on marine organisms have focused on the impacts on various species of phytoplankton. Adverse effects on phytoplankton exposed to micro(nano)plastics were found, including reduced cell growth[462–464], increased levels of reactive oxygen species,[462,465] decreases in lipid content[466] and chlorophyll content.[467] However, most studies assessing the impact of micro(nano)plastics on phytoplankton use either small virgin microplastic beads (1-2 μm in size) or virgin nanoplastic beads

(40-500 nm in size). These commercially made beads allow for consistent experimentation; however, they may not reflect the most common polymer type, shape, or chemical additive concentrations of micro(nano)plastics in the environment. Many organic UV filters act as xenobiotics in marine communities and directly harm aquatic life.[48,91,339,342,468] Most research has focused on their impacts on coral reefs, with adverse effects such as coral bleaching, DNA damage, planula deformities, mortality, and skeletal endocrine disruption observed.[59,99,325,469] However, adverse effects of UV filters have also been documented in phytoplankton. Environmentally relevant concentrations (22.8ng/L) of BP3 were found to significantly reduce chlorophyll content in Chlorella sp. after 20 days,[112] with higher concentrations of BP3 (1000µg/L) reducing growth rate and chlorophyll content in Chlamydomonas reinhardtii within ten days.[106] Although UV filters are expected to be present in many micro(nano)plastics in the environment, no studies have assessed the combined toxic effects of micro(nano)plastics and UV filters on phytoplankton. Na et al., 2021[104] reports synergistic toxicity, where combined effects are more harmful than the sum of individual effects, in Daphnia magna, a freshwater zooplankton, following exposure to microplastic fragments with sorbed BP3. However, using virgin microplastics, Beiras *et al.* 2018[470] reported no toxic effects on marine zooplankton, even at higher concentrations of both microplastics and BP3. A few studies have been done on other marine organisms, including clams and marine medaka, demonstrating neurotoxic effects, oxidative stress, and reduced growth when exposed to microplastics with sorbed BP3.[109,471] Due to these varied effects, it is necessary to establish acute and chronic effects of combined

exposure to micro(nano)plastics and UV filters on many types of marine species to understand the relative risk to marine food webs.

### 6.4.2 Policy recommendations

The global toxic burden in the oceans is increasing, and this impact is placing oceanic biodiversity and primary productivity at risk. Phytoplankton constitute much of the primary productivity in the ocean and are vital to the planet's health. Plastics and UV filters adversely impact and modulate the life cycle of phytoplankton and other biological organisms in the oceans. It is imperative to better constrain the ecotoxicology of these anthropogenic pollutants in realistic marine matrices and mixtures. If the primary productivity of phytoplankton continues its downward trend, the oceans will have a reduced ability to sequester carbon, leading to increased ocean acidification. Additionally, reductions in phytoplankton will lead to destabilized food webs, threatening ecologically and economically significant fish stocks. It is essential to guard the ocean's health through careful research and policymaking around reducing marine pollutants.

Micro(nano)plastic prevalence is overwhelmingly documented in the literature yet has been the recipient of limited policy action. However, macroplastic pollution policy has had a lot of success in the US and abroad, and we can use a similar methodology to incite interest in implementing policy directed towards reducing and preventing micro(nano)plastic pollution. Therefore, we recommend the following:

1. *Reduce plastic production and use*

Most micro(nano)plastics are generated from the breakdown of macroplastics into small particles.[472] To reduce micro(nano)plastic pollution in the environment, the

volume of macroplastics produced, used, and disposed of must be drastically reduced. Because this requires an overhaul of the entire consumer-based economy, legislation must be passed banning the production and sale of unnecessary and harmful plastic products until this can be achieved. Current negotiations around the Global Plastics Treaty will outline a legally binding international approach to eliminate plastic waste.[430] A funding mechanism that charges a small fee for producing primary plastic polymers would help reduce their production and provide funding for other portions of the circular economy.[473]

2. *Pass local policy measures that require microplastic catchment technology in storm drains*

In many municipalities across the US, particularly in California, storm drains are required to contain catchment filters for trash larger than 5mm. However, this leaves all micro(nano)plastics to flow into storm drains and local waterways. For municipalities with identified issues with micro(nano)plastic input into stormwater from tire wear or litter, micro(nano)plastic catchment technology needs to be implemented to reduce micro(nano)plastic input into local waterways.

3. *Create incentives for washing machine manufacturers to include microfiber filters in all new washing machines*

Microfibers, tiny flexible fibers shed from textiles during use and washing, are often the most prevalent microplastic shape found in marine surface waters,[472,474] yet input through wastewater can be efficiently and drastically reduced with simple microfiber filters on washing machines. Currently, washing machine filters are available to consumers but are expensive and must be installed by the buyer.

Washing machine manufacturers must be pressured to include microfiber filters in all washing machines and provide maintenance instructions to all customers.

### 6.5 Academic service during a climate crisis

On September 20th, 2019, over 4 million people worldwide protested as a part of Fridays for Future's Global Week for Future, led by Greta Thunberg. At UC San Diego, the "Green New Deal at UCSD" was formed to put on a protest to begin our Fall Quarter. As a second-year graduate student, I stood in the crowd as Dr. Veerabhadran "Ram" Ramanathan, a world-renowned climate scientist, spoke. His speech outlined our shared "climate predicament," and he spoke directly about the responsibility of those who know the most about the climate crisis, i.e., climate and climate adjacent scientists, to speak out and promote positive change. I took his message to heart and sought to make UC San Diego and the UC System a better place. I accomplished this formally through the student government (as the Legislative Liaison for State Affairs, as a member of the Climate Action & Policy committee, and as the Director of Organizing for the UC Graduate and Professional Student Council) and as a student representative on the Academic Senate Committee on Campus Climate Change and the University of California Office of the President's Pathways to a Fossil Free Future Taskforce. I also organized as a member of the UC Green New Deal Coalition, a social movement throughout all ten UC campuses dedicated to transforming our institutions to prepare our students better to face the climate crisis. In our first five years, in which I was a principal member, we accomplished:

1. Implementation of a climate change general education requirement for UCSD's >30,000 undergraduate students, the largest student body with such a requirement in the world

2. A change in the UC Policy on Sustainable Practices from a “carbon neutral” policy focused on procurement of controversial carbon offsets to a policy focused on emissions reductions
3. The procurement of $13M to produce plans to decarbonize the ten-campus UC system, which will reduce annual carbon emissions by 1 million metric tons per annum
4. The most robust funding transparency policy in the U.S., based on the observed strategy of the fossil fuel industry to abuse donations and research funding to produce favorable research
5. The replacement of the Chase Bank retail location on campus with a University Credit Union branch

I repeat the message that shaped my understanding of my role in graduate school with the reader: we do not only inhabit academic spaces for our research. We also exist to provide institutional service to the systems that support us, those around us, and the community that hosts us in whatever way our unique skills and talents may be helpful.

**6.6. Acknowledgements**

Co-authors Dr. Mickey Rogers, Kara Wiggin, and Prof. Jonathan Slade have agreed to permit the re-distribution of the article “We Need a “Keeling Curve” Approach for Contaminants of Emerging Concern,” which may be found in *ACS Environmental Science & Technology*. I would also like to thank Victor Wang, Quynh Nguyen, Gwen Chodur, Hayden Schill, Pat Ordonez-Kim, Vianni Ledesma, Ido Shoshoni, Megan Nguyen, Victoria Abrenica, Taylor McKie, Luke Stroth, and Caroline Hung for the development of my policy understanding.

# Chapter 7 Conclusions and Future Work

## 7.1. Synopsis

This thesis explores three interconnected studies broadly investigating the dynamics of chemical contaminants and biogenic gases in coastal marine environments. **Chapter 3** reveals significant concentrations of emerging pollutants in ocean and air samples influenced by pollution from the Tijuana River. Sea spray aerosols (SSA) are identified as vectors for transporting illicit drugs and chemicals from various sources, posing heightened health risks to coastal residents and visitors. This airborne pathway underscores the need for revised health assessments in polluted coastal regions worldwide. **Chapter 4** examines the photo-induced degradation kinetics of oxybenzone (BP3) in seawater and SSA mimics, highlighting its faster degradation in aerosols compared to bulk solutions. Despite this rapid degradation, the formation of toxic transformation products suggests sustained environmental and health risks. **Chapter 5** explores the organic composition of secondary marine aerosols (SMA) generated during phytoplankton blooms, revealing high concentrations of sulfur- and nitrogen-containing compounds that promote SMA growth and influence marine atmospheric chemistry. The study introduces EESI-TOF MS for real-time characterization of SMA, showcasing its efficacy in identifying organic aerosol components and their transformation pathways. These findings emphasize the intricate interactions between pollutants, natural marine processes, and atmospheric dynamics, calling for integrated approaches to mitigate environmental impacts and safeguard public health in coastal ecosystems.

## 7.2. Conclusions

### 7.2.1. Illicit and Anthropogenic Chemicals in Coastal Marine Aerosols: Spatiotemporal Distributions and Links to Sea Spray

**Chapter 3** reported novel and significant concentrations of emerging contaminants in ocean and air samples from an area heavily affected by pollution from the Tijuana River. The study reveals that sea spray aerosol (SSA) could be an atmospheric source of illicit drugs and chemicals from tire and personal care products. We estimate that 100 g of methamphetamine may transfer onshore per day and could expose residents to an inhaled dose of 240 ng per day. Pollutants with high octanol-water partition and bubble scavenging coefficients are found to be more likely enriched in aerosols during onshore winds from the sea, thereby posing increased health risks to residents and visitors, including those inland from the coast. Global estimates indicate substantial onshore fluxes of these contaminants. This airborne pathway underscores a previously overlooked route of exposure, necessitating a reassessment of health evaluations near polluted coastal areas worldwide.

### 7.2.2. Photo-initiated degradation kinetics of the organic UV filter oxybenzone in solutions and aerosols: impacts of salt, photosensitizers, and the medium

**Chapter 4** demonstrated the photo-induced degradation kinetics for oxybenzone (BP3) in seawater and SSA mimics. Our findings indicate that BP3 degrades significantly faster in the aerosol phase than in bulk solutions, which we attribute to reduced solvent cage effects in aerosols with greater surface area-to-volume ratios than bulk seawater. This implies that the ocean is a reservoir while the daytime atmosphere is a rapid removal pathway for these compounds. Analysis of transformation products reveals a potential twofold increase in aerosol toxicity, highlighting that rapid degradation does not mitigate public health risks. Furthermore, our systematic

investigation shows that photosensitizing materials notably accelerate degradation in seawater, whereas salt has minimal impact. Conversely, salt enhances degradation rates in SSA more prominently than photosensitizing materials, likely due to surface enrichment of BP3 within aerosols.

### 7.2.3. Online Characterization of Secondary Marine Aerosol Using Extractive Electrospray Ionization Mass Spectrometry

**Chapter 5** provided a comprehensive initial analysis of secondary marine aerosols (SMA) generated from the oxidation of marine-derived volatile organic compounds (VOCs) emitted throughout a phytoplankton bloom by OH and $O_3$. Elevated biological activity and the release of biogenic VOCs lead to increased sulfur- and nitrogen-containing compounds in SMA, which exhibit lower volatilities and promote SMA growth. Phytoplankton-driven dimethyl sulfide (DMS) emissions regulate the marine sulfur budget, particularly in cleaner coastal environments. From our measurements of organonitrogen compounds in SMA, we hypothesize that alkyl amines from bacterial blooms can impact the nitrogen budget, affecting the abundance of CHON species like organonitrates under low NOx conditions. Rapid oxidative degradation of SMA's organic components suggests a smaller proportion of organic material in highly aged plumes. This research represents the first use of EESI-TOF MS for online characterization of SMA, highlighting its capability in real-time measurement of bulk organic properties and identifying ionization strategies that effectively probe different SMA components, from early oxidation products and SVOCs-IVOCs in positive mode to highly oxygenated molecules, organosulfur compounds, and ELVOCs-SVOCs in negative mode.

## 7.3. Ongoing and future work

### 7.3.1. Measuring Airbourne Toxins and Determining Oceanic Relationships (MATADOR) field study

I helped design and supervise the first two field deployments of the Slade Lab's "Measuring Airbourne Toxins and Determining Oceanic Relationships (MATADOR)" field study at the SIO pier. Specifically, I developed our offline sample collection and analysis protocol alongside Slade Group members Maya Morris and Diana Tran, who will lead the analysis of collected samples.

Compared to a distributed approach, as in **Chapter 3,** our decision to focus solely on the SIO Pier as our research location has some unique benefits. The Pier's co-located, publicly available suite of measurements allows for greater incorporation of the environmental parameters that influence ocean-to-air transfer. We were fortunate to coincide with the Atmospheric Radiation Measurement's (ARM) Eastern Pacific Cloud Aerosol Precipitation Experiment (EPCAPE), further enhancing the scope and depth of our data collection. However, we do lose insights into the spatial distribution of these pollutants.

The main modifications to the offline sample collection were to collect diurnal samples by switching sample filters near sunrise and sunset to allow both the investigation of daytime and nighttime chemistry and the separation of the diurnal sea breeze circulation. An essential offline analysis technique added was Ion Chromatography to determine the presence of NaCl in collected aerosols to allow for the determination of aerosol enrichment factors.

Additionally, I supervised the first field deployment of our EESI-ToF mass spectrometer to sample real marine aerosol. To our knowledge, this is the first time EESI was used in a natural coastal environment. Preliminary data analysis

demonstrates our capability to detect airborne pollutants and link the changes in their airborne concentrations with factors that control SSA generation, like wind speed and wave height. The higher time resolution offered by EESI compared to offline techniques allows for better correlative analysis to environmental parameters such as wave height and wind speed & direction. A representative analysis can be found below in **Fig 1**, in which hourly periods with higher wave heights lead to larger concentrations of seven different pollutants in the aerosol phase**.**

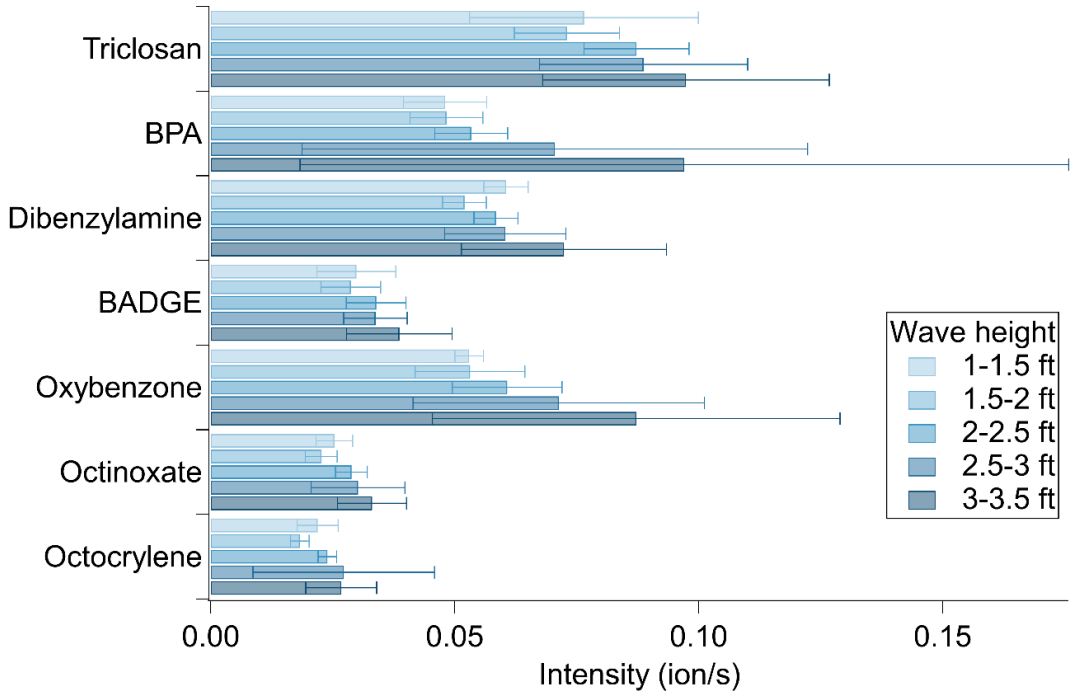


**Figure 7.1** Background subtracted signal intensity of different pollutants as a function of wave height.

Future incorporation of eddy flux measurements of SSA emissions would allow for more confident reporting of SSA emissions in the real marine atmosphere. This would address challenges in identifying ocean-to-air transfer solely from ambient measurements of ocean water and air. However, this remains technically challenging

due to the very high sensitivity required to detect trace amounts of freshly aerosolized SSA. Additional instrumental development, including the development of new ionization schemes for EESI, would enable this type of analysis.

### 7.3.2. Photo-induced degradation of UV filters and other pollutants

This dissertation focused on oxybenzone in **Chapter 5** as a well-studied and well-behaved model compound. An expansion of analysis to other organic UV filters, such as octinoxate and octocrylene, is planned to better capture the dynamics of photo-induced degradation across various compounds. Additionally, studies using more realistic SSA generation (using a Marine Aerosol Reference Tank) and investigating the photochemistry of mixtures of different UV filters together will be conducted by other members of the Slade Group. This will allow for experimental insights into my field measurements – such as if octinoxate had a low observed aerosolization factor in **Chapter 3** because of insufficient scavenging or via rapid removal via photolysis (as shown for BP3 in **Chapter 4**.)

Similar photo-induced degradation studies are planned for other UV-absorbing contaminants of concern, such as Triclosan.

An unexplored area of inquiry is to determine the contribution of anthropogenic compounds like UVF filters to marine chromophoric dissolved organic matter. As UV filters absorb light themselves, they may act as photosensitizers in the marine environment. A study investigating their efficiency as photosensitizing the degradation of nonabsorbing compounds could reveal their potential significant contributions to marine photochemistry in highly polluted regions.

### 7.3.3. Secondary organic aerosol formation from organic UV Filters

In a study by McDonald *et al.* 2018[44], it was noted that volatile chemical products are becoming the dominant VOC precursors to secondary aerosol in urban environments, surpassing combustion. Subsequently, a study by Shah *et al.* 2020[262] found that sunscreen vapors are highly effective precursors of SOA, using a similar PAM-OFR to the one utilized in this research.

However, robust studies of SOA formation of UV filters must contend with the influence of large photon fluxes of UV light typically used to generate OH *in situ*. To address this challenge, the Slade Lab is developing techniques for dark OH generation (through the ozonation of tetramethyl ethylene) and OH using higher wavelength light (utilizing isopropyl nitrite and 369 nm light). These advancements will enhance our ability to study the OH oxidation of UV-absorbing compounds.

As $O_3$ is a long-lived enough oxidant to generate in a separate chamber, preliminary work was done to investigate the $O_3$-initiated SOA formation from BP3 vapor. **Figure 2** shows a preliminary SOA yield curve from an initial experiment. It exhibits a yield between that of two common biogenic SOA precursors, isoprene and alpha-pinene. These preliminary findings motivate the potential large contribution of SOA mass from UV filters in urban atmospheres.

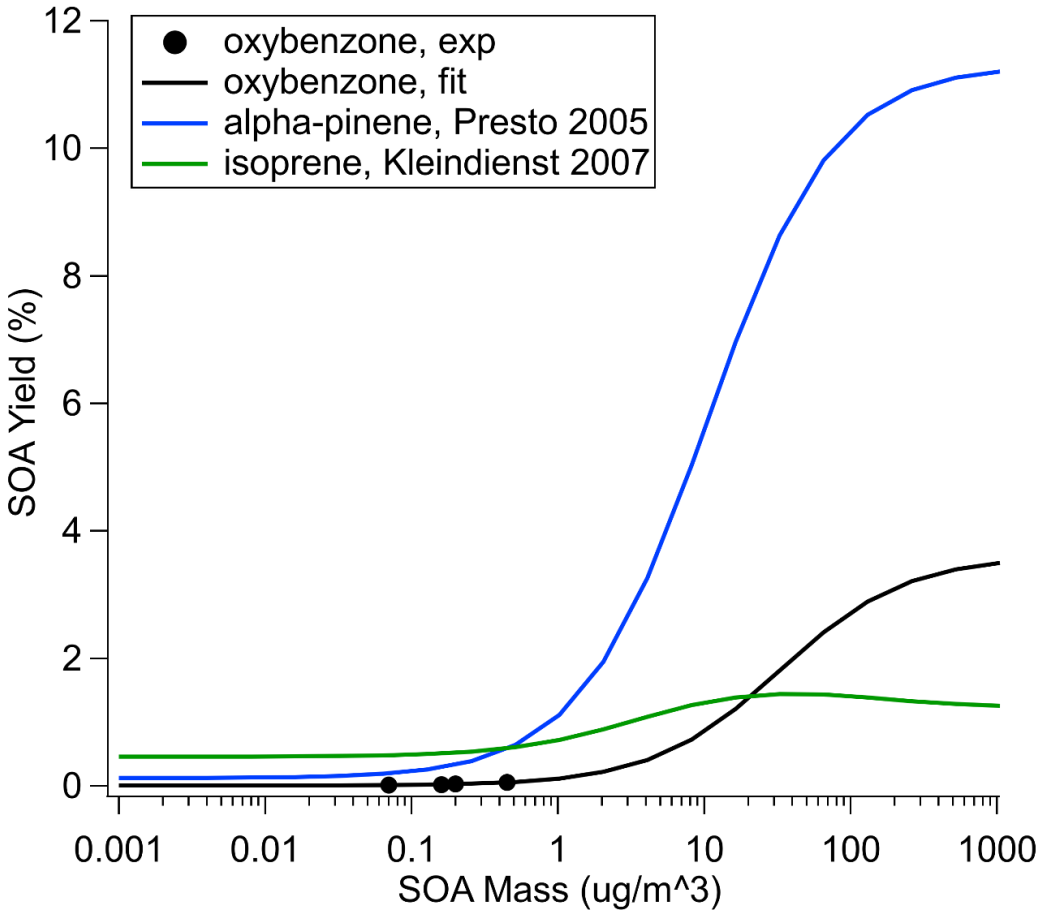


**Figure 7.2** SOA yield curve for the ozonation of oxybenzone, compared to literature yields for isoprene and alpha-pinene.

## References


(1) Ramanathan, V.; Crutzen, P. J.; Kiehl, J. T.; Rosenfeld, D. Aerosols, Climate and the Hydrological Cycle. *Science (1979)* **2001**, *294* (December), 2119–2125.

(2) Signorell, R.; Bertram, A. Physical Chemistry of Aerosols. *Physical Chemistry Chemical Physics* **2009**, *11* (36), 7759. https://doi.org/10.1039/b916865f.

(3) Mauderly, J. L.; Chow, J. C. Health Effects of Organic Aerosols. *http://dx.doi.org/10.1080/08958370701866008* **2008**, *20* (3), 257–288. https://doi.org/10.1080/08958370701866008.

(4) Li, J.; Carlson, B. E.; Yung, Y. L.; Lv, D.; Hansen, J.; Penner, J. E.; Liao, H.; Ramaswamy, V.; Kahn, R. A.; Zhang, P.; Dubovik, O.; Ding, A.; Lacis, A. A.; Zhang, L.; Dong, Y. Scattering and Absorbing Aerosols in the Climate System. *Nat Rev Earth Environ* **2022**, *3* (6), 363–379. https://doi.org/10.1038/s43017-022-00296-7.

(5) Gantt, B.; Meskhidze, N. The Physical and Chemical Characteristics of Marine Primary Organic Aerosol: A Review. *Atmos Chem Phys* **2013**, *13* (8), 3979–3996. https://doi.org/10.5194/acp-13-3979-2013.

(6) Hallquist, M.; Wenger, J. C.; Baltensperger, U.; Rudich, Y.; Simpson, D.; Claeys, M.; Dommen, J.; Donahue, N. M.; George, C.; Goldstein, A. H.; Hamilton, J. F.; Herrmann, H.; Hoffmann, T.; Iinuma, Y.; Jang, M.; Jenkin, M. E.; Jimenez, J. L.; Kiendler-Scharr, A.; Maenhaut, W.; McFiggans, G.; Mentel, T. F.; Monod, A.; Prévôt, A. S. H.; Seinfeld, J. H.; Surratt, J. D.; Szmigielski, R.; Wildt, J. The Formation, Properties and Impact of Secondary Organic Aerosol: Current and Emerging Issues. *Atmos Chem Phys* **2009**, *9* (14), 5155–5236. https://doi.org/10.5194/acp-9-5155-2009.

(7) Kroll, J. H.; Seinfeld, J. H. Chemistry of Secondary Organic Aerosol: Formation and Evolution of Low-Volatility Organics in the Atmosphere. *Atmos Environ* **2008**, *42* (16), 3593–3624. https://doi.org/https://doi.org/10.1016/j.atmosenv.2008.01.003.

(8) Tsigaridis, K.; Kanakidou, M. Secondary Organic Aerosol Importance in the Future Atmosphere. *Atmos Environ* **2007**. https://doi.org/10.1016/j.atmosenv.2007.03.045.

(9) Sareen, N.; Moussa, S. G.; McNeill, V. F. Photochemical Aging of Light-Absorbing Secondary Organic Aerosol Material. *Journal of Physical Chemistry A* **2013**, *117* (14), 2987–2996. https://doi.org/10.1021/jp309413j.

(10) Kessler, S. H.; Nah, T.; Daumit, K. E.; Smith, J. D.; Leone, S. R.; Kolb, C. E.; Worsnop, D. R.; Wilson, K. R.; Kroll, J. H. OH-Initiated Heterogeneous Aging of Highly Oxidized Organic Aerosol. **2012**. https://doi.org/10.1021/jp212131m.

(11) Kroll, J. H.; Lim, C. Y.; Kessler, S. H.; Wilson, K. R. Heterogeneous Oxidation of Atmospheric Organic Aerosol: Kinetics of Changes to the Amount and Oxidation State of Particle-Phase Organic Carbon. *Journal of Physical Chemistry A* **2015**, *119* (44), 10767–10783. https://doi.org/10.1021/acs.jpca.5b06946.

(12) George, I. J.; Abbatt, J. P. D. Heterogeneous Oxidation of Atmospheric Aerosol Particles by Gas-Phase Radicals. *Nature Publishing Group* **2010**, *2* (auGust), 713–722. https://doi.org/10.1038/nchem.806.

(13) Health Effects Institute. *State of Global Air 2024*; Boston, MA, 2024.

(14) Shiraiwa, M.; Ueda, K.; Pozzer, A.; Lammel, G.; Kampf, C. J.; Fushimi, A.; Enami, S.; Arangio, A. M.; Fro, J.; Fujitani, Y.; Furuyama, A.; Lakey, P. S. J.; Lelieveld, J.; Lucas, K.; Morino, Y.; Po, U.; Takahama, S.; Takami, A.; Tong, H.; Weber, B.; Yoshino, A.; Sato, K. Aerosol Health E Ff Ects from Molecular to Global Scales. **2017**. https://doi.org/10.1021/acs.est.7b04417.

(15) Prata, J. C. Airborne Microplastics: Consequences to Human Health? *Environmental Pollution* **2018**, *234*, 115–126. https://doi.org/10.1016/J.ENVPOL.2017.11.043.

(16) Yadav, D.; Rangabhashiyam, S.; Verma, P.; Singh, P.; Devi, P.; Kumar, P.; Hussain, C. M.; Gaurav, G. K.; Kumar, K. S. Environmental and Health Impacts of Contaminants of Emerging Concerns: Recent Treatment Challenges and Approaches. *Chemosphere* **2021**, *272*, 129492. https://doi.org/10.1016/j.chemosphere.2020.129492.

(17) Suh, H. H.; Bahadori, T.; Vallarino, J.; Spengler, J. D. Criteria Air Pollutants and Toxic Air Pollutants. *Environ Health Perspect* **2000**, *108* (SUPPL. 4), 625–633. https://doi.org/10.1289/EHP.00108S4625.

(18) Thomas, V. The Elimination of Lead in Gasoline. *Annual Review of Energy and the Environment* **2002**, *20* (1), 301–324. https://doi.org/10.1146/annurev.energy.20.1.301.

(19) Title 42 - The Public Health and Welfare, Chapter 85 - Air Pollution Prevention and Control. *United States Code, Clean Air Act* **2008**, 5673–5965.

(20) Burden of Disease from the Joint Effects of Household and Ambient Air Pollution for 2016. **2018**, No. May.

(21) Hart, K. M.; Pankow, J. F. Comparison of N-Alkane and PAH Concentrations Collected on Quartz Fiber and Teflon Membrane Filters in an Urban Environment. *J Aerosol Sci* **1990**, *21* (SUPPL. 1), S377–S380. https://doi.org/10.1016/0021-8502(90)90261-U.

(22) Shrivastava, M.; Lou, S.; Zelenyuk, A.; Easter, R. C.; Corley, R. A.; Thrall, B. D.; Rasch, P. J.; Fast, J. D.; Simonich, S. L. M.; Shen, H.; Tao, S. Global Long-

Range Transport and Lung Cancer Risk from Polycyclic Aromatic Hydrocarbons Shielded by Coatings of Organic Aerosol. *Proc Natl Acad Sci U S A* **2017**, *114* (6), 1246–1251. https://doi.org/10.1073/PNAS.1618475114/SUPPL_FILE/PNAS.1618475114.SAPP.PDF.

(23) Castro-Jiménez, J.; Berrojalbiz, N.; Wollgast, J.; Dachs, J. Polycyclic Aromatic Hydrocarbons (PAHs) in the Mediterranean Sea: Atmospheric Occurrence, Deposition and Decoupling with Settling Fluxes in the Water Column. *Environmental Pollution* **2012**, *166*, 40–47. https://doi.org/10.1016/j.envpol.2012.03.003.

(24) Zeng, E. Y.; Vista, C. L. Organic Pollutants in the Coastal Environment off San Diego, California. 1. Source Identification and Assessment by Compositional Indices of Polycyclic Aromatic Hydrocarbons. *Environ Toxicol Chem* **1997**, *16* (2), 179–188. https://doi.org/10.1897/1551-5028(1997)016<0179:OPITCE>2.3.CO;2.

(25) Sammarco, P. W.; Kolian, S. R.; Warby, R. A. F.; Bouldin, J. L.; Subra, W. A.; Porter, S. A. Distribution and Concentrations of Petroleum Hydrocarbons Associated with the BP/Deepwater Horizon Oil Spill, Gulf of Mexico. *Mar Pollut Bull* **2013**, *73* (1), 129–143. https://doi.org/10.1016/j.marpolbul.2013.05.029.

(26) Cousins, I. T.; Johansson, J. H.; Salter, M. E.; Sha, B.; Scheringer, M. Outside the Safe Operating Space of a New Planetary Boundary for Per- and Polyfluoroalkyl Substances (PFAS). *Environ Sci Technol* **2022**, *56* (16), 11172–11179. https://doi.org/10.1021/acs.est.2c02765.

(27) Allen, D.; Allen, S.; Abbasi, S.; Baker, A.; Bergmann, M.; Brahney, J.; Butler, T.; Duce, R. A.; Eckhardt, S.; Evangeliou, N.; Jickells, T.; Kanakidou, M.; Kershaw, P.; Laj, P.; Levermore, J.; Li, D.; Liss, P.; Liu, K.; Mahowald, N.; Masque, P.; Materić, D.; Mayes, A. G.; McGinnity, P.; Osvath, I.; Prather, K. A.; Prospero, J. M.; Revell, L. E.; Sander, S. G.; Shim, W. J.; Slade, J.; Stein, A.; Tarasova, O.; Wright, S. Microplastics and Nanoplastics in the Marine-Atmosphere Environment. *Nature Reviews Earth & Environment 2022* **2022**, 1–13. https://doi.org/10.1038/s43017-022-00292-x.

(28) Capone, D.; Carpenter, E.; Karentz, P.; Falkowski, D. The Perfect Haze: Scientists Link 1999 U.S. Pollution Episode to Midwest Aerosol Plumes and Kennedy Plane Crash. *Eos, Transactions American Geophysical Union* **2000**, *81* (2), 13–14. https://doi.org/10.1029/00EO00009.

(29) *AR5 Synthesis Report: Climate Change 2014 — IPCC*. https://www.ipcc.ch/report/ar5/syr/ (accessed 2020-03-13).

(30) [Core Writing Team, R. K. P. and L. A. M. (eds. )]. IPCC, 2014: Climate Change 2014: Synthesis Report. Contribution of Working Groups I, II and III to the Fifth Assessment Report of the Intergovernmental Panel on Climate Change. *IPCC, Geneva, Switzerland* **2014**, 151 pp.

(31) (IPCC), I. P. on C. C. The Earth's Energy Budget, Climate Feedbacks and Climate Sensitivity. *Climate Change 2021 – The Physical Science Basis* **2023**, 923–1054. https://doi.org/10.1017/9781009157896.009.

(32) Slade, J. H.; Shiraiwa, M.; Arangio, A.; Su, H.; Pöschl, U.; Wang, J.; Knopf, D. A. Cloud Droplet Activation through Oxidation of Organic Aerosol Influenced by Temperature and Particle Phase State. *Geophys Res Lett* **2017**, *44* (3), 1583–1591. https://doi.org/10.1002/2016GL072424.

(33) Petters, M. D.; Kreidenweis, S. M. A Single Parameter Representation of Hygroscopic Growth and Cloud Condensation Nucleus Activity-Part 3: Including Surfactant Partitioning. *Atmos Chem Phys* **2013**, *13* (2), 1081–1091. https://doi.org/10.5194/acp-13-1081-2013.

(34) Bony, S.; Dufresne, J. L. Marine Boundary Layer Clouds at the Heart of Tropical Cloud Feedback Uncertainties in Climate Models. *Geophys Res Lett* **2005**, *32* (20), 1–4. https://doi.org/10.1029/2005GL023851.

(35) Satheesh, S. K.; Krishna Moorthy, K. Radiative Effects of Natural Aerosols: A Review. *Atmos Environ* **2005**, *39* (11), 2089–2110. https://doi.org/10.1016/j.atmosenv.2004.12.029.

(36) De Leeuw, G.; Andreas, E. L.; Anguelova, M. D.; Fairall, C. W.; Lewis, E. R.; O'Dowd, C.; Schulz, M.; Schwartz, S. E. Production Flux of Sea Spray Aerosol. *Reviews of Geophysics* **2011**, *49* (2), 1–39. https://doi.org/10.1029/2010RG000349.

(37) Bilgili, L. Life Cycle Comparison of Marine Fuels for IMO 2020 Sulphur Cap. *Science of The Total Environment* **2021**, *774*, 145719. https://doi.org/10.1016/J.SCITOTENV.2021.145719.

(38) Yuan, T.; Song, H.; Oreopoulos, L.; Wood, R.; Bian, H.; Breen, K.; Chin, M.; Yu, H.; Barahona, D.; Meyer, K.; Platnick, S. Abrupt Reduction in Shipping Emission as an Inadvertent Geoengineering Termination Shock Produces Substantial Radiative Warming. *Commun Earth Environ* **2024**, *5* (1), 1–8. https://doi.org/10.1038/s43247-024-01442-3.

(39) Esper, J.; Torbenson, M.; Büntgen, U. 2023 Summer Warmth Unparalleled Over the Past 2,000 Years. *Nature* **2024**. https://doi.org/10.1038/s41586-024-07512-y.

(40) United Nations Framework Convention on Climate Change. The Paris Agreement. *UNFCCC* **2016**. https://doi.org/10.1038/127600a0.

(41) CIEL. Fuel To The Fire - How Geoengineering Threatens to Entrench Fossil Fuels and Accelerate the Climate Crisis. **2019**.

(42) Boettcher, M.; Chai, F.; Cullen, J.; Goeschl, T.; Lampitt, R.; Lenton, A.; Oschlies, A.; Rau, G.; Rickaby, R.; Ricke, K.; Wanninkhof, R. High Level Review of a Wide Range of Proposed Marine Geoengineering Techniques. **2019**.

(43) Field, C.; Cheung, W. W. L.; Dilling, L.; Frumhoff, P. C.; Greely, H. (Hank); Hordequin, M. E.; Hurrell, J.; Light, A.; Lin, A.; MacMartin, D.; McHenry, R.; Moreno-Cruz, J.; Ricke, K.; Russell, L.; Sagar, A.; Wennberg, P. Reflecting Sunlight: Recommendations for Solar Geoengineering Research and Research Governance. **2021**. https://doi.org/10.2172/1781700.

(44) McDonald, B. C.; De Gouw, J. A.; Gilman, J. B.; Jathar, S. H.; Akherati, A.; Cappa, C. D.; Jimenez, J. L.; Lee-Taylor, J.; Hayes, P. L.; McKeen, S. A.; Cui, Y. Y.; Kim, S. W.; Gentner, D. R.; Isaacman-VanWertz, G.; Goldstein, A. H.; Harley, R. A.; Frost, G. J.; Roberts, J. M.; Ryerson, T. B.; Trainer, M. Volatile Chemical Products Emerging as Largest Petrochemical Source of Urban Organic Emissions. *Science (1979)* **2018**, *359* (6377), 760–764. https://doi.org/10.1126/science.aaq0524.

(45) Eriksen, M.; Cowger, W.; Erdle, L. M.; Coffin, S.; Villarrubia-Gómez, P.; Moore, C. J.; Carpenter, E. J.; Day, R. H.; Thiel, M.; Wilcox, C. A Growing Plastic Smog, Now Estimated to Be over 170 Trillion Plastic Particles Afloat in the World's Oceans—Urgent Solutions Required. *PLoS One* **2023**, *18* (3), e0281596. https://doi.org/10.1371/JOURNAL.PONE.0281596.

(46) *Plastics - the Facts 2020 • Plastics Europe*. https://plasticseurope.org/knowledge-hub/plastics-the-facts-2020/ (accessed 2024-06-12).

(47) Geyer, R.; Jambeck, J. R.; Law, K. L. Production, Use, and Fate of All Plastics Ever Made. *Sci Adv* **2017**, *3* (7), 25–29. https://doi.org/10.1126/sciadv.1700782.

(48) Tovar-Sánchez, A.; Sánchez-Quiles, D.; Basterretxea, G.; Benedé, J. L.; Chisvert, A.; Salvador, A.; Moreno-Garrido, I.; Blasco, J. Sunscreen Products as Emerging Pollutants to Coastal Waters. *PLoS One* **2013**, *8* (6), e65451. https://doi.org/10.1371/journal.pone.0065451.

(49) Sánchez-Quiles, D.; Blasco, J.; Tovar-Sánchez, A. Sunscreen Components Are a New Environmental Concern in Coastal Waters: An Overview. *Handbook of Environmental Chemistry* **2020**, *94*, 1–14. https://doi.org/10.1007/698_2019_439.

(50) *The Future of Petrochemicals – Analysis - IEA*. https://www.iea.org/reports/the-future-of-petrochemicals (accessed 2023-04-08).

(51) Ma, Y.; Yoo, J. History of Sunscreen: An Updated View. *J Cosmet Dermatol* **2021**, *20* (4), 1044–1049. https://doi.org/10.1111/jocd.14004.

(52) National Acadmies Press. *Review of Fate, Exposure, and Effects of Sunscreens in Aquatic Environments and Implications for Sunscreen Usage and Human Health*; 2022. https://doi.org/10.17226/26381.

(53) Serpone, N.; Dondi, D.; Albini, A. Inorganic and Organic UV Filters: Their Role and Efficacy in Sunscreens and Suncare Products. *Inorganica Chim Acta* **2007**, *360* (3), 794–802. https://doi.org/10.1016/j.ica.2005.12.057.

(54) Bennett, S. J. Implications of Climate Change for the Petrochemical Industry: Mitigation Measures and Feedstock Transitions. In *Handbook of Climate Change Mitigation*; Chen, W.-Y., Seiner, J., Suzuki, T., Lackner, M., Eds.; Springer US: New York, NY, 2012; pp 319–357. https://doi.org/10.1007/978-1-4419-7991-9_10.

(55) Jambeck, J. R.; Geyer, R.; Wilcox, C.; Siegler, T. R.; Perryman, M.; Andrady, A.; Narayan, R.; Law, K. L. Plastic Waste Inputs from Land into the Ocean. *American Association for the Advancement of Science* **2015**, *347* (6223), 768–771. https://doi.org/https://doi.org/10.1126/science.1260352.

(56) Galloway, T. S.; Lewis, C. N. Marine Microplastics Spell Big Problems for Future Generations. *PNAS* **2016**, *113* (9), 2331–2333. https://doi.org/10.1073/pnas.1600715113.

(57) Wright, S. L.; Kelly, F. J. Plastic and Human Health: A Micro Issue? *Environ Sci Technol* **2017**, *51* (12), 6634–6647. https://doi.org/10.1021/acs.est.7b00423.

(58) Tsui, M. M. P.; Leung, H. W.; Wai, T. C.; Yamashita, N.; Taniyasu, S.; Liu, W.; Lam, P. K. S.; Murphy, M. B. Occurrence, Distribution and Ecological Risk Assessment of Multiple Classes of UV Filters in Surface Waters from Different Countries. *Water Res* **2014**, *67*, 55–65. https://doi.org/10.1016/j.watres.2014.09.013.

(59) Downs, C. A.; Kramarsky-Winter, E.; Segal, R.; Fauth, J.; Knutson, S.; Bronstein, O.; Ciner, F. R.; Jeger, R.; Lichtenfeld, Y.; Woodley, C. M.; Pennington, P.; Cadenas, K.; Kushmaro, A.; Loya, Y. Toxicopathological Effects of the Sunscreen UV Filter, Oxybenzone (Benzophenone-3), on Coral Planulae and Cultured Primary Cells and Its Environmental Contamination in Hawaii and the U.S. Virgin Islands. *Arch Environ Contam Toxicol* **2016**, *70* (2), 265–288. https://doi.org/10.1007/s00244-015-0227-7.

(60) Christen, V.; Zucchi, S.; Fent, K. Effects of the UV-Filter 2-Ethyl-Hexyl-4-Trimethoxycinnamate (EHMC) on Expression of Genes Involved in Hormonal Pathways in Fathead Minnows (Pimephales Promelas) and Link to Vitellogenin Induction and Histology. *Aquatic Toxicology* **2011**, *102* (3–4), 167–176. https://doi.org/10.1016/j.aquatox.2011.01.013.

(61) Meng, Q.; Yeung, K.; Chan, K. M. Toxic Effects of Octocrylene on Zebrafish Larvae and Liver Cell Line (ZFL). *Aquatic Toxicology* **2021**, *236*, 105843. https://doi.org/10.1016/j.aquatox.2021.105843.

(62) Yan, S.; Liang, M.; Chen, R.; Hong, X.; Zha, J. Reproductive Toxicity and Estrogen Activity in Japanese Medaka (Oryzias Latipes) Exposed to

Environmentally Relevant Concentrations of Octocrylene. *Environmental Pollution* **2020**, *261*. https://doi.org/10.1016/j.envpol.2020.114104.

(63) Zhang, Y.; Shah, P.; Wu, F.; Liu, P.; You, J.; Goss, G. Potentiation of Lethal and Sub-Lethal Effects of Benzophenone and Oxybenzone by UV Light in Zebrafish Embryos. *Aquatic Toxicology* **2021**, *235* (March), 105835. https://doi.org/10.1016/j.aquatox.2021.105835.

(64) Lee, I.; Lee, J.; Jung, D.; Kim, S.; Choi, K. Two-Generation Exposure to 2-Ethylhexyl 4-Methoxycinnamate (EHMC) in Japanese Medaka (Oryzias Latipes) and Its Reproduction and Endocrine Related Effects. *Chemosphere* **2019**, *228*, 478–484. https://doi.org/10.1016/j.chemosphere.2019.04.123.

(65) Wang, J.; Meng, X.; Feng, C.; Xiao, J.; Zhao, X.; Xiong, B.; Feng, J. Benzophenone-3 Induced Abnormal Development of Enteric Nervous System in Zebrafish through MAPK/ERK Signaling Pathway. *Chemosphere* **2021**, *280* (May), 130670. https://doi.org/10.1016/j.chemosphere.2021.130670.

(66) Lam, C. S.; Ramanathan, S.; Carbery, M.; Gray, K.; Vanka, K. S.; Maurin, C.; Bush, R.; Palanisami, T. A Comprehensive Analysis of Plastics and Microplastic Legislation Worldwide. *Water Air Soil Pollut* **2018**, *229* (11), 1–19. https://doi.org/10.1007/S11270-018-4002-Z/METRICS.

(67) United Nations Environment Program. Combating Marine Plastic Litter and Microplastics: An Assessment of the Effectiveness of Relevant International, Regional and Subregional Governance Strategies and Approaches. **2018**, No. May.

(68) Rios-Mendoza, L. M.; Ontiveros-Cuadras, J. F.; Leon-Vargas, D.; Ruiz-Fernández, A. C.; Rangel-García, M.; Pérez-Bernal, L. H.; Sanchez-Cabeza, J. A. Microplastic Contamination and Fluxes in a Touristic Area at the SE Gulf of California. *Mar Pollut Bull* **2021**, *170* (June). https://doi.org/10.1016/j.marpolbul.2021.112638.

(69) Allen, S.; Allen, D.; Moss, K.; Le Roux, G.; Phoenix, V. R.; Sonke, J. E. Examination of the Ocean as a Source for Atmospheric Microplastics. *PLoS One* **2020**, *15* (5), 1–14. https://doi.org/10.1371/journal.pone.0232746.

(70) Rani, M.; Shim, W. J.; Han, G. M.; Jang, M.; Song, Y. K.; Hong, S. H. Benzotriazole-Type Ultraviolet Stabilizers and Antioxidants in Plastic Marine Debris and Their New Products. *Science of The Total Environment* **2017**, *579*, 745–754. https://doi.org/https://doi.org/10.1016/j.scitotenv.2016.11.033.

(71) Anderson, W. A. C.; Castle, L. Benzophenone in Cartonboard Packaging Materials and the Factors That Influence Its Migration into Food. *Food Addit Contam* **2003**, *20* (6), 607–618. https://doi.org/10.1080/0265203031000109486.

(72) Salvador, A.; Chisvert, A. Sunscreen Analysis: A Critical Survey on UV Filters Determination. *Anal Chim Acta* **2005**, *537* (1–2), 1–14. https://doi.org/10.1016/j.aca.2005.01.055.

(73) Transparency Market Research. *Sun Care Market*.

(74) Mao, F.; He, Y.; Gin, K. Y. H. Occurrence and Fate of Benzophenone-Type UV Filters in Aquatic Environments: A Review. *Environ Sci (Camb)* **2019**, *5* (2), 209–223. https://doi.org/10.1039/c8ew00539g.

(75) Ramos, S.; Homem, V.; Alves, A.; Santos, L. Advances in Analytical Methods and Occurrence of Organic UV-Filters in the Environment - A Review. *Science of the Total Environment* **2015**, *526*, 278–311. https://doi.org/10.1016/j.scitotenv.2015.04.055.

(76) Schlumpf, M.; Durrer, S.; Faass, O.; Ehnes, C.; Fuetsch, M.; Gaille, C.; Henseler, M.; Hofkamp, L.; Maerkel, K.; Reolon, S.; Timms, B.; Tresguerres, J. A. F.; Lichtensteiger, W. Developmental Toxicity of UV Filters and Environmental Exposure: A Review. *Int J Androl* **2008**, *31* (2), 144–151. https://doi.org/10.1111/j.1365-2605.2007.00856.x.

(77) Wick, A.; Jacobs, B.; Kunkel, U.; Heininger, P.; Ternes, T. A. Benzotriazole UV Stabilizers in Sediments, Suspended Particulate Matter and Fish of German Rivers: New Insights into Occurrence, Time Trends and Persistency. *Environmental Pollution* **2016**, *212*, 401–412. https://doi.org/https://doi.org/10.1016/j.envpol.2016.01.024.

(78) Jeon, H.-K.; Chung, Y.; Ryu, J.-C. Simultaneous Determination of Benzophenone-Type UV Filters in Water and Soil by Gas Chromatography–Mass Spectrometry. *J Chromatogr A* **2006**, *1131* (1), 192–202. https://doi.org/https://doi.org/10.1016/j.chroma.2006.07.036.

(79) US EPA. Estimation Programs Interface Suite™ for Microsoft® Windows, v 4.11. *United States Environmental Protection Agency, Washington, DC, USA.*

(80) Repeta, D. J. *Chemical Characterization and Cycling of Dissolved Organic Matter*, Second Edi.; Elsevier Inc., 2015. https://doi.org/10.1016/B978-0-12-405940-5.00002-9.

(81) Ramos, S.; Homem, V.; Alves, A.; Santos, L. A Review of Organic UV-Filters in Wastewater Treatment Plants. *Environment International*. 2016, pp 24–44. https://doi.org/10.1016/j.envint.2015.10.004.

(82) *Quality and Wastewater | UN-Water*. https://www.unwater.org/water-facts/quality-and-wastewater/ (accessed 2022-07-29).

(83) Goksøyr, A.; Tollefsen, K. E.; Grung, M.; Løken, K.; Lie, E.; Zenker, A.; Fent, K.; Schlabach, M.; Huber, S. Balsa Raft Crossing the Pacific Finds Low Contaminant

Levels. *Environ Sci Technol* **2009**, *43* (13), 4783–4790. https://doi.org/10.1021/es900154h.

(84) Ho, W.-K.; Leung, K. S.-Y. Sorption and Desorption of Organic UV Filters onto Microplastics in Single and Multi-Solute Systems. *Environmental Pollution* **2019**, *254*, 113066. https://doi.org/https://doi.org/10.1016/j.envpol.2019.113066.

(85) Hansen, E.; Nilsson, N.; Slot Ravnholt Vium, K. *Hazardous Substances in Plastics*; 2014. www.mst.dk/english.

(86) Santana-viera, S.; Montesdeoca-esponda, S.; Sosa-ferrera, Z.; Santana-, J. UV Filters and UV Stabilisers Adsorbed in Microplastic Debris from Beach Sand. **2021**, *168* (May). https://doi.org/10.1016/j.marpolbul.2021.112434.

(87) Poiger, T.; Buser, H. R.; Balmer, M. E.; Bergqvist, P. A.; Müller, M. D. Occurrence of UV Filter Compounds from Sunscreens in Surface Waters: Regional Mass Balance in Two Swiss Lakes. *Chemosphere* **2004**, *55* (7), 951–963. https://doi.org/10.1016/j.chemosphere.2004.01.012.

(88) Pegoraro, C. N.; Harner, T.; Su, K.; Ahrens, L. Occurrence and Gas-Particle Partitioning of Organic UV Filters in Urban Air. **2020**, 0–32. https://doi.org/10.1021/acs.est.0c02665.

(89) O'Malley, E.; O'Brien, J. W.; Verhagen, R.; Mueller, J. F. Annual Release of Selected UV Filters via Effluent from Wastewater Treatment Plants in Australia. *Chemosphere* **2020**, *247*, 125887. https://doi.org/10.1016/j.chemosphere.2020.125887.

(90) Giokas, D. L.; Sakkas, V. A.; Albanis, T. A.; Lampropoulou, D. A. Determination of UV-Filter Residues in Bathing Waters by Liquid Chromatography UV-Diode Array and Gas Chromatography – Mass Spectrometry after Micelle Mediated Extraction-Solvent Back Extraction. **2005**, *1077*, 19–27. https://doi.org/10.1016/j.chroma.2005.04.074.

(91) Silvia Díaz-Cruz, M.; Llorca, M.; Barceló, D. Organic UV Filters and Their Photodegradates, Metabolites and Disinfection by-Products in the Aquatic Environment. *TrAC - Trends in Analytical Chemistry* **2008**, *27* (10), 873–887. https://doi.org/10.1016/j.trac.2008.08.012.

(92) Fagervold, S. K.; Rodrigues, A. S.; Rohée, C.; Roe, R.; Bourrain, M.; Stien, D.; Lebaron, P. Occurrence and Environmental Distribution of 5 UV Filters During the Summer Season in Different Water Bodies. *Water Air Soil Pollut* **2019**, *230* (7). https://doi.org/10.1007/s11270-019-4217-7.

(93) Balmer, M. E.; Buser, H. R.; Müller, M. D.; Poiger, T. Occurrence of Some Organic UV Filters in Wastewater, in Surface Waters, and in Fish from Swiss Lakes. *Environ Sci Technol* **2005**, *39* (4), 953–962. https://doi.org/10.1021/es040055r.

(94) D, Y. S.; Brett, J. Investigating the Exposure and Impacts of Chemical UV-Filters in Coral Reef Ecosystems : Review and Research Gap Prioritisation. **2021**. https://doi.org/10.1002/ieam.4411.

(95) Fall from GRASE: The Sunsetting of the Sunscreen Innovation Act. *American Journal of Dermatological Research and Reviews* **2021**, 39. https://doi.org/10.28933/ajodrr-2020-12-2805.

(96) Schwartz, M. *Key West To Ban Popular Sunscreen Ingredients To Protect Coral Reef*. npr.

(97) Krause, M.; Klit, A.; Blomberg Jensen, M.; Søeborg, T.; Frederiksen, H.; Schlumpf, M.; Lichtensteiger, W.; Skakkebaek, N. E.; Drzewiecki, K. T. Sunscreens: Are They Beneficial for Health? An Overview of Endocrine Disrupting Properties of UV-Filters. *Int J Androl* **2012**, *35* (3), 424–436. https://doi.org/10.1111/j.1365-2605.2012.01280.x.

(98) *Safe Sunscreen Act*; Republic of the Marshall Islands.

(99) Raffa, R. B.; Pergolizzi, J. V.; Taylor, R.; Kitzen, J. M. Sunscreen Bans: Coral Reefs and Skin Cancer. *J Clin Pharm Ther* **2019**, *44* (1), 134–139. https://doi.org/10.1111/jcpt.12778.

(100) Lee, Y. M.; Lee, G.; Zoh, K. D. Benzophenone-3 Degradation via UV/H2O2 and UV/Persulfate Reactions. *J Hazard Mater* **2021**, *403* (July 2020), 123591. https://doi.org/10.1016/j.jhazmat.2020.123591.

(101) Peng, M.-G.; Li, H.-J.; Du, E.-D.; Feng, H.-Q.; Wang, J.-L.; Li, D.-D.; Zhou, J. OH-Initiated Oxidation Mechanism and Kinetics of Organic Sunscreen Benzophenone-3: A Theoretical Study. *Chemical Papers* **2016**, *70* (6), 857–870.

(102) Lee, Y. M.; Lee, G.; Kim, M. K.; Zoh, K. D. Kinetics and Degradation Mechanism of Benzophenone-3 in Chlorination and UV/Chlorination Reactions. *Chemical Engineering Journal* **2020**, *393* (November 2019), 124780. https://doi.org/10.1016/j.cej.2020.124780.

(103) Li, Y.; Qiao, X.; Zhou, C.; Zhang, Y. nan; Fu, Z.; Chen, J. Photochemical Transformation of Sunscreen Agent Benzophenone-3 and Its Metabolite in Surface Freshwater and Seawater. *Chemosphere* **2016**, *153*, 494–499. https://doi.org/10.1016/j.chemosphere.2016.03.080.

(104) Na, J.; Song, J.; Achar, J. C.; Jung, J. Synergistic Effect of Microplastic Fragments and Benzophenone-3 Additives on Lethal and Sublethal Daphnia Magna Toxicity. *J Hazard Mater* **2021**, *402* (May 2020). https://doi.org/10.1016/j.jhazmat.2020.123845.

(105) Liu, Y. S.; Ying, G. G.; Shareef, A.; Kookana, R. S. Photostability of the UV Filter Benzophenone-3 and Its Effect on the Photodegradation of Benzotriazole in

Water. *Environmental Chemistry* **2011**, *8* (6), 581–588. https://doi.org/10.1071/EN11068.

(106) Mao, F.; He, Y.; Kushmaro, A.; Gin, K. Y. E Ff Ects of Benzophenone-3 on the Green Alga Chlamydomonas Reinhardtii and the Cyanobacterium Microcystis Aeruginosa. *Aquatic Toxicology* **2017**, *193* (April), 1–8. https://doi.org/10.1016/j.aquatox.2017.09.029.

(107) Vione, D.; Caringella, R.; De Laurentiis, E.; Pazzi, M.; Minero, C. Phototransformation of the Sunlight Filter Benzophenone-3 (2-Hydroxy-4-Methoxybenzophenone) under Conditions Relevant to Surface Waters. *Science of the Total Environment* **2013**, *463–464*, 243–251. https://doi.org/10.1016/j.scitotenv.2013.05.090.

(108) Grzyb, K.; Frański, R.; Pedzinski, T. Sensitized Photoreduction of Selected Benzophenones. Mass Spectrometry Studies of Radical Cross-Coupling Reactions. *J Photochem Photobiol B* **2022**, *234* (August), 1–10. https://doi.org/10.1016/j.jphotobiol.2022.112536.

(109) O'Donovan, S.; Mestre, N. C.; Abel, S.; Fonseca, T. G.; Carteny, C. C.; Willems, T.; Prinsen, E.; Cormier, B.; Keiter, S. S.; Bebianno, M. J. Effects of the UV Filter, Oxybenzone, Adsorbed to Microplastics in the Clam Scrobicularia Plana. *Science of The Total Environment* **2020**, *733*, 139102. https://doi.org/10.1016/J.SCITOTENV.2020.139102.

(110) Hopkins, Z. R.; Snowberger, S.; Blaney, L. Ozonation of the Oxybenzone, Octinoxate, and Octocrylene UV-Filters: Reaction Kinetics, Absorbance Characteristics, and Transformation Products. *J Hazard Mater* **2017**, *338*, 23–32. https://doi.org/10.1016/j.jhazmat.2017.05.016.

(111) Baker, L. A.; Horbury, M. D.; Greenough, S. E.; Coulter, P. M.; Karsili, T. N. V.; Roberts, G. M.; Orr-Ewing, A. J.; Ashfold, M. N. R.; Stavros, V. G. Probing the Ultrafast Energy Dissipation Mechanism of the Sunscreen Oxybenzone after UVA Irradiation. *Journal of Physical Chemistry Letters* **2015**, *6* (8), 1363–1368. https://doi.org/10.1021/acs.jpclett.5b00417.

(112) Zhong, X.; Downs, C. A.; Che, X.; Zhang, Z.; Li, Y.; Liu, B.; Li, Q.; Li, Y.; Gao, H. The Toxicological Effects of Oxybenzone, an Active Ingredient in Suncream Personal Care Products, on Prokaryotic Alga Arthrospira Sp. and Eukaryotic Alga Chlorella Sp. *Aquatic Toxicology* **2019**, *216*, 105295. https://doi.org/10.1016/J.AQUATOX.2019.105295.

(113) Wong, N. G. K.; Berenbeim, J. A.; Hawkridge, M.; Matthews, E.; Dessent, C. E. H. Mapping the Intrinsic Absorption Properties and Photodegradation Pathways of the Protonated and Deprotonated Forms of the Sunscreen Oxybenzone. *Physical Chemistry Chemical Physics* **2019**, *21* (26), 14311–14321. https://doi.org/10.1039/c8cp06794e.

(114) *Understanding the Tijuana River Sewage Crisis – An Overview of Causes and Consequences - San Diego Coastkeeper*. https://www.sdcoastkeeper.org/blog/tijuana-river-sewage-crisis-causes-consequences/ (accessed 2024-06-23).

(115) *USMCA Tijuana River Watershed | US EPA*. https://www.epa.gov/sustainable-water-infrastructure/usmca-tijuana-river-watershed (accessed 2024-06-23).

(116) Gersberg, R. M.; Daft, D.; Yorkey, D. Temporal Pattern of Toxicity in Runoff from the Tijuana River Watershed. *Water Res* **2004**, *38* (3), 559–568. https://doi.org/10.1016/j.watres.2003.11.002.

(117) Svejkovsky, J.; Nezlin, N. P.; Mustain, N. M.; Kum, J. B. Tracking Stormwater Discharge Plumes and Water Quality of the Tijuana River with Multispectral Aerial Imagery. *Estuar Coast Shelf Sci* **2010**, *87* (3), 387–398. https://doi.org/10.1016/j.ecss.2010.01.022.

(118) Feddersen, F.; Boehm, A. B.; Giddings, S. N.; Wu, X.; Liden, D. Modeling Untreated Wastewater Evolution and Swimmer Illness for Four Wastewater Infrastructure Scenarios in the San Diego-Tijuana (US/MX) Border Region. *Geohealth* **2021**, *5* (11), 1–20. https://doi.org/10.1029/2021GH000490.

(119) Pendergraft, M. A.; Grimes, D. J.; Giddings, S. N.; Feddersen, F.; Beall, C. M.; Lee, C.; Santander, M. V; Prather, K. A. Airborne Transmission Pathway for Coastal Water Pollution. **2021**, 1–18. https://doi.org/10.7717/peerj.11358.

(120) Pendergraft, M. A.; Beldá-Ferre, P.; Petras, D.; Morris, C. K.; Aron, A. T.; Bryant, M.; Schwartz, T.; Ackerman, G.; Humphrey, G.; Kaandorp, E.; Dorrestein, P. C.; Knight, R.; Prather, K. A. Bacterial and Chemical Evidence of Coastal Water Pollution from the Tijuana River in Sea Spray Aerosol. **2022**. https://doi.org/10.1021/acs.est.2c02312.

(121) United Nations Environment Program. *Coastal zone management*. https://www.unep.org/topics/ocean-seas-and-coasts/regional-seas-programme/coastal-zone-management.

(122) Van Eijk, A. M. J.; Kusmierczyk-Michulec, J. T.; Francius, M. J.; Tedeschi, G.; Piazzola, J.; Merritt, D. L.; Fontana, J. D. Sea-Spray Aerosol Particles Generated in the Surf Zone. *Journal of Geophysical Research: Atmospheres* **2011**, *116* (D19), 19210. https://doi.org/10.1029/2011JD015602.

(123) De Leeuw, G.; Neele, F. P.; Hill, M.; Smith, M. H.; Vignati, E. Production of Sea Spray Aerosol in the Surf Zone. *Journal of Geophysical Research Atmospheres* **2000**, *105* (D24), 29397–29409. https://doi.org/10.1029/2000JD900549.

(124) Bertram, T. H.; Cochran, R. E.; Grassian, V. H.; Stone, E. A. Sea Spray Aerosol Chemical Composition: Elemental and Molecular Mimics for Laboratory Studies of

Heterogeneous and Multiphase Reactions. *Chem Soc Rev* **2018**, *47* (7), 2374–2400. https://doi.org/10.1039/c7cs00008a.

(125) Cochran, R. E.; Ryder, O. S.; Grassian, V. H.; Prather, K. A. Sea Spray Aerosol: The Chemical Link between the Oceans, Atmosphere, and Climate. *Acc Chem Res* **2017**, *50* (3), 599–604. https://doi.org/10.1021/acs.accounts.6b00603.

(126) Prather, K. A.; Bertram, T. H.; Grassian, V. H.; Deane, G. B.; Stokes, M. D.; DeMott, P. J.; Aluwihare, L. I.; Palenik, B. P.; Azam, F.; Seinfeld, J. H.; Moffet, R. C.; Molina, M. J.; Cappa, C. D.; Geiger, F. M.; Roberts, G. C.; Russell, L. M.; Ault, A. P.; Baltrusaitis, J.; Collins, D. B.; Corrigan, C. E.; Cuadra-Rodriguez, L. A.; Ebben, C. J.; Forestieri, S. D.; Guasco, T. L.; Hersey, S. P.; Kim, M. J.; Lambert, W. F.; Modini, R. L.; Mui, W.; Pedler, B. E.; Ruppel, M. J.; Ryder, O. S.; Schoepp, N. G.; Sullivan, R. C.; Zhao, D. Bringing the Ocean into the Laboratory to Probe the Chemical Complexity of Sea Spray Aerosol. *Proceedings of the National Academy of Sciences* **2013**, *110* (19), 7550–7555. https://doi.org/10.1073/pnas.1300262110.

(127) Stokes, M. D.; Deane, G. B.; Prather, K.; Bertram, T. H.; Ruppel, M. J.; Ryder, O. S.; Brady, J. M.; Zhao, D. A Marine Aerosol Reference Tank System as a Breaking Wave Analogue for the Production of Foam and Sea-Spray Aerosols. *Atmos Meas Tech* **2013**, *6* (4), 1085–1094. https://doi.org/10.5194/amt-6-1085-2013.

(128) Wurl, O.; Obbard, J. P. A Review of Pollutants in the Sea-Surface Microlayer (SML): A Unique Habitat for Marine Organisms. *Mar Pollut Bull* **2004**, *48* (11–12), 1016–1030. https://doi.org/10.1016/j.marpolbul.2004.03.016.

(129) Engel, A.; Bange, H. W.; Cunliffe, M.; Burrows, S. M.; Friedrichs, G.; Galgani, L.; Herrmann, H.; Hertkorn, N.; Johnson, M.; Liss, P. S.; Quinn, P. K.; Schartau, M.; Soloviev, A.; Stolle, C.; Upstill-Goddard, R. C.; van Pinxteren, M.; Zäncker, B. The Ocean's Vital Skin: Toward an Integrated Understanding of the Sea Surface Microlayer. *Front Mar Sci* **2017**, *4* (MAY), 1–14. https://doi.org/10.3389/fmars.2017.00165.

(130) Wurl, O.; Ekau, W.; Landing, W. M.; Zappa, C. J. Sea Surface Microlayer in a Changing Ocean - A Perspective. *Elementa* **2017**, *5*. https://doi.org/10.1525/elementa.228.

(131) Triesch, N.; Van Pinxteren, M.; Frka, S.; Stolle, C.; Spranger, T.; Hoffmann, E. H.; Gong, X.; Wex, H.; Schulz-Bull, D.; Gašparovi´cgašparovi´c, B.; Herrmann, H. Concerted Measurements of Lipids in Seawater and on Submicrometer Aerosol Particles at the Cabo Verde Islands: Biogenic Sources, Selective Transfer and High Enrichments. *Atmos. Chem. Phys* **2021**, *21*, 4267–4283. https://doi.org/10.5194/acp-21-4267-2021.

(132) Cochran, R. E.; Laskina, O.; Jayarathne, T.; Laskin, A.; Laskin, J.; Lin, P.; Sultana, C.; Lee, C.; Moore, K. A.; Cappa, C. D.; Bertram, T. H.; Prather, K. A.;

Grassian, V. H.; Stone, E. A. Analysis of Organic Anionic Surfactants in Fine and Coarse Fractions of Freshly Emitted Sea Spray Aerosol. *Environ Sci Technol* **2016**, *50* (5), 2477–2486. https://doi.org/10.1021/acs.est.5b04053.

(133) Syzdek, L. D.; Appel, C. Virus Transfer. **1977**, No. November, 575–580.

(134) Aller, J. Y.; Kuznetsova, M. R.; Jahns, C. J.; Kemp, P. F. The Sea Surface Microlayer as a Source of Viral and Bacterial Enrichment in Marine Aerosols. *J Aerosol Sci* **2005**, *36* (5–6), 801–812. https://doi.org/10.1016/j.jaerosci.2004.10.012.

(135) Glüge, J.; Scheringer, M.; Cousins, I. T.; Dewitt, J. C.; Goldenman, G.; Herzke, D.; Lohmann, R.; Ng, C. A.; Trier, X.; Wang, Z. An Overview of the Uses of Per- and Polyfluoroalkyl Substances (PFAS). *Environ Sci Process Impacts* **2020**, *22* (12), 2345–2373. https://doi.org/10.1039/D0EM00291G.

(136) Substances, P. An Overview of Per- and Polyfluoroalkyl Substances (PFAS) in the Environment: Source, Fate, Risk and Regulations. **2020**, 1–28.

(137) Johansson, J. H.; Salter, M. E.; Acosta Navarro, J. C.; Leck, C.; Nilsson, E. D.; Cousins, I. T. Global Transport of Perfluoroalkyl Acids via Sea Spray Aerosol. *Environ Sci Process Impacts* **2019**, *21* (4), 635–649. https://doi.org/10.1039/c8em00525g.

(138) Sha, B.; Johansson, J. H.; Tunved, P.; Bohlin-Nizzetto, P.; Cousins, I. T.; Salter, M. E. Sea Spray Aerosol (SSA) as a Source of Perfluoroalkyl Acids (PFAAs) to the Atmosphere: Field Evidence from Long-Term Air Monitoring. *Environ Sci Technol* **2021**. https://doi.org/10.1021/acs.est.1c04277.

(139) Pawlak, F.; Koziol, K.; Frankowski, M.; Nowicki, Ł.; Marlin, C.; Sulej-Suchomska, A. M.; Polkowska, Ż. Sea Spray as a Secondary Source of Chlorinated Persistent Organic Pollutants? - Conclusions from a Comparison of Seven Fresh Snowfall Events in 2019 and 2021. *Science of The Total Environment* **2023**, *891*, 164357. https://doi.org/10.1016/J.SCITOTENV.2023.164357.

(140) Pike, K. A.; Edmiston, P. L.; Morrison, J. J.; Faust, J. A. Correlation Analysis of Perfluoroalkyl Substances in Regional U.S. Precipitation Events. *Water Res* **2021**, *190*. https://doi.org/10.1016/j.watres.2020.116685.

(141) Shao, L.; Li, Y.; Jones, T.; Santosh, M.; Liu, P.; Zhang, M.; Xu, L.; Li, W.; Lu, J.; Yang, C. X.; Zhang, D.; Feng, X.; BéruBé, K. Airborne Microplastics: A Review of Current Perspectives and Environmental Implications. *J Clean Prod* **2022**, *347*, 131048. https://doi.org/10.1016/J.JCLEPRO.2022.131048.

(142) Evangeliou, N.; Grythe, H.; Klimont, Z.; Heyes, C.; Eckhardt, S.; Lopez-Aparicio, S.; Stohl, A. Atmospheric Transport Is a Major Pathway of Microplastics to Remote Regions. *Nat Commun* **2020**, *11* (1). https://doi.org/10.1038/s41467-020-17201-9.

(143) Liss, P. S. Microplastics: All up in the Air? *Mar Pollut Bull* **2020**, *153*, 110952. https://doi.org/10.1016/J.MARPOLBUL.2020.110952.

(144) Brahney, J.; Mahowald, N.; Prank, M.; Cornwell, G.; Klimont, Z.; Matsui, H.; Prather, K. A. Constraining the Atmospheric Limb of the Plastic Cycle. *Proc Natl Acad Sci U S A* **2021**, *118* (16), 1–10. https://doi.org/10.1073/pnas.2020719118.

(145) Yang, S.; Lu, X.; Wang, X. A Perspective on the Controversy over Global Emission Fluxes of Microplastics from Ocean into the Atmosphere. *Environ Sci Technol* **2024**. https://doi.org/10.1021/ACS.EST.4C03182/ASSET/IMAGES/LARGE/ES4C03182_0001.JPEG.

(146) Mayol-Bracero, O. L.; Rosario, O.; Corrigan, C. E.; Morales, R.; Torres, I.; Pérez, V. Chemical Characterization of Submicron Organic Aerosols in the Tropical Trade Winds of the Caribbean Using Gas Chromatography/Mass Spectrometry. *Atmos Environ* **2001**, *35* (10), 1735–1745. https://doi.org/10.1016/S1352-2310(00)00524-0.

(147) Franklin, E. B.; Amiri, S.; Crocker, D.; Morris, C.; Mayer, K.; Sauer, J. S.; Weber, R. J.; Lee, C.; Malfatti, F.; Cappa, C. D.; Bertram, T. H.; Prather, K. A.; Goldstein, A. H. Anthropogenic and Biogenic Contributions to the Organic Composition of Coastal Submicron Sea Spray Aerosol. *Environ Sci Technol* **2022**, *56* (23), 16633–16642. https://doi.org/10.1021/ACS.EST.2C04848/SUPPL_FILE/ES2C04848_SI_003.XLSX.

(148) Sauer, J. S.; Mayer, K. J.; Lee, C.; Alves, M. R.; Amiri, S.; Bahaveolos, C.; Barnes, E. B.; Crocker, D. R.; Dinasquet, J.; Garofalo, L. A.; Kaluarachchi, C. P.; Dang, D.; Kilgour, D.; Mael, L.; Mitts, B. A.; Moon, D. R.; Morris, C. K.; Moore, A. N.; Ni, C.-M.; Pendergraft, M. A.; Petras, D.; Simpson, R.; Smith, S.; Tumminello, P. R.; Walker, J. L.; DeMott, P. J.; Farmer, D. K.; Goldstein, A. H.; Grassian, V. H.; Jaffe, J. S.; Malfatti, F.; Martz, T. R.; Slade, J.; Tivanski, A. V.; Bertram, T. H.; Cappa, C. D.; Prather, K. A. The Sea Spray Chemistry and Particle Evolution Study (SeaSCAPE): Overview and Experimental Methods. *Environ Sci Process Impacts* **2021**.

(149) Mayer, K. J.; Wang, X.; Santander, M. V.; Mitts, B. A.; Sauer, J. S.; Sultana, C. M.; Cappa, C. D.; Prather, K. A. Secondary Marine Aerosol Plays a Dominant Role over Primary Sea Spray Aerosol in Cloud Formation. *ACS Cent Sci* **2020**, No. 1. https://doi.org/10.1021/acscentsci.0c00793.

(150) Rinaldi, M.; Decesari, S.; Finessi, E.; Giulianelli, L.; Carbone, C.; Fuzzi, S.; O'Dowd, C. D.; Ceburnis, D.; Facchini, M. C. Primary and Secondary Organic Marine Aerosol and Oceanic Biological Activity: Recent Results and New Perspectives for Future Studies. *Advances in Meteorology* **2010**, *2010*, 1–10. https://doi.org/10.1155/2010/310682.

(151) Trueblood, J. V; Wang, X.; Or, V. W.; Alves, M. R.; Santander, M. V; Prather, K. A.; Grassian, V. H.; Jolla, L.; Diego, S.; Jolla, L.; Diego, S.; Jolla, L. The Old and the New : Aging of Sea Spray Aerosols and Formation of Secondary Marine Aerosol Through OH Oxidation Reactions. 1–27.

(152) *Biologic Processes That Influence the Production of Dimethylsulfide(DMS) from Marine Phytoplankton--《Periodical of Ocean University of China》2009年03期*. http://en.cnki.com.cn/Article_en/CJFDTOTAL-QDHY200903017.htm (accessed 2019-06-03).

(153) Charlson, R. J.; Lovelock, J. E.; Andreaei, M. O.; Warren, S. G. Oceanic Phytoplankton, Atmospheric Sulphur, Cloud. *Nature* **1987**, *330*, 1987.

(154) Dall'Osto, M.; Airs, R. L.; Beale, R.; Cree, C.; Fitzsimons, M. F.; Beddows, D.; Harrison, R. M.; Ceburnis, D.; O'Dowd, C.; Rinaldi, M.; Paglione, M.; Nenes, A.; Decesari, S.; Simó, R. Simultaneous Detection of Alkylamines in the Surface Ocean and Atmosphere of the Antarctic Sympagic Environment. *ACS Earth Space Chem* **2019**, *3* (5), 854–862. https://doi.org/10.1021/ACSEARTHSPACECHEM.9B00028/SUPPL_FILE/SP9B00028_SI_001.PDF.

(155) Facchini, M. C.; Decesari, S.; Rinaldi, M.; Carbone, C.; Finessi, E.; Mircea, M.; Fuzzi, S.; Moretti, F.; Tagliavini, E.; Ceburnis, D.; O'Dowd, C. D. Important Source of Marine Secondary Organic Aerosol from Biogenic Amines. *Environ Sci Technol* **2008**, *42* (24), 9116–9121. https://doi.org/10.1021/es8018385.

(156) Saha, M.; Fink, P. Algal Volatiles – the Overlooked Chemical Language of Aquatic Primary Producers. *Biological Reviews* **2022**, *97* (6), 2162–2173. https://doi.org/10.1111/BRV.12887.

(157) Bravo-Linares, C. M.; Mudge, S. M.; Loyola-Sepulveda, R. H. PRODUCTION OF VOLATILE ORGANIC COMPOUNDS (VOCS) BY TEMPERATE MACROALGAE: THE USE OF SOLID PHASE MICROEXTRACTION (SPME) COUPLED TO GC-MS AS METHOD OF ANALYSIS. *Journal of the Chilean Chemical Society* **2010**, *55* (2), 227–232. https://doi.org/10.4067/S0717-97072010000200018.

(158) Zuo, Z. Why Algae Release Volatile Organic Compounds - The Emission and Roles. *Front Microbiol* **2019**, *10* (MAR). https://doi.org/10.3389/FMICB.2019.00491/PDF.

(159) Shaw, S. L.; Gantt, B.; Meskhidze, N. Production and Emissions of Marine Isoprene and Monoterpenes: A Review. *Advances in Meteorology* **2010**, *2010* (1), 1–24. https://doi.org/10.1155/2010/408696.

(160) Cui, T.; Green, H. S.; Selleck, P. W.; Zhang, Z.; O'Brien, R. E.; Gold, A.; Keywood, M.; Kroll, J. H.; Surratt, J. D. Chemical Characterization of Isoprene- and Monoterpene-Derived Secondary Organic Aerosol Tracers in Remote Marine

Aerosols over a Quarter Century. *ACS Earth Space Chem* **2019**, *3* (6), 935–946. https://doi.org/10.1021/acsearthspacechem.9b00061.

(161) Kilgour, D. B.; Jernigan, C. M.; Zhou, S.; Azevedo, E. B. de; Wang, J.; Zawadowicz, M. A.; Bertram, T. H. Contribution of Speciated Monoterpenes to Secondary Aerosol in the Eastern North Atlantic. *ACS ES&T Air* **2024**, 555–566. https://doi.org/10.1021/ACSESTAIR.3C00112.

(162) Kilgour, D. B.; Novak, G. A.; Sauer, J. S.; Moore, A. N.; Dinasquet, J.; Amiri, S.; Franklin, E. B.; Mayer, K.; Winter, M.; Morris, C. K.; Price, T.; Malfatti, F.; Crocker, D. R.; Lee, C.; Cappa, C. D.; Goldstein, A. H.; Prather, K. A.; Bertram, T. H. Marine Gas-Phase Sulfur Emissions during an Induced Phytoplankton Bloom. *Atmos Chem Phys* **2022**, *22* (2), 1601–1613. https://doi.org/10.5194/acp-22-1601-2022.

(163) Friedman, B.; Farmer, D. K. SOA and Gas Phase Organic Acid Yields from the Sequential Photooxidation of Seven Monoterpenes. *Atmos Environ* **2018**, *187* (January), 335–345. https://doi.org/10.1016/j.atmosenv.2018.06.003.

(164) Mutzel, A.; Rodigast, M.; Iinuma, Y.; Böge, O.; Herrmann, H. Monoterpene SOA - Contribution of First-Generation Oxidation Products to Formation and Chemical Composition. *Atmos Environ* **2016**, *130*, 136–144. https://doi.org/10.1016/j.atmosenv.2015.10.080.

(165) Darer, A. I.; Cole-Filipiak, N. C.; O'Connor, A. E.; Elrod, M. J. Formation and Stability of Atmospherically Relevant Isoprene-Derived Organosulfates and Organonitrates. *Environ Sci Technol* **2011**, *45* (5), 1895–1902. https://doi.org/10.1021/ES103797Z/SUPPL_FILE/ES103797Z_SI_001.PDF.

(166) Cape, J. N.; Cornell, S. E.; Jickells, T. D.; Nemitz, E. Organic Nitrogen in the Atmosphere — Where Does It Come from? A Review of Sources and Methods. *Atmos Res* **2011**, *102* (1–2), 30–48. https://doi.org/10.1016/J.ATMOSRES.2011.07.009.

(167) Odum, J. R.; Hoffmann, T.; Bowman, F.; Collins, D.; Flagan, R. C.; Seinfeld, J. H. Gas/Particle Partitioning and Secondary Organic Aerosol Yields. *Environ Sci Technol* **1996**, *30* (8), 2580–2585. https://doi.org/10.1021/es950943+.

(168) Dall'osto, M.; Ceburnis, D.; Monahan, C.; Worsnop, D. R.; Bialek, J.; Kulmala, M.; Kurtén, T.; Ehn, M.; Wenger, J.; Sodeau, J.; Healy, R.; O'dowd, C. Nitrogenated and Aliphatic Organic Vapors as Possible Drivers for Marine Secondary Organic Aerosol Growth. *J. Geophys. Res 117*, 12311. https://doi.org/10.1029/2012JD017522.

(169) Kirkby, J.; Duplissy, J.; Sengupta, K.; Frege, C.; Gordon, H.; Williamson, C.; Heinritzi, M.; Simon, M.; Yan, C.; Almeida, J.; Trostl, J.; Nieminen, T.; Ortega, I. K.; Wagner, R.; Adamov, A.; Amorim, A.; Bernhammer, A. K.; Bianchi, F.; Breitenlechner, M.; Brilke, S.; Chen, X.; Craven, J.; Dias, A.; Ehrhart, S.; Flagan,

R. C.; Franchin, A.; Fuchs, C.; Guida, R.; Hakala, J.; Hoyle, C. R.; Jokinen, T.; Junninen, H.; Kangasluoma, J.; Kim, J.; Krapf, M.; Kurten, A.; Laaksonen, A.; Lehtipalo, K.; Makhmutov, V.; Mathot, S.; Molteni, U.; Onnela, A.; Perakyla, O.; Piel, F.; Petaja, T.; Praplan, A. P.; Pringle, K.; Rap, A.; Richards, N. A. D.; Riipinen, I.; Rissanen, M. P.; Rondo, L.; Sarnela, N.; Schobesberger, S.; Scott, C. E.; Seinfeld, J. H.; Sipila, M.; Steiner, G.; Stozhkov, Y.; Stratmann, F.; Tomé, A.; Virtanen, A.; Vogel, A. L.; Wagner, A. C.; Wagner, P. E.; Weingartner, E.; Wimmer, D.; Winkler, P. M.; Ye, P.; Zhang, X.; Hansel, A.; Dommen, J.; Donahue, N. M.; Worsnop, D. R.; Baltensperger, U.; Kulmala, M.; Carslaw, K. S.; Curtius, J. Ion-Induced Nucleation of Pure Biogenic Particles. *Nature* **2016**, *533* (7604), 521–526. https://doi.org/10.1038/nature17953.

(170) Riccobono, F.; Schobesberger, S.; Scott, C. E.; Dommen, J.; Ortega, I. K.; Rondo, L.; Almeida, J.; Amorim, A.; Bianchi, F.; Breitenlechner, M.; David, A.; Downard, A.; Dunne, E. M.; Duplissy, J.; Ehrhart, S.; Flagan, R. C.; Franchin, A.; Hansel, A.; Junninen, H.; Kajos, M.; Keskinen, H.; Kupc, A.; Kürten, A.; Kvashin, A. N.; Laaksonen, A.; Lehtipalo, K.; Makhmutov, V.; Mathot, S.; Nieminen, T.; Onnela, A.; Petäjä, T.; Praplan, A. P.; Santos, F. D.; Schallhart, S.; Seinfeld, J. H.; Sipilä, M.; Spracklen, D. V; Stozhkov, Y.; Stratmann, F.; Tomé, A.; Tsagkogeorgas, G.; Vaattovaara, P.; Viisanen, Y.; Vrtala, A.; Wagner, P. E.; Weingartner, E.; Wex, H.; Wimmer, D.; Carslaw, K. S.; Curtius, J.; Donahue, N. M.; Kirkby, J.; Kulmala, M.; Worsnop, D. R.; Baltensperger, U. Oxidation Products of Biogenic Emissions Contribute to Nucleation of Atmospheric Particles. *Science (1979)* **2014**, *344* (6185), 717–721. https://doi.org/10.1126/science.1243527.

(171) Molina, M. J.; Ivanov, A. V; Trakhtenberg, S.; Molina, L. T. Atmospheric Evolution of Organic Aerosol. **2004**, *31* (2), 2–6. https://doi.org/10.1029/2004GL020910.

(172) Chen, T.; Jang, M. Secondary Organic Aerosol Formation from Photooxidation of a Mixture of Dimethyl Sulfide and Isoprene. *Atmos Environ* **2012**, *46*, 271–278. https://doi.org/10.1016/J.ATMOSENV.2011.09.082.

(173) Gligorovski, S.; Strekowski, R.; Barbati, S.; Vione, D. Environmental Implications of Hydroxyl Radicals (•OH). *Chem Rev* **2015**, *115* (24), 13051–13092. https://doi.org/10.1021/cr500310b.

(174) Murphy, S. M.; Sorooshian, A.; Kroll, J. H.; Ng, N. L.; Chhabra, P.; Tong, C.; Surratt, J. D.; Knipping, E.; Flagan, R. C.; Seinfeld, J. H. Secondary Aerosol Formation from Atmospheric Reactions of Aliphatic Amines. *Atmos Chem Phys* **2007**, *7* (9), 2313–2337. https://doi.org/10.5194/acp-7-2313-2007.

(175) Angeling, S.; Suess, D. T.; Prather, K. A. Formation of Aerosol Particles from Reactions of Secondary and Tertiary Alkylamines: Characterization by Aerosol Time-of-Flight Mass Spectrometry. *Environ Sci Technol* **2001**, *35* (15), 3130–3138. https://doi.org/10.1021/es0015444.

(176) Olenius, T.; Halonen, R.; Kurtén, T.; Henschel, H.; Kupiainen-Määttä, O.; Ortega, I. K.; Jen, C. N.; Vehkamäki, H.; Riipinen, I. New Particle Formation from Sulfuric Acid and Amines: Comparison of Monomethylamine, Dimethylamine, and Trimethylamine. *J Geophys Res* **2017**, *122* (13), 7103–7118. https://doi.org/10.1002/2017JD026501.

(177) O'Dowd, C. D.; De Leeuw, G. Marine Aerosol Production: A Review of the Current Knowledge. *Philosophical Transactions of the Royal Society A: Mathematical, Physical and Engineering Sciences* **2007**, *365* (1856), 1753–1774. https://doi.org/10.1098/rsta.2007.2043.

(178) Youn, J. S.; Crosbie, E.; Maudlin, L. C.; Wang, Z.; Sorooshian, A. Dimethylamine as a Major Alkyl Amine Species in Particles and Cloud Water: Observations in Semi-Arid and Coastal Regions. *Atmos Environ* **2015**, *122*, 250–258. https://doi.org/10.1016/j.atmosenv.2015.09.061.

(179) Berta, V. Z.; Russell, L. M.; Price, D. J.; Chen, C. L.; Lee, A. K. Y.; Quinn, P. K.; Bates, T. S.; Bell, T. G.; Behrenfeld, M. J. Non-Volatile Marine and Non-Refractory Continental Sources of Particle-Phase Amine during the North Atlantic Aerosols and Marine Ecosystems Study (NAAMES). *Atmos Chem Phys* **2023**, *23* (4), 2765–2787. https://doi.org/10.5194/ACP-23-2765-2023.

(180) Barnes, I.; Hjorth, J.; Mihalapoulos, N. Dimethyl Sulfide and Dimethyl Sulfoxide and Their Oxidation in the Atmosphere. *Chem Rev* **2006**, *106* (3), 940–975. https://doi.org/10.1021/cr020529+.

(181) Lovelock, J. *The Revenge of Gaia*; 2006.

(182) Boyce, D. G.; Lewis, M. R.; Worm, B. Global Phytoplankton Decline over the Past Century. *Nature* **2010**, *466* (7306), 591–596. https://doi.org/10.1038/nature09268.

(183) Häder, D. P.; Gao, K. Interactions of Anthropogenic Stress Factors on Marine Phytoplankton. *Front Environ Sci* **2015**, *3* (MAR), 1–14. https://doi.org/10.3389/fenvs.2015.00014.

(184) Dryden, H.; Duncan, D. Climate Disruption Caused by a Decline in Marine Biodiversity and Pollution. *International Journal of Environment and Climate Change* **2022**, No. October, 3414–3436. https://doi.org/10.9734/ijecc/2022/v12i111392.

(185) Liu, J.; Zhang, F.; Xu, W.; Sun, Y.; Chen, L.; Li, S.; Ren, J. Hygroscopicity of Organic Aerosols Linked to Formation Mechanisms. https://doi.org/10.1029/2020GL091683.

(186) Zhang, Z.; Qin, X.; Wang, W. Study of Cloud Condensation Nuclei Activities and Hygroscopic Properties Based on Core-Shell Model. *Pure Appl Geophys* **2022**, *179* (4), 1421–1432. https://doi.org/10.1007/s00024-022-02976-3.

(187) Massoli, P.; Lambe, A. T.; Ahern, A. T.; Williams, L. R.; Ehn, M.; Mikkilä, J.; Canagaratna, M. R.; Brune, W. H.; Onasch, T. B.; Jayne, J. T.; Petäjä, T.; Kulmala, M.; Laaksonen, A.; Kolb, C. E.; Davidovits, P.; Worsnop, D. R. Relationship between Aerosol Oxidation Level and Hygroscopic Properties of Laboratory Generated Secondary Organic Aerosol (SOA) Particles. *Geophys Res Lett* **2010**, *37* (24), 1–5. https://doi.org/10.1029/2010GL045258.

(188) Li, W.; Teng, X.; Chen, X.; Liu, L.; Xu, L.; Zhang, J.; Wang, Y.; Zhang, Y.; Shi, Z. Organic Coating Reduces Hygroscopic Growth of Phase-Separated Aerosol Particles. *Environ Sci Technol* **2021**, *55* (24), 16339–16346. https://doi.org/10.1021/acs.est.1c05901.

(189) Haagen-Smit, A. J. Chemistry and Physiology of Los Angeles Smog. *Ind Eng Chem* **2002**, *44* (6), 1342–1346. https://doi.org/10.1021/IE50510A045.

(190) Riedel, K.; Lassey, K. Detergent of the Atmosphere. *Water & Atmosphere* **2008**, *16* (1), 22–23.

(191) Calvert, J.; Pitts, J. *Photochemistry*; John Wiley & Sons, Inc., 1966.

(192) George, C.; Ammann, M.; D'Anna, B.; Donaldson, D. J.; Nizkorodov, S. A. Heterogeneous Photochemistry in the Atmosphere. *Chem Rev* **2015**, *115* (10), 4218–4258. https://doi.org/10.1021/cr500648z.

(193) Vione, D.; Maurino, V.; Minero, C.; Pelizzetti, E.; Harrison, M. A. J.; Olariu, R. I.; Arsene, C. Photochemical Reactions in the Tropospheric Aqueous Phase and on Particulate Matter. *Chem Soc Rev* **2006**, *35* (5), 441–453. https://doi.org/10.1039/b510796m.

(194) Jacobson, M. Z. Atmospheric Pollution: History, Science, and Regulation. **2002**. https://doi.org/10.1017/CBO9780511802287.

(195) Laskin, A.; Laskin, J.; Nizkorodov, S. A. Chemistry of Atmospheric Brown Carbon. *Chem Rev* **2015**, *115* (10), 4335–4382. https://doi.org/10.1021/cr5006167.

(196) Kaur, R.; Labins, J. R.; Helbock, S. S.; Jiang, W.; Bein, K.; Zhang, Q.; Anastasio, C. Photooxidants from Brown Carbon and Other Chromophores in Illuminated Particle Extracts. *Atmospheric Chemistry and Physics Discussions* **2018**, *6* (December), 1–34. https://doi.org/10.5194/acp-2018-1258.

(197) Chen, L. W. A.; Chow, J. C.; Wang, X.; Cao, J.; Mao, J.; Watson, J. G. Brownness of Organic Aerosol over the United States: Evidence for Seasonal Biomass Burning and Photobleaching Effects. *Environ Sci Technol* **2021**, *55* (13), 8561–8572. https://doi.org/10.1021/ACS.EST.0C08706.

(198) Helms, J. R.; Stubbins, A.; Ritchie, J. D.; Minor, E. C.; Kieber, D. J.; Mopper, K. Absorption Spectral Slopes and Slope Ratios as Indicators of Molecular Weight,

Source, and Photobleaching of Chromophoric Dissolved Organic Matter. *Limnol Oceanogr* **2008**, *53* (3), 955–969. https://doi.org/10.4319/lo.2008.53.3.0955.

(199) Wong, J. P. S.; Zhou, S.; Abbatt, J. P. D. Changes in Secondary Organic Aerosol Composition and Mass Due to Photolysis: Relative Humidity Dependence. *Journal of Physical Chemistry A* **2015**, *119* (19), 4309–4316. https://doi.org/10.1021/jp506898c.

(200) Zawadowicz, M. A.; Lee, B. H.; Shrivastava, M.; Zelenyuk, A.; Zaveri, R. A.; Flynn, C.; Thornton, J. A.; Shilling, J. E. Photolysis Controls Atmospheric Budgets of Biogenic Secondary Organic Aerosol. *Environ Sci Technol* **2020**. https://doi.org/10.1021/acs.est.9b07051.

(201) Hodzic, A.; Madronich, S.; Kasibhatla, P. S.; Tyndall, G.; Aumont, B.; Jimenez, J. L.; Lee-Taylor, J.; Orlando, J. Organic Photolysis Reactions in Tropospheric Aerosols: Effect on Secondary Organic Aerosol Formation and Lifetime. *Atmos Chem Phys* **2015**, *15* (16), 9253–9269. https://doi.org/10.5194/acp-15-9253-2015.

(202) Quina, F. H.; Silva, G. T. M. The Photophysics of Photosensitization: A Brief Overview. *J Photochem Photobiol* **2021**, *7* (May), 100042. https://doi.org/10.1016/j.jpap.2021.100042.

(203) Martins-Costa, M. T. C.; Anglada, J. M.; Francisco, J. S.; Ruiz-López, M. F. Photosensitization Mechanisms at the Air-Water Interface of Aqueous Aerosols . *Chem Sci* **2022**. https://doi.org/10.1039/d1sc06866k.

(204) Anglada, J. M.; Martins-Costa, M.; Francisco, J. S.; Ruiz-López, M. F. Interconnection of Reactive Oxygen Species Chemistry across the Interfaces of Atmospheric, Environmental, and Biological Processes. *Acc Chem Res* **2015**, *48* (3), 575–583. https://doi.org/10.1021/ar500412p.

(205) Alves, M. R.; Coward, E. K.; Gonzales, D.; Sauer, J. S.; Mayer, K. J.; Prather, K. A.; Grassian, V. H. Changes in Light Absorption and Composition of Chromophoric Marine-Dissolved Organic Matter across a Microbial Bloom. *Environ Sci Process Impacts* **2022**, *24* (10), 1923–1933. https://doi.org/10.1039/d2em00150k.

(206) Trueblood, J. V.; Alves, M. R.; Power, D.; Santander, M. V.; Cochran, R. E.; Prather, K. A.; Grassian, V. H. Shedding Light on Photosensitized Reactions within Marine-Relevant Organic Thin Films. *ACS Earth Space Chem* **2019**, *3* (8), 1614–1623. https://doi.org/10.1021/acsearthspacechem.9b00066.

(207) Ault, A. P.; Waters, C. M. Scratching the Surface of Individual Aerosol Particle Properties. *ACS Cent Sci* **2023**, *9* (11), 2009. https://doi.org/10.1021/ACSCENTSCI.3C01362.

(208) Mekic, M.; Brigante, M.; Vione, D.; Gligorovski, S. Exploring the Ionic Strength Effects on the Photochemical Degradation of Pyruvic Acid in Atmospheric

Deliquescent Aerosol Particles. *Atmos Environ* **2018**, *185*, 237–242. https://doi.org/10.1016/J.ATMOSENV.2018.05.016.

(209) Nissenson, P.; Knox, C. J. H.; Finlayson-Pitts, B. J.; Phillips, L. F.; Dabdub, D. Enhanced Photolysis in Aerosols: Evidence for Important Surface Effects. *Physical Chemistry Chemical Physics* **2006**, *8* (40), 4700–4710. https://doi.org/10.1039/b609219e.

(210) Li, K.; Gong, K.; Liu, J.; Ohnoutek, L.; Ao, J.; Liu, Y.; Chen, X.; Xu, G.; Ruan, X.; Cheng, H.; Han, J.; Sui, G.; Ji, M.; Valev, V. K.; Zhang, L. Significantly Accelerated Photochemical and Photocatalytic Reactions in Microdroplets. *Cell Rep Phys Sci* **2022**, *3* (6). https://doi.org/10.1016/j.xcrp.2022.100917.

(211) Wei, Z.; Li, Y.; Cooks, R. G.; Yan, X. Accelerated Reaction Kinetics in Microdroplets: Overview and Recent Developments. *Annu Rev Phys Chem* **2020**, *71*, 31–51. https://doi.org/10.1146/annurev-physchem-121319-110654.

(212) Hanson, K. M.; Narayanan, S.; Nichols, V. M.; Bardeen, C. J. Photochemical Degradation of the UV Filter Octyl Methoxycinnamate in Solution and in Aggregates. *Photochemical and Photobiological Sciences* **2015**, *14* (9), 1607–1616. https://doi.org/10.1039/c5pp00074b.

(213) Tinel, L.; Rossignol, S.; Bianco, A.; Passananti, M.; Perrier, S.; Wang, X.; Brigante, M.; Donaldson, D. J.; George, C. Mechanistic Insights on the Photosensitized Chemistry of a Fatty Acid at the Air/Water Interface. *Environ Sci Technol* **2016**, *50* (20), 11041–11048. https://doi.org/10.1021/ACS.EST.6B03165/ASSET/IMAGES/LARGE/ES-2016-03165Z_0006.JPEG.

(214) Rodil, R.; Moeder, M.; Altenburger, R.; Schmitt-Jansen, M. Photostability and Phytotoxicity of Selected Sunscreen Agents and Their Degradation Mixtures in Water. *Anal Bioanal Chem* **2009**, *395* (5), 1513–1524. https://doi.org/10.1007/s00216-009-3113-1.

(215) Kruse, S. M.; Slade, J. H. Heterogeneous and Photosensitized Oxidative Degradation Kinetics of the Plastic Additive Bisphenol-A in Sea Spray Aerosol Mimics. *Journal of Physical Chemistry A* **2023**. https://doi.org/10.1021/acs.jpca.3c00127.

(216) McMurry, P. H. A Review of Atmospheric Aerosol Measurements. *Atmos Environ* **2000**, *34* (12–14), 1959–1999. https://doi.org/10.1016/S1352-2310(99)00455-0.

(217) Sun, J.; Yin, Y.; Li, W.; Jin, O.; Na, N. CHEMICAL REACTION MONITORING BY AMBIENT MASS SPECTROMETRY. *Mass Spectrom Rev* **2022**, *41* (1), 70–99. https://doi.org/10.1002/MAS.21668.

(218) Zhang, K.; Xu, Z.; Gao, J.; Xu, Z.; Wang, Z. Review of Online Measurement Techniques for Chemical Composition of Atmospheric Clusters and Sub-20 Nm

Particles. *Front Environ Sci* **2022**, *10*, 937006. https://doi.org/10.3389/FENVS.2022.937006/BIBTEX.

(219) Davis, W. D. Surface Ionization Mass Spectroscopy of Airborne Particulates. *Journal of Vacuum Science and Technology* **1973**, *10* (1), 278.

(220) Prather, K. A.; Nordmeyer, T.; Salt, K. Real-Time Characterization of Individual Aerosol Particles Using Time-of-Flight Mass Spectrometry. *Anal Chem* **1994**, *66* (9), 1403–1407. https://doi.org/10.1021/ac00081a007.

(221) Jayne, J. T.; Leard, D. C.; Zhang, X.; Davidovits, P.; Smith, K. A.; Kolb, C. E.; Worsnop, D. R. Development of an Aerosol Mass Spectrometer for Size and Composition Analysis of Submicron Particles. *Aerosol Science and Technology* **2000**, *33* (1–2), 49–70. https://doi.org/10.1080/027868200410840.

(222) Tobias, H. J.; Ziemann, P. J. Compound Identification in Organic Aerosols Using Temperature-Programmed Thermal Desorption Particle Beam Mass Spectrometry. *Anal Chem* **1999**, *71* (16), 3428–3435. https://doi.org/10.1021/ac990056f.

(223) Lopez-Hilfiker, F. D.; Mohr, C.; Ehn, M.; Rubach, F.; Kleist, E.; Wildt, J.; Mentel, T. F.; Lutz, A.; Hallquist, M.; Worsnop, D.; Thornton, J. A. A Novel Method for Online Analysis of Gas and Particle Composition: Description and Evaluation of a Filter Inlet for Gases and AEROsols (FIGAERO). *Atmos Meas Tech* **2014**, *7* (4), 983–1001. https://doi.org/10.5194/amt-7-983-2014.

(224) Claflin, M. S.; Pagonis, D.; Finewax, Z.; Handschy, A. V.; Day, D. A.; Brown, W. L.; Jayne, J. T.; Worsnop, D. R.; Jimenez, J. L.; Ziemann, P. J.; De Gouw, J.; Lerner, B. M. An in Situ Gas Chromatograph with Automatic Detector Switching between PTR-and EI-TOF-MS: Isomer-Resolved Measurements of Indoor Air. *Atmos Meas Tech* **2021**, *14* (1), 133–152. https://doi.org/10.5194/AMT-14-133-2021.

(225) Wang, R.; Gröhn, A. J.; Zhu, L.; Dietiker, R.; Wegner, K.; Günther, D.; Zenobi, R. On the Mechanism of Extractive Electrospray Ionization (EESI) in the Dual-Spray Configuration. *Anal Bioanal Chem* **2012**, *402* (8), 2633–2643. https://doi.org/10.1007/s00216-011-5471-8.

(226) Chen, H.; Venter, A.; Cooks, R. G. Extractive Electrospray Ionization for Direct Analysis of Undiluted Urine, Milk and Other Complex Mixtures without Sample Preparation. *Chemical Communications* **2006**, No. 19, 2042–2044. https://doi.org/10.1039/b602614a.

(227) Gallimore, P.; Kalberer, M. Characterizing an Extractive Electrospray Ionization (EESI) Source for the Online Mass Spectrometry Analysis of Organic Aerosols. Environ Sci Technol 2013.

(228) Doezema, L. A.; Longin, T.; Cody, W.; Perraud, V.; Dawson, M. L.; Ezell, M. J.; Greaves, J.; Johnson, K. R.; Finlayson-Pitts, B. J. Analysis of Secondary Organic Aerosols in Air Using Extractive Electrospray Ionization Mass Spectrometry (EESI-MS). *RSC Adv* **2012**, *2* (7), 2930–2938. https://doi.org/10.1039/c2ra00961g.

(229) Lopez-hilfiker, F. D.; Pospisilova, V.; Huang, W.; Kalberer, M.; Mohr, C. An Extractive Electrospray Ionization Time-of-Flight Mass Spectrometer ( EESI-TOF ) for Online Measurement of Atmospheric Aerosol Particles. *Atmos Meas Tech* **2019**, 4867–4886.

(230) Wang, R.; Gröhn, A. J.; Zhu, L.; Dietiker, R.; Wegner, K.; Günther, D.; Zenobi, R. On the Mechanism of Extractive Electrospray Ionization (EESI) in the Dual-Spray Configuration. *Anal Bioanal Chem* **2012**, *402* (8), 2633–2643. https://doi.org/10.1007/s00216-011-5471-8.

(231) Kumbhani, S.; Longin, T.; Wingen, L. M.; Kidd, C.; Perraud, V.; Finlayson-Pitts, B. J. New Mechanism of Extractive Electrospray Ionization Mass Spectrometry for Heterogeneous Solid Particles. *Anal Chem* **2018**, *90* (3), 2055–2062. https://doi.org/10.1021/acs.analchem.7b04164.

(232) Lee, C. P.; Surdu, M.; Bell, D. M.; Lamkaddam, H.; Wang, M.; Ataei, F.; Hofbauer, V.; Lopez, B.; Donahue, N. M.; Dommen, J.; Prevot, A. S. H.; Slowik, J. G.; Wang, D.; Baltensperger, U.; El Haddad, I. Effects of Aerosol Size and Coating Thickness on the Molecular Detection Using Extractive Electrospray Ionization. *Atmos Meas Tech* **2021**, *14* (9), 5913–5923. https://doi.org/10.5194/AMT-14-5913-2021.

(233) Wilm, M. Principles of Electrospray Ionization. *Mol Cell Proteomics* **2011**, *10* (7). https://doi.org/10.1074/MCP.M111.009407.

(234) Brophy, P.; Farmer, D. K. Clustering, Methodology, and Mechanistic Insights into Acetate Chemical Ionization Using High-Resolution Time-of-Flight Mass Spectrometry. *Atmos Meas Tech* **2016**, *9* (8), 3969–3986. https://doi.org/10.5194/amt-9-3969-2016.

(235) Stark, H.; Yatavelli, R. L. N.; Thompson, S. L.; Kimmel, J. R.; Cubison, M. J.; Chhabra, P. S.; Canagaratna, M. R.; Jayne, J. T.; Worsnop, D. R.; Jimenez, J. L. Methods to Extract Molecular and Bulk Chemical Information from Series of Complex Mass Spectra with Limited Mass Resolution. *Int J Mass Spectrom* **2015**, *389*, 26–38. https://doi.org/https://doi.org/10.1016/j.ijms.2015.08.011.

(236) Telepchak, M. J. The Mechanism of Reverse Phase Liquid-Solid Chromatography. *Chromatographia* **1973**, *6* (5), 234–236. https://doi.org/10.1007/BF02311733.

(237) Cancelada, L.; Torres, R. R.; Garrafa Luna, J.; Dorrestein, P. C.; Aluwihare, L. I.; Prather, K. A.; Petras, D. Assessment of Styrene-divinylbenzene Polymer (PPL)

Solid-phase Extraction and Non-targeted Tandem Mass Spectrometry for the Analysis of Xenobiotics in Seawater. *Limnol Oceanogr Methods* **2021**. https://doi.org/10.1002/lom3.10470.

(238) Petras, D.; Minich, J. J.; Cancelada, L. B.; Torres, R. R.; Kunselman, E.; Wang, M.; White, M. E.; Allen, E. E.; Prather, K. A.; Aluwihare, L. I.; Dorrestein, P. C. Non-Targeted Tandem Mass Spectrometry Enables the Visualization of Organic Matter Chemotype Shifts in Coastal Seawater. *Chemosphere* **2021**, *271*, 129450. https://doi.org/10.1016/J.CHEMOSPHERE.2020.129450.

(239) *Orbitrap*. Wikipedia. https://en.wikipedia.org/wiki/Orbitrap#/media/File:OrbitrapMA&Injector.png.

(240) Wang, M.; Carver, J. J.; Phelan, V. V.; Sanchez, L. M.; Garg, N.; Peng, Y.; Nguyen, D. D.; Watrous, J.; Kapono, C. A.; Luzzatto-Knaan, T.; Porto, C.; Bouslimani, A.; Melnik, A. V.; Meehan, M. J.; Liu, W. T.; Crüsemann, M.; Boudreau, P. D.; Esquenazi, E.; Sandoval-Calderón, M.; Kersten, R. D.; Pace, L. A.; Quinn, R. A.; Duncan, K. R.; Hsu, C. C.; Floros, D. J.; Gavilan, R. G.; Kleigrewe, K.; Northen, T.; Dutton, R. J.; Parrot, D.; Carlson, E. E.; Aigle, B.; Michelsen, C. F.; Jelsbak, L.; Sohlenkamp, C.; Pevzner, P.; Edlund, A.; McLean, J.; Piel, J.; Murphy, B. T.; Gerwick, L.; Liaw, C. C.; Yang, Y. L.; Humpf, H. U.; Maansson, M.; Keyzers, R. A.; Sims, A. C.; Johnson, A. R.; Sidebottom, A. M.; Sedio, B. E.; Klitgaard, A.; Larson, C. B.; Boya, C. A. P.; Torres-Mendoza, D.; Gonzalez, D. J.; Silva, D. B.; Marques, L. M.; Demarque, D. P.; Pociute, E.; O'Neill, E. C.; Briand, E.; Helfrich, E. J. N.; Granatosky, E. A.; Glukhov, E.; Ryffel, F.; Houson, H.; Mohimani, H.; Kharbush, J. J.; Zeng, Y.; Vorholt, J. A.; Kurita, K. L.; Charusanti, P.; McPhail, K. L.; Nielsen, K. F.; Vuong, L.; Elfeki, M.; Traxler, M. F.; Engene, N.; Koyama, N.; Vining, O. B.; Baric, R.; Silva, R. R.; Mascuch, S. J.; Tomasi, S.; Jenkins, S.; Macherla, V.; Hoffman, T.; Agarwal, V.; Williams, P. G.; Dai, J.; Neupane, R.; Gurr, J.; Rodríguez, A. M. C.; Lamsa, A.; Zhang, C.; Dorrestein, K.; Duggan, B. M.; Almaliti, J.; Allard, P. M.; Phapale, P.; Nothias, L. F.; Alexandrov, T.; Litaudon, M.; Wolfender, J. L.; Kyle, J. E.; Metz, T. O.; Peryea, T.; Nguyen, D. T.; VanLeer, D.; Shinn, P.; Jadhav, A.; Müller, R.; Waters, K. M.; Shi, W.; Liu, X.; Zhang, L.; Knight, R.; Jensen, P. R.; Palsson, B.; Pogliano, K.; Linington, R. G.; Gutiérrez, M.; Lopes, N. P.; Gerwick, W. H.; Moore, B. S.; Dorrestein, P. C.; Bandeira, N. Sharing and Community Curation of Mass Spectrometry Data with Global Natural Products Social Molecular Networking. *Nat Biotechnol* **2016**, *34* (8), 828–837. https://doi.org/10.1038/nbt.3597.

(241) Perkin Elmer. UV Vis Spectrometer User's Guide. *Perkin Elmer* **2000**, No. 888.

(242) TSI INC. Instruction Manual: Constant Output Atomizer (Model 3075 / 3076). *ReVision* **2003**, No. November.

(243) Willeke, K.; Degarmo, S. J. Passive Versus Active Aerosol Monitoring. *Applied Industrial Hygiene* **1988**, *3* (9), 263–266. https://doi.org/10.1080/08828032.1988.10389845.

(244) Markovic, M. Z.; Prokop, S.; Staebler, R. M.; Liggio, J.; Harner, T. Evaluation of the Particle Infiltration Efficiency of Three Passive Samplers and the PS-1 Active Air Sampler. *Atmos Environ* **2015**, *112*, 289–293. https://doi.org/10.1016/j.atmosenv.2015.04.051.

(245) Liu, B. Y. H.; Pui, D. Y. H. Aerosol Sampling Inlets and Inhalable Particles. *Atmospheric Environment (1967)* **1981**, *15* (4), 589–600. https://doi.org/10.1016/0004-6981(81)90190-6.

(246) Perrino, C.; Canepari, S.; Catrambone, M. Comparing the Performance of Teflon and Quartz Membrane Filters Collecting Atmospheric PM: Influence of Atmospheric Water. *Aerosol Air Qual Res* **2013**, *13* (1), 137–147. https://doi.org/10.4209/AAQR.2012.07.0167.

(247) McMurry, P. H. A Review of Atmospheric Aerosol Measurements. *Atmos Environ* **2000**, *34* (12–14), 1959–1999. https://doi.org/10.1016/S1352-2310(99)00455-0.

(248) Kataoka, H. Sample Preparation for Liquid Chromatography. *Liquid Chromatography: Applications* **2023**, 1–48. https://doi.org/10.1016/B978-0-323-99969-4.00006-1.

(249) Pietrogrande, M. C.; Bacco, D.; Chiereghin, S. GC/MS Analysis of Water-Soluble Organics in Atmospheric Aerosol: Optimization of a Solvent Extraction Procedure for Simultaneous Analysis of Carboxylic Acids and Sugars. *Anal Bioanal Chem* **2013**, *405* (2–3), 1095–1104. https://doi.org/10.1007/s00216-012-6592-4.

(250) Bein, K. J.; Wexler, A. S. A High-Efficiency, Low-Bias Method for Extracting Particulate Matter from Filter and Impactor Substrates. *Atmos Environ* **2014**, *90*, 87–95. https://doi.org/10.1016/j.atmosenv.2014.03.042.

(251) Wang, S. C.; Flagan, R. C. Scanning Electrical Mobility Spectrometer. *Aerosol Science and Technology* **1990**, *13* (2), 230–240. https://doi.org/10.1080/02786829008959441.

(252) Brechtel. Instrument Manual SEMS 2100 Overview. **2019**, 0–84.

(253) Robbins, R. C.; Cadle, R. D. KINETICS OF THE REACTION BETWEEN GASEOUS AMMONIA AND SULFURIC ACID DROPLETS IN AN AEROSOL1. *J Phys Chem* **1958**, *471* (6), 1950–1952.

(254) Peng, Z.; Jimenez, J. L. Radical Chemistry in Oxidation Flow Reactors for Atmospheric Chemistry Research. *Chem Soc Rev* **2020**, 15–17. https://doi.org/10.1039/C9CS00766K.

(255) Pan, T.; Lambe, A. T.; Hu, W.; He, Y.; Hu, M.; Zhou, H.; Wang, X.; Hu, Q.; Chen, H.; Zhao, Y.; Huang, Y.; Peng, Z.; Morris, M. A.; Day, D. A.; Campuzano-Jost, P.; Jimenez, J.-L.; Jathar, S. H. A Comprehensive Evaluation of Enhanced

Temperature Influence on Gas and Aerosol Chemistry in the Lamp-Enclosed Oxidation Flow Reactor (OFR) System. **2023**, No. November, 1–34.

(256) Gardner, E. P.; Sperry, P. D.; Calvert, J. G. Primary Quantum Yields of NO2 Photodissociation. *Journal of Geophysical Research: Atmospheres* **1987**, *92* (D6), 6642–6652. https://doi.org/10.1029/JD092ID06P06642.

(257) Meylan, W. M.; Howard, P. H. A Review of Quantitative Structure-Activity Relationship Methods for the Prediction of Atmospheric Oxidation of Organic Chemicals. *Environ Toxicol Chem* **2003**, *22* (8), 1724–1732. https://doi.org/10.1897/01-275.

(258) Tropsha, A. Best Practices for QSAR Model Development, Validation, and Exploitation. *Mol Inform* **2010**, *29* (6–7), 476–488. https://doi.org/10.1002/MINF.201000061.

(259) Chuang, W. K.; Donahue, N. M. A Two-Dimensional Volatility Basis Set-Part 3: Prognostic Modeling and NOx Dependence. *Atmos Chem Phys* **2016**, *16* (1), 123–134. https://doi.org/10.5194/acp-16-123-2016.

(260) Donahue, N. M.; Epstein, S. A.; Pandis, S. N.; Robinson, A. L. A Two-Dimensional Volatility Basis Set: 1. Organic-Aerosol Mixing Thermodynamics. *Atmos Chem Phys* **2011**, *11* (7), 3303–3318. https://doi.org/10.5194/acp-11-3303-2011.

(261) Donahue, N. M.; Kroll, J. H.; Pandis, S. N.; Robinson, A. L. A Two-Dimensional Volatility Basis Set-Part 2: Diagnostics of Organic-Aerosol Evolution. *Atmos Chem Phys* **2012**, *12* (2), 615–634. https://doi.org/10.5194/acp-12-615-2012.

(262) Shah, R. U.; Coggon, M. M.; Gkatzelis, G. I.; McDonald, B. C.; Tasoglou, A.; Huber, H.; Gilman, J.; Warneke, C.; Robinson, A. L.; Presto, A. A. Urban Oxidation Flow Reactor Measurements Reveal Significant Secondary Organic Aerosol Contributions from Volatile Emissions of Emerging Importance. *Environ Sci Technol* **2020**, *54*, 714–725. https://doi.org/10.1021/acs.est.9b06531.

(263) Surdu, M.; Pospisilova, V.; Xiao, M.; Wang, M.; Mentler, B.; Simon, M.; Stolzenburg, D.; Hoyle, C. R.; Bell, D. M.; Lee, C. P.; Lamkaddam, H.; Lopez-Hilfiker, F.; Ahonen, L. R.; Amorim, A.; Baccarini, A.; Chen, D.; Dada, L.; Duplissy, J.; Finkenzeller, H.; He, X. C.; Hofbauer, V.; Kim, C.; Kürten, A.; Kvashnin, A.; Lehtipalo, K.; Makhmutov, V.; Molteni, U.; Nie, W.; Onnela, A.; Petäjä, T.; Quéléver, L. L. J.; Tauber, C.; Tomé, A.; Wagner, R.; Yan, C.; Prevot, A. S. H.; Dommen, J.; Donahue, N. M.; Hansel, A.; Curtius, J.; Winkler, P. M.; Kulmala, M.; Volkamer, R.; Flagan, R. C.; Kirkby, J.; Worsnop, D. R.; Slowik, J. G.; Wang, D. S.; Baltensperger, U.; El Haddad, I. Molecular Characterization of Ultrafine Particles Using Extractive Electrospray Time-of-Flight Mass Spectrometry. *Environmental Science: Atmospheres* **2021**, *1* (6), 434–448. https://doi.org/10.1039/D1EA00050K.

(264) Li, Y.; Pöschl, U.; Shiraiwa, M. Molecular Corridors and Parameterizations of Volatility in the Chemical Evolution of Organic Aerosols. *Atmos Chem Phys* **2016**, *16* (5), 3327–3344. https://doi.org/10.5194/acp-16-3327-2016.

(265) Fernandez, L. Wastewater Pollution Abatement across an International Border. *Environ Dev Econ* **2009**, *14* (1), 67–88. https://doi.org/10.1017/S1355770X08004543.

(266) County of San Diego Board of Supervisors. FRAMEWORK FOR OUR FUTURE: DECLARING POLLUTION AT THE TIJUANA RIVER VALLEY A PUBLIC HEALTH CRISIS (DISTRICTS: ALL). **2021**, No. 11, 1–2.

(267) United States Environmental Protection Agency. Joint Record of Decision for the Final Programmatic Environmental Impact Statement for United States-Mexico-Canada Agreement Mitigation of Contaminated Transboundary Flows Project. **2023**.

(268) Yadav, M. K.; Short, M. D.; Aryal, R.; Gerber, C.; Akker, B. Van Den; Saint, C. P. Occurrence of Illicit Drugs in Water and Wastewater and Their Removal during Wastewater Treatment. *Water Res* **2017**, *124*, 713–727. https://doi.org/10.1016/j.watres.2017.07.068.

(269) Bolong, N.; Ismail, A. F.; Salim, M. R.; Matsuura, T. A Review of the Effects of Emerging Contaminants in Wastewater and Options for Their Removal. *Desalination* **2009**, *239* (1–3), 229–246. https://doi.org/10.1016/J.DESAL.2008.03.020.

(270) Yuan, X.; Hu, J.; Li, S.; Yu, M. Occurrence, Fate, and Mass Balance of Selected Pharmaceutical and Personal Care Products (PPCPs) in an Urbanized River. *Environmental Pollution* **2020**, *266*, 115340. https://doi.org/10.1016/j.envpol.2020.115340.

(271) Liu, W. R.; Yang, Y. Y.; Liu, Y. S.; Zhang, L. J.; Zhao, J. L.; Zhang, Q. Q.; Zhang, M.; Zhang, J. N.; Jiang, Y. X.; Ying, G. G. Biocides in Wastewater Treatment Plants: Mass Balance Analysis and Pollution Load Estimation. *J Hazard Mater* **2017**, *329*, 310–320. https://doi.org/10.1016/j.jhazmat.2017.01.057.

(272) Gogoi, A.; Mazumder, P.; Tyagi, V. K.; Tushara Chaminda, G. G.; An, A. K.; Kumar, M. Occurrence and Fate of Emerging Contaminants in Water Environment: A Review. *Groundw Sustain Dev* **2018**, *6*, 169–180. https://doi.org/10.1016/J.GSD.2017.12.009.

(273) Fu, L.; Li, J.; Wang, G.; Luan, Y.; Dai, W. Ecotoxicology and Environmental Safety Adsorption Behavior of Organic Pollutants on Microplastics. *Ecotoxicol Environ Saf* **2021**, *217* (November 2020), 112207. https://doi.org/10.1016/j.ecoenv.2021.112207.

(274) Cuadrat, R. R. C.; Sorokina, M.; Andrade, B. G.; Goris, T.; Dávila, A. M. R. Global Ocean Resistome Revealed: Exploring Antibiotic Resistance Gene Abundance and Distribution in TARA Oceans Samples. *Gigascience* **2020**, *9* (5), 1–12. https://doi.org/10.1093/gigascience/giaa046.

(275) Sha, B.; Johansson, J. H.; Salter, M. E.; Blichner, S. M.; Cousins, I. T. Constraining Global Transport of Perfluoroalkyl Acids on Sea Spray Aerosol Using Field Measurements. *Sci Adv* **2024**, *10* (14), 1026. https://doi.org/10.1126/SCIADV.ADL1026/SUPPL_FILE/SCIADV.ADL1026_DATA_S1_AND_S2.ZIP.

(276) Harb, C.; Pokhrel, N.; Foroutan, H. Quantification of the Emission of Atmospheric Microplastics and Nanoplastics via Sea Spray. *Environ Sci Technol Lett* **2023**, *10* (6), 513–519. https://doi.org/10.1021/ACS.ESTLETT.3C00164/SUPPL_FILE/EZ3C00164_SI_001.PDF.

(277) Sha, B.; Ungerovich, E.; Salter, M. E.; Cousins, I. T.; Johansson, J. H. Enrichment of Perfluoroalkyl Acids on Sea Spray Aerosol in Laboratory Experiments: The Role of Dissolved Organic Matter, Air Entrainment Rate and Inorganic Ion Composition. *Environ Sci Technol Lett* **2024**, 0–5. https://doi.org/10.1021/acs.estlett.4c00287.

(278) Quinn, P. K.; Collins, D. B.; Grassian, V. H.; Prather, K. A.; Bates, T. S. Chemistry and Related Properties of Freshly Emitted Sea Spray Aerosol. *Chem Rev* **2015**, *115* (10), 4383–4399. https://doi.org/10.1021/cr500713g.

(279) Russell, L. M.; Hawkins, L. N.; Frossard, A. A.; Quinn, P. K.; Bates, T. S. Carbohydrate-like Composition of Submicron Atmospheric Particles and Their Production from Ocean Bubble Bursting. https://doi.org/10.1073/pnas.0908905107.

(280) Trainic, M.; Flores, J. M.; Pinkas, I.; Pedrotti, M. L.; Lombard, F.; Bourdin, G.; Gorsky, G.; Boss, E.; Rudich, Y.; Vardi, A.; Koren, I. Airborne Microplastic Particles Detected in the Remote Marine Atmosphere. *Commun Earth Environ* **2020**, *1* (1), 1–9. https://doi.org/10.1038/s43247-020-00061-y.

(281) Small, M. *Imperial beach closed almost 900 days due to Tijuana river sewage issue*. ABC 10 News San Diego.

(282) Park, J.; Jang, J.; Yoon, Y. J.; Kang, S.; Kang, H.; Park, K.; Cho, K. H.; Kim, J. H.; Dall'Osto, M.; Lee, B. Y. When River Water Meets Seawater: Insights into Primary Marine Aerosol Production. *Science of the Total Environment* **2022**, *807*, 150866. https://doi.org/10.1016/j.scitotenv.2021.150866.

(283) May, N. W.; Axson, J. L.; Watson, A.; Pratt, K. A.; Ault, A. P. Lake Spray Aerosol Generation: A Method for Producing Representative Particles from Freshwater

Wave Breaking. *Atmos Meas Tech* **2016**, *9* (9), 4311–4325. https://doi.org/10.5194/AMT-9-4311-2016.

(284) (Sedac), S. D. and A. C. Percentage of Total Population Living in Coastal Areas. *United Nations* **2008**, 170–175.

(285) Tuholske, C.; Halpern, B. S.; Blasco, G.; Villasenor, J. C.; Frazier, M.; Caylor, K. Mapping Global Inputs and Impacts from of Human Sewage in Coastal Ecosystems. *PLoS One* **2021**, *16* (11 November), 1–16. https://doi.org/10.1371/journal.pone.0258898.

(286) Mimura, N. Sea-Level Rise Caused by Climate Change and Its Implications for Society. *Proc Jpn Acad Ser B Phys Biol Sci* **2013**, *89* (7), 281–301. https://doi.org/10.2183/pjab.89.281.

(287) International Boundary and Water Commission. *Water Data Portal*. https://waterdata.ibwc.gov/AQWebportal.

(288) CDIP. *Coastal Data Information Program*. Scripps Institution of Oceanography. http://cdip.ucsd.edu/themes/data/download/?station=155&stream=p1&sub_stream=p1&public=1&start=202001&end=202005&file_type=pm&download_mode=browser (accessed 2022-06-05).

(289) Gaston, C. J.; Quinn, P. K.; Bates, T. S.; Gilman, J. B.; Bon, D. M.; Kuster, W. C.; Prather, K. A. The Impact of Shipping, Agricultural, and Urban Emissions on Single Particle Chemistry Observed Aboard the R/V Atlantis during CalNex. *Journal of Geophysical Research Atmospheres* **2013**, *118* (10), 5003–5017. https://doi.org/10.1002/jgrd.50427.

(290) NERRS. *NOAA National Estuarine Research Reserve System*. NERSS. http://www.nerrsdata.org (accessed 2022-05-03).

(291) CDIP. *Coastal Data Information Program*. Scripps Institution of Oceanography. http://cdip.ucsd.edu/themes/data/download/?station=073&stream=p1&sub_stream=p2&public=1&start=202001&end=202003&file_type=dw&download_mode=browser (accessed 2022-05-01).

(292) Pereira, D. *Wind Rose*. MATLAB Central File Exchange. https://www.mathworks.com/matlabcentral/fileexchange/47248-wind-rose (accessed 2017-05-31).

(293) Corral, A. F.; Dadashazar, H.; Stahl, C.; Edwards, E. Lou; Zuidema, P.; Sorooshian, A. Source Apportionment of Aerosol at a Coastal Site and Relationships with Precipitation Chemistry: A Case Study over the Southeast United States. *Atmosphere (Basel)* **2020**, *11* (11). https://doi.org/10.3390/ATMOS11111212.

(294) Ault, A. P.; Moore, M. J.; Furutani, H.; Prather, K. A. Impact of Emissions from the Los Angeles Port Region on San Diego Air Quality during Regional Transport Events. *Environ Sci Technol* **2009**, *43* (10), 3500–3506. https://doi.org/10.1021/ES8018918/SUPPL_FILE/ES8018918_SI_001.PDF.

(295) Stohl, A.; Hittenberger, M.; Wotawa, G. Validation of the Lagrangian Particle Dispersion Model FLEXPART against Large-Scale Tracer Experiment Data. *Atmos Environ* **1998**, *32* (24), 4245–4264. https://doi.org/10.1016/S1352-2310(98)00184-8.

(296) Saha, S.; Moorthi, S.; Wu, X.; Wang, J.; Nadiga, S.; Tripp, P.; Behringer, D.; Hou, Y.-T.; Chuang, H.; Iredell, M.; Ek, M.; Meng, J.; Yang, R.; Mendez, M. P.; van den Dool, H.; Zhang, Q.; Wang, W.; Chen, M.; Becker, E. NCEP Climate Forecast System Version 2 (CFSv2) 6-Hourly Products. Research Data Archive at the National Center for Atmospheric Research, Computational and Information Systems Laboratory: Boulder CO 2011. https://doi.org/10.5065/D61C1TXF.

(297) Chen, X.; Zhang, F.; Zhao, K. Diurnal Variations of the Land–Sea Breeze and Its Related Precipitation over South China. *J Atmos Sci* **2016**, *73* (12), 4793–4815. https://doi.org/10.1175/JAS-D-16-0106.1.

(298) Miller, S. T. K.; Keim, B. D.; Talbot, R. W.; Mao, H. Sea Breeze: Structure, Forecasting, and Impacts. *Reviews of Geophysics* **2003**, *41* (3), 1011. https://doi.org/10.1029/2003RG000124.

(299) Lo, J. C. F.; Lau, A. K. H.; Fung, J. C. H.; Chen, F.; Lo, C. :; Lau, A. K. H.; Fung, J. C. H.; Chen, F. Investigation of Enhanced Cross-City Transport and Trapping of Air Pollutants by Coastal and Urban Land-Sea Breeze Circulations. *Journal of Geophysical Research: Atmospheres* **2006**, *111* (D14), 14104. https://doi.org/10.1029/2005JD006837.

(300) Dittmar, T.; Koch, B.; Hertkorn, N.; Kattner, G. A Simple and Efficient Method for the Solid-Phase Extraction of Dissolved Organic Matter (SPE-DOM) from Seawater. *Limnol Oceanogr Methods* **2008**, *6* (6), 230–235. https://doi.org/10.4319/lom.2008.6.230.

(301) Petras, D.; Koester, I.; Silva, R. Da; Stephens, B. M.; Haas, A. F.; Nelson, C. E.; Kelly, L. W.; Aluwihare, L. I.; Dorrestein, P. C. High-Resolution Liquid Chromatography Tandem Mass Spectrometry Enables Large Scale Molecular Characterization of Dissolved Organic Matter. *Frontiers in Marine Science*. 2017. https://doi.org/10.3389/fmars.2017.00405.

(302) Chambers, M. C.; MacLean, B.; Burke, R.; Amodei, D.; Ruderman, D. L.; Neumann, S.; Gatto, L.; Fischer, B.; Pratt, B.; Egertson, J.; Hoff, K.; Kessner, D.; Tasman, N.; Shulman, N.; Frewen, B.; Baker, T. A.; Brusniak, M. Y.; Paulse, C.; Creasy, D.; Flashner, L.; Kani, K.; Moulding, C.; Seymour, S. L.; Nuwaysir, L. M.; Lefebvre, B.; Kuhlmann, F.; Roark, J.; Rainer, P.; Detlev, S.; Hemenway, T.; Huhmer, A.; Langridge, J.; Connolly, B.; Chadick, T.; Holly, K.; Eckels, J.;

Deutsch, E. W.; Moritz, R. L.; Katz, J. E.; Agus, D. B.; MacCoss, M.; Tabb, D. L.; Mallick, P. A Cross-Platform Toolkit for Mass Spectrometry and Proteomics. *Nat Biotechnol* **2012**, *30* (10), 918–920. https://doi.org/10.1038/nbt.2377.

(303) Pluskal, T.; Castillo, S.; Villar-Briones, A.; Orešič, M. MZmine 2: Modular Framework for Processing, Visualizing, and Analyzing Mass Spectrometry-Based Molecular Profile Data. *BMC Bioinformatics* **2010**, *11*. https://doi.org/10.1186/1471-2105-11-395.

(304) Buerge, I. J.; Poiger, T.; Müller, M. D.; Buser, H. R. Caffeine, an Anthropogenic Marker for Wastewater Contamination of Surface Waters. *Environ Sci Technol* **2003**, *37* (4), 691–700. https://doi.org/10.1021/es020125z.

(305) Li, S.; Wen, J.; He, B.; Wang, J.; Hu, X.; Liu, J. Occurrence of Caffeine in the Freshwater Environment: Implications for Ecopharmacovigilance. *Environmental Pollution* **2020**, *263*, 114371. https://doi.org/10.1016/j.envpol.2020.114371.

(306) Vieira, L. R.; Soares, A. M. V. M.; Freitas, R. Caffeine as a Contaminant of Concern: A Review on Concentrations and Impacts in Marine Coastal Systems. *Chemosphere* **2022**, *286* (P2), 131675. https://doi.org/10.1016/j.chemosphere.2021.131675.

(307) IBWC. Binational Water Quality Study of the Tijuana River and Adjacent Canyons and Drains: December 2018 to November 2019. **2020**, No. November 2019.

(308) Müller, K.; Hübner, D.; Huppertsberg, S.; Knepper, T. P.; Zahn, D. Probing the Chemical Complexity of Tires: Identification of Potential Tire-Borne Water Contaminants with High-Resolution Mass Spectrometry. *Science of the Total Environment* **2022**, *802*. https://doi.org/10.1016/J.SCITOTENV.2021.149799.

(309) Dsikowitzky, L.; Nordhaus, I.; Sujatha, C. H.; Akhil, P. S.; Soman, K.; Schwarzbauer, J. A Combined Chemical and Biological Assessment of Industrial Contamination in an Estuarine System in Kerala, India. *Science of the Total Environment* **2014**, *485–486* (1), 348–362. https://doi.org/10.1016/j.scitotenv.2014.03.034.

(310) Shoeib, M.; Schuster, J.; Rauert, C.; Su, K.; Smyth, S. A.; Harner, T. Emission of Poly and Perfluoroalkyl Substances, UV-Filters and Siloxanes to Air from Wastewater Treatment Plants. *Environmental Pollution* **2016**, *218*, 595–604. https://doi.org/10.1016/j.envpol.2016.07.043.

(311) Johnson, O. E.; Patel, H.; Miskelly, G. M.; Rindelaub, J. D. Drug Substances in the Air of a New Zealand City. *Atmos Pollut Res* **2023**, *14* (5), 101750. https://doi.org/10.1016/j.apr.2023.101750.

(312) Raynor, P. C.; Bartekova, A.; Griggs, J. G.; Simcik, M. F.; Adgate, J. L. Airborne Diazinon Concentrations during and after Outdoor Spray Application. *J Occup*

*Environ Hyg* **2010**, *7* (9), 506–515. https://doi.org/10.1080/15459624.2010.486699.

(313) Zuccato, E.; Chiabrando, C.; Castiglioni, S.; Calamari, D.; Bagnati, R.; Schiarea, S.; Fanelli, R. Cocaine in Surface Waters: A New Evidence-Based Tool to Monitor Community Drug Abuse. *Environmental Health* **2005**, *4*, 14. https://doi.org/10.1186/1476-069X-4-14.

(314) Viana, M.; Postigo, C.; Querol, X.; Alastuey, A.; López De Alda, M. J.; Barceló, D.; Artíñano, B.; López-Mahia, P.; García Gacio, D.; Cots, N. Cocaine and Other Illicit Drugs in Airborne Particulates in Urban Environments: A Reflection of Social Conduct and Population Size. *Environmental Pollution* **2011**, *159* (5), 1241–1247. https://doi.org/10.1016/J.ENVPOL.2011.01.032.

(315) Grythe, H.; Ström, J.; Krejci, R.; Quinn, P.; Stohl, A. A Review of Sea-Spray Aerosol Source Functions Using a Large Global Set of Sea Salt Aerosol Concentration Measurements. *Atmos Chem Phys* **2014**, *14* (3), 1277–1297. https://doi.org/10.5194/acp-14-1277-2014.

(316) Salter, M. E.; Zieger, P.; Acosta Navarro, J. C.; Grythe, H.; Kirkeväg, A.; Rosati, B.; Riipinen, I.; Nilsson, E. D. An Empirically Derived Inorganic Sea Spray Source Function Incorporating Sea Surface Temperature. *Atmos Chem Phys* **2015**, *15* (19), 11047–11066. https://doi.org/10.5194/acp-15-11047-2015.

(317) Lewis, R.; Schwartz, E. *Sea Salt Aerosol Production: Mechanisms, Methods, Measurements and Models—A Critical Review*; Geophysical Monograph Series; American Geophysical Union: Washington, D. C., 2004; Vol. 152. https://doi.org/10.1029/GM152.

(318) Socorro, J.; Durand, A.; Temime-roussel, B.; Gligorovski, S.; Wortham, H.; Quivet, E. The Persistence of Pesticides in Atmospheric Particulate Phase : An Emerging Air Quality Issue. *Nature Publishing Group* **2016**, No. May, 1–7. https://doi.org/10.1038/srep33456.

(319) Olson, N. E.; Cooke, M. E.; Shi, J. H.; Birbeck, J. A.; Westrick, J. A.; Ault, A. P. Harmful Algal Bloom Toxins in Aerosol Generated from Inland Lake Water. *Environ Sci Technol* **2020**, *54* (8), 4769–4780. https://doi.org/10.1021/acs.est.9b07727.

(320) Hansch, C.; Leo, A.; Hoekman, D. Hydrophobic, Electronic, and Steric Constants. *ACS Professional Reference Book*. American Chemical Society: Washington, DC 1995, p 17.

(321) Finizio, A.; Mackay, D.; Bidleman, T.; Harner, T. Octanol-Air Partition Coefficient as a Predictor of Partitioning of Semi-Volatile Organic Chemicals to Aerosols. *Atmos Environ* **1997**, *31* (15), 2289–2296. https://doi.org/10.1016/S1352-2310(97)00013-7.

(322) Bondy, A. L.; Wang, B.; Laskin, A.; Craig, R. L.; Nhliziyo, M. V.; Bertman, S. B.; Pratt, K. A.; Shepson, P. B.; Ault, A. P. Inland Sea Spray Aerosol Transport and Incomplete Chloride Depletion: Varying Degrees of Reactive Processing Observed during SOAS. *Environ Sci Technol* **2017**, *51* (17), 9533–9542. https://doi.org/10.1021/ACS.EST.7B02085/SUPPL_FILE/ES7B02085_SI_001.PDF.

(323) Reid, M. J.; Langford, K. H.; Mørland, J.; Thomas, K. V. Quantitative Assessment of Time Dependent Drug-Use Trends by the Analysis of Drugs and Related Metabolites in Raw Sewage. *Drug Alcohol Depend* **2011**, *119* (3), 179–186. https://doi.org/10.1016/j.drugalcdep.2011.06.007.

(324) Horký, P.; Grabic, R.; Grabicová, K.; Brooks, B. W.; Douda, K.; Slavik, O.; Hubená, P.; Santos, E. M. S.; Randák, T. Methamphetamine Pollution Elicits Addiction in Wild Fish. *J Exp Biol* **2021**, *224* (13). https://doi.org/10.1242/JEB.242145.

(325) Danovaro, R.; Bongiorni, L.; Corinaldesi, C.; Giovannelli, D.; Damiani, E.; Astolfi, P.; Greci, L.; Pusceddu, A. Sunscreens Cause Coral Bleaching by Promoting Viral Infections. **2008**, *116* (4), 441–447. https://doi.org/10.1289/ehp.10966.

(326) Williams, B. A.; Watson, J. E. M.; Beyer, H. L.; Klein, C. J.; Montgomery, J.; Runting, R. K.; Roberson, L. A.; Halpern, B. S.; Grantham, H. S.; Kuempel, C. D.; Frazier, M.; Venter, O.; Wenger, A. Global Rarity of Intact Coastal Regions. *Conservation Biology* **2022**, *36* (4), e13874. https://doi.org/10.1111/COBI.13874.

(327) Tumminello, P. R.; James, R. C.; Kruse, S.; Kawasaki, A.; Cooper, A.; Guadalupe-Diaz, I.; Zepeda, K. L.; Crocker, D. R.; Mayer, K. J.; Sauer, J. S.; Lee, C.; Prather, K. A.; Slade, J. H. Evolution of Sea Spray Aerosol Particle Phase State across a Phytoplankton Bloom. *ACS Earth Space Chem* **2021**, *5* (11), 2995–3007. https://doi.org/10.1021/acsearthspacechem.1c00186.

(328) Slade, J. H.; Vanreken, T. M.; Mwaniki, G. R.; Bertman, S.; Stirm, B.; Shepson, P. B. Aerosol Production from the Surface of the Great Lakes. *Geophys Res Lett* **2010**, *37* (18). https://doi.org/10.1029/2010GL043852.

(329) Best, J. Anthropogenic Stresses on the World's Big Rivers. *Nat Geosci* **2019**, *12* (1), 7–21. https://doi.org/10.1038/s41561-018-0262-x.

(330) Wright, L. P.; Zhang, L.; Cheng, I.; Aherne, J.; Wentworth, G. R. Impacts and Effects Indicators of Atmospheric Deposition of Major Pollutants to Various Ecosystems-A Review. *Aerosol Air Qual Res* **2018**, *18* (8), 1953–1992. https://doi.org/10.4209/aaqr.2018.03.0107.

(331) Cooper, A. W.; Rogers, M. M.; Wiggin, K. J.; Slade, J. H. We Need a "Keeling Curve" Approach for Contaminants of Emerging Concern. *Environ Sci Technol* **2023**, 28–31. https://doi.org/10.1021/acs.est.3c03813.

(332) Lamb, J. B.; Van De Water, J. A. J. M.; Bourne, D. G.; Altier, C.; Hein, M. Y.; Fiorenza, E. A.; Abu, N.; Jompa, J.; Harvell, C. D. Seagrass Ecosystems Reduce Exposure to Bacterial Pathogens of Humans, Fishes, and Invertebrates. *Science (1979)* **2017**, *355* (6326), 731–733. https://doi.org/10.1126/SCIENCE.AAL1956/SUPPL_FILE/LAMB.SM.PDF.

(333) Ghanbari, M.; Arabi, M.; Kao, S. C.; Obeysekera, J.; Sweet, W. Climate Change and Changes in Compound Coastal-Riverine Flooding Hazard Along the U.S. Coasts. *Earths Future* **2021**, *9* (5), 1–17. https://doi.org/10.1029/2021EF002055.

(334) US EPA. Estimation Programs Interface Suite™ for Microsoft® Windows, v 4.11. *United States Environmental Protection Agency, Washington, DC, USA.* **2012**.

(335) Archer, C. L.; Jacobson, M. Z. Evaluation of Global Wind Power. *Journal of Geophysical Research D: Atmospheres* **2005**, *110* (12), 1–20. https://doi.org/10.1029/2004JD005462.

(336) EPA. Inhalation Rates. *Exposure Factors Handbook* **2011**.

(337) Steele, J. A.; Blackwood, A. D.; Griffith, J. F.; Noble, R. T.; Schiff, K. C. Quantification of Pathogens and Markers of Fecal Contamination during Storm Events along Popular Surfing Beaches in San Diego, California. *Water Res* **2018**, *136*, 137–149. https://doi.org/10.1016/J.WATRES.2018.01.056.

(338) Jaeglé, L.; Quinn, P. K.; Bates, T. S.; Alexander, B.; Lin, J. T. Global Distribution of Sea Salt Aerosols: New Constraints from in Situ and Remote Sensing Observations. *Atmos Chem Phys* **2011**, *11* (7), 3137–3157. https://doi.org/10.5194/acp-11-3137-2011.

(339) Juliano, C.; Magrini, G. Cosmetic Ingredients as Emerging Pollutants of Environmental and Health Concern. A Mini-Review. *Cosmetics* **2017**, *4* (4), 11. https://doi.org/10.3390/cosmetics4020011.

(340) Baker, L. A.; Horbury, M. D.; Stavros, V. G. Ultrafast Photoprotective Properties of the Sunscreening Agent Octocrylene. *Opt Express* **2016**, *24* (10), 10700. https://doi.org/10.1364/oe.24.010700.

(341) Bratkovics, S.; Sapozhnikova, Y. Determination of Seven Commonly Used Organic UV Filters in Fresh and Saline Waters by Liquid Chromatography-Tandem Mass Spectrometry. *Analytical Methods* **2011**, *3* (12), 2943–2950. https://doi.org/10.1039/c1ay05390f.

(342) Schneider, S. L.; Lim, H. W. Review of Environmental Effects of Oxybenzone and Other Sunscreen Active Ingredients. *J Am Acad Dermatol* **2018**, *80* (1), 266–271. https://doi.org/10.1007/s10556-005-0100-z.

(343) Lozano, C.; Lee, C.; Wattiez, R.; Lebaron, P.; Matallana-Surget, S. Unraveling the Molecular Effects of Oxybenzone on the Proteome of an Environmentally

Relevant Marine Bacterium. *Science of The Total Environment* **2021**, *793*, 148431. https://doi.org/10.1016/j.scitotenv.2021.148431.

(344) Wang, J.; Pan, L.; Wu, S.; Lu, L.; Xu, Y.; Zhu, Y.; Guo, M.; Zhuang, S. Recent Advances on Endocrine Disrupting Effects of UV Filters. *Int J Environ Res Public Health* **2016**, *13* (8), 1–11. https://doi.org/10.3390/ijerph13080782.

(345) DiNardo, J. C.; Downs, C. A. Can Oxybenzone Cause Hirschsprung's Disease? *Reproductive Toxicology* **2019**, *86*, 98–100. https://doi.org/10.1016/J.REPROTOX.2019.02.014.

(346) Wan, Y.; Xue, J.; Kannan, K. Occurrence of Benzophenone-3 in Indoor Air from Albany, New York, USA, and Its Implications for Inhalation Exposure. *Science of the Total Environment* **2015**, *537*, 304–308. https://doi.org/10.1016/j.scitotenv.2015.08.020.

(347) Durand, L.; Habran, N.; Denis, C.; Meulders, L.; Henschel, V.; Amighi, K. Influence of Different Parameters on Droplet Size and Size Distribution of Sprayable Sunscreen Emulsions with High Concentration of UV-Filters. *Int J Cosmet Sci* **2007**, *29* (6), 461–471. https://doi.org/10.1111/J.1468-2494.2007.00408.X.

(348) May, N. W.; Olson, N. E.; Panas, M.; Axson, J. L.; Tirella, P. S.; Kirpes, R. M.; Craig, R. L.; Gunsch, M. J.; China, S.; Laskin, A.; Ault, A. P.; Pratt, K. A. Aerosol Emissions from Great Lakes Harmful Algal Blooms. *Environ Sci Technol* **2018**, *52* (2), 397–405. https://doi.org/10.1021/ACS.EST.7B03609/SUPPL_FILE/ES7B03609_SI_001.PDF.

(349) Japan Chemical Industry Ecology - Toxicology and Information Center. Chemicals Inspection and Testing Institute; Biodegradation and Bioaccumulation Data of Existing Chemicals Based on the CSCL Japan. Hazardous Substances Data Bank (HSDB) 1992.

(350) Lignell, H.; Hinks, M. L.; Nizkorodov, S. A. Exploring Matrix Effects on Photochemistry of Organic Aerosols. *Proc Natl Acad Sci U S A* **2014**, *111* (38), 13780–13785. https://doi.org/10.1073/PNAS.1322106111/-/DCSUPPLEMENTAL.

(351) Barsotti, F.; Bartels-Rausch, T.; De Laurentiis, E.; Ammann, M.; Brigante, M.; Mailhot, G.; Maurino, V.; Minero, C.; Vione, D. Photochemical Formation of Nitrite and Nitrous Acid (HONO) upon Irradiation of Nitrophenols in Aqueous Solution and in Viscous Secondary Organic Aerosol Proxy. *Environ Sci Technol* **2017**, *51* (13), 7486–7495. https://doi.org/10.1021/acs.est.7b01397.

(352) California Ocean Observing Systems Data Portal. *Scripps Pier Automated Shore Station with SeapHOx*. https://data.caloos.org/#metadata/120738/station/data.

(353) Cloern, J. E. Phytoplankton Bloom Dynamics in Coastal Ecosystems: A Review with Some General Lessons from Sustained Investigation of San Francisco Bay, California. *Reviews of Geophysics* **1996**, *34* (2), 127–168. https://doi.org/10.1029/96RG00986.

(354) Menges, F. Spectragryph - Optical Spectroscopy Software. 2022.

(355) Kang, E.; Root, M. J.; Toohey, D. W.; Brune, W. H. Introducing the Concept of Potential Aerosol Mass (PAM). *Atmos Chem Phys* **2007**, *7* (22), 5727–5744. https://doi.org/10.5194/acp-7-5727-2007.

(356) Lambe, A. T.; Krechmer, J. E.; Peng, Z.; Casar, J. R.; Carrasquillo, A. J.; Raff, J. D.; Jimenez, J. L.; Worsnop, D. R. HO x and NO x Production in Oxidation Flow Reactors via Photolysis of Isopropyl Nitrite, Isopropyl Nitrite-d 7 , and 1,3-Propyl Dinitrite at λ = 254, 350, and 369nm. *Atmos Meas Tech* **2019**, *12* (1), 299–311. https://doi.org/10.5194/AMT-12-299-2019.

(357) Peng, Z.; Jimenez, J. L. KinSim: A Research-Grade, User-Friendly, Visual Kinetics Simulator for Chemical-Kinetics and Environmental-Chemistry Teaching. *J Chem Educ* **2019**, *96* (4), 806–811. https://doi.org/10.1021/ACS.JCHEMED.9B00033.

(358) US.EPA. Compendium Method IO-5: Sampling and Analysis for Vapor and Particle Phase Mercury in Ambient Air Utilizing Cold Vapor Atomic Fluorescence Spectrometry (CVAFS). **1999**, No. June.

(359) Neese, F. The ORCA Program System. *Wiley Interdiscip Rev Comput Mol Sci* **2012**, *2* (1), 73–78. https://doi.org/10.1002/WCMS.81.

(360) Neese, F. Software Update: The ORCA Program System, Version 4.0. *Wiley Interdiscip Rev Comput Mol Sci* **2018**, *8* (1), e1327. https://doi.org/10.1002/WCMS.1327.

(361) Garcia-Ratés, M.; Becker, U.; Neese, F. Implicit Solvation in Domain Based Pair Natural Orbital Coupled Cluster (DLPNO-CCSD) Theory. *J Comput Chem* **2021**, *42* (27), 1959–1973. https://doi.org/10.1002/jcc.26726.

(362) Momma, K.; Izumi, F. VESTA3 for Three-Dimensional Visualization of Crystal, Volumetric and Morphology Data. *J Appl Crystallogr* **2011**, *44* (6), 1272–1276. https://doi.org/10.1107/S0021889811038970.

(363) U.S. Environmental Protection Agency. Toxicity Estimation Software Tool (TEST). **2016**, 2–7.

(364) Semones, M. C.; Sharpless, C. M.; MacKay, A. A.; Chin, Y. P. Photodegradation of UV Filters Oxybenzone and Sulisobenzone in Wastewater Effluent and by Dissolved Organic Matter. *Applied Geochemistry* **2017**, *83*, 150–157. https://doi.org/10.1016/J.APGEOCHEM.2017.02.008.

(365) Gago-Ferrero, P.; Badia-Fabregat, M.; Olivares, A.; Piña, B.; Blánquez, P.; Vicent, T.; Caminal, G.; Díaz-Cruz, M. S.; Barceló, D. Evaluation of Fungal- and Photo-Degradation as Potential Treatments for the Removal of Sunscreens BP3 and BP1. *Science of the Total Environment* **2012**, *427–428*, 355–363. https://doi.org/10.1016/j.scitotenv.2012.03.089.

(366) Reid, J. P.; Bertram, A. K.; Topping, D. O.; Laskin, A.; Martin, S. T.; Petters, M. D.; Pope, F. D.; Rovelli, G. The Viscosity of Atmospherically Relevant Organic Particles. *Nat Commun* **2018**, *9* (1). https://doi.org/10.1038/S41467-018-03027-Z.

(367) Ehrlich, R. S.; Dasgupta, S.; Jessup, R. E.; Teppang, K. L.; Shiao, A. L.; Jeoung, K. Y.; Su, X.; Shivkumar, A.; Theodorakis, E. A.; Paesani, F.; Yang, J. Excited State Rotational Freedom Impacts Viscosity Sensitivity in Arylcyanoamide Fluorescent Molecular Rotor Dyes. *Journal of Physical Chemistry B* **2024**. https://doi.org/10.1021/ACS.JPCB.4C00033/SUPPL_FILE/JP4C00033_SI_001.PDF.

(368) Sreejaya, M. M.; Pillai, V. M.; Ayesha, A.; Baby, M.; Bera, M.; Gangopadhyay, M. Mechanistic Analysis of Viscosity-Sensitive Fluorescent Probes for Applications in Diabetes Detection. *J Mater Chem B* **2024**, *12* (12), 2917–2937. https://doi.org/10.1039/D3TB02697C.

(369) Berenbeim, J. A.; Wong, N. G. K.; Cockett, M. C. R. Sodium Cationization Can Disrupt the Intramolecular Hydrogen Bond That Mediates the Sunscreen Activity of Oxybenzone †. **2020**, 19522–19531. https://doi.org/10.1039/d0cp03152f.

(370) Lee, H. D.; Morris, H. S.; Laskina, O.; Sultana, C. M.; Lee, C.; Jayarathne, T.; Cox, J. L.; Wang, X.; Hasenecz, E. S.; Demott, P. J.; Bertram, T. H.; Cappa, C. D.; Stone, E. A.; Prather, K. A.; Grassian, V. H.; Tivanski, A. V. Organic Enrichment, Physical Phase State, and Surface Tension Depression of Nascent Core-Shell Sea Spray Aerosols during Two Phytoplankton Blooms. *ACS Earth Space Chem* **2020**, *4* (4), 650–660. https://doi.org/10.1021/acsearthspacechem.0c00032.

(371) Tinel, L.; Dumas, S.; George, C. A Time-Resolved Study of the Multiphase Chemistry of Excited Carbonyls: Imidazole-2-Carboxaldehyde and Halides. *Comptes Rendus Chimie* **2014**, *17* (7–8), 801–807. https://doi.org/10.1016/J.CRCI.2014.03.008.

(372) Tufail, A.; Price, W. E.; Hai, F. I. Impact of Inorganic Ions and Organic Matter on the Removal of Trace Organic Contaminants by Combined Direct Contact Membrane Distillation–UV Photolysis. *Membranes (Basel)* **2020**, *10* (12), 1–15. https://doi.org/10.3390/membranes10120428.

(373) Cuquerella, M. C.; Lhiaubet-vallet, V.; Cadet, J.; Miranda, M. A. Benzophenone Photosensitized DNA Damage. *Acc Chem Res* **2012**, *45* (9), 1558–1570.

(374) Fuentealba, P.; Pérez, P.; Contreras, R. On the Condensed Fukui Function. *Journal of Chemical Physics* **2000**, *113* (7), 2544–2551. https://doi.org/10.1063/1.1305879.

(375) Endo, S.; Pfennigsdorff, A.; Goss, K. U. Salting-out Effect in Aqueous NaCl Solutions: Trends with Size and Polarity of Solute Molecules. *Environ Sci Technol* **2012**, *46* (3), 1496–1503. https://doi.org/10.1021/ES203183Z.

(376) You, Y.; Bertram, A. K. Effects of Molecular Weight and Temperature on Liquid-Liquid Phase Separation in Particles Containing Organic Species and Inorganic Salts. *Atmos Chem Phys* **2015**, *15* (3), 1351–1365. https://doi.org/10.5194/acp-15-1351-2015.

(377) Grassian, V. H.; Alija, O.; Garcı, L. M.; Gerber, R. B.; Navea, J. G. PH Dependence of the Speciation and Optical Properties of 4-Benzoylbenzoic Acid †. **2023**, 17306–17319. https://doi.org/10.1039/d3cp01520c.

(378) Rissman, T. A.; Varutbangkul, V.; Surratt, J. D.; Topping, D. O.; McFiggans, G.; Flagan, R. C.; Seinfeld, J. H. Cloud Condensation Nucleus (CCN) Behavior of Organic Aerosol Particles Generated by Atomization of Water and Methanol Solutions. *Atmos Chem Phys* **2007**, *7* (11), 2949–2971. https://doi.org/10.5194/acp-7-2949-2007.

(379) Gupta, D.; Eom, H. J.; Cho, H. R.; Ro, C. U. Hygroscopic Behavior of NaCl-MgCl2 Mixture Particles as Nascent Sea-Spray Aerosol Surrogates and Observation of Efflorescence during Humidification. *Atmos Chem Phys* **2015**, *15* (19), 11273–11290. https://doi.org/10.5194/acp-15-11273-2015.

(380) Smith, M. L.; Bertram, A. K.; Martin, S. T. Deliquescence, Efflorescence, and Phase Miscibility of Mixed Particles of Ammonium Sulfate and Isoprene-Derived Secondary Organic Material. *Atmos Chem Phys* **2012**, *12* (20), 9613–9628. https://doi.org/10.5194/ACP-12-9613-2012.

(381) Peckhaus, A.; Grass, S.; Treuel, L.; Zellner, R. Deliquescence and Efflorescence Behavior of Ternary Inorganic/Organic/Water Aerosol Particles. *Journal of Physical Chemistry A* **2012**, *116* (24), 6199–6210. https://doi.org/10.1021/JP211522T/SUPPL_FILE/JP211522T_SI_001.PDF.

(382) Lambe, A. T.; Onasch, T. B.; Croasdale, D. R.; Wright, J. P.; Martin, A. T.; Franklin, J. P.; Massoli, P.; Kroll, J. H.; Canagaratna, M. R.; Brune, W. H.; Worsnop, D. R.; Davidovits, P. Transitions from Functionalization to Fragmentation Reactions of Laboratory Secondary Organic Aerosol (SOA) Generated from the OH Oxidation of Alkane Precursors. *Environ Sci Technol* **2012**, *46* (10), 5430–5437. https://doi.org/10.1021/es300274t.

(383) Ceburnis, D.; Rinaldi, M.; Ovadnevaite, J.; Martucci, G.; Giulianelli, L.; Dowd, C. Marine Submicron Aerosol Gradients, Sources and Sinks. *Atmos Chem Phys* **2016**, *16* (19), 12425–12439. https://doi.org/10.5194/acp-16-12425-2016.

(384) Chen, Q.; Sherwen, T.; Evans, M.; Alexander, B. DMS Oxidation and Sulfur Aerosol Formation in the Marine Troposphere: A Focus on Reactive Halogen and Multiphase Chemistry. *Atmos Chem Phys* **2018**, *18* (18), 13617–13637. https://doi.org/10.5194/acp-18-13617-2018.

(385) Franklin, E. B.; Alves, M. R.; Moore, A. N.; Kilgour, D. B.; Novak, G. A.; Mayer, K.; Sauer, J. S.; Weber, R. J.; Dang, D.; Winter, M.; Lee, C.; Cappa, C. D.; Bertram, T. H.; Prather, K. A.; Grassian, V. H.; Goldstein, A. H. Atmospheric Benzothiazoles in a Coastal Marine Environment. *Environ Sci Technol* **2021**, *55* (23), 15705–15714. https://doi.org/10.1021/acs.est.1c04422.

(386) Fu, P. Q.; Kawamura, K.; Chen, J.; Charrière, B.; Sempéré, R. Organic Molecular Composition of Marine Aerosols over the Arctic Ocean in Summer: Contributions of Primary Emission and Secondary Aerosol Formation. *Biogeosciences* **2013**, *10* (2), 653–667. https://doi.org/10.5194/bg-10-653-2013.

(387) Slade, J. H.; Thalman, R.; Wang, J.; Knopf, D. A. Chemical Aging of Single and Multicomponent Biomass Burning Aerosol Surrogate Particles by OH: Implications for Cloud Condensation Nucleus Activity. *Atmos Chem Phys* **2015**, *15* (17), 10183–10201. https://doi.org/10.5194/acp-15-10183-2015.

(388) Hodshire, A. L.; Campuzano-Jost, P.; Kodros, J. K.; Croft, B.; Nault, B. A.; Schroder, J. C.; Jimenez, J. L.; Pierce, J. R. The Potential Role of Methanesulfonic Acid (MSA) in Aerosol Formation and Growth and the Associated Radiative Forcings. *Atmos Chem Phys* **2019**, *19* (5), 3137–3160. https://doi.org/10.5194/ACP-19-3137-2019.

(389) Moore, A. N.; Cancelada, L.; Kimble, K. A.; Prather, K. A. Secondary Aerosol Formation from Mixtures of Marine Volatile Organic Compounds in a Potential Aerosol Mass Oxidative Flow Reactor. *Environmental Science: Atmospheres* **2024**, *4* (3), 351–361. https://doi.org/10.1039/d3ea00169e.

(390) Lawler, M. J.; Lewis, S. L.; Russell, L. M.; Quinn, P. K.; Bates, T. S.; Coffman, D. J.; Upchurch, L. M.; Saltzman, E. S. North Atlantic Marine Organic Aerosol Characterized by Novel Offline Thermal Desorption Mass Spectrometry: Polysaccharides, Recalcitrant Material, and Secondary Organics. *Atmos Chem Phys* **2020**, *20* (24), 16007–16022. https://doi.org/10.5194/acp-20-16007-2020.

(391) Farmer, D. K.; Matsunaga, A.; Docherty, K. S.; Surratt, J. D.; Seinfeld, J. H.; Ziemann, P. J.; Jimenez, J. L. Response of an Aerosol Mass Spectrometer to Organonitrates and Organosulfates and Implications for Atmospheric Chemistry. *Proc Natl Acad Sci U S A* **2010**, *107* (15), 6670–6675. https://doi.org/10.1073/pnas.0912340107.

(392) Surratt, J. D.; Gómez-González, Y.; Chan, A. W. H.; Vermeylen, R.; Shahgholi, M.; Kleindienst, T. E.; Edney, E. O.; Offenberg, J. H.; Lewandowski, M.; Jaoui, M.; Maenhaut, W.; Claeys, M.; Flagan, R. C.; Seinfeld, J. H. Organosulfate Formation

in Biogenic Secondary Organic Aerosol. *Journal of Physical Chemistry A* **2008**, *112* (36), 8345–8378. https://doi.org/10.1021/jp802310p.

(393) Riva, M.; Chen, Y.; Zhang, Y.; Lei, Z.; Olson, N. E.; Boyer Chelmo, H. C.; Narayan, S.; Yee, L. D.; Green, H. S.; Cui, T.; Zhang, Z.; Baumann, K.; Fort, M.; Edgerton, E.; Budisulistiorini, S. H.; Rose, C. A.; Ribeiro, I. O.; e Oliveira, R. L.; dos Santos, E. O.; Machado, C. M. D.; Szopa, S.; Zhao, Y.; Alves, E. G.; de Sá, S. S.; Hu, W.; Knipping, E. M.; Shaw, S. L.; Duvoisin Junior, S.; de Souza, R. A. F.; Palm, B. B.; Jimenez, J. L.; Glasius, M.; Goldstein, A. H.; Pye, H. O. T.; Gold, A.; Turpin, B. J.; Vizuete, W.; Martin, S. T.; Thornton, J. A.; Dutcher, C. S.; Ault, A. P.; Surratt, J. D. Rising Importance of Organosulfur Species for Aerosol Properties and Future Air Quality. *ChemRxiv* **2019**, 1–29. https://doi.org/10.26434/chemrxiv.7597397.

(394) Nozière, B.; Ekström, S.; Alsberg, T.; Holmström, S. Radical-Initiated Formation of Organosulfates and Surfactants in Atmospheric Aerosols. *Geophys Res Lett* **2010**, *37* (5), 1–6. https://doi.org/10.1029/2009GL041683.

(395) Brüggemann, M.; Xu, R.; Tilgner, A.; Kwong, K. C.; Mutzel, A.; Poon, H. Y.; Otto, T.; Schaefer, T.; Poulain, L.; Chan, M. N.; Herrmann, H. Organosulfates in Ambient Aerosol: State of Knowledge and Future Research Directions on Formation, Abundance, Fate, and Importance. *Environ Sci Technol* **2020**, *54* (7), 3767–3782. https://doi.org/10.1021/acs.est.9b06751.

(396) Hawkins, L. N.; Russell, L. M.; Covert, D. S.; Quinn, P. K.; Bates, T. S. Carboxylic Acids, Sulfates, and Organosulfates in Processed Continental Organic Aerosol over the Southeast Pacific Ocean during VOCALS-REx 2008. *Journal of Geophysical Research Atmospheres* **2010**, *115* (13), 1–16. https://doi.org/10.1029/2009JD013276.

(397) Riva, M.; Chen, Y.; Zhang, Y.; Lei, Z.; Olson, N. E.; Boyer, H. C.; Narayan, S.; Yee, L. D.; Green, H. S.; Cui, T.; Zhang, Z.; Baumann, K.; Fort, M.; Edgerton, E.; Budisulistiorini, S. H.; Rose, C. A.; Ribeiro, I. O.; Oliveira, R. L. E.; Dos Santos, E. O.; Machado, C. M. D.; Szopa, S.; Zhao, Y.; Alves, E. G.; De Sá, S. S.; Hu, W.; Knipping, E. M.; Shaw, S. L.; Duvoisin Junior, S.; De Souza, R. A. F.; Palm, B. B.; Jimenez, J. L.; Glasius, M.; Goldstein, A. H.; Pye, H. O. T.; Gold, A.; Turpin, B. J.; Vizuete, W.; Martin, S. T.; Thornton, J. A.; Dutcher, C. S.; Ault, A. P.; Surratt, J. D. Increasing Isoprene Epoxydiol-to-Inorganic Sulfate Aerosol Ratio Results in Extensive Conversion of Inorganic Sulfate to Organosulfur Forms: Implications for Aerosol Physicochemical Properties. *Environ Sci Technol* **2019**, *53* (15), 8682–8694. https://doi.org/10.1021/acs.est.9b01019.

(398) Wong, J. P. S.; Lee, A. K. Y.; Abbatt, J. P. D. Impacts of Sulfate Seed Acidity and Water Content on Isoprene Secondary Organic Aerosol Formation. *Environ Sci Technol* **2015**, *49* (22), 13215–13221. https://doi.org/10.1021/acs.est.5b02686.

(399) Ye, J.; Abbatt, J. P. D.; Chan, A. W. H. Novel Pathway of SO<Sub>2</Sub> Oxidation in the Atmosphere: Reactions with Monoterpene Ozonolysis Intermediates and Secondary Organic Aerosol. *Atmospheric Chemistry and Physics Discussions* **2017**, 1–35. https://doi.org/10.5194/acp-2017-1054.

(400) Lambe, A. T.; Ahern, A. T.; Williams, L. R.; Slowik, J. G.; Wong, J. P. S.; Abbatt, J. P. D.; Brune, W. H.; Ng, N. L.; Wright, J. P.; Croasdale, D. R.; Worsnop, D. R.; Davidovits, P.; Onasch, T. B. Characterization of Aerosol Photooxidation Flow Reactors: Heterogeneous Oxidation, Secondary Organic Aerosol Formation and Cloud Condensation Nuclei Activity Measurements. *Atmos Meas Tech* **2011**, *4* (3), 445–461. https://doi.org/10.5194/amt-4-445-2011.

(401) Lambe, A. T.; Chhabra, P. S.; Onasch, T. B.; Brune, W. H.; Hunter, J. F.; Kroll, J. H.; Cummings, M. J.; Brogan, J. F.; Parmar, Y.; Worsnop, D. R.; Kolb, C. E.; Davidovits, P. Effect of Oxidant Concentration, Exposure Time, and Seed Particles on Secondary Organic Aerosol Chemical Composition and Yield. *Atmos Chem Phys* **2015**, *15* (6), 3063–3075. https://doi.org/10.5194/acp-15-3063-2015.

(402) Krechmer, J.; Lopez-Hilfiker, F.; Koss, A.; Hutterli, M.; Stoermer, C.; Deming, B.; Kimmel, J.; Warneke, C.; Holzinger, R.; Jayne, J.; Worsnop, D.; Fuhrer, K.; Gonin, M.; De Gouw, J. Evaluation of a New Reagent-Ion Source and Focusing Ion-Molecule Reactor for Use in Proton-Transfer-Reaction Mass Spectrometry. *Anal Chem* **2018**, *90* (20), 12011–12018. https://doi.org/10.1021/ACS.ANALCHEM.8B02641/SUPPL_FILE/AC8B02641_SI_001.PDF.

(403) Kilgour, D. B.; Novak, G. A.; Claflin, M. S.; Lerner, B. M.; Bertram, T. H. Production of Oxygenated Volatile Organic Compounds from the Ozonolysis of Coastal Seawater. *Atmos Chem Phys* **2024**, *24* (6), 3729–3742. https://doi.org/10.5194/acp-24-3729-2024.

(404) Lavi, A.; Vermeuel, M. P.; Novak, G. A.; Bertram, T. H. The Sensitivity of Benzene Cluster Cation Chemical Ionization Mass Spectrometry to Select Biogenic Terpenes. *Atmos Meas Tech* **2018**, *11* (6), 3251–3262. https://doi.org/10.5194/amt-11-3251-2018.

(405) Kercher, J. P.; Riedel, T. P.; Thornton, J. A. Chlorine Activation by N2O5: Simultaneous, in Situ Detection of ClNO2 and N2O5 by Chemical Ionization Mass Spectrometry. *Atmos Meas Tech* **2009**, *2* (1), 193–204. https://doi.org/10.5194/amt-2-193-2009.

(406) Kruve, A.; Kaupmees, K.; Liigand, J.; Oss, M.; Leito, I. Sodium Adduct Formation Efficiency in ESI Source. *Journal of Mass Spectrometry* **2013**, *48* (6), 695–702. https://doi.org/10.1002/jms.3218.

(407) Zhou, S.; Hamburger, M. Formation of Sodium Cluster Ions in Electrospray Mass Spectrometry. *Rapid Communications in Mass Spectrometry* **1996**, *10* (7), 797–

800. https://doi.org/10.1002/(SICI)1097-0231(199605)10:7<797::AID-RCM550>3.0.CO;2-7.

(408) DeCarlo, P. F.; Kimmel, J. R.; Trimborn, A.; Northway, M. J.; Jayne, J. T.; Aiken, A. C.; Gonin, M.; Fuhrer, K.; Horvath, T.; Docherty, K. S.; Worsnop, D. R.; Jimenez, J. L. Field-Deployable, High-Resolution, Time-of-Flight Aerosol Mass Spectrometer. *Anal Chem* **2006**, *78* (24), 8281–8289. https://doi.org/10.1021/AC061249N/SUPPL_FILE/AC061249NSI20060905_075156.PDF.

(409) Nakao, S.; Tang, P.; Tang, X.; Clark, C. H.; Qi, L.; Seo, E.; Asa-Awuku, A.; Cocker, D. Density and Elemental Ratios of Secondary Organic Aerosol: Application of a Density Prediction Method. *Atmos Environ* **2013**, *68*, 273–277. https://doi.org/10.1016/J.ATMOSENV.2012.11.006.

(410) Ristimäki, J.; Virtanen, A.; Marjamäki, M.; Rostedt, A.; Keskinen, J. On-Line Measurement of Size Distribution and Effective Density of Submicron Aerosol Particles. *J Aerosol Sci* **2002**, *33* (11), 1541–1557. https://doi.org/10.1016/S0021-8502(02)00106-4.

(411) Carlton, A. G.; Wiedinmyer, C.; Kroll, J. H. A Review of Secondary Organic Aerosol (SOA) Formation from Isoprene. *Atmos Chem Phys* **2009**, *9* (14), 4987–5005. https://doi.org/10.5194/acp-9-4987-2009.

(412) Nestorowicz, K.; Jaoui, M.; Jan Rudzinski, K.; Lewandowski, M.; Kleindienst, T. E.; Spólnik, G.; Danikiewicz, W.; Szmigielski, R. Chemical Composition of Isoprene SOA under Acidic and Non-Acidic Conditions: Effect of Relative Humidity. *Atmos Chem Phys* **2018**, *18* (24), 18101–18121. https://doi.org/10.5194/acp-18-18101-2018.

(413) Jaoui, M.; Piletic, I. R.; Szmigielski, R.; Rudzinski, K. J.; Lewandowski, M.; Riedel, T. P.; Kleindienst, T. E. Rapid Production of Highly Oxidized Molecules in Isoprene Aerosol via Peroxy and Alkoxy Radical Isomerization Pathways in Low and High NOx Environments: Combined Laboratory, Computational and Field Studies. *Science of the Total Environment* **2021**, *775*, 145592. https://doi.org/10.1016/j.scitotenv.2021.145592.

(414) Zhang, H.; Yee, L. D.; Lee, B. H.; Curtis, M. P.; Worton, D. R.; Isaacman-VanWertz, G.; Offenberg, J. H.; Lewandowski, M.; Kleindienst, T. E.; Beaver, M. R.; Holder, A. L.; Lonneman, W. A.; Docherty, K. S.; Jaoui, M.; Pye, H. O. T.; Hu, W.; Day, D. A.; Campuzano-Jost, P.; Jimenez, J. L.; Guo, H.; Weber, R. J.; de Gouw, J.; Koss, A. R.; Edgerton, E. S.; Brune, W.; Mohr, C.; Lopez-Hilfiker, F. D.; Lutz, A.; Kreisberg, N. M.; Spielman, S. R.; Hering, S. V.; Wilson, K. R.; Thornton, J. A.; Goldstein, A. H. Monoterpenes Are the Largest Source of Summertime Organic Aerosol in the Southeastern United States. *Proceedings of the National Academy of Sciences* **2018**, 201717513. https://doi.org/10.1073/pnas.1717513115.

(415) Saunders, S. M.; Jenkin, M. E.; Derwent, R. G.; Pilling, M. J. Protocol for the Development of the Master Chemical Mechanism, MCM v3 (Part A): Tropospheric Degradation of Non-Aromatic Volatile Organic Compounds. *Atmos Chem Phys* **2003**, *3* (1), 161–180. https://doi.org/10.5194/ACP-3-161-2003.

(416) Wolfe, G. M.; Marvin, M. R.; Roberts, S. J.; Travis, K. R.; Liao, J. The Framework for 0-D Atmospheric Modeling (F0AM) v3.1. *Geosci Model Dev* **2016**, *9* (9), 3309–3319. https://doi.org/10.5194/gmd-9-3309-2016.

(417) Handbook of Property Estimation Methods for Chemicals. *Handbook of Property Estimation Methods for Chemicals* **2000**. https://doi.org/10.1201/9781420026283/HANDBOOK-PROPERTY-ESTIMATION-METHODS-CHEMICALS-DONALD-MACKAY-ROBERT-BOETHLING.

(418) Azam, F.; Fenchel, T.; Field, J.; Gray, J.; Meyer-Reil, L.; Thingstad, F. The Ecological Role of Water-Column Microbes in the Sea. *Mar Ecol Prog Ser* **1983**, *10*, 257–263. https://doi.org/10.3354/meps010257.

(419) Mayer, K. J.; Sauer, J. S.; Dinasquet, J.; Prather, K. A. CAICE Studies: Insights from a Decade of Ocean-Atmosphere Experiments in the Laboratory. *Acc Chem Res* **2020**. https://doi.org/10.1021/acs.accounts.0c00504.

(420) Lee, A.; Goldstein, A. H.; Kroll, J. H.; Ng, N. L.; Varutbangkul, V.; Flagan, R. C.; Seinfeld, J. H. Gas-Phase Products and Secondary Aerosol Yields from the Photooxidation of 16 Different Terpenes. *Journal of Geophysical Research Atmospheres* **2006**, *111* (17), 1–25. https://doi.org/10.1029/2006JD007050.

(421) Qi, L.; Chen, M.; Stefenelli, G.; Pospisilova, V.; Tong, Y.; Bertrand, A.; Hueglin, C.; Ge, X.; Baltensperger, U.; Prévôt, A. S. H.; Slowik, J. G. Organic Aerosol Source Apportionment in Zurich Using an Extractive Electrospray Ionization Time-of-Flight Mass Spectrometer (EESI-TOF-MS) - Part 2: Biomass Burning Influences in Winter. *Atmos Chem Phys* **2019**, *19* (12), 8037–8062. https://doi.org/10.5194/acp-19-8037-2019.

(422) Siegel, K.; Karlsson, L.; Zieger, P.; Baccarini, A.; Schmale, J.; Lawler, M.; Salter, M.; Leck, C.; Ekman, A. M. L.; Riipinen, I.; Mohr, C. Insights into the Molecular Composition of Semivolatile Aerosols in the Summertime Central Arctic Ocean Using FIGAERO-CIMS. *Environmental Science: Atmospheres* **2021**, *1* (4), 161–175. https://doi.org/10.1039/d0ea00023j.

(423) Zhang, H.; Yee, L. D.; Lee, B. H.; Curtis, M. P.; Worton, D. R.; Isaacman-VanWertz, G.; Offenberg, J. H.; Lewandowski, M.; Kleindienst, T. E.; Beaver, M. R.; Holder, A. L.; Lonneman, W. A.; Docherty, K. S.; Jaoui, M.; Pye, H. O. T.; Hu, W.; Day, D. A.; Campuzano-Jost, P.; Jimenez, J. L.; Guo, H.; Weber, R. J.; De Gouw, J.; Koss, A. R.; Edgerton, E. S.; Brune, W.; Mohr, C.; Lopez-Hilfiker, F. D.; Lutz, A.; Kreisberg, N. M.; Spielman, S. R.; Hering, S. V.; Wilson, K. R.; Thornton, J. A.; Goldstein, A. H. Monoterpenes Are the Largest Source of Summertime

Organic Aerosol in the Southeastern United States. *Proc Natl Acad Sci U S A* **2018**, *115* (9), 2038–2043. https://doi.org/10.1073/pnas.1717513115.

(424) Wennberg, P. O.; Bates, K. H.; Crounse, J. D.; Dodson, L. G.; McVay, R. C.; Mertens, L. A.; Nguyen, T. B.; Praske, E.; Schwantes, R. H.; Smarte, M. D.; St Clair, J. M.; Teng, A. P.; Zhang, X.; Seinfeld, J. H. Gas-Phase Reactions of Isoprene and Its Major Oxidation Products. *Chem Rev* **2018**, *118* (7), 3337–3390. https://doi.org/10.1021/acs.chemrev.7b00439.

(425) Kwong, K. C.; Chim, M. M.; Hoffmann, E. H.; Tilgner, A.; Herrmann, H.; Davies, J. F.; Wilson, K. R.; Chan, M. N. Chemical Transformation of Methanesulfonic Acid and Sodium Methanesulfonate through Heterogeneous OH Oxidation. *ACS Earth Space Chem* **2018**, *2* (9), 895–903. https://doi.org/10.1021/acsearthspacechem.8b00072.

(426) Mora Garcia, S. L.; Pandit, S.; Navea, J. G.; Grassian, V. H. Nitrous Acid (HONO) Formation from the Irradiation of Aqueous Nitrate Solutions in the Presence of Marine Chromophoric Dissolved Organic Matter: Comparison to Other Organic Photosensitizers. *ACS Earth Space Chem* **2021**, *5* (11), 3056–3064. https://doi.org/10.1021/ACSEARTHSPACECHEM.1C00292/SUPPL_FILE/SP1C00292_SI_001.PDF.

(427) Kaluarachchi, C. P.; Or, V. W.; Lan, Y.; Hasenecz, E. S.; Kim, D.; Madawala, C. K.; Dorcé, G. P.; Mayer, K. J.; Sauer, J. S.; Lee, C.; Cappa, C. D.; Bertram, T. H.; Stone, E. A.; Prather, K. A.; Grassian, V. H.; Tivanski, A. V. Effects of Atmospheric Aging Processes on Nascent Sea Spray Aerosol Physicochemical Properties. *ACS Earth Space Chem* **2022**, *6* (11), 2732–2744. https://doi.org/10.1021/ACSEARTHSPACECHEM.2C00258/ASSET/IMAGES/LARGE/SP2C00258_0008.JPEG.

(428) Lee, C. P.; Riva, M.; Wang, D.; Tomaz, S.; Li, D.; Perrier, S.; Slowik, J. G.; Bourgain, F.; Schmale, J.; Prevot, A. S. H.; Baltensperger, U.; George, C.; El Haddad, I. Online Aerosol Chemical Characterization by Extractive Electrospray Ionization - Ultrahigh Resolution Mass Spectrometry (EESI-Orbitrap). *Environ Sci Technol* **2020**. https://doi.org/10.1021/acs.est.9b07090.

(429) Keeling, C. D. The Concentration and Isotopic Abundances of Carbon Dioxide in the Atmosphere. *Tellus* **1960**, *12* (2), 200–203. https://doi.org/10.3402/TELLUSA.V12I2.9366.

(430) United Nations. Nations Agree to End Plastic Pollution | United Nations. **2022**.

(431) Sarathana, D.; Winijkul, E. Concentrations of Airborne Microplastics during the Dry Season at Five Locations in Bangkok Metropolitan Region, Thailand. *Atmosphere (Basel)* **2022**, *14* (1), 28. https://doi.org/10.3390/atmos14010028.

(432) González-Pleiter, M.; Edo, C.; Aguilera, Á.; Viúdez-Moreiras, D.; Pulido-Reyes, G.; González-Toril, E.; Osuna, S.; de Diego-Castilla, G.; Leganés, F.; Fernández-

Piñas, F.; Rosal, R. Occurrence and Transport of Microplastics Sampled within and above the Planetary Boundary Layer. *Science of the Total Environment* **2021**, *761*, 143213. https://doi.org/10.1016/j.scitotenv.2020.143213.

(433) Huang, Y.; Qing, X.; Wang, W.; Han, G.; Wang, J. Mini-Review on Current Studies of Airborne Microplastics: Analytical Methods, Occurrence, Sources, Fate and Potential Risk to Human Beings. *TrAC - Trends in Analytical Chemistry* **2020**, *125*, 115821. https://doi.org/10.1016/j.trac.2020.115821.

(434) Boakes, L. C.; Patmore, I. R.; Bancone, C. E. P.; Rose, N. L. High Temporal Resolution Records of Outdoor and Indoor Airborne Microplastics. *Environmental Science and Pollution Research* **2023**, *3*, 39246–39257. https://doi.org/10.1007/s11356-022-24935-0.

(435) Ferrero, L.; Scibetta, L.; Markuszewski, P.; Mazurkiewicz, M.; Drozdowska, V.; Makuch, P.; Jutrzenka-Trzebiatowska, P.; Zaleska-Medynska, A.; Andò, S.; Saliu, F.; Nilsson, E. D.; Bolzacchini, E. Airborne and Marine Microplastics from an Oceanographic Survey at the Baltic Sea: An Emerging Role of Air-Sea Interaction? *Sci Total Environ* **2022**, *824*, 153709. https://doi.org/10.1016/j.scitotenv.2022.153709.

(436) Li, Y.; Shao, L.; Wang, W.; Zhang, M.; Feng, X.; Li, W.; Zhang, D. Airborne Fiber Particles: Types, Size and Concentration Observed in Beijing. *Sci Total Environ* **2020**, *705*, 135967. https://doi.org/10.1016/j.scitotenv.2019.135967.

(437) Yuan, Z.; Li, H. X.; Lin, L.; Pan, Y. F.; Liu, S.; Hou, R.; Xu, X. R. Occurrence and Human Exposure Risks of Atmospheric Microplastics: A Review. *Gondwana Research* **2022**, *108*, 200–212. https://doi.org/10.1016/j.gr.2022.02.001.

(438) Allen, S.; Allen, D.; Phoenix, V. R.; Le Roux, G.; Durántez Jiménez, P.; Simonneau, A.; Binet, S.; Galop, D. Atmospheric Transport and Deposition of Microplastics in a Remote Mountain Catchment. *Nat Geosci* **2019**. https://doi.org/10.1038/s41561-019-0335-5.

(439) Ward, C. P.; Reddy, C. M. We Need Better Data about the Environmental Persistence of Plastic Goods. *Proc Natl Acad Sci U S A* **2020**, *117* (26), 14618–14621. https://doi.org/10.1073/PNAS.2008009117/SUPPL_FILE/PNAS.2008009117.SD01.XLSX.

(440) Malone, K. San Diego and Tijuana's Shared Sewage Problem Has a Long History. *The Washington Post*. June 2, 2020. https://www.washingtonpost.com/outlook/2020/06/02/san-diego-tijuanas-shared-sewage-problem-has-long-history/ (accessed 2024-06-23).

(441) Smythe, W. E. *History of San Diego, 1542-1908*; Jazzybee Verlag, 1908.

(442) Price, J. A. Tijuana: A Study of Symbosis. *New Mexico Quartlery*.

(443) Thompson, L.; Weil, A. White House Swears in First Class of American Climate Corps. *NBC News*. 2024.

(444) Elmer, M. Newsom Won't Explain Why Tijuana River Isn't an Emergency. *Voice of San Diego*. 2023.

(445) *Additional Funding Secured to Address Tijuana River Sewage Crisis*. California Office of the Governor.

(446) SSA, O. Medicare Coverage for Individuals Exposed to Environmental Health Hazards.

(447) McNicholas, G.; Cotton, M. Stakeholder Perceptions of Marine Plastic Waste Management in the United Kingdom. *Ecological Economics* **2019**, *163* (April), 77–87. https://doi.org/10.1016/j.ecolecon.2019.04.022.

(448) Gattringer, C. W. A Revisited Conceptualization of Plastic Pollution Accumulation in Marine Environments: Insights from a Social Ecological Economics Perspective. *Mar Policy* **2018**, *96*, 221–226. https://doi.org/10.1016/J.MARPOL.2017.11.036.

(449) *Montreal Protocol on Substances That Deplete the Ozone Layer*; 1989; Vol. 1, pp 128–136. https://doi.org/10.1093/jel/1.1.128.

(450) *S.B. NO. 2571 A Bill for an Act Relating to Water Pollution*; The Senate, State of Hawai, 2018.

(451) *Act NO. 8185*; The thirty-third legislature of the Virgin Islands, 2019.

(452) *H.B. NO. 21-28, HD1, SSI*; House of Representartives of the Commonwealth of the Northern Marianas Islands.

(453) *The Responsible Tourism Education Act of 2018*; Republic of Palau.

(454) Jack, R. *Sunscreen Innovation Act*; United States Congress.

(455) *Law No. 67 of 2019*; Parliament of Aruba.

(456) DeSantis Signs Controversial Sunscreen Law Blocking Cities from Banning Chemicals That Could Harm Reefs. *Sun Sentinel*.

(457) Nery, É. M.; Martinez, R. M.; Velasco, M. V. R.; Baby, A. R. A Short Review of Alternative Ingredients and Technologies of Inorganic UV Filters. *J Cosmet Dermatol* **2021**, *20* (4), 1061–1065. https://doi.org/https://doi.org/10.1111/jocd.13694.

(458) Manaia, E. B.; Kaminski, R. C. K.; Corrêa, M. A.; Chiavacci, L. A. Inorganic UV Filters. *Brazilian Journal of Pharmaceutical Sciences* **2013**, *49* (2), 201–209. https://doi.org/10.1590/S1984-82502013000200002.

(459) Shandilya, N.; Capron, I. Safer-by-Design Hybrid Nanostructures: An Alternative to Conventional Titanium Dioxide UV Filters in Skin Care Products. *RSC Adv* **2017**, *7* (33), 20430–20439. https://doi.org/10.1039/C7RA02506H.

(460) *Proposition 65 - OEHHA*. https://oehha.ca.gov/proposition-65 (accessed 2024-07-03).

(461) *Senate Bill 2053*; Senate of Hawaii, 2024.

(462) González-Fernández, C.; Toullec, J.; Lambert, C.; Le Goïc, N.; Seoane, M.; Moriceau, B.; Huvet, A.; Berchel, M.; Vincent, D.; Courcot, L.; Soudant, P.; Paul-Pont, I. Do Transparent Exopolymeric Particles (TEP) Affect the Toxicity of Nanoplastics on Chaetoceros Neogracile? *Environmental Pollution* **2019**, *250*, 873–882. https://doi.org/10.1016/J.ENVPOL.2019.04.093.

(463) Zhang, C.; Chen, X.; Wang, J.; Tan, L. Toxic Effects of Microplastic on Marine Microalgae Skeletonema Costatum: Interactions between Microplastic and Algae. *Environmental Pollution* **2017**, *220*, 1282–1288. https://doi.org/10.1016/J.ENVPOL.2016.11.005.

(464) Venâncio, C.; Ferreira, I.; Martins, M. A.; Soares, A. M. V. M.; Lopes, I.; Oliveira, M. The Effects of Nanoplastics on Marine Plankton: A Case Study with Polymethylmethacrylate. *Ecotoxicol Environ Saf* **2019**, *184*, 109632. https://doi.org/10.1016/J.ECOENV.2019.109632.

(465) Sendra, M.; Staffieri, E.; Yeste, M. P.; Moreno-Garrido, I.; Gatica, J. M.; Corsi, I.; Blasco, J. Are the Primary Characteristics of Polystyrene Nanoplastics Responsible for Toxicity and Ad/Absorption in the Marine Diatom Phaeodactylum Tricornutum? *Environmental Pollution* **2019**, *249*, 610–619. https://doi.org/10.1016/J.ENVPOL.2019.03.047.

(466) Seoane, M.; González-Fernández, C.; Soudant, P.; Huvet, A.; Esperanza, M.; Cid, Á.; Paul-Pont, I. Polystyrene Microbeads Modulate the Energy Metabolism of the Marine Diatom Chaetoceros Neogracile. *Environ Pollut* **2019**, *251*, 363–371. https://doi.org/10.1016/J.ENVPOL.2019.04.142.

(467) Wang, S.; Wang, Y.; Liang, Y.; Cao, W.; Sun, C.; Ju, P.; Zheng, L. The Interactions between Microplastic Polyvinyl Chloride and Marine Diatoms: Physiological, Morphological, and Growth Effects. *Ecotoxicol Environ Saf* **2020**, *203*, 111000. https://doi.org/10.1016/J.ECOENV.2020.111000.

(468) Lozano, C.; Matallana-Surget, S.; Givens, J.; Nouet, S.; Arbuckle, L.; Lambert, Z.; Lebaron, P. Toxicity of UV Filters on Marine Bacteria: Combined Effects with

Damaging Solar Radiation. *Science of The Total Environment* **2020**, *722*, 137803. https://doi.org/10.1016/j.scitotenv.2020.137803.

(469) Tashiro, Y.; Kameda, Y. Concentration of Organic Sun-Blocking Agents in Seawater of Beaches and Coral Reefs of Okinawa Island , Japan. *Mar Pollut Bull* **2013**, *77* (1–2), 333–340. https://doi.org/10.1016/j.marpolbul.2013.09.013.

(470) Beiras, R.; Bellas, J.; Cachot, J.; Cormier, B.; Cousin, X.; Engwall, M.; Gambardella, C. Ingestion and Contact with Polyethylene Microplastics Does Not Cause Acute Toxicity on Marine Zooplankton. **2018**, *360* (August), 452–460. https://doi.org/10.1016/j.jhazmat.2018.07.101.

(471) Le Bihanic, F.; Clérandeau, C.; Cormier, B.; Crebassa, J. C.; Keiter, S. H.; Beiras, R.; Morin, B.; Bégout, M. L.; Cousin, X.; Cachot, J. Organic Contaminants Sorbed to Microplastics Affect Marine Medaka Fish Early Life Stages Development. *Mar Pollut Bull* **2020**, *154*, 111059. https://doi.org/10.1016/J.MARPOLBUL.2020.111059.

(472) Rezania, S.; Park, J.; Md Din, M. F.; Mat Taib, S.; Talaiekhozani, A.; Kumar Yadav, K.; Kamyab, H. Microplastics Pollution in Different Aquatic Environments and Biota: A Review of Recent Studies. *Mar Pollut Bull* **2018**, *133*, 191–208. https://doi.org/10.1016/J.MARPOLBUL.2018.05.022.

(473) Fletcher, S.; Azoulay, D.; Barnaba, M.; Cortat, L.; Grabiel, T.; Millar, I.; Tobin, G.; Sagar, A.; Spicer, M.; Degagny, S. A Fee on Plastic Pollution. **2024**.

(474) Barrows, A. P. W.; Cathey, S. E.; Petersen, C. W. Marine Environment Microfiber Contamination: Global Patterns and the Diversity of Microparticle Origins. *Environmental Pollution* **2018**.